Doctoral Dissertation

Coupled Aero-Hydro-Elastoplastic Simulation for FOWT Subjected to Blade Pitch Control Malfunction

(ブレードピッチ制御誤作動時の浮体式風車の空力・流力・弾塑性連成シミュレーション)

SRINIVASAMURTHY, SHARATH

July 2016

Graduate School of Engineering,

Osaka University

Table of Contents

List of Figures

List of Tables

1 Introduction

1.1 Overview and Background

Renewable energy is the need of the hour and wind is the fastest growing clean and renewable energy source. During decades' development, the on-land wind power has proven that wind energy can be an excellent alternative to substitute the traditional fossil-fuel energy. However, some disadvantages of on-land wind power are also obvious and to compensate these weaknesses, offshore wind power system is attracting more and more attention all around the world in recent times.

Compared with on-land wind turbine, offshore wind power has several key benefits and advantages.

- Offshore wind power does not require any land.

  Traditional wind turbine not only needs considerable amount of land but also causes serious noise pollution. So besides the place of wind farm, the surrounding area is also not appropriate for human habitation. It is of great limitation for establishing on-land wind turbine systems in major cities and in places where land source is crucial for other infrastructural developments.

- Offshore wind is typically much stronger than wind on land.

  Unlike wind that hits land, offshore breezes can be strong even in the middle of the afternoon making it much easier to match the power demands of the population. It is advantageous to harness abundantly available offshore wind energy.

Europe is the world leader in offshore wind power, with the first offshore wind farm being installed in Denmark in 1991. In 2008, offshore wind power contributed 0.8 gigawatt (GW) of the total 28 GW of wind power capacity constructed that year. By October 2009, 26 offshore wind farms had been constructed in Europe with an average rated capacity of 76 MW. At the end of 2012, 1,662 turbines at 55 offshore wind farms across 10 European countries were generating electricity enough to power almost five million households [1]. Figure 1.1 shows the annual and cumulative installations of offshore wind in Europe [1].

At the end of 2011, there were 53 European offshore wind farms in waters off Belgium, Denmark, Finland, Germany, Ireland, the Netherlands, Norway, Sweden and the United Kingdom, with an operating capacity of 3,813 MW, while 5,603 MW is under construction [2]. More than 100 GW (or 100,000 MW) of offshore projects are proposed or under development in Europe. The European Wind Energy Association has set a target of 40 GW installed by 2020 and 150 GW by 2030 [3].

As of July 2013, the 175-turbine London Array in the United Kingdom is the largest offshore wind farm in the world with a capacity of 630 MW, followed by Greater Gabbard (504 MW), also in the United Kingdom, Anholt (400 MW) in Denmark, and BARD Offshore 1 (400 MW) in Germany.

There are many large offshore wind farms under construction including Gwynt y Môr (576 MW), Borkum West II (400 MW), and West of Duddon Sands (389 MW) [4]. Table 1.1 presents the largest offshore wind farms in the world until 2014 [4]. The overview of London Array, which is the largest offshore wind farm, is shown in Figure 1.2.

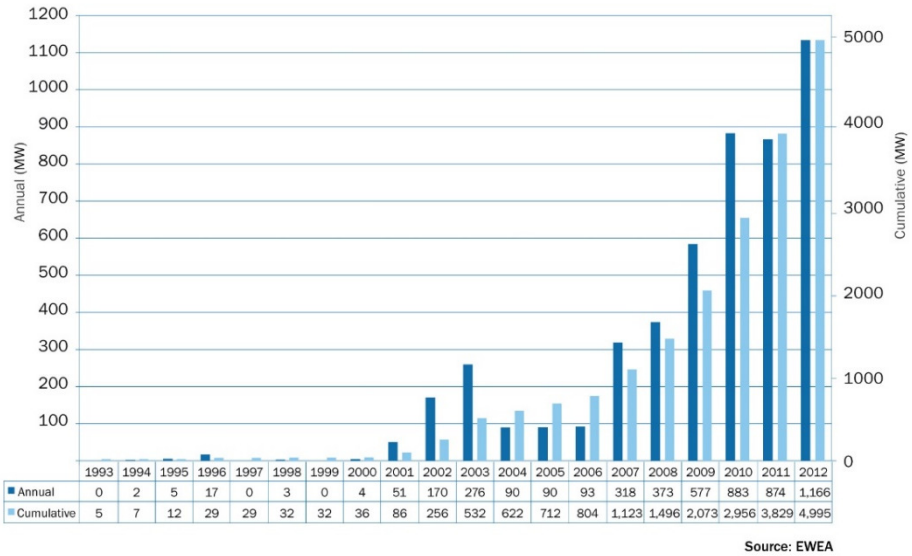

	1993	1994	1995	1996	1997	1998	1999	2000	2001	2002	2003	2004	2005	2006	2007	2008	2009	2010	2011	2012
Annual	0	2	5	17	0	3	0	4	51	170	276	90	90	93	318	373	577	883	874	1,166
Cumulative	5	7	12	29	29	32	32	36	86	256	532	622	712	804	1,123	1,496	2,073	2,956	3,829	4,995

Figure 1.1 Annual and Cumulative Installations of Offshore Wind in Europe. (Reproduced from Reference [1])

Figure 1.2 Overview of London Array. (Reproduced from Reference [4])

Table 1.1 World's largest offshore wind farms.

Wind farm	Capacity (MW)	Country	Turbines and model	Commissioned
London Array	630	United Kingdom	175 × Siemens SWT-3.6	2012
Greater Gabbard	504	United Kingdom	140 × Siemens SWT-3.6	2012
Anholt	400	Denmark	111 × Siemens SWT-3.6-120	2013
BARD Offshore 1	400	Germany	80 x BARD 5.0 turbines	2013
Walney	367	United Kingdom	102 × Siemens SWT-3.6	2012
Thorntonbank	325	Belgium	54 × Senvion 6 MW	2013
Sheringham Shoal	317	United Kingdom	88 × Siemens 3.6	2013
Thanet	300	United Kingdom	100 × Vestas V90-3MW	2010
Meerwind Süd/Ost	288	Germany	80 × Siemens SWT-3.6-120	2014
Lincs	270	United Kingdom	75 × Siemens 3.6	2013
Horns Rev II	209	Denmark	91 × Siemens 2.3-93	2009

(Reproduced from Reference [4])

As of 2015, there are no offshore wind farms in the United States. However, projects are under development in wind-rich areas of the East Coast, Great Lakes, and Pacific coast [5]. The Department of Energy approved ‘wind energy areas’ off the coast where projects can move through the regulatory approval process more quickly. The Department of Energy selected demonstration projects, Virginia Offshore Wind Technology Advancement Project and Fishermen’s Atlantic City Windfarm in May 2014 for the advancement of offshore wind technology. Deepwater Wind is responsible for the first offshore wind farm in the United States, and is expected to be 30-megawatt, 5 turbine Block Island Wind Farm scheduled to be online in late 2016 [6]. Therefore the world is moving into utilizing offshore wind energy rapidly.

All the wind farms mentioned above utilizes the bottom-fixed type of platform (mostly monopole, e.g. London Array or Jacket foundation e.g. Atlantic City Wind Farm) which means the available water depth has to be limited to 30 meters. According to the research of National Renewable Energy Laboratory [7], worldwide deep-water wind resources are extremely abundant in subsea areas with depths up to 600 meters, which are thought to best facilitate transmission of the generated electric power to shore communities.

For Japan, the country's energy landscape is shifting dramatically in the wake of Fukushima crisis, the world's worst nuclear disaster since Chernobyl in 1986. A so-called feed-in tariff (FIT) program that guarantees higher price above the market rates for clean energy to accelerate investment in renewable energy is already started. Citing Germany and China as examples, it is wind, not solar will grow the most under FIT schemes.

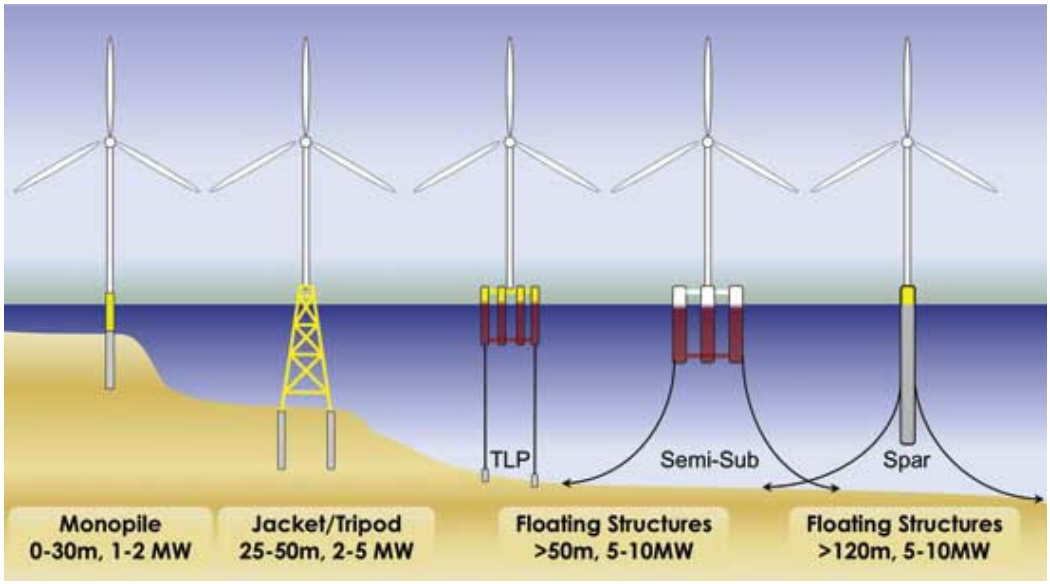

Figure 1.3 Different kinds of offshore wind turbines.
(Reproduced from Reference [7])

Japan Wind Power Association estimates Japan's potential for wind is 144,000 megawatts for onshore and 608,000 megawatts for offshore [8]. Comparing with the 49,000 megawatts of nuclear power, it is possible for Japan to replace the nuclear power by wind energy. Land-Based wind-energy development is limited by Japan's mountains and land scarcity, making offshore developments more viable. Also, from offshore wind speed map (Figure 1.4), opportunity of offshore wind energy potential is convincing [9]. Having the world's 6th largest sea space, the realistic offshore wind potential in Japan is estimated to be 600 GW, with 80% of its wind resources located in deep water (>50m) and this poses challenges to offshore wind turbines. With the advent of new concepts summarized in Figure 1.3, it gives a new outlook to harness the abundant energy potential in deep waters (Figure 1.5) [10].

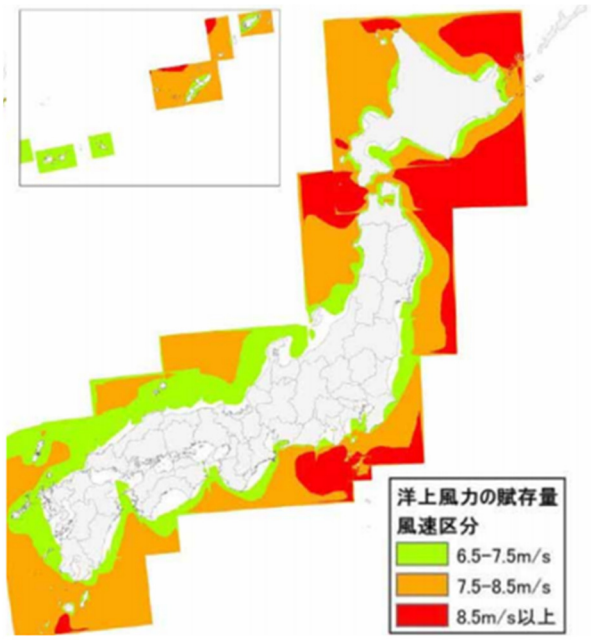

Figure 1.4 Offshore wind speed map in Japan.
(Reproduced from Reference [9])

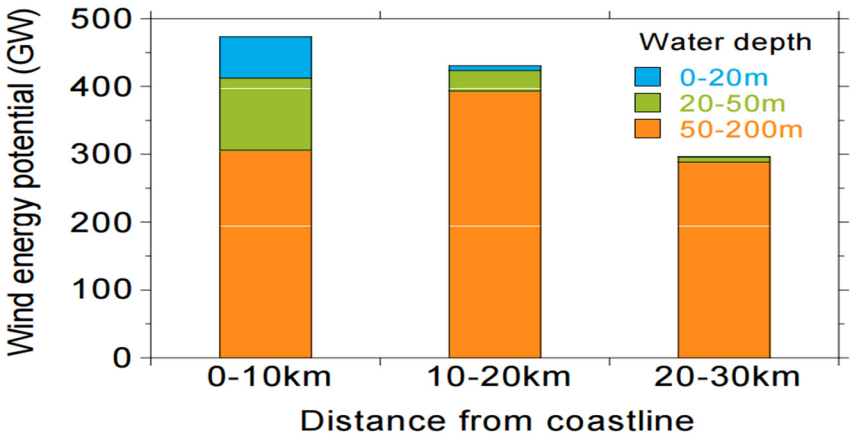

Figure 1.5 Offshore wind energy potential in deep waters.
(Reproduced from Reference [10])

The main requirement and rational solution for such kinds of offshore wind turbines is to have a stable floating platform. This leads us to explore the technology for Floating Offshore Wind Turbine (FOWT) systems which are presently looked at with great interest with huge prospects for solving the world energy crisis. The world's first operational deep-water floating large-capacity wind turbine is the Hywind, in the North Sea off Norway. The 2.3-megawatt turbine was constructed by Siemens Wind Power and mounted on a floating tower with a 100-metre deep draft. This paved way for the various full-scale demonstration projects across the globe. In Japan,

Fukushima floating offshore wind farm (Fukushima Forward) [11] and Goto Island FOWT [12] demonstration projects are under way. The demonstrations so far shows promising alternative to produce sustainable renewable energy systems from deep water floating offshore wind turbines. However the technology for Floating Offshore Wind Turbine (FOWT) systems is still in infancy when compared with the conventional method of deploying bottom fixed counterparts and other FPSOs.

The technology specific to FOWT needs to be addressed from the analysis and design point of view. It is necessary to have a holistic analysis approach for such technologies due to the complexities of FOWT systems. The complexities of FOWT arises from different floaters adopted, such as SPAR, TLP, semi-submersible and barge types and their interaction with the aerodynamic loadings. Equally important are the numerical tools which would help researchers and designers to understand the behavior and response of complex FOWT systems under various environmental conditions. FOWT systems have to tackle both wind and wave loads and various concepts of floater types have been proposed over the years. The sheer intricacies of type of floaters and their interaction with aerodynamics makes it important to have a holistic numerical tool which adopts a combined response approach which can simulate various environmental conditions.

Many researches have been conducted for simulation of the response of FOWT system. The simulation can be classified into two categories, frequency-domain analysis and time-domain analysis. For frequency-domain model, the computational time is much less compared with the time-domain model. So it will be much convenient to utilize the frequency-domain model to obtain the response amplitude operators (RAOs) which is important when designing the floater. A typical frequency-domain model was built by Bulder [13] to obtain the RAOs for the six rigid-body modes which is designed for a 5-MW turbine. Lee [14] also conducted a similar simulation to analyze a TLP design and Spar-Buoy design for 1.5-MW turbine. The research team from NREL and MIT analyzed multiple TLP designs and a shallow drafted barge design for a 5-MW wind turbine [15] [16].

The frequency-domain model however has limitations that it cannot be used to analyze the nonlinear behavior such as the nonlinear structural stiffness or dynamics, nonlinear aerodynamics, nonlinear hydrodynamics and nonlinear coupling influence between mooring-floater and floater-turbine. To overcome these limitations, a coupled time-domain analysis is proposed even though it may take much more computational time.

ISSC2015 report on Offshore Renewable Energy summarizes the numerical codes developed and state of the art research in offshore wind energy [17]. Offshore Code Comparison Collaboration Continuation (OC4) project which operates under the International Energy Agency Wind Task 30 has been started to verify the popular time domain simulation tools [18]. Table 1.2 shows the verified codes and the corresponding developers. It also summarizes the handling of structural dynamics of various codes developed.

Table 1.2 Overview of offshore wind modelling tool capabilities.

Code	Developer	Structural Dynamics
FAST	NREL	T: Mod/MB, P: Rigid
FAST v8	NREL	T: Mod/MB, P: Rigid
CHARM3D+FAST	TAMU+NREL	T: Mod/MB, P: Rigid
OPASS+FAST	CENER+NREL	T: Mod/MB, P: Rigid
UOU+FAST	UOU+NREL	T: Mod/MB, P: Rigid
Bladed	GH	T: Mod/MB, P: Rigid
Bladed Advanced Hydro Beta	GH	T: Mod/MB, P: Rigid
OrcaFlex	Orcina	T: FE, P: Rigid
HAWC2	DTU	T: MB/FE, P: MB/FE
hydro-GAST	NTUA	T: MB/FE, P: MB/FE
Simo+Riflex+AeroDyn	MARINTEK+NREL	T: FE, P: FE
Riflex-Coupled	MARINTEK	T: FE, P: Rigid
3Dfloat	IFE+UMB	T: FE (co-rotated), P: FE
SWT	SAMTEC	T: FE+Mod/MB, P:FE+Mod/MB
DeepLinesWT	PRINCIPIA-IFPEN	T: FE, P: FE
SIMPACK+HydroDyn	SIMPACK	T: FE, P: Rigid
CAsT	University of Tokyo	T: FE, P: FE
Wavec2Wire	WavEC	T: N/A, P: Rigid
WAMSIM	DHI	T: N/A, P: Rigid

T: turbine, P: platform, Mod: modal, MB: multi-body, FE: finite element, N/A: not applicable

(Reproduced and modified from Reference [17])

Among these codes, FAST which is developed by NREL is the one of the most advanced codes to analyze the response of wind turbine system. Based on blade-element/momentum (BEM), generalized dynamic wake (GDW) and dynamic stall theory, the simulation results of aerodynamics can offer a very good correlation with model tests. However, to save the computational time-consuming, the response of flexible structure is obtained by the mode theory

which is not enough when the structural nonlinearity is of interest. From the view of hydrodynamics, the WAMIT which is based the potential theory has been utilized in most codes and shows an acceptable feasibility. However, as it is not an open source and the objects in fluid are always assumed as rigid body, it is not easy to adopt the WAMIT in the simulation of FOWT when considering the structural flexibility.

CHARM3D+FAST is a coupled tool proposed by the cooperation between TAMU and NREL [19]. The rigid platform and dynamic FE mooring is modeled in CHARM3D and the wind turbine and wind tower is handled by FAST. The hydrodynamics of CHARM3D basted on WAMIT is mature in which the linear and nonlinear (e.g. mean drift, Newman's approximation, instantaneous water level et al.) fluid influence can be considered.

Simo+Riflex+AeroDyn [20] is developed mainly by MARINTEK. The aerodynamic force is referred to the AeroDyn which is an independent module in FAST. The structural model in Simo+Riflex+AeroDyn is the most advanced in Table 1.2 as all of the wind tower, platform and mooring are built as FE model. The hydrodynamics in Simo+Riflex+AeroDyn is basically based on first order panel model with considering the mean drift forces due to the first order solution.

The CAsT [21] is developed by the team in University of Tokyo. Linear beam element is utilized to build the wind tower and platform. Mooring is calculated according to lumped mass method. Hydrodynamic load is calculated by the Morison equation. For the Aerodynamic load, they developed their own BEM simulation model.

In most of the numerical simulation tools developed for the response analysis of FOWT system so far, the floater is considered to be a rigid body or linear FE model and it is a huge restriction while considering the natural frequency of the floater and resulting response. The new coupled simulation methodology proposed overcomes the limitation of the floater to be a rigid body and considers the flexibility feature. One of the primary objectives of this research is to overcome the limitation of the floating structure as a rigid body while evaluating the response of floating offshore wind turbines with due considerations to rotor-floater dynamics. One more advantage of considering the flexibility is that the structural load is directly predicted within one-step, instead of usual two-step procedure. With this background, a coupled simulation technique is developed to understand the complex behavior of FOWT system in time-domain.

A number of large onshore wind turbine accidents and eventual collapse of tower have been reported. Caithness Windfarm Information Forum (CWIF) [22] summarizes the statistics of wind turbine accidents (Figure 1.6). CWIF believes that it may only be the "tip of the iceberg" in terms of numbers of accidents and their frequency. Indeed on 11 December 2011 the Daily Telegraph reported that RenewableUK confirmed that there had been 1500 wind turbine accidents and incidents in the UK alone in the past 5 years. Data here reports only 142 UK accidents from 2006-2010 and so the figures here may only represent 9% of actual accidents.

The data does however give an excellent cross-section of the types of accidents which can and do occur, and their consequences. The trend is as expected – as more turbines are built, more accidents occur. Numbers of recorded accidents reflect this, with an average of 21 accidents per year from 1996-2000 inclusive; 57 accidents per year from 2001-2005 inclusive; 118 accidents per year from 2006-10 inclusive, and 163 accidents per year from 2011-15 inclusive.

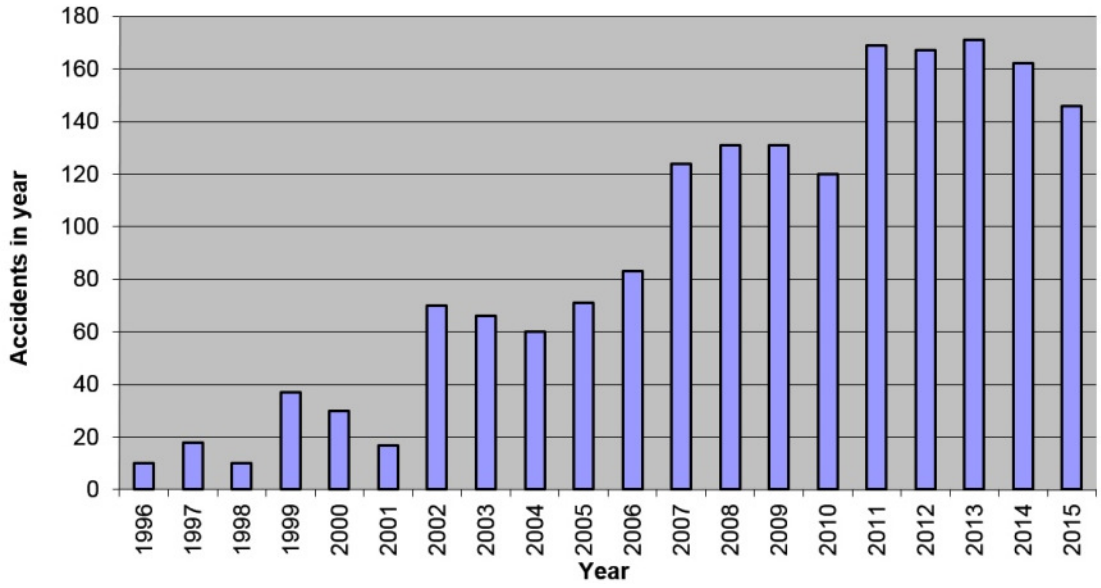

Figure 1.6 Summary of Onshore Wind Turbine Accidents.
(Reproduced from Reference [22])

From the data obtained, structural failure is found to be among one of the major accident causes. It was also the same in Hornslet wind-turbine accident case [23] where structural failure was induced by blade taking off and hitting the tower half-way after control malfunction. These accidents reveals the uncertainties pertinent to structural aspects of onshore wind turbine.

Blade pitch is one of the primary and most important control system implemented for nearly all large modern horizontal-axis wind turbines. The malfunction of blade pitching is possible when the control system fails due to various reasons such as loss of power, control system feedback failure, mechanical failure, etc. The failure of blade pitch control has been found to be an important risk factor for the land based wind turbines as observed in the wind mills accidents at Aoyama in Japan [24]. A 328 foot tall onshore wind turbine worth more than £2 million buckled and collapsed on a mountainside in Northern Ireland [25] on January 2, 2015. The reports suggested the blades of the turbine spun out of control despite only light wind speeds before the structure came crashing to the ground as can be observed in Figure 1.7. The Northern Ireland wind turbine collapse under light winds may also be associated with structural failure due to buckling induced by control malfunction.

Figure 1.7 Northern Ireland wind turbine collapse.
(Reproduced from Reference [25])

The risk involved with failure of control system to onshore wind turbines is clear from above accidents. However, such critical modes of failure for Floating Offshore Wind Turbine system is still not explored. It is necessary to understand the behavior of FOWT systems under the malfunction of blade pitch control as it is one of the most prominent control systems adopted in a wind turbine. The effects of malfunction of blade pitch control needs to be considered and resulting structural load characteristics as well as motion characteristics need to be evaluated. Further, the collapse behavior of FOWT systems due to malfunction of blade pitch control needs to be addressed at elastic and plastic regions from the design point of view to evaluate the risk of structural failure.

1.2 Research Objectives

The present research therefore is targeted to overcome the limitation of the floating structure as a rigid body and considering blade pitch control malfunction into the analysis. In this study, a coupled simulation technique to understand the structural behavior of FOWT system due to blade pitch malfunction, which is simulated in the time series is developed. The effects of malfunction of blade pitch control are considered and resulting structural load characteristics as well as motion characteristics are evaluated. The elastic-plastic analysis is carried out from design point of view after the malfunction of blade pitch control. The collapse behavior is simulated and efforts are made to understand the behavior for a flexible FOWT in the plastic region. With this approach, it is possible to predict the failure modes of the FOWT due to the blade pitch control malfunction and in turn the important parameters for risk assessment. This study will be of importance for the engineering application of the developed coupled concept for the FOWT systems.

In summary, the objectives of this research are as follows.

- Development of a coupled simulation for flexible FOWT system
  Coupled Simulation in time-domain to evaluate the combined response of FOWT system under the combined action of wind and wave. The flexibility of the floating structure is considered.

- Effects of blade pitch control malfunction for FOWT system
  To address the effects of malfunction of blade pitch control and resulting structural load characteristics as well as motion characteristics. To understand the rotor-floater dynamics and it's interaction with the structural load.

- Collapse behavior simulation
  To understand the collapse behavior of FOWT systems due to malfunction of blade pitch control and evaluate the parameters for structural risk assessment. To mitigate the structural failure of FOWT systems arising due to blade pitch malfunction.

1.3 Organization of the Thesis

This section describes the organization of the thesis. It briefly summarizes the chapters' relevance and importance to the present study.

In Chapter 2, the theoretical background of numerical simulation is discussed for the present study. FAST, an aerodynamic load evaluation tool is introduced. The general description of the aerodynamic load evaluation is given and theory used in FAST is discussed. Hydrodynamic load evaluation tool, DYNABEAM is introduced. The linear wave potential theory is introduced and forces evaluated using DYNABEAM model are described. The equation of motion to be solved is also described. The coupling methodology developed in the research is introduced and coupling strategy proposed is discussed from numerical simulation point of view. The working feature of the coupling in 6 DOFs is discussed with preliminary results.

The validation work for numerical simulation code developed between FAST and DYNABEAM is presented in Chapter 3. The validation method and validation strategy employed are discussed. The model of analysis using which the validation work is carried out is also introduced. The RAOs for the motions of the floater is compared for the validity of the code developed. Comparisons between the model of analysis and well established model are discussed and numerical simulation validity for a FOWT system is confirmed. Further, the validation work is concluded with the comparative analysis.

In Chapter 4, blade pitch control is introduced and its effects on the FOWT system are discussed. The numerical simulation under the malfunction of blade pitch control is developed and the strategy of simulation is discussed. The rotor thrust and structural bending moments measured during a scaled model tests are compared with the numerical simulation results for validation. The analytical solutions are also compared with the numerical predictions. The elastic-structural response analysis for the FOWT system under malfunction of blade pitch control is discussed from the design viewpoint. The results of the chapter is summarized in the conclusions.

In Chapter 5, elastic and elastic-plastic behavior analysis methodology is developed adopting coupled simulation code which considers the flexibility of the floater and blade pitch control malfunction. The analysis methodology using capacity curve is introduced. The elastic response is compared with analytical solutions and elastic-plastic response is demonstrated for the severity of strength by simulating a tower structure collapse when it is subjected to extreme vertical bending moment exceeding the ultimate strength capacity. The influence of structural modeling on the response is also discussed.

In Chapter 6, the elastic-plastic analysis of the flexible FOWT system under the malfunction of blade pitch control is given importance and collapse behavior of FOWT system based on parametric dependencies is discussed. Different environmental conditions such as only-wind,

combined wind and wave, various wave periods and wave amplitudes are considered and discussed. The comparison between onshore and floating offshore wind turbine cases are also summarized.

Chapter 7 concludes the thesis with a summary of the main findings. An outlook on possible improvements and future tasks are proposed.

2 Numerical Simulation Theory

In this chapter, the theory utilized for the development of coupled analysis tool is introduced for both the aerodynamic and hydrodynamic load evaluation. Further, the coupling methodology is introduced and preliminary results of coupling are discussed.

2.1 Aerodynamic Load Evaluation

In the present study, aerodynamic load is estimated using the FAST (Fatigue, Aerodynamics, Structures, and Turbulence) Code [26]. It is a comprehensive aero-elastic simulator capable of predicting both the extreme and fatigue loads of two- and three-bladed horizontal-axis wind turbines (HAWTs). This computer aided engineering tool has been developed in National Renewable Energy Laboratory, USA.

2.1.1 General Description

The FAST code can model the dynamic response of both two- and three-bladed, conventional, horizontal-axis wind turbines. The FAST model employs a combined modal and multibody dynamics formulation. The model for two-bladed turbines relates nine rigid bodies (earth, support platform, base plate, nacelle, armature, gears, hub, tail, and structure furling with the rotor) and four flexible bodies (tower, two blades, and drive shaft) through 22 degrees of freedom (DOFs). Accounted for in the degrees of freedom are platform translation and rotation (6 DOF), tower flexibility (4 DOF), nacelle yaw (1 DOF), variable generator and rotor speeds (2 DOF), blade teetering (1 DOF), blade flexibility (6 DOF), rotor-furl (1 DOF), and tail-furl (1 DOF). Flexibility in the blades and tower are characterized using a linear modal representation that assumes small deflections. The three rotational DOFs of the support platform (roll, pitch, and yaw) also employ a small angle approximation. The remaining DOFs may exhibit large displacements without loss of accuracy. The DOFs are summarized in Table 2.1 and further described below.

The first six DOFs originate from the translational (surge, sway, and heave) and rotational (roll, pitch, and yaw) motions of the support platform relative to the inertia frame. Two DOFs originate from the first bending mode of the tower in the longitudinal and transverse directions. Two more DOFs model the second bending mode in the same directions. The tower is rigidly attached to the support platform through a cantilever connection. It is at this location the floater dynamics are coupled in this research. The details of it are discussed in Section 2.3 of the chapter.

Another DOF accounts for the nacelle yaw motion, which can be free or fixed with a torsional yaw spring. The rotor can be either upwind or downwind with the rotor providing yaw loads. The next

DOF accounts for variations in generator speed. Another DOF accounts for drivetrain flexibility associated with torsional motion between the generator and the hub/rotor. Another DOF accounts for teeter motion of the blades about a pin located on the hub. Dampers, springs, or a combination of both can restrict teeter motion.

The next two DOFs arise from the first flapwise bending mode of each blade. Two more DOFs originate from the second flapwise bending modes. Blade edgewise motion accounts for the next two DOFs. The blades are rigidly attached to the hub through a cantilever connection. Motion of the blades is along the local principal axes.

Table 2.1 FAST Degree of Freedom (DOF) Description.

DOF#	2 Bladed Wind Turbine	3 Bladed Wind Turbine
1	Platform Surge	Platform Surge
2	Platform Sway	Platform Sway
3	Platform Heave	Platform Heave
4	Platform Roll	Platform Roll
5	Platform Pitch	Platform Pitch
6	Platform Yaw	Platform Yaw
7	Tower Fore-Aft (Mode 1)	Tower Fore-Aft (Mode 1)
8	Tower Side-to-Side (Mode 1)	Tower Side-to-Side (Mode 1)
9	Tower Fore-Aft (Mode 2)	Tower Fore-Aft (Mode 2)
10	Tower Side-to-Side (Mode 2)	Tower Side-to-Side (Mode 2)
11	Nacelle Yaw	Nacelle Yaw
12	Rotor-Furl	Rotor-Furl
13	Generator Azimuth	Generator Azimuth
14	Drivetrain Torsion	Drivetrain Torsion
15	Tail-Furl	Tail-Furl
16	Blade 1 (Flap Mode 1)	Blade 1 (Flap Mode 1)
17	Blade 1 (Edge Mode 1)	Blade 1 (Edge Mode 1)
18	Blade 1 (Flap Mode 2)	Blade 1 (Flap Mode 2)
19	Blade 2 (Flap Mode 1)	Blade 2 (Flap Mode 1)
20	Blade 2 (Edge Mode 1)	Blade 2 (Edge Mode 1)
21	Blade 2 (Flap Mode 2)	Blade 2 (Flap Mode 2)
22	Rotor-Teeter	Blade 3 (Flap Mode 1)
23		Blade 3 (Edge Mode 1)
24		Blade 3 (Flap Mode 2)

(Reproduced and modified from Reference [26])

The last two DOFs are associated with furling of the rotor and tail about the yawing-portion of the structure atop the tower. The rotor-furl DOF can also be used to model torsional flexibility in the

gearbox mounting if you align the rotor-furl axis with the rotor shaft axis. The amount of furling motion can be restricted with springs, dampers, or a combination of both.

The FAST code can also model a three-bladed HAWT with 24 DOFs. The first six DOFs originate from the translational (surge, sway, and heave) and rotational (roll, pitch, and yaw) motions of the support platform relative to the inertia frame. The next four DOFs account for tower motion; two are longitudinal modes, and two are lateral modes. Yawing motion of the nacelle provides another DOF. The next DOF is for the generator azimuth angle, and another DOF is the compliance in the drivetrain between the generator and hub/rotor. These DOFs account for variable rotor speed and drive-shaft flexibility. The next three DOFs are the blade flapwise tip motion for the first mode.

Three more DOFs give the tip displacement for each blade for the second flapwise mode. The next three DOFs are for the blade edgewise tip displacement for the first edgewise mode. The last two DOFs are for rotor- and tail-furl.

For both the two- and three-bladed wind turbine configurations, we can enable any combination of the available DOFs and features during analysis. The DOFs and features most applicable are dictated by the configuration of the wind turbine.

The FAST input and output files configuration is summarized in Figure 2.1. The configuration consists of the various input parameters of which platform feature can also be incorporated. However, the platform itself is modelled as a rigid body and this limitation leads us to incorporate coupling between aerodynamics and hydrodynamics. Before we discuss about the coupling, the theoretical background for each model is presented. Firstly, the aerodynamic load evaluation is discussed.

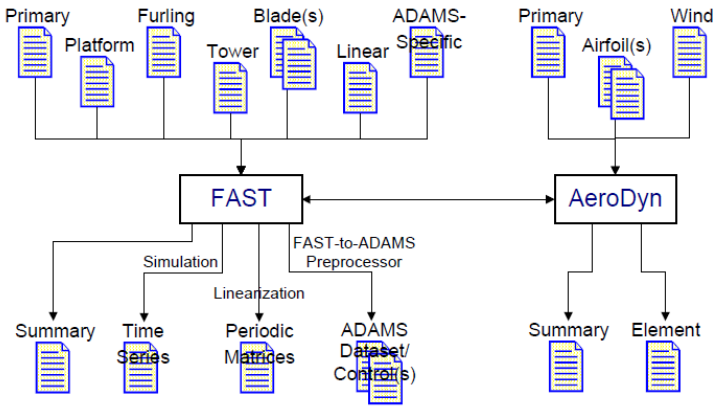

Figure 2.1 FAST Input and Output files.
(Reproduced from Reference [26])

A description of the layout of a conventional, three-bladed turbine is shown in Figure 2.2. Based on this, the co-ordinate systems for setting up the equation is described in the upcoming section.

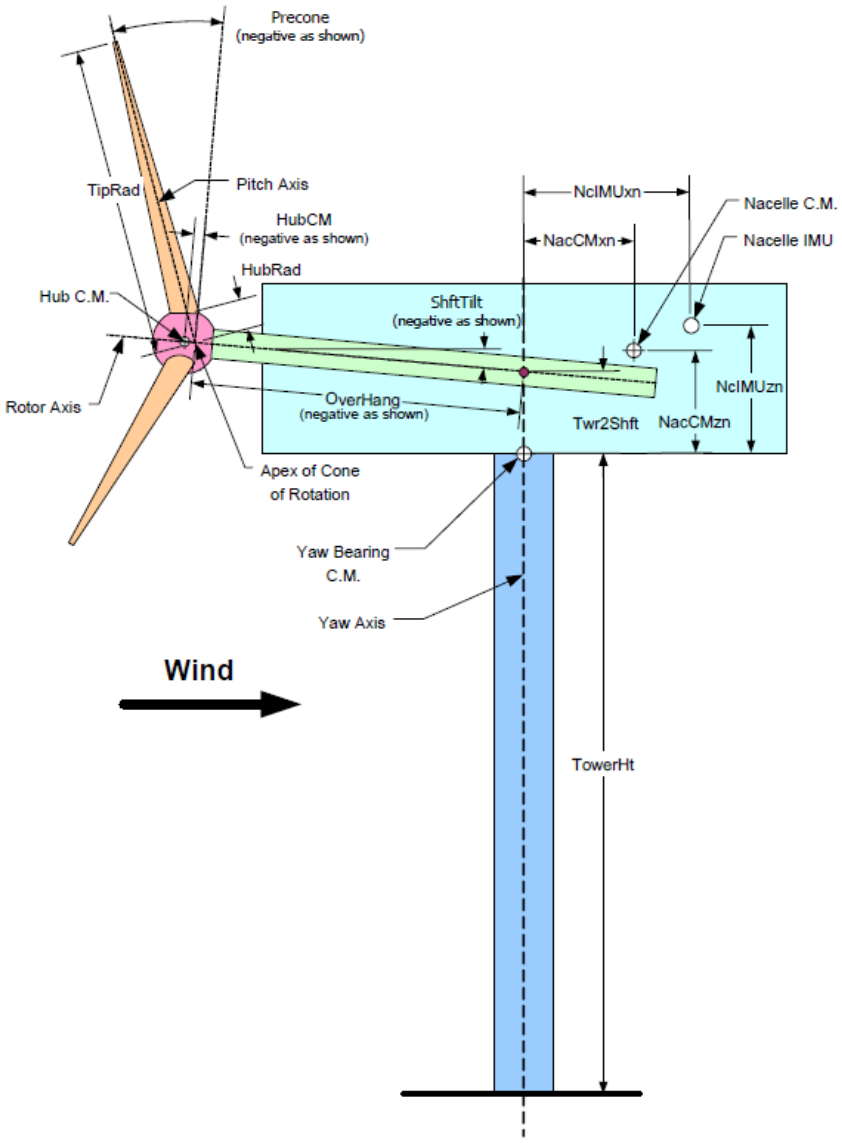

Figure 2.2 Layout of a conventional three-bladed turbine.
(Reproduced from Reference [26])

a)Co-ordinate Systems

The co-ordinate system used for setting up equations of motion for wind turbine is described in this section. Figure 2.3 through Figure 2.9 show the coordinate systems used for input and output parameters. Coordinate systems t, n, h, and b conform to the International Electrotechnical Commission (IEC) standard for wind turbines [27]. Additional coordinate systems i, p, a, s, and c are necessary for interpreting some of the output parameters.

Inertial Frame Coordinate System

Origin	The point about which the translational motions of the support platform (surge, sway, and heave) are defined.
x_i axis	Pointing in the nominal (0°) downwind direction.
y_i axis	Pointing to the left when looking in the nominal downwind direction.
z_i axis	Pointing vertically upward opposite to gravity.

Tower-Base Coordinate System

This coordinate system is fixed in the support platform so that it translates and rotates with the platform.

Origin	Intersection of the center of the tower and the tower base connection to the support platform.
x_t axis	When the support platform has no pitch or yaw displacement, it is aligned with the x_i axis (pointing horizontally in the nominal downwind direction).
y_t axis	When the support platform has no roll or yaw displacement, it is aligned with the y_i axis (pointing to the left when looking in the nominal downwind direction).
z_t axis	Pointing up from the center of the tower.

Figure 2.3 Tower-base co-ordinate system.
(Reproduced from Reference [26])

Tower-Top/Base-Plate Coordinate System

This coordinate system is fixed to the top of the tower. It translates and rotates as the platform moves and the tower bends, but it does not yaw with the nacelle.

Origin	A point on the yaw axis at a height of TowerHt above ground level (see Figure 2.2)
x_p axis	When the tower is not deflected, it is aligned with the x_t axis.
y_p axis	When the tower is not deflected, it is aligned with the y_t axis.
z_p axis	When the tower is not deflected, it is aligned with the z_t axis. It is also the yaw axis.

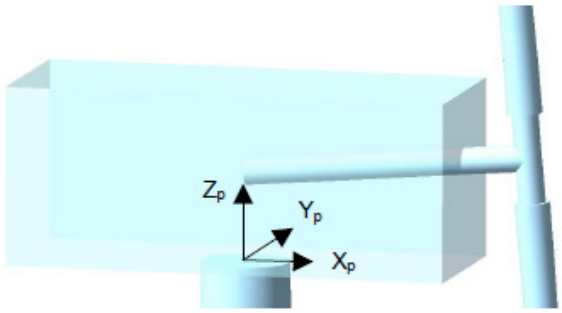

Figure 2.4 Tower-top/base-plate coordinate system.
(Reproduced from Reference [26])

Nacelle/Yaw Coordinate System

This coordinate system translates and rotates with the top of the tower, plus it yaws with the nacelle.

Origin	The origin is the same as that for the tower-top/base-plate coordinate system.
x_n axis	Pointing horizontally toward the nominally downwind end of the nacelle.
y_n axis	Pointing to the left when looking toward the nominally downwind end of the nacelle.
z_n axis	Coaxial with the tower/yaw axis and pointing up.

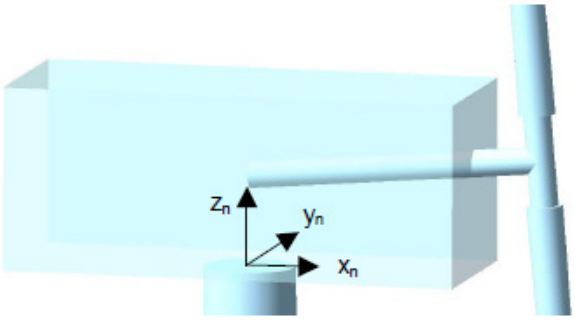

Figure 2.5 Nacelle/Yaw coordinate system.
(Reproduced from Reference [26])

Shaft Coordinate System

The shaft coordinate system does not rotate with the rotor, but it does translate and rotate with the tower and it yaws with the nacelle and furls with the rotor.

Origin	Intersection of the y_n-/z_n - plane and the rotor axis.
x_s axis	Pointing along the (possibly tilted) shaft in the nominally downwind direction.
y_s axis	Pointing to the left when looking from the tower toward the nominally downwind end of the nacelle.
z_s axis	Orthogonal with the x_s and y_s axes such that they form a right-handed coordinate system.

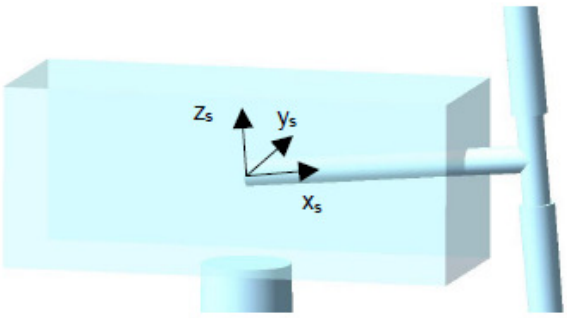

Figure 2.6 Shaft coordinate system.
(Reproduced from Reference [26])

Azimuth Coordinate System

The azimuth, or a, coordinate system is located at the origin of the shaft coordinate system, but it rotates with the rotor. When Blade 1 points up, the azimuth and shaft coordinate systems are parallel. For three bladed rotors, blade 3 is ahead of blade 2, which is ahead of blade 1, so that the order of blades passing through a given azimuth is 3-2-1-repeat.

Hub Coordinate System

The hub coordinate system rotates with the rotor. It also teeters in two-bladed models.

Origin	Intersection of the rotor axis and the plane of rotation (non-coned rotors) or the apex of the cone of rotation (coned rotors).
x_h axis	Pointing along the hub centerline in the nominal downwind direction.
y_h axis	Orthogonal with the x_h and z_h axes such that they form a right-handed coordinate system.
z_h axis	Perpendicular to the hub centerline with the same azimuth as Blade 1.

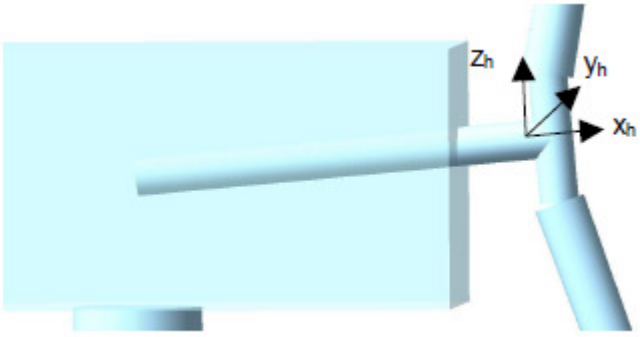

Figure 2.7 Hub coordinate system.
(Reproduced from Reference [26])

Coned Coordinate System

There is a coned coordinate system for each blade that rotates with the rotor. The coordinate system does not pitch with the blades and it also teeters in two bladed models. For three-bladed rotors, blade 3 is ahead of blade 2, which is ahead of blade 1, so that the order of blades passing through a given azimuth is 3-2-1-repeat.

Origin	The origin is the same as that for the hub coordinate system.
$x_{c,i}$ axis	Orthogonal with the yc,i and zc,i axes such that they form a right-handed coordinate system. (i = 1, 2, or 3 for blades 1, 2, or 3, respectively)
$y_{c,i}$ axis	Pointing towards the trailing edge of blade i if the pitch and twist were zero and parallel with the chord line. (i = 1, 2, or 3 for blades 1, 2, or 3, respectively)
$z_{c,i}$ axis	Pointing along the pitch axis towards the tip of blade i. (i = 1, 2, or 3 for blades 1, 2, or 3, respectively)

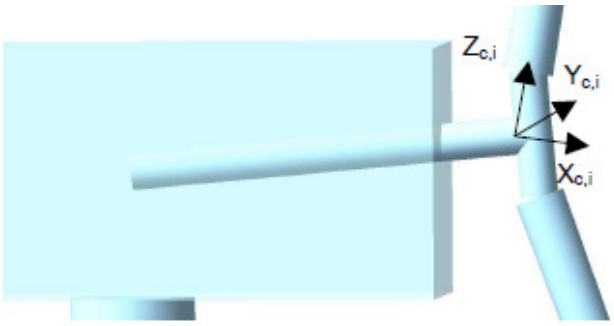

Figure 2.8 Coned coordinate system.
(Reproduced from Reference [26])

Blade Coordinate Systems

These coordinate systems are the same as the coned coordinate systems, except that they pitch with the blades and their origins are at the blade root. For three-bladed rotors, blade 3 is ahead of blade 2, which is ahead of blade 1, so that the order of blades passing through a given azimuth is 3-2-1-repeat.

Origin	Intersection of the blade's pitch axis and the blade root.
$x_{b,i}$ axis	Orthogonal with the yb and zb axes such that they form a right-handed coordinate system. (i = 1, 2, or 3 for blades 1, 2, or 3, respectively)
$y_{b,i}$ axis	Pointing towards the trailing edge of blade i and parallel with the chord line at the zero-twist blade station. (i = 1, 2, or 3 for blades 1, 2, or 3, respectively)
$z_{b,i}$ axis	Pointing along the pitch axis towards the tip of blade i. (i = 1, 2, or 3 for blades 1, 2, or 3, respectively)

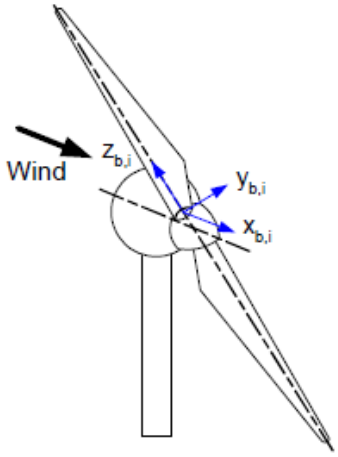

Figure 2.9 Blade coordinate system.
(Reproduced from Reference [26])

b)Flexible Tower and Blades

FAST models flexible elements, such as the tower and blades, using a linear modal representation. The reliability of this representation depends on the generation of accurate mode shapes, which are input into FAST. A program called Modes [28] can be used to generate these shapes and copy its output to our FAST input file. Modes uses essentially the same structural data as FAST.

FAST allows to specify four different mode shapes for the tower. The two fore-aft modes are defined separately from the two side-to-side modes. The mode shapes take the form of a sixth-order polynomial with the zeroth and first terms always being zero. This is because the mode shapes are cantilevered at the base so they must have zero deflection and slope there. At the top of the tower, where the normalized height is 1, the deflection must have a normalized value of 1. This means the sum of the polynomial coefficients must add to 1. See Figure 2.10 for a graphic example of tower mode shapes.

Figure 2.10 Tower mode shapes.
(Reproduced from Reference [26])

The blade mode shapes are defined in a way similar to that of the tower. For the blades, FAST can use two flapwise modes and one edgewise mode. The modes are defined with respect to the local structural twist, that is, the shapes twist with the blade, are three dimensional, and do not lie within a single plane. In the case of a twisted blade, the tip will deflect in both the in-plane and out-of-plane directions due to a pure flapwise deflection. The edgewise mode works in a similar fashion.

c) Support Platform

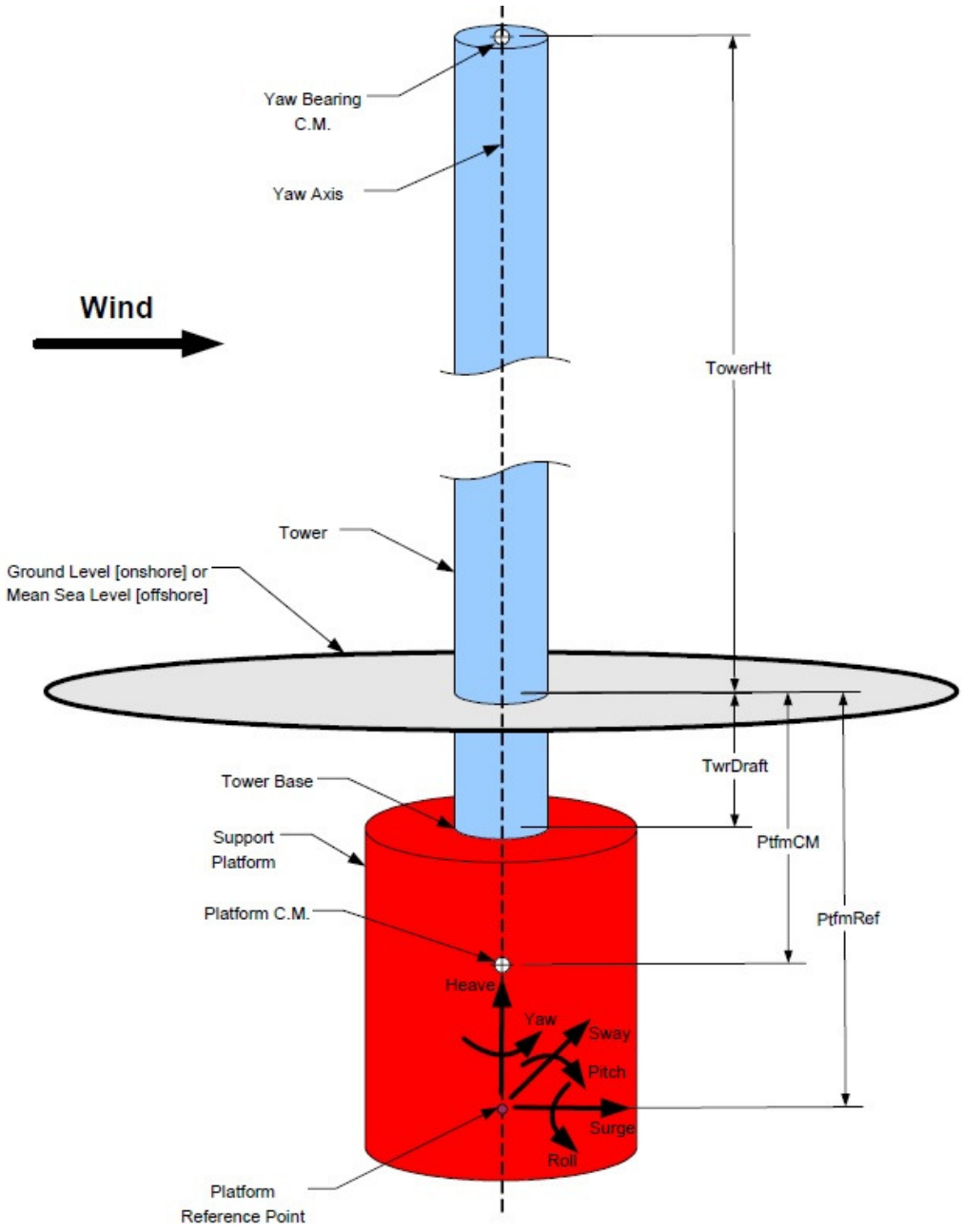

Figure 2.11 Support platform / foundation layout.
(Reproduced from Reference [26])

The support platform can be modelled FAST different configurations such as an onshore foundation, fixed bottom offshore foundation, or floating offshore configuration by setting the

value of input switch PtfmModel from the primary input file to 1, 2, or 3, respectively. Setting PtfmModel to 0 disables the platform models—in this case, FAST will rigidly attach the tower to the inertia frame (ground) through a cantilever connection.

A layout of the configuration properties available for the support platform is given in Figure 2.11. The platform reference point, located by input parameter PtfmRef, is the origin in the platform about which the translational (surge, sway, and heave) and rotational (roll, pitch, and yaw) motions of the support platform are defined. It is also the point at which external loading is applied to the platform. It is at this external point the coupling simulation between the two models is carried out. The details of which will be discussed in later sections.

If PtfmLdMod is set to 1, FAST will call a user defined routine named UserPtfmLd() to compute the platform loading. The platform loads returned by UserPtfmLd() should contain contributions from any external load acting on the platform other than loads transmitted from the wind turbine. For example, these loads should contain contributions from foundation stiffness and damping (not floating) or mooring line restoring and damping (floating), as well as hydrostatic and hydrodynamic contributions (offshore). The platform loads will be applied on the platform at the instantaneous platform reference position. This flexible feature is adopted for coupling purposes.

2.1.2 Wind Turbine Aerodynamics Theory

The AeroDyn [29] aerodynamic subroutine library supplies the aerodynamics algorithms for the rotor. AeroDyn is a set of routines used in conjunction with an aeroelastic simulation code to predict the aerodynamics of horizontal axis wind turbines. These subroutines provide several different models whose theoretical bases are described in this manual. AeroDyn contains two models for calculating the effect of wind turbine wakes: the blade element momentum theory and the generalized dynamic-wake theory [30].

Blade element momentum theory is the classical standard used by many wind turbine designers and generalized dynamic wake theory is a more recent model useful for modeling skewed and unsteady wake dynamics. When using the blade element momentum theory, various corrections are available for the user, such as incorporating the aerodynamic effects of tip losses, hub losses, and skewed wakes. With the generalized dynamic wake, all of these effects are automatically included. Both of these methods are used to calculate the axial induced velocities from the wake in the rotor plane. The user also has the option of calculating the rotational induced velocity. In addition, AeroDyn contains an important model for dynamic stall based on the semi-empirical Beddoes-Leishman model [31] [32]. This model is particularly important for yawed wind turbines. Another aerodynamic model in AeroDyn is a tower shadow model based on potential flow around a cylinder and an expanding wake. Finally, AeroDyn has the ability to read several different

formats of wind input, including single-point hub-height wind files or multiple-point turbulent winds.

Blade Element Momentum

Blade element momentum (BEM) theory is one of the oldest and most commonly used methods for calculating induced velocities on wind turbine blades. This theory is an extension of actuator disk theory, first proposed by the pioneering propeller work of Rankine and Froude in the late 19th century. The BEM theory, generally attributed to Betz and Glauert [33], actually originates from two different theories: blade element theory and momentum theory [34].

Blade element theory assumes that blades can be divided into small elements that act independently of surrounding elements and operate aerodynamically as two-dimensional airfoils whose aerodynamic forces can be calculated based on the local flow conditions. These elemental forces are summed along the span of the blade to calculate the total forces and moments exerted on the turbine.

The other half of BEM, the momentum theory, assumes that the loss of pressure or momentum in the rotor plane is caused by the work done by the airflow passing through the rotor plane on the blade elements. Using the momentum theory, one can calculate the induced velocities from the momentum lost in the flow in the axial and tangential directions. These induced velocities affect the inflow in the rotor plane and therefore also affect the forces calculated by blade element theory. This coupling of two theories ties together blade element momentum theory and sets up an iterative process to determine the aerodynamic forces and also the induced velocities near the rotor.

In practice, BEM theory is implemented by breaking the blades of a wind turbine into many elements along the span. As these elements rotate in the rotor plane, they trace out annular regions, shown in Figure 2.12, across which the momentum balance takes place. These annular regions are also where the induced velocities from the wake change the local flow velocity at the rotor plane. BEM can also be used to analyze stream tubes through the rotor disk, which can be smaller than the annular regions and provide more computational fidelity. However, as currently written, AeroDyn only allows analysis using annular regions.

The advantage of the BEM theory is that each blade element is modeled as a two-dimensional airfoil. Figure 2.13 is an example of an airfoil with the velocities and angles that determine the forces on the element and also the induced velocities from the wake influence. Figure 2.14 shows the resultant aerodynamic forces on the element and their components perpendicular and parallel to the rotor plane. These are the forces that dictate the thrust (perpendicular) and torque (parallel) of the rotor, which are the dominant forces for turbine design. In Figure 2.13, the angle relating the lift and drag of the airfoil element to the thrust and torque forces is the local inflow angle, ϕ.

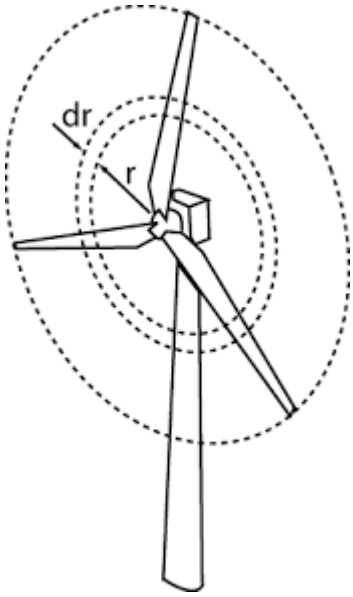

Figure 2.12 Annular plane used in blade element momentum theory. (Reproduced from Reference [30])

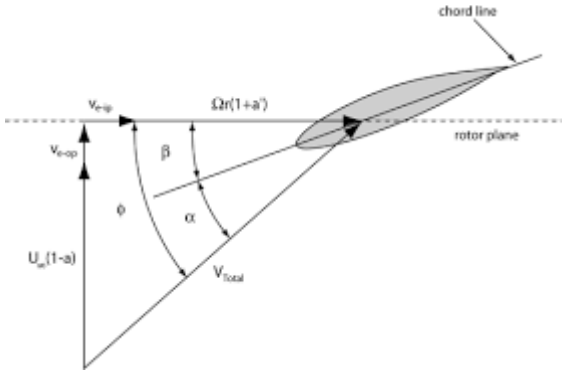

Figure 2.13 Local element velocities and flow angles. (Reproduced from Reference [30])

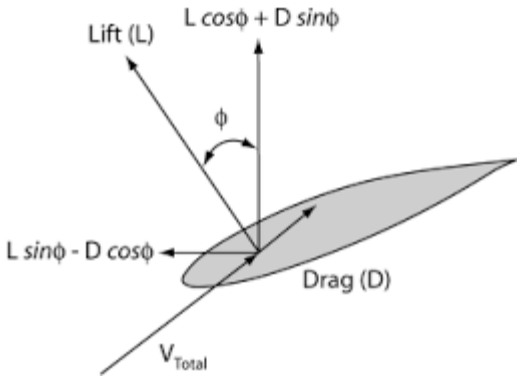

Figure 2.14 Local elemental forces.
(Reproduced from Reference [30])

As shown in Figure 2.13, this inflow angle is the sum of the local pitch angle of the blade β, and the angle of attack α. The local pitch angle is dependent on the static blade geometry, elastic deflections, and the active or passive blade pitch control system. The angle of attack is a function of the local velocity vector, which is in turn constrained by the incoming local wind speed, rotor speed, and blade element velocities and induced velocities. It is to be noted in Figure 2.13 that the velocities of the element from blade deflections ($v_{e\text{-}op}$ and $v_{e\text{-}ip}$) affect the inflow angle and angle of attack, but are not directly affected by the induced velocities from the wake. This assumption is consistent with momentum theory, but it might not be the appropriate physical model for the element-wake coupling.

Because we are required to obtain the angle of attack to determine the aerodynamic forces on an element, we must first determine the inflow angle based on the two components of the local velocity vector. Assuming that the blade motion is very small, the resulting equation is dependent on the induced velocities in both the axial and tangential directions as well as the local tip speed ratio:

$$\tan\phi = \frac{U_\infty(1-a)}{\Omega r(1+a')} = \frac{1-a}{(1+a')\lambda_r} \qquad (\mathbf{2.1})$$

where, a is axial interference or induction factor defined as the fractional decrease in wind velocity between the free stream and rotor plane, a' is the angular induction factor, λ_r is the tip speed ratio, U_∞ is the free stream air flow velocity, Ω is the angular velocity of the wind turbine rotor and r is the radial distance in the section. However, if the blade motion is significant we must include the local velocities in the calculation of the inflow angle, as follows:

$$\tan\phi = \frac{U_\infty(1-a)+v_{e-op}}{\Omega r(1+a')+v_{e-ip}} \qquad (\mathbf{2.2})$$

This equation holds for all elements of the blade along the span, although typically the inflow angle changes with element location.

The induced velocity components in Equations 2.1 and 2.2 are a function of the forces on the blades and BEM theory is used to calculate them. A thorough derivation of these equations can be found in wind turbine design handbooks [35] [36] and it is summarized here. From blade element theory and Figure 2.14, the thrust distributed around an annulus of width *dr* (as in Figure 2.12) is equivalent to

$$dT = B\frac{1}{2}\rho V_{total}^2(C_l \cos\phi + C_d \sin\phi)cdr \qquad (\mathbf{2.3})$$

and the torque produced by the blade elements in the annulus is equivalent to

$$dQ = B\frac{1}{2}\rho V_{total}^2(C_l \sin\phi - C_d \cos\phi)crdr \qquad (\mathbf{2.4})$$

where, B is the number of blades, ρ is the air density, C_l is the two-dimensional lift coefficient, C_d is the two-dimensional drag coefficient and c is the chord length.

Now, to relate the induced velocities in the rotor plane to the elemental forces of Equations 2.3 and 2.4 we incorporate the momentum part of the theory, which states that the thrust extracted by each rotor annulus is equivalent to

$$dT = 4\pi r\rho U_\infty^2(1-a)adr \qquad (\mathbf{2.5})$$

and the torque extracted from each annular section is equivalent to

$$dQ = 4\pi r^3\rho U_\infty \Omega(1-a)a'dr \qquad (\mathbf{2.6})$$

Thus, when we include two-dimensional airfoil tables of lift and drag coefficient as a function of the angle of attack α, we have a set of equations that can be iteratively solved for the induced velocities and the forces on each blade element. However, before solving system of equations, several corrections to the BEM theory needs to be taken into account. These corrections include tip- and hub-loss models to account for vortices shed at these locations, the Glauert correction to account for large induced velocities, and the skewed wake correction to model the effects of incoming flow that is not perpendicular to the rotor plane. Thus in FAST, aerodynamic loads are evaluated using Blade Element Momentum theory.

2.1.3 FAST Kinetics

The basic idea of solving entire set of equations of motion used in FAST is discussed in this section for a 3-bladed turbine configuration. By a direct result of Newton's laws of motion, Kane's equations of motion for a simple holonomic system with 24 DOFs can be stated as follows [37]:

$$F_r + F_r^* = 0 \quad (r = 1,2,\ldots,24) \qquad \mathbf{(2.7)}$$

where, for a set of w rigid bodies characterized by reference frame N_i and center of mass point X_i:

The generalized active forces are:

$$F_r = \sum_{i=1}^{w} {}^{E}\boldsymbol{v}_r^{X_i} \cdot \boldsymbol{F}^{X_i} + {}^{E}\boldsymbol{\omega}_r^{N_i} \cdot \boldsymbol{M}^{N_i} \quad (r = 1,2,\ldots,24) \tag{2.8}$$

and the generalized inertia forces are:

$$F_r^* = \sum_{i=1}^{w} {}^{E}\boldsymbol{v}_r^{X_i} \cdot \left(-m^{N_i}\, {}^{E}\boldsymbol{a}^{X_i}\right) + {}^{E}\boldsymbol{\omega}_r^{N_i} \cdot \left(-{}^{E}\dot{\boldsymbol{H}}^{N_i}\right) \quad (r = 1,2,\ldots,24) \tag{2.9}$$

where it is assumed that for each rigid body N_i, the active forces are applied at the center of mass point X_i. The time derivative of the angular momentum of rigid body N_i about its center of mass X_i in the inertial frame can be found as follows:

$${}^{E}\dot{\boldsymbol{H}}^{N_i} = \begin{cases} \left(\dot{\boldsymbol{H}}^{N_i}\right) + {}^{E}\boldsymbol{\omega}^{N_i} \times {}^{E}\boldsymbol{H}^{N_i} \\ \qquad or \\ \bar{\bar{\boldsymbol{I}}}^{N_i} \cdot {}^{E}\boldsymbol{\alpha}^{N_i} + {}^{E}\boldsymbol{\omega}^{N_i} \times \bar{\bar{\boldsymbol{I}}}^{N_i} \cdot {}^{E}\boldsymbol{\omega}^{N_i} \end{cases} \tag{2.10}$$

For the wind turbine modeled in FAST, the mass of the platform, tower, yaw bearing, nacelle, structure that furls with the rotor, hub, blades, generator, and tail contribute to the total generalized inertia forces as follows:

$$F_r^* = F_r^*\big|_X + F_r^*\big|_T + F_r^*\big|_N + F_r^*\big|_R + F_r^*\big|_H + F_r^*\big|_{B1} + F_r^*\big|_{B2} + F_r^*\big|_G + F_r^*\big|_A \quad (r = 1,2,\ldots,24) \tag{2.11}$$

Generalized active forces are the result of forces applied directly on the wind turbine system, forces that ensure constraint relationships between the various rigid bodies, and internal forces within flexible members. Forces applied directly on the wind turbine system include aerodynamic forces acting on the blades, tower, and tail fin; hydrostatic, hydrodynamic, mooring and/or foundation elasticity and damping forces, including added mass effects, acting on the platform; gravitational forces acting on the platform, tower, yaw bearing, nacelle, structure that furls with the rotor, hub, blades, tip brakes, and tail; generator torque; HSS brake; and gearbox friction forces. Forces that enforce constraint relationships between the various rigid bodies include springs and dampers for yaw, rotor-furl, teeter, and tail-furl (the simple workless constraint forces, for example frictionless pins or rigid connections, do not contribute to the generalized active forces). Internal forces within flexible members include elasticity and damping in the tower, blades, and drivetrain. Thus,

$$F_r = F_r\big|_{Aero} + F_r\big|_{Hydro} + F_r\big|_{Grav} + F_r\big|_{Spring} + F_r\big|_{Damp} + F_r\big|_{Gen} + F_r\big|_{Brake} + F_r\big|_{Elastic} \quad (r = 1,2,\ldots,24) \tag{2.12}$$

In this way, the external forces from each component can be set up. The hydrostatic and hydrodynamic forces are evaluated from the hydrodynamic load evaluation tool during coupling. The complete set of Kane's equations of motion for the wind turbine model can be written as follows.

$$\boldsymbol{M}(\boldsymbol{q},\boldsymbol{u},\boldsymbol{t})\ddot{\boldsymbol{q}} + \boldsymbol{f}(\boldsymbol{q},\dot{\boldsymbol{q}},\boldsymbol{u},\boldsymbol{u_d},\boldsymbol{t}) = \boldsymbol{0} \tag{2.13}$$

where $\boldsymbol{M}$ is the mass matrix, $\boldsymbol{f}$ is the forcing function, $\boldsymbol{u}$ and $\boldsymbol{u_d}$ are the set of wind turbine control inputs and wind inputs, respectively. $\boldsymbol{q}$, $\dot{\boldsymbol{q}}$ and $\ddot{\boldsymbol{q}}$ are the vectors of wind turbine motions, velocities and accelerations, and $\boldsymbol{t}$ is time. The forcing function in the present study includes the reaction force obtained from the hydrodynamic module (discussed in next section) along with the rotor-nacelle dynamics, tower dynamics and all the other features of FAST.

2.2 Hydrodynamic Load Evaluation

DYNABEAM is a dynamic structural model to obtain the response of a floating structure under the hydrodynamic loading. In the present research, time domain analysis [38] is adopted since it has advantages in future comparisons and coupling. Also to consider the non-linearity of system, time domain analysis is employed. The basics of analysis method employed are explained in this section. The equations are reproduced from Ozaki's paper [39].

2.2.1 Element Subdivision

The structure of platform is divided into finite elements as shown in Figure 2.15 [39].

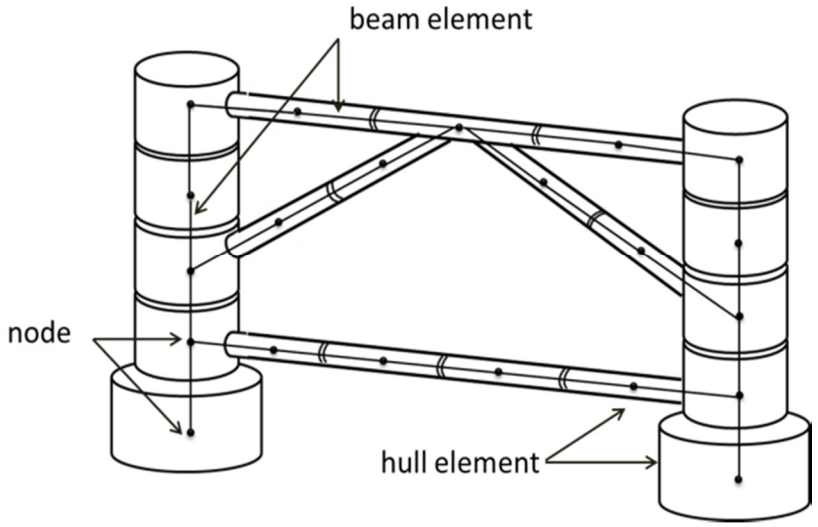

Figure 2.15 Two Kinds of Analysis Elements.
(Reproduced from Reference [39])

The hull element is used for estimating external forces (including inertia force for convenience). During simulation, all the external forces are integrated along the surface or the volume of the element to derive a concentrated force and moment in the node which representing all the external forces acting on the element.

Beam element is defined as straight column whose ends are located on the node of hull element. Based on the stiffness matrix, the beam element provides another viewpoint to evaluate the external force in both ends. Due to the assumption of small displacement, the stiffness matrix is considered as constant.

Finally, the equation of motion will be derived because the force for both kinds of element should be equivalent.

2.2.2 Coordinate System

In the formulation of the equations of motion, five kinds of coordinate systems are used as shown in Figure 2.16.

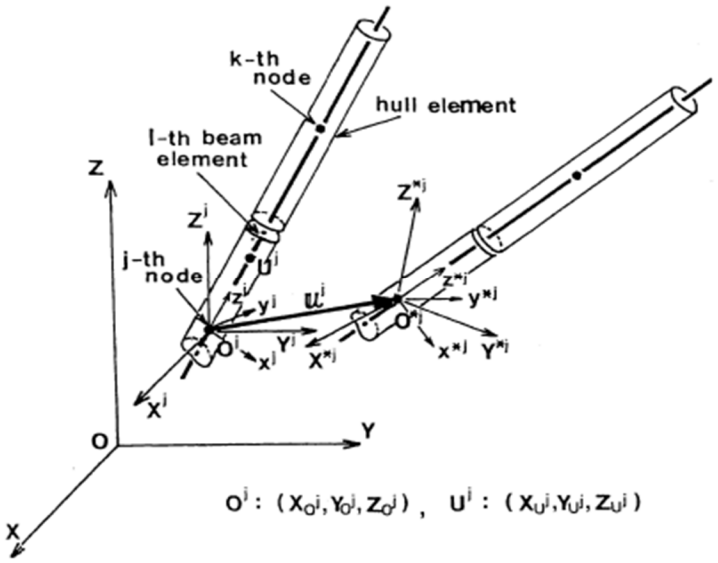

Figure 2.16 Coordinate Systems.
(Reproduced from Reference [30])

- O-XYZ is a space-fixed global coordinate system, where the origin is located at the distance d below the still-water surface. The XY-plane is parallel to the still-water surface and the Z-axis is positive upwards. In this coordinate system, an incident wave is expressed as follows:

$$\eta = a\,cos\{k(Xcosx + Ysinx) - \omega t\}, \qquad Z \le d \tag{2.14}$$

$$\Phi = \frac{ga}{w}\frac{\cosh\{k(Z-d+h)\}}{\cosh(kh)} sin\{k(Xcosx + Ysinx) - \omega t\} \quad Z \le d \tag{2.15}$$

where,

η: surface elevation

Φ: velocity potential

a: wave amplitude

k: circular wave number

χ:	angle of incident wave
ω:	circular frequency
t:	time
g:	acceleration of gravity
h:	water depth
d:	draft

- O^j-$X^jY^jZ^j$ is element-wise space-fixed coordinate system whose originO^j is taken at the pre-displacement position of J-th node and the axes are parallel to the global ones. This coordinate system is mainly used to deal with the buoyancy force. Meanwhile, it also acts as an intermediate system to transform the external force into O^{*j}-$X^{*j}Y^{*j}Z^{*j}$.

- o^j-$x^jy^jz^j$is also element-wise space-fixed coordinate system. But its z-axis is taken at the pre-displace-ment position of the longitudinal axis of the element and the x-axis is defined so that the x^jz^j-plane may become vertical in the space. This system is also used as an intermediate system.

- O^{*j}-$X^{*j}Y^{*j}Z^{*j}$ is element-fixed coordinate system. It initially coincides with O^j-$X^jY^jZ^j$ and move with the element. The equation of motion is derived from the equalivent of force in this system.

- o^{*j}-$x^{*j}y^{*j}z^{*j}$ is also so-called element-fixed coordinate systems. But it coincide with o^j-$x^jy^jz^j$which is different with O^{*j}-$X^{*j}Y^{*j}Z^{*j}$. It's mainly used to calculate the inertia force, hydrodynamic force and the stiffness matrix of beam element.

The following are reasons why element-fixed coordinate systems are introduced in spite of the assumption of small amplitude and of linear process. At each hull element, there is some difference between the gravity force and the static buoyancy in the magnitude, and this difference is balanced initially with static structural forces of the connected beam element.

Position vectors X, X^j, x^j, $X^{*j}$and x^{*j} are defined in the coordinate system implied by each symbolic nomenclature. In the same manner, the translational displacement vectors are defined as $\boldsymbol{U^j} = \{U^jV^jW^j\}^T$ and $\boldsymbol{u^j} = \{u^jv^jw^j\}^T$ corresponding to X^j and x^j, respectively and the rotational displacement vectors are defined as $\boldsymbol{\Theta^j} = \{\Phi^j\Theta^j\Psi^j\}^T$and $\boldsymbol{\theta^j} = \{\varphi^j\theta^j\psi^j\}^T$which are

positive if they are clockwise about each axis of the corresponding coordinate system. The force vectors F^j, f^j, F^{*j}, f^{*j} are defined corresponding to X^j, x^j, X^{*j}, x^{*j} respectively and the moment vectors M^j, m^j, M^{*j}, m^{*j} are defined as to be clockwise about each axis of the corresponding coordinate system.

The transformation matrix C_s^j between the coordinate system O^j-$X^jY^jZ^j$ and o^j-$x^jy^jz^j$ is defined as follows.

$$x^j = C_S^j X^j \tag{2.16}$$

where,

$$C_s^{\ j} = \begin{pmatrix} a_x & b_x & c_x \\ a_y & b_y & c_y \\ a_z & b_z & c_z \end{pmatrix} = \begin{pmatrix} \frac{\Delta_x \Delta_z}{\Delta} & \frac{\Delta_y \Delta_z}{\Delta} & -\Delta \\ -\frac{\Delta_y}{\Delta} & \frac{\Delta_x}{\Delta} & 0 \\ \Delta_x & \Delta_y & \Delta_z \end{pmatrix}$$

$$\Delta_x = \frac{(X_u^{\ j} - X_0^{\ j})}{L_0}, \Delta_y = \frac{(Y_u^{\ j} - Y_0^{\ j})}{L_0}, \Delta_z = \frac{(Z_u^{\ j} - Z_0^{\ j})}{L_0}$$

$$\Delta = \sqrt{\Delta_x^{\ 2} + \Delta_y^{\ 2}}, L_0 = \sqrt{(X_u^{\ j} - X_0^{\ j})^2 + (Y_u^{\ j} - Y_0^{\ j})^2 + (Z_u^{\ j} - Z_0^{\ j})^2}$$

C_s^j can also be utilized to transform the coordinate system O^{*j}-$X^{*j}Y^{*j}Z^{*j}$ and o^{*j}-$x^{*j}y^{*j}z^{*j}$ as

$$x^{*j} = C_S^j X^{*j} \tag{2.17}$$

Moreover, the transformation of the displacement, force and moment are obtained as follows,

$$\begin{aligned} u^j &= C_S^j U^j \quad , \quad \theta^j = C_S^j \Theta^j \\ f^j &= C_S^j F^j \quad , \quad m^j = C_S^j M^j \\ f^{*j} &= C_S^j F^{*j}, \quad m^{*j} = C_S^j M^{*j} \end{aligned} \tag{2.18}$$

On the other hand, the transformation matrices between the space-fixed coordinate systems and the element-fixed ones contain the displacements temporarily and are expressed as follow,

$$X^{*j} = A_S^j \left(X^j - U^j\right) \tag{2.19}$$

$$x^{*j} = a_S^j\left(x^j - u^j\right) \tag{2.20}$$

where,

$$A_s^{\ j} = \begin{pmatrix} 1 & \Psi^j & -\Theta^j \\ -\Psi^j & 1 & \Phi^j \\ \Theta^j & -\Phi^j & 1 \end{pmatrix} \qquad a_s^{\ j} = \begin{pmatrix} 1 & \psi^j & -\theta^j \\ -\psi^j & 1 & \phi^j \\ \theta^j & -\phi^j & 1 \end{pmatrix}$$

The relations of the force and moment vectors in the two kinds of coordinate system are expressed as

$$\begin{aligned} F^{*j} &= A_S^j F^j \quad , \quad M^{*j} = A_S^j M^j \\ f^{*j} &= a_S^j f^j \quad , \quad m^{*j} = a_S^j m^j \end{aligned} \tag{2.21}$$

2.2.3 External Forces of Hull Element

External forces of hull element include gravity force, inertia force, hydrostatic force, hydrodynamic force. To keep the mathematical unitarily for different force, all of these forces should be described at the same coordinate system at last. For convenience of calculation, the coordinate system O^{*j}-$X^{*j}Y^{*j}Z^{*j}$ is selected.

- **Gravity Force**

The gravity force vector of *j*-*t*h hull element is expressed in O^{*j}-$X^{*j}Y^{*j}Z^{*j}$ using A_s^j as follows,

$$F_G^{*j} = A_S^j\left\{0 \;\; 0 \;\; -M^j g\right\}^T = \begin{Bmatrix} 0 \\ 0 \\ -M^j g \end{Bmatrix} - \begin{bmatrix} 0 & -M^j g & 0 \\ M^j g & 0 & 0 \\ 0 & 0 & 0 \end{bmatrix} \Theta^j \tag{2.22}$$

$$\begin{aligned} M_G^{*j} &= C_S^{jT}\left(\begin{Bmatrix} 0 \\ 0 \\ l_z^j \end{Bmatrix} \times C_S^j F_G^{*j}\right) \\ &= M^j g l_z^j \begin{Bmatrix} -b_z \\ a_z \\ 0 \end{Bmatrix} + M^j g l_z^j \begin{bmatrix} c_z & 0 & 0 \\ 0 & c_z & 0 \\ -a_z & -b_z & 0 \end{bmatrix} \Theta^j \end{aligned} \tag{2.23}$$

where, l_z^j is the distance between the node and the center of gravity of the element.

a_z, b_z, c_z are defined in transformation matrix C_S^j.

- **Inertia Force**

The inertia force and moment are expressed as follows,

$$f_{Ig}^{*j} = -\begin{bmatrix} M^j & 0 & 0 \\ 0 & M^j & 0 \\ 0 & 0 & M^j \end{bmatrix} \ddot{u}_g^j \tag{2.24}$$

$$m_{Ig}^{*j} = -\begin{bmatrix} I_\varphi^j & 0 & 0 \\ 0 & I_\theta^j & 0 \\ 0 & 0 & I_\psi^j \end{bmatrix} \ddot{\theta}_g^j \tag{2.25}$$

The subscript g means this vector is defined at the center of gravity of the element. I_φ^j, I_θ^j, I_ψ^j are the moments of inertia of the element.

Then, transforming f_{Ig}^{*j} and m_{Ig}^{*j} to f_I^{*j} and m_I^{*j} whose acting point is the node of the hull element.

$$f_I^{*j} = f_{Ig}^{*j} \tag{2.26}$$

$$m_I^{*j} = m_{Ig}^{*j} + \begin{Bmatrix} 0 \\ 0 \\ l_z^j \end{Bmatrix} \times f_I^{*j} \tag{2.27}$$

$$\ddot{u}_g^j = \ddot{u}^j - \begin{Bmatrix} 0 \\ 0 \\ l_z^j \end{Bmatrix} \times \ddot{\theta}^j \tag{2.28}$$

$$\ddot{\theta}_g^j = \ddot{\theta}^j \tag{2.29}$$

where $\ddot{u}^j$ and $\ddot{\theta}^j$ are acceleration vectors at the node.

Thus the force and moment in O^{*j}-$X^{*j}Y^{*j}Z^{*j}$ are obtained by using C_S^j as follows,

$$F_I^{*j} = -{C_S^j}^T \begin{bmatrix} M^j & 0 & 0 \\ 0 & M^j & 0 \\ 0 & 0 & M^j \end{bmatrix} C_S^j \ddot{U}^j \tag{2.30}$$

$$-C_S^{j^T}\begin{bmatrix} 0 & M^j l_z^j & 0 \\ -M^j l_z^j & 0 & 0 \\ 0 & 0 & 0 \end{bmatrix} C_S^j \ddot{\Theta}^j$$

$$M_I^{*j} = -C_S^{j^T}\begin{bmatrix} 0 & -M^j l_z^j & 0 \\ M^j l_z^j & 0 & 0 \\ 0 & 0 & 0 \end{bmatrix} C_S^j \ddot{U}^j$$

$$-C_S^{j^T}\begin{bmatrix} I_\varphi^j + M^j {l_z^j}^2 & 0 & 0 \\ 0 & I_\theta^j + M^j {l_z^j}^2 & 0 \\ 0 & 0 & I_\psi^j \end{bmatrix} C_S^j \ddot{\Theta}^j \qquad \textbf{(2.31)}$$

- **Hydrostatic Force**

The hydrostatic force is caused by the buoyancy due to static water pressure. As the definition of the wave surface elevation, the static water pressure can be estimated as

$$p_s = \rho g(d - Z), \qquad Z \le d + \eta \qquad \textbf{(2.32)}$$

If the element is partially immersed, the region of integration varies with time due to the relative motion between the element and the water surface elevation. For simplifying the process of integration, the force is calculated under coordinate system o^{*j}-$x^{*j}y^{*j}z^{*j}$. And then transform the force f^{*j} into F^{*j} using transformation matrix C_s^j. The specific procedure is shown below:

$$\mathrm{X} = C_S^{j^T}\left(a_S^{j^T} x^{*j} + u^j\right) + X_0^j \qquad \textbf{(2.33)}$$

The component Z is written as,

$$\mathrm{Z} = c_x\left(x^{*j} - y^{*j}\psi^j + z^{*j}\theta^j + u^j\right) + c_y\left(y^{*j} - z^{*j}\varphi^j + x^{*j}\psi^j + v^j\right)$$

$$+c_z\left(z^{*j} - x^{*j}\theta^j + y^{+j}\varphi^j + w^j\right) + Z_0^j \qquad \textbf{(2.34)}$$

In the pre-displacement condition, the free surface is expressed by $Z=d$.

Therefore, the following equation is formed on the center axis of the element$\left(x^{*j} = y^{*j} = 0\right)$

$$c_z z^{*j} = d - Z_0^j \qquad \textbf{(2.35)}$$

The above equation can be used for judging by substituting l_2^j or l_1^j into z^{*j} whether the element is fully-immersed or not, where l_2^j or l_1^j is the distance between node and upper or lower end of the hull element.

$$z_u^{*j} = l_2^j \qquad \text{(fully-immersed element)}$$

$$z_u^{*j} = \frac{d - Z_0^j}{c_z} - \frac{\eta}{c_z} - \frac{c_x u^j + c_y v^j + c_z w^j}{c_z} - \frac{\left(d - Z_0^j\right)\left(c_y \varphi^j - c_z \theta^j\right)}{{c_z}^2} \qquad \textbf{(2.36)}$$

(partially-immersed element)

On the other hand, the static water pressure is expressed in o^{*j}-$x^{*j}y^{*j}z^{*j}$ using Eq.(2.18) as follows.

$$p_s = \rho g \{d - Z_0^j - \left(c_z + c_y \psi^j - c_z \theta^j\right) x^{*j} - \left(c_y + c_z \varphi^j - c_x \psi^j\right) y^{*j} - \left(c_z + c_x \theta^j - c_y \varphi^j\right) y^{*j} - c_x u^j - c_y v^j - c_z w^j\} \qquad \textbf{(2.37)}$$

Integrating p_s over the immersed surface, the buoyancy due to static water pressure is approximately estimated under assumption that incident wave are regular waves with small amplitude and the length of wave is long enough compared with sectional of structural members.

$$f_S^{*j} = \iint p_S n \; ds^{*j} = \iiint_V -\nabla^{*j} p_S dv^{*j} \qquad \textbf{(2.38)}$$

$$\approx \int_{-l_1^j}^{z_u^{*j}} -\rho g A^j \begin{Bmatrix} -c_x - c_y \psi^j + c_z \theta^j \\ -c_y - c_z \varphi^j + c_x \psi^j \\ -c_z - c_x \theta^j + c_y \varphi^j \end{Bmatrix} dz^{*j}$$

where,

$$\nabla^{*j} \equiv \left\{ \frac{\partial}{\partial x^{*j}} \quad \frac{\partial}{\partial y^{*j}} \quad \frac{\partial}{\partial z^{*j}} \right\}^T$$

n is the normal vector of submerged surface (positive direction is into the submerged surface). $\iint ds^{*j}$ and $\iiint_V dv^{*j}$ are integrations over area and volume. A^j is the sectional area of the element.

Consequently, the force due to static water pressure is estimated in O^{*j}-$X^{*j}Y^{*j}Z^{*j}$ as follows,

For fully-immersed element,

$$F_S^{*j} = \begin{Bmatrix} 0 \\ 0 \\ \rho g A^j \left(l_2^j + l_1^j\right) \end{Bmatrix} \qquad \textbf{(2.39)}$$

$$-\rho g A^j \left(l_2^j + l_1^j\right) C_S^{jT} \begin{bmatrix} 0 & c_z & -c_y \\ -c_z & 0 & c_x \\ c_y & -c_x & 0 \end{bmatrix} C_S^j \Theta^j$$

For partially-immersed element,

$$\begin{aligned} F_S^{*j} &= \begin{Bmatrix} 0 \\ 0 \\ \rho g A^j \left(\frac{d - Z_0^j}{c_z} + l_1^j\right) \end{Bmatrix} \\ &-\rho g A^j \left(\frac{d - Z_0^j}{c_z} + l_1^j\right) C_S^{jT} \begin{bmatrix} 0 & c_z & -c_y \\ -c_z & 0 & c_x \\ c_y & -c_x & 0 \end{bmatrix} C_S^j \Theta^j \\ &-\frac{\rho g A^j}{c_z} C_S^{jT} \begin{bmatrix} c_x^2 & c_x c_y & c_x c_z \\ c_x c_y & c_y^2 & c_y c_z \\ c_x c_z & c_y c_z & c_z^2 \end{bmatrix} C_S^j U^j \\ &-\frac{\rho g A^j \left(d - Z_0^j\right)}{{c_z}^2} C_S^{jT} \begin{bmatrix} -c_x c_y & c_x^2 & 0 \\ -c_y^2 & c_x c_y & 0 \\ -c_y c_z & c_x c_z & 0 \end{bmatrix} C_S^j \Theta^j \end{aligned} \quad \textbf{(2.40)}$$

The moment due to buoyancy is estimated as follows,

$$m_S^{*j} = \iiint_V \begin{Bmatrix} x^{*j} \\ y^{*j} \\ z^{*j} \end{Bmatrix} \times \left(-\nabla^{*j} p_S\right) dv^{*j} \quad \textbf{(2.41)}$$

For fully-immersed element,

$$\begin{aligned} M_S^{*j} &= \rho g A^j \frac{l_2^{j2} - l_1^{j2}}{2} \begin{Bmatrix} b_z \\ -a_z \\ 0 \end{Bmatrix} \\ &-\rho g A^j \frac{l_2^{j2} - l_1^{j2}}{2} C_S^{jT} \begin{bmatrix} c_z & 0 & -c_x \\ 0 & c_z & -c_y \\ 0 & 0 & 0 \end{bmatrix} C_S^j \Theta^j \end{aligned} \quad \textbf{(2.42)}$$

For partially-immersed element,

$$M_S^{*j} = \rho g A^j \frac{\left(\frac{d - Z_0^j}{c_z}\right)^2 - l_1^{j2}}{2} \begin{Bmatrix} b_z \\ -a_z \\ 0 \end{Bmatrix} - \rho g A^j \frac{\left(\frac{d - Z_0^j}{c_z}\right)^2 - l_1^{j2}}{2} C_S^{jT} \begin{bmatrix} c_z & 0 & -c_x \\ 0 & c_z & -c_y \\ 0 & 0 & 0 \end{bmatrix} C_S^j \Theta^j$$

$$-\rho g A^j \frac{d - Z_0^j}{{c_z}^2} C_S^{jT} \begin{bmatrix} -c_x c_y & -c_y^2 & -c_y c_z \\ c_x^2 & c_x c_y & c_x c_z \\ 0 & 0 & 0 \end{bmatrix} C_S^j U^j$$

$$-\rho g A^j \frac{\left(d - Z_0^j\right)^2}{{c_z}^2} C_S^{jT} \begin{bmatrix} c_y^2 & -c_x c_y & 0 \\ -c_x c_y & c_x^2 & 0 \\ 0 & 0 & 0 \end{bmatrix} C_S^j \Theta^j$$

$$-\frac{\rho g \pi {R^j}^4}{4 c_z} C_S^{jT} \begin{bmatrix} c_x^2 & 0 & -c_x c_z \\ 0 & c_z^2 & -c_y c_z \\ -c_x c_z & -c_y c_z & c_x^2 + c_y^2 \end{bmatrix}$$

$$+\rho g A^j \frac{d - Z_0^j}{c_z} a C_S^{jT} \begin{Bmatrix} -{c_y}/{c_z} \\ {c_x}/{c_z} \\ 0 \end{Bmatrix} \cos\left\{\kappa\left(\mu_0 + \mu_z \frac{d - Z_0^j}{c_z}\right) - \omega t\right\} \qquad (\mathbf{2.43})$$

- **Hydrodynamic force**

The hydrodynamic forces are caused by the small amplitude wave and motion. Moreover, they are not related to the static force. Therefore, the transformation between the space-fixed coordinate systems and the element-fixed ones are ignored and consequently the upper limit of integration of the partially-immersed element can be treated as constant $(d\text{-}Z_o^i)/c_z$. Hereafter, l_2^j is used for convenience as the upper limit of integration of the partially- immersed element as well as the fully-immersed element.

Froude-Krylov force

The Froude-Krylov force is obtained by integratingp_v over the immersed surface of the element.

$$f_F^{*j} = \iint p_v n \, ds^{*j}$$

$$= \oint -\nabla^{*j} p_v \, dv^{*j} \qquad (\mathbf{2.44})$$

When $C_z^2 + \mu_z^2 \neq 0$

$$F_F^{*j} = \frac{\rho g A^j a}{\cosh \kappa h} \frac{1}{c_z^2 + \mu_z^2} \left[C_S^{jT} \begin{Bmatrix} -c_x c_z - \mu_x \mu_z \\ -c_y c_z - \mu_y \mu_z \\ -c_z^2 - \mu_z^2 \end{Bmatrix} (\cosh \varepsilon_{z2} \cos \Omega_2 - \cosh \varepsilon_{z1} \cos \Omega_1) \right.$$
$$\left. + C_S^{jT} \begin{Bmatrix} -c_x \mu_z + c_z \mu_x \\ -c_y \mu_z + c_z \mu_y \\ 0 \end{Bmatrix} (\sinh \varepsilon_{z2} \, \varepsilon_{z2} \sin \Omega_2 - \sinh \varepsilon_{z1} \sin \Omega_1) \right] \qquad (\mathbf{2.45})$$

When $C_z^2 + \mu_z^2 = 0$

$$F_F^{*j} = \frac{\rho g A^j a \kappa \left(l_2^j + l_1^j\right)}{\cosh \kappa h} \left[C_S^{jT} \begin{Bmatrix} -c_x \\ -c_y \\ 0 \end{Bmatrix} \sinh \varepsilon_{z0} \sin \Omega_0 + C_S^{jT} \begin{Bmatrix} \mu_x \\ \mu_y \\ 0 \end{Bmatrix} \cosh \varepsilon_{z0} \cos \Omega_0 \right] \qquad (\mathbf{2.46})$$

Where,

$$\mu_x = a_x \cos\chi + b_x \sin\chi, \qquad \mu_y = a_y \cos\chi + b_y \sin\chi$$

$$\varepsilon_{z2} = \kappa\left(c_z l_2^j + Z_0^j - d + h\right), \qquad \varepsilon_{z1} = \kappa\left(-c_z l_1^j + Z_0^j - d + h\right)$$

$$\varepsilon_{z0} = \kappa\left(Z_0^j - d + h\right), \qquad \Omega_2 = \kappa\left(\mu_z l_2^j + \mu_0\right) - \omega t$$

$$\Omega_1 = \kappa\left(-\mu_z l_1^j + \mu_0\right) - \omega t, \qquad \Omega_1 = \kappa\mu_0 - \omega t$$

By analogy to the force, the moment due to Froude-Krylov force is estimated as follows,

$$m_F^{*j} = \oint \begin{Bmatrix} x^{*j} \\ y^{*j} \\ z^{*j} \end{Bmatrix} \times \left(-\nabla^{*j} p_v\right) dv^{*j} \tag{2.47}$$

When $c_z^2 + \mu_z^2 \neq 0$,

$$M_F^{*j} = \frac{\rho g A^j a}{\cosh\kappa h} \frac{1}{c_z^2 + \mu_z^2} \begin{bmatrix} C_S^{jT} \begin{Bmatrix} c_y c_z + \mu_y \mu_z \\ -c_x c_z - \mu_x \mu_z \\ 0 \end{Bmatrix} \left(l_2^j \cosh\varepsilon_{z2} \cos\Omega_2 + l_1^j \cosh\varepsilon_{z1} \cos\Omega_1\right) \\ + C_S^{jT} \begin{Bmatrix} c_y \mu_z + c_z y \\ -c_x \mu_z + c_z \mu_x \\ 0 \end{Bmatrix} \left(l_2^j \sinh\varepsilon_{z2}\, \varepsilon_{z2} \sin\Omega_2 + l_1^j \sinh\varepsilon_{z1} \sin\Omega_1\right) \end{bmatrix}$$

$$+ \frac{\rho g A^j a}{\cosh\kappa h} \frac{1}{\kappa(c_z^2 + \mu_z^2)^2} \begin{bmatrix} C_S^{jT} \begin{Bmatrix} -c_y(c_z^2 - \mu_z^2) - 2c_z \mu_y \mu_z \\ c_x(c_z^2 - \mu_z^2) + 2c_z \mu_x \mu_z \\ 0 \end{Bmatrix} \left(\sinh\varepsilon_{z2}\, \varepsilon_{z2} \sin\Omega_2 - \sinh\varepsilon_{z1} \sin\Omega_1\right) \\ + C_S^{jT} \begin{Bmatrix} -2c_y c_z \mu_z - \mu_y(c_z^2 - \mu_z^2) \\ 2c_x c_z \mu_z - \mu_x(c_z^2 - \mu_z^2) \\ 0 \end{Bmatrix} \left(\cosh\varepsilon_{z2} \cos\Omega_2 - \cosh\varepsilon_{z1} \cos\Omega_1\right) \end{bmatrix} \tag{2.48}$$

When $c_z = \mu_z = 0$

$$M_F^{*j} = \frac{\rho g A^j a \kappa}{\cosh\kappa h} \frac{l_2^j - l_1^j}{2} \left[C_S^{jT} \begin{Bmatrix} c_y \\ -c_x \\ 0 \end{Bmatrix} \sinh\varepsilon_{z0} \cos\Omega_0 + C_S^{jT} \begin{Bmatrix} -\mu_y \\ \mu_x \\ 0 \end{Bmatrix} \cosh\varepsilon_{z0} \sin\Omega_0 \right] \tag{2.49}$$

Hydrodynamic mass force

Hydrodynamic mass force can also be called as radiation force. It's usually normal to the central axis of the element and proportional to the difference of acceleration between fluid particle and element motion which is called relative acceleration. In the case of the element with ends exposed to the ambient water pressure, the component parallel to the central axis is also estimated. The upper limit of integration can be decided from the solution of boundary condition if it's necessary.

When $c_z^2 + \mu_z^2 \neq 0$

$$
\begin{aligned}
F_A^{*j} = & \frac{\rho g A^j a}{\cosh \kappa h} \frac{1}{c_z^2 + \mu_z^2} \left[C_S^{jT} \begin{Bmatrix} c_{my}^j(-c_y c_z - \mu_y \mu_z) \\ c_{mx}^j(c_x c_z + \mu_x \mu_z) \\ 0 \end{Bmatrix} \left(l_2^j \cosh \varepsilon_{z2} \cos \Omega_2 - l_1^j \cosh \varepsilon_{z1} \cos \Omega_1 \right) \right. \\
& + C_S^{jT} \begin{Bmatrix} c_{my}^j(c_y \mu_z - c_z \mu_y) \\ c_{mx}^j(-c_x \mu_z + c_z \mu_x) \\ 0 \end{Bmatrix} \left. \left(l_2^j \sinh \varepsilon_{z2}\, \varepsilon_{z2} \sin \Omega_2 - l_1^j \sinh \varepsilon_{z1} \sin \Omega_1 \right) \right] \\
& - \rho A^j \left(l_2^j + l_1^j \right) C_S^{jT} \begin{bmatrix} c_{my}^j & 0 & 0 \\ 0 & c_{mx}^j & 0 \\ 0 & 0 & 0 \end{bmatrix} \begin{bmatrix} 0 & -c_{my}^j & 0 \\ c_{mx}^j & 0 & 0 \\ 0 & 0 & 0 \end{bmatrix} C_S^j \ddot{U}^j \\
& - \rho A^j \frac{l_2^{j2} - l_1^{j2}}{2} C_S^{jT} \begin{bmatrix} 0 & c_{my}^j & 0 \\ -c_{mx}^j & 0 & 0 \\ 0 & 0 & 0 \end{bmatrix} C_S^j \dot{\theta}^j \qquad (\mathbf{2.50})
\end{aligned}
$$

$$
\begin{aligned}
M_A^{*j} = & \frac{\rho g A^j a}{\cosh \kappa h} \frac{1}{c_z^2 + \mu_z^2} \left[C_S^{jT} \begin{Bmatrix} c_{my}^j(c_y c_z + \mu_y \mu_z) \\ c_{mx}^j(-c_x c_z - \mu_x \mu_z) \\ 0 \end{Bmatrix} \left(l_2^j \cosh \varepsilon_{z2} \cos \Omega_2 + l_1^j \cosh \varepsilon_{z1} \cos \Omega_1 \right) + \right. \\
& \left. C_S^{jT} \begin{Bmatrix} c_{my}^j(c_y \mu_z - c_z \mu_y) \\ c_{mx}^j(-c_x \mu_z + c_z \mu_x) \\ 0 \end{Bmatrix} \left(l_2^j \sinh \varepsilon_{z2}\, \varepsilon_{z2} \sin \Omega_2 + l_1^j \sinh \varepsilon_{z1} \sin \Omega_1 \right) \right] + \\
& \frac{\rho g A^j a}{\cosh \kappa h} \frac{1}{\kappa (c_z^2 + \mu_z^2)^2} \left[C_S^{jT} \begin{Bmatrix} c_{my}^j[c_y(c_z^2 - \mu_z^2) - 2c_z \mu_y \mu_z] \\ c_{mx}^j[-c_x(c_z^2 - \mu_z^2) + 2c_z \mu_x \mu_z] \\ 0 \end{Bmatrix} (\sinh \varepsilon_{z2}\, \varepsilon_{z2} \sin \Omega_2 - \sinh \varepsilon_{z1} \sin \Omega_1) + \right. \\
& \left. C_S^{jT} \begin{Bmatrix} c_{my}^j[-2c_y c_z \mu_z + \mu_y(c_z^2 - \mu_z^2)] \\ c_{mx}^j[2c_x c_z \mu_z - \mu_x(c_z^2 - \mu_z^2)] \\ 0 \end{Bmatrix} (\cosh \varepsilon_{z2} \cos \Omega_2 - \cosh \varepsilon_{z1} \cos \Omega_1) \right] - \\
& \rho A^j \frac{l_2^{j2} - l_1^{j2}}{2} C_S^{jT} \begin{bmatrix} 0 & -c_{my}^j & 0 \\ c_{mx}^j & 0 & 0 \\ 0 & 0 & 0 \end{bmatrix} C_S^j \ddot{U}^j - \rho A^j \frac{l_2^{j3} + l_1^{j3}}{3} C_S^{jT} \begin{bmatrix} c_{my}^j & 0 & 0 \\ 0 & c_{mx}^j & 0 \\ 0 & 0 & 0 \end{bmatrix} C_S^j \ddot{\theta}^j \qquad \mathbf{(2.51)}
\end{aligned}
$$

When $c_z = \mu_z = 0$

$$F_A^{*j} = \frac{\rho g A^j a\kappa\left(l_2^j+l_1^j\right)}{\cosh\kappa h}\left[C_S^{jT}\begin{Bmatrix}-c_{mx}^j c_x\\-c_{my}^j c_y\\0\end{Bmatrix}\sinh\varepsilon_{z0}\sin\Omega_0 + C_S^{jT}\begin{Bmatrix}c_{mx}^j\mu_x\\c_{my}^j\mu_y\\0\end{Bmatrix}\cosh\varepsilon_{z0}\cos\Omega_0\right] -$$
$$\rho A^j\left(l_2^j+l_1^j\right)C_S^{jT}\begin{bmatrix}c_{mx}^j & 0 & 0\\0 & c_{my}^j & 0\end{bmatrix}C_S^j\ddot{U}^j -$$
$$\rho A^j\frac{l_2^{j2}-l_1^{j2}}{2}C_S^{jT}\begin{bmatrix}0 & c_{mx}^j & 0\\-c_{my}^j & 0 & 0\end{bmatrix}C_S^j\ddot{\Theta}^j \qquad \textbf{(2.52)}$$

$$M_V^{*j} = \frac{\rho g A^j a\kappa}{\cosh\kappa h}\frac{l_2^{j2}-l_1^{j2}}{2}\left[C_S^{jT}\begin{Bmatrix}c_{my}^j c_y\\-c_{mx}^j c_x\\0\end{Bmatrix}\sinh\varepsilon_{z0}\sin\Omega_0 + C_S^{jT}\begin{Bmatrix}-c_{my}^j\mu_y\\c_{mx}^j\mu_x\\0\end{Bmatrix}\cosh\varepsilon_{z0}\cos\Omega_0\right] -$$
$$\rho A^j\frac{l_2^{j2}-l_1^{j2}}{2}C_S^{jT}\begin{bmatrix}0 & -c_{my}^j & 0\\c_{mx}^j & 0 & 0\\0 & 0 & 0\end{bmatrix}C_S^j\ddot{U}^j - \rho A^j\frac{l_2^{j3}+l_1^{j3}}{3}C_S^{jT}\begin{bmatrix}c_{my}^j & 0 & 0\\0 & c_{mx}^j & 0\\0 & 0 & 0\end{bmatrix}C_S^j\ddot{\Theta}^j \qquad \textbf{(2.53)}$$

where $c^j{}_{mx}$ and $c^j{}_{mn}$are the non-dimensional added mass coefficients defined as,

$$c_{mx}^j = \frac{M_{ax}^j}{\rho A^j\left(l_2^j+l_1^j\right)}, \qquad c_{my}^j = \frac{M_{ay}^j}{\rho A^j\left(l_2^j+l_1^j\right)}$$

$M^j{}_{ax}$, $M^j{}_{ay}$ are the added masses.

If there are any ends, the following forces are properly added,

$$F_{Al}^{*j} = C_S^{jT}\begin{Bmatrix}0\\0\\M_{azl}^j\frac{g\kappa a}{\cosh\kappa h}\left[-c_z\sinh\varepsilon_{z1}\sin\Omega_1 + \mu_z\cosh\varepsilon_{z1}\cos\Omega_1\right]\end{Bmatrix} -$$
$$C_S^{jT}\begin{bmatrix}0 & 0 & 0\\0 & 0 & 0\\0 & 0 & M_{azl}^j\end{bmatrix}C_S^j\ddot{U}^j \qquad (3.42)$$

$$F_{Au}^{*j} = C_S^{jT}\begin{Bmatrix}0\\0\\M_{azu}^j\frac{g\kappa a}{\cosh\kappa h}\left[-c_z\sinh\varepsilon_{z2}\sin\Omega_2 + \mu_z\cosh\varepsilon_{z2}\cos\Omega_2\right]\end{Bmatrix}$$
$$- C_S^{jT}\begin{bmatrix}0 & 0 & 0\\0 & 0 & 0\\0 & 0 & M_{azu}^j\end{bmatrix}C_S^j\ddot{U}^j \qquad (\mathbf{2.54})$$

2.2.4 Stiffness Matrix of Beam Element

From the viewpoint of Beam Element, the external force acting on the node can be also calculated by stiffness matrix of beam element. It's assumed that the displacement of beam element is small and the linearized displacement-strain relationship is accurate enough which means that:

$$\begin{aligned} \varepsilon_x &= \frac{\partial u_x}{\partial x} & \gamma_{xy} &= \frac{\partial u_y}{\partial x} + \frac{\partial u_x}{\partial y} \\ \varepsilon_y &= \frac{\partial u_y}{\partial y} & \gamma_{xz} &= \frac{\partial u_z}{\partial x} + \frac{\partial u_x}{\partial z} \\ \varepsilon_z &= \frac{\partial u_z}{\partial z} & \gamma_{yz} &= \frac{\partial u_z}{\partial y} + \frac{\partial u_y}{\partial z} \end{aligned} \tag{2.55}$$

Based on the principle of virtual work, it is easily to obtain the linearized stiffness matrix:

$$\{\delta u\}^T \{F_l\} = \int (\sigma_x \delta \varepsilon_x) dxdydz = \{\delta u\}^T \int ([B_l]^T E[B_l]) dxdydz \{u\}$$

Then the external force should be:

$$\{F_l\} = \int ([B_l]^T E[B_l]) dxdydz \{u\}$$

Therefore, the linearized stiffness matrix can be defined as:

$$[K_l] = \int ([B_l]^T E[B_l]) dxdydz$$

(The detail of deriving process is shown in Chapter 3.)

Finally, the external force can be calculated as:

$$\begin{Bmatrix} f_B^{*j} \\ m_B^{*j} \\ f_B^{*k} \\ m_B^{*k} \end{Bmatrix} = - \begin{bmatrix} K_{jj}^l & K_{jk}^l \\ K_{kj}^l & K_{kk}^l \end{bmatrix} \begin{Bmatrix} u^j \\ \theta^j \\ u^k \\ \theta^k \end{Bmatrix} \tag{2.59}$$

Where script j, k means the number of node,

$$K_{jj}^{l}=\begin{bmatrix} 12EI_\theta/l^3 & 0 & 0 & 0 & 6EI_\theta/l^2 & 0 \\ & 12EI_\varphi/l^3 & 0 & -6EI_\varphi/l^2 & 0 & 0 \\ & & EA/l & 0 & 0 & 0 \\ & & & 4EI_\varphi/l & 0 & 0 \\ & (sym.) & & & 4EI_\theta/l & 0 \\ & & & & & -GJ_\psi/l \end{bmatrix} \quad (\mathbf{2.60})$$

$$K_{jk}^{l}=\begin{bmatrix} -12EI_\theta/l^3 & 0 & 0 & 0 & 6EI_\theta/l^2 & 0 \\ 0 & -12EI_\varphi/l^3 & 0 & -6EI_\varphi/l^2 & 0 & 0 \\ 0 & 0 & -EA/l & 0 & 0 & 0 \\ 0 & 6EI_\varphi/l^2 & 0 & 2EI_\varphi/l & 0 & 0 \\ -6EI_\theta/l^2 & 0 & 0 & 0 & 2EI_\theta/l & 0 \\ 0 & 0 & 0 & 0 & 0 & -GJ_\psi/l \end{bmatrix}$$

$$K_{kj}^{l}=K_{jk}^{l}$$

$$K_{jj}^{l}=\begin{bmatrix} 12EI_\theta/l^3 & 0 & 0 & 0 & -6EI_\theta/l^2 & 0 \\ & 12EI_\varphi/l^3 & 0 & -6EI_\varphi/l^2 & 0 & 0 \\ & & EA/l & 0 & 0 & 0 \\ & & & 4EI_\varphi/l & 0 & 0 \\ & (sym.) & & & 4EI_\theta/l & 0 \\ & & & & & GJ_\psi/l \end{bmatrix}$$

Where EA is axial rigidity, EI_φ and EI_θ are bending rigidities, GJ_ψ is torsional rigidity and l is the length of the beam element.

Then, transfer the above force from coordinate system o*j-x*jy*jz*j to coordinate system O*j-X*jY*jZ*j:

$$\begin{Bmatrix} F_B^{*j} \\ M_B^{*j} \\ F_B^{*k} \\ M_B^{*k} \end{Bmatrix} = -\begin{bmatrix} C^{jT}K_{jj}^{l}C^{l} & C^{jT}K_{jk}^{l}C^{l} \\ C^{jT}K_{kj}^{l}C^{l} & C^{jT}K_{kk}^{l}C^{l} \end{bmatrix} \begin{Bmatrix} \delta^j \\ \\ \delta^k \end{Bmatrix} \quad (\mathbf{2.61})$$

where C^j is the coordinate transformation matrix which is defined as in hull element.

2.2.5 Equation of Motion

Assembling the forces and moments evaluated at all nodes, the equations of motion of a whole structure are formulated as follows,

$$K_m\ddot{\delta} + K_d\dot{\delta} + (K_r + K_B + K_T)\delta = F_{wave} + F_{wind} + F_m \qquad (\mathbf{2.62})$$

where

K_m: virtual mass matrix

K_d: damping coefficient matrix

K_r: restoring coefficient matrix due to hull element

K_B: restoring coefficient matrix due to beam element

K_T: restoring coefficient matrix due to mooring element

F_{wave}:wave exciting force vector (linear and non-linear due to drag force)

F_{wind}: wind load force vector

F_m: machinery load force vector

δ :the displacement vector

Due to the degree of freedom is six, the size of all the above matrix is 6N×6N and the size of force vector is 6N, where N is the number of free nodes. The Equation of Motion solved is summarized as shown in Figure 2.17.

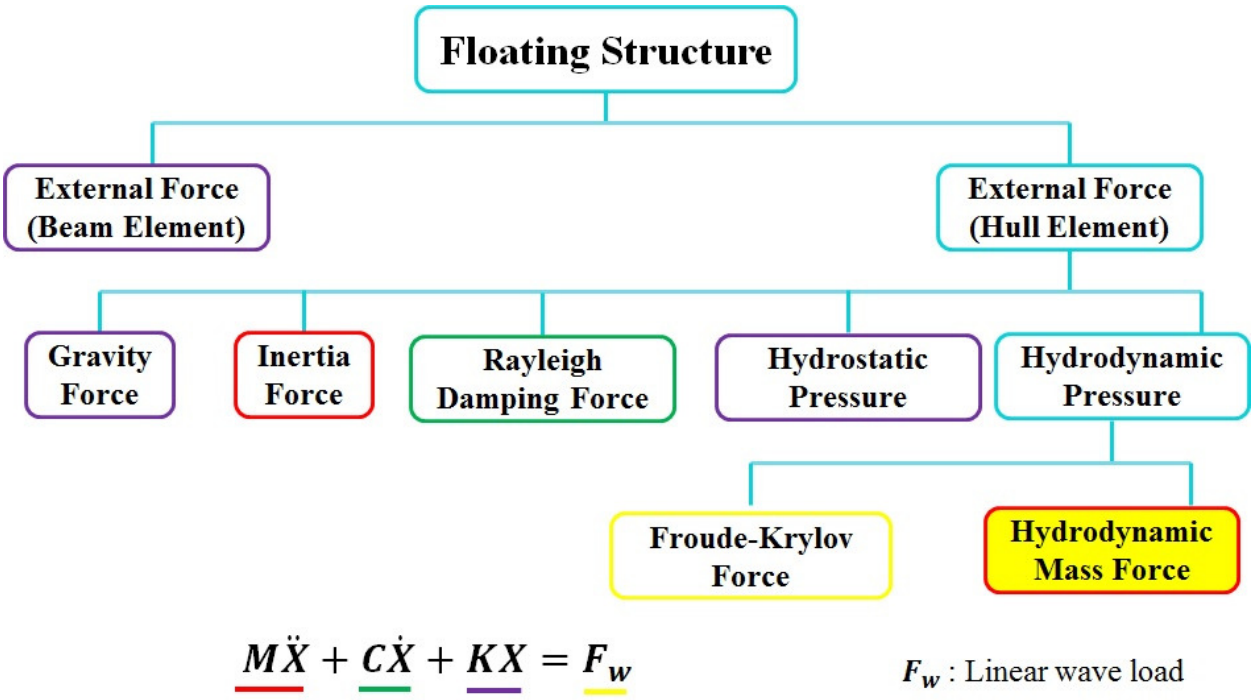

Figure 2.17 Equation of Motion in DYNABEAM.

By solving this equation of motion, the nodal displacements are obtained. Then, the stress and strain can be obtained for each element. As the rotation angle is assumed small enough, the nonlinearity of transformation matrix is neglected.

2.3 Coupling

This section explains about the coupling methodology, coupling strategy and coupling technique utilized in the present study. The time domain analysis tool for rotor-floater coupled dynamic system is developed. Aero-hydro-control dynamic coupling is essential for the holistic combined approach analysis for FOWT systems. The wind turbine dynamics are computed by FAST and floater dynamics are computed by DYNABEAM as explained in the previous sections.

2.3.1 Development of Coupled tool

The basic concept of coupling is presented in Figure 2.18 [41]. The two modules, one for aerodynamics and one for hydrodynamics are coupled using a weakly coupled algorithm. Weakly coupling methodology is developed in time domain even though it consumes more time in the simulation since the coupling aerodynamics, hydrodynamics and control might lead to non-linear response. The coupling involves exchange of platform motions such as displacement, velocity and acceleration with reaction forces and moments between the two modules, FAST and DYNABEAM. The coupled tool is developed with due considerations to the flexibility of the floater and its resultant response.

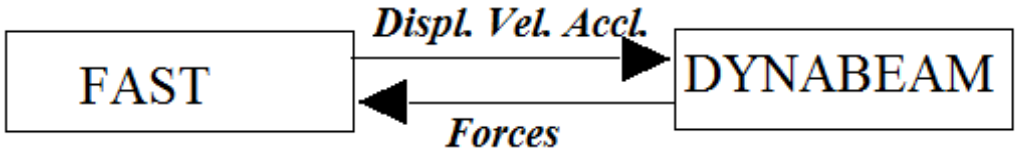

Figure 2.18 Basic Concept of Coupling.

2.3.2 Coupling Strategy

The coupling strategy includes using an interface between the two modules where exchange of physical quantities is possible. The wind turbine dynamics are computed by FAST. The user defined subroutine UserPtfmLd in FAST is utilized for interface between the two modules. The subroutine UserPtfmLd is the user defined platform loading feature in FAST.

DYNABEAM calculates all of the forces acting on the platform, including the gravity and buoyancy and feeds the reaction forces to FAST at each time step. Then FAST fills out the forcing function defined in Equation (2.13) using forces from DYNABEAM, and solves accelerations of all degrees of freedom of wind turbine.

Then, FAST solves the equations of motion. Those obtained platform kinematic data, which include displacement, velocity and acceleration, are then fed into DYNABEAM side in order to update reaction forces and moments. Once again, the reaction forces and moments will be fed again to FAST for the next time step. For the present coupled simulation, the same time incremental step is employed between the systems which means that at every time interval of FAST, the DYNABEAM internally calculates 1 step, and returns the resultant data to FAST. The coupling strategy of rotor-floater coupling is schematically explained in Figure 2.19.

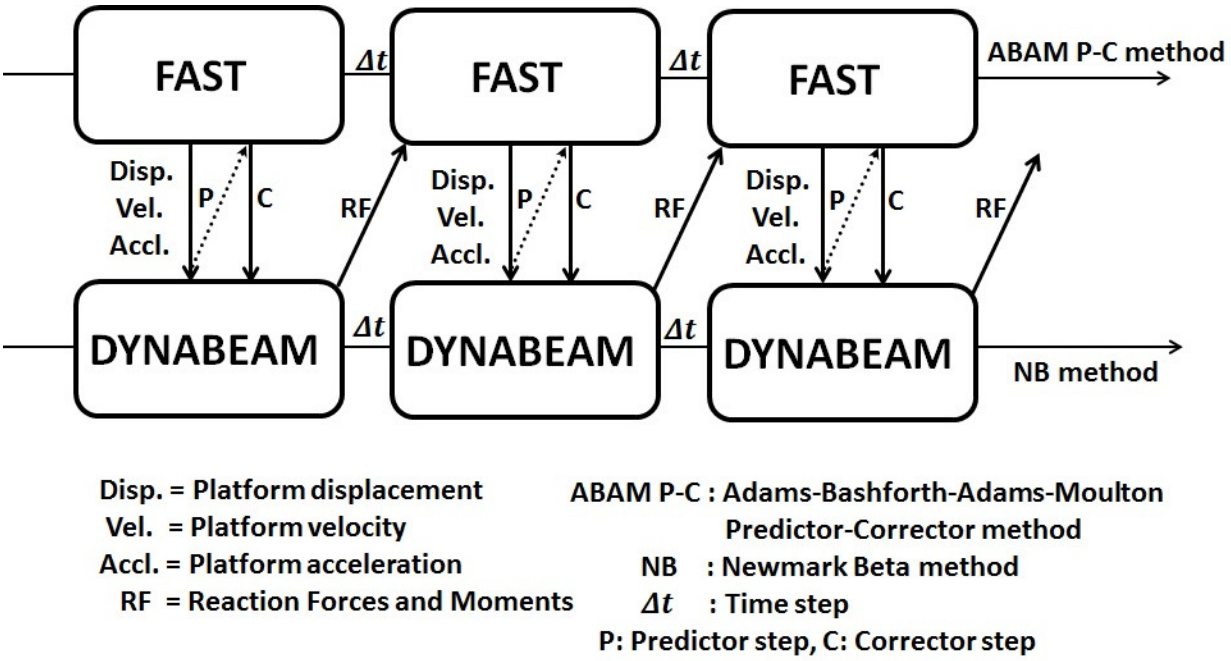

Figure 2.19 Coupling Procedure.

FAST and DYNABEAM both uses different numerical methods for simulation. FAST uses the time integration using the 4th order Adams-Bashforth Adams-Moulton Predictor-Corrector scheme after initialized by 4th order Runge-Kutta explicit scheme. DYNABEAM uses Newmark Beta method for numerical simulations. It is very important to select smaller time steps for simulation during coupling since structural stiffness is quite high in DYNABEAM model. Because of this varied numerical schemes employed, the DYNABEAM is called twice within one step (once each for predictor and corrector phase) of the FAST. This feature is therefore adopted in the coupled tool.

The formulated equations of motion of a floating structure and rotor-nacelle-tower assembly with multi degree of freedom expression are solved independently in time domain. A junction or a node is selected for this purpose where the platform motions and reaction forces are exchanged at each time step. The junction selected for present study will be explained in the upcoming section for

each model analyzed. It should be noted that a junction is selected only from the view point of convenience and has no significant contribution to the platform motions.

The equation of motion for the floating body is modified to accommodate forced displacement, forced velocity and forced acceleration at forced node of the model as per Figure 2.20. The other nodes are free and thereby flexible floater is simulated with the use of beam elements.

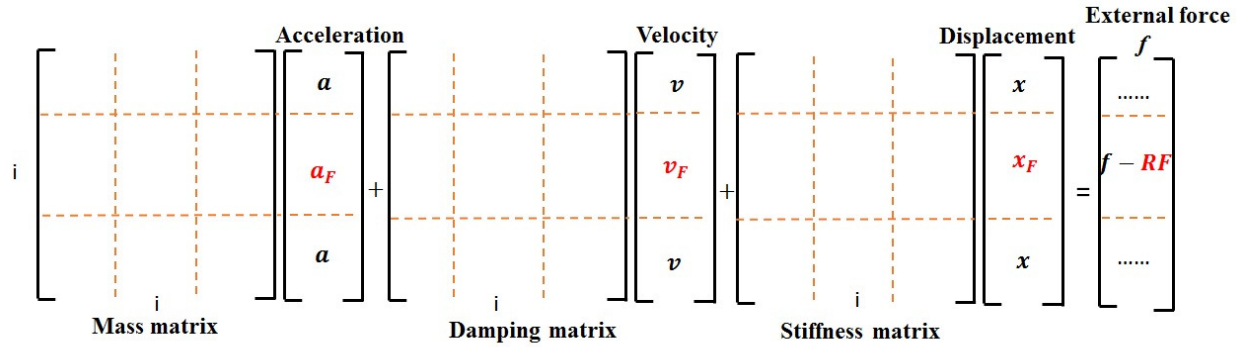

Figure 2.20 Matrix showing the method of obtaining 6 DOF Reaction Force at any junction.

Let us assume $\boldsymbol{x_F}$, $\boldsymbol{\dot{x}_F}$ and $\boldsymbol{\ddot{x}_F}$ are the forced displacement, forced velocity and forced acceleration at any junction or node. After transforming all of the mass, damping and stiffness matrices according to the forced acceleration, velocity and displacement, the displacement based incremental Newmark-Beta method is adopted to solve equation of motion. ***RF*** in the form of 3 degrees of motion reaction forces and 3 degrees of motion reaction moments is obtained at any selected junction between the main floater and the rotor-nacelle-tower system in the simulation. The reaction force thus evaluated in DYNABEAM module is used in Equation (2.13) as the forcing function is coupling scheme.

2.3.3 Coupled results and discussion

For understanding the coupled behavior and working methodology of coupling, preliminary results are discussed in this section. Before we get into the results, the model of analysis utilized has to be defined. In order to understand the basic coupling behavior, a semi-submersible model [40] is selected. The semi-submersible model with the junction is shown in Figure 2.21. It is at this junction the platform motions and reaction forces are exchanged at each time step and the motions are coupled by weak coupling algorithm explained.

A scaled model used for experimentation [42] is scaled up according to Froude's law of scaling to accommodate the NREL 5MW Baseline turbine [43]. The principal particulars of the main floater

is tabulated in Table 2.2. The model consists of 21 hull and 21 beam elements. 15 nodes are modelled in DYNABEAM and Nodes 16 to 21 is modelled directly in FAST as uniform tower for convenience. The junction is selected at Node 15 for the present analysis to understand coupling process. Mass of the model is 13130 tons and draft is 25 meters. Linear moorings are provided at Node 4, Node 5 and Node 6 to avoid the platform from drifting away.

Table 2.2 Principal particulars of main floater for verifying coupling process.

Item	Full scale model		Scale model	
	Value	Unit	Value	Unit
Mass	13130	t	13130	g
Draft	25	m	250	mm
Distance between Columns	75	m	750	mm
Column Diameter	11	m	110	mm
Column Height	33	m	330	mm
Column Height (with tower)	53	m	530	mm
Lower Hull Breadth	6	m	60	mm
Lower Hull Depth	6	m	60	mm
GM	7.13	m	71.3	mm

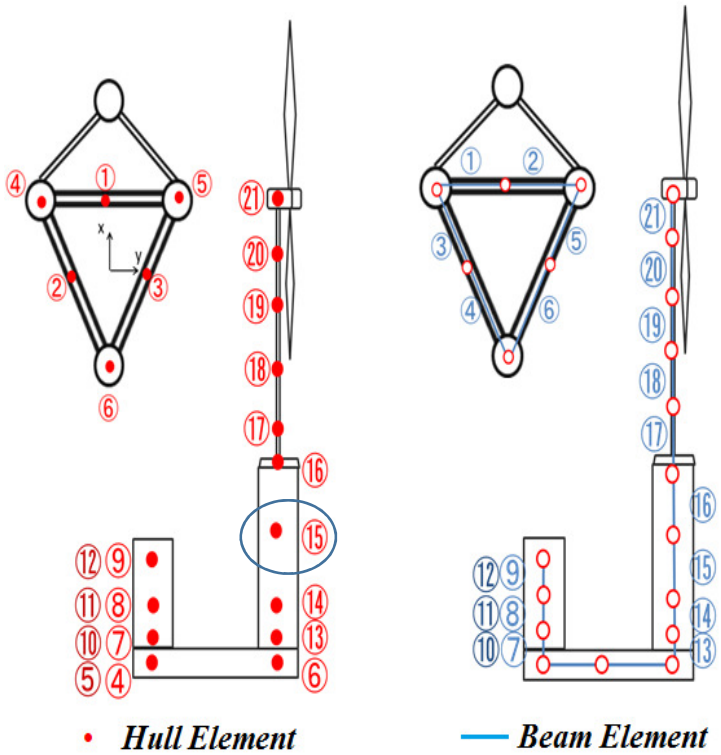

Figure 2.21 Semisubmersible model used for understanding coupling process.

The results shown in this section can be divided into three types to understand the coupling process and are defined as follows.

- Parking – These simulations are used to confirm the hydrostatic balance between the coupled modules. The FOWT system is parked by turning off wind and wind. The idea is to obtain close to zero platform displacements and rotations when parked.
- Only-wind – These simulations are used to understand the coupled FOWT response under only wind conditions. Still water condition is simulated by turning off the wave in these simulations such that response of the FOWT reflects only wind conditions acting on the FOWT system. The steady wind of 7mps is adopted in all simulations for confirming coupling process.
- Combined – Combined is the condition when both wind and wave acts on the platform. This condition is simulated to understand the complete response of FOWT systems. The coupled process is understood with the help of combined response. The steady wind of 7mps along with regular wave of wave amplitude 1.5m and wave period of 10s is employed for combined condition in all simulations.

The platform motions at junction (Node 15 in Figure 2.21) is obtained for all six degrees of freedom is obtained for parking, only-wind and combined conditions. Figures 2.22 and 2.23 shows the platform heave motion and the corresponding reaction force associated with it.

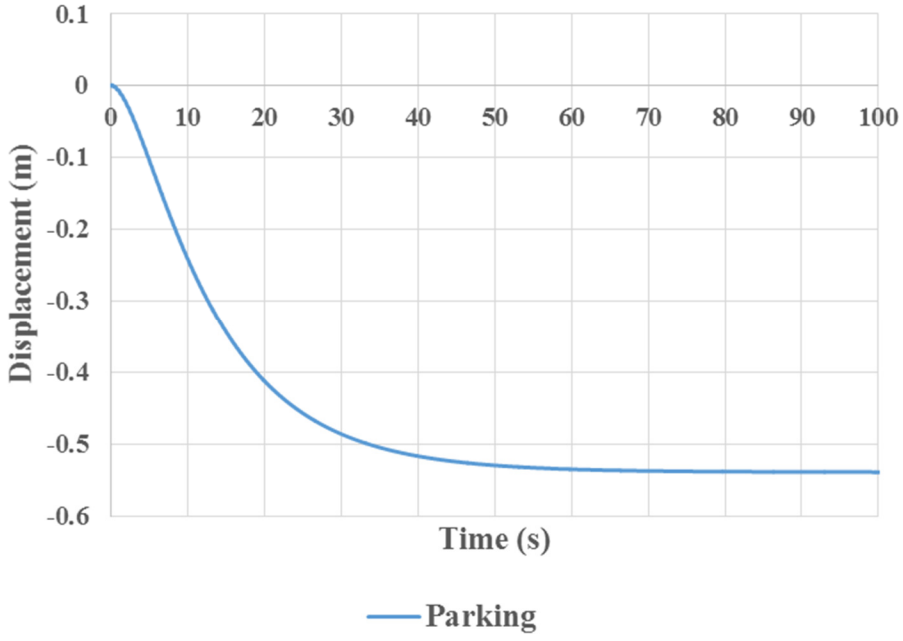

Figure 2.22 Displacement in Heave direction at junction – Parking.

As expected, the heave displacement at junction (Figure 2.22) is found to be close to zero in parking condition. The value of 0.5m shows that the model is balanced and the buoyancy and gravity forces balance out with each other. This can be confirmed from Figure 2.23 where the

reaction force obtained is due to the mass of the tower since junction divides the FOWT into floater and tower. The mass of the tower for the FOWT system is 1.26×10^6 kg. The value of about minus 1.23×10^4 kN (1.26×10^6 kg multiplied by acceleration due to gravity $-9.81 ms^{-2}$) is obtained. This arises from gravity force of tower given by the buoyancy from platform as reaction force in simulation. Hydrostatic balance is thus achieved and coupling between two module works.

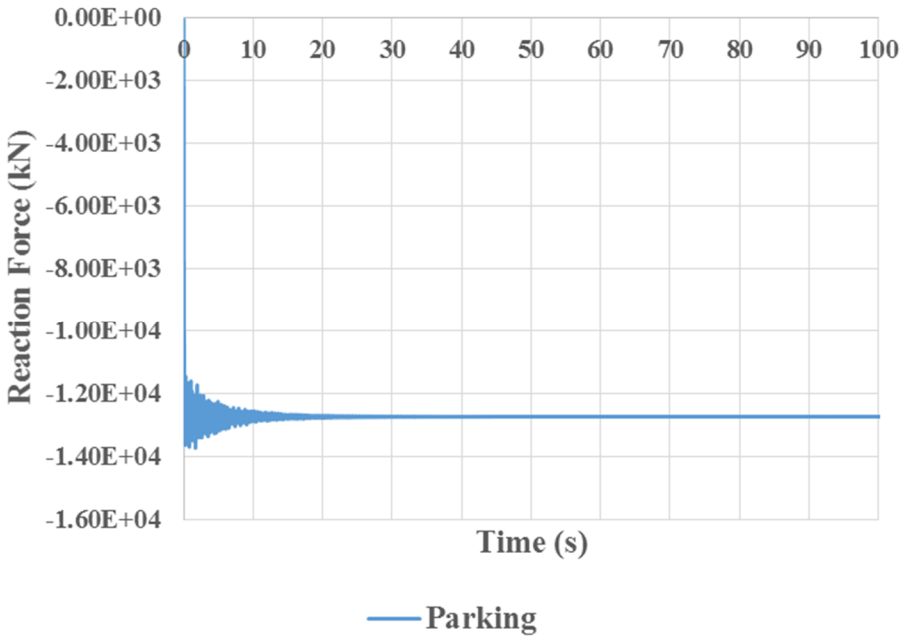

Figure 2.23 Reaction Force in Heave direction at junction – Parking.

Now, let us proceed for the discussion for platform motions in all six degrees of freedom. Figures 2.24 to 2.29 compares the parking, only-wind and combined simulations for displacement in surge, sway and heave directions as well as rotations in roll, pitch and yaw directions. It can be observed from Figure 2.24 that the parking response is close to zero when no wind and wave acts on the platform. It is also observed that only-wind response of about 0.6m is obtained due to steady wind of 7mps. From the combined curve it is possible to understand the combined dynamic response due to coupling of wind and wave loads. The 10 peaks observed between 0 and 100s of the simulation describes the dynamic response since wave period of 10s is applied on the floater.

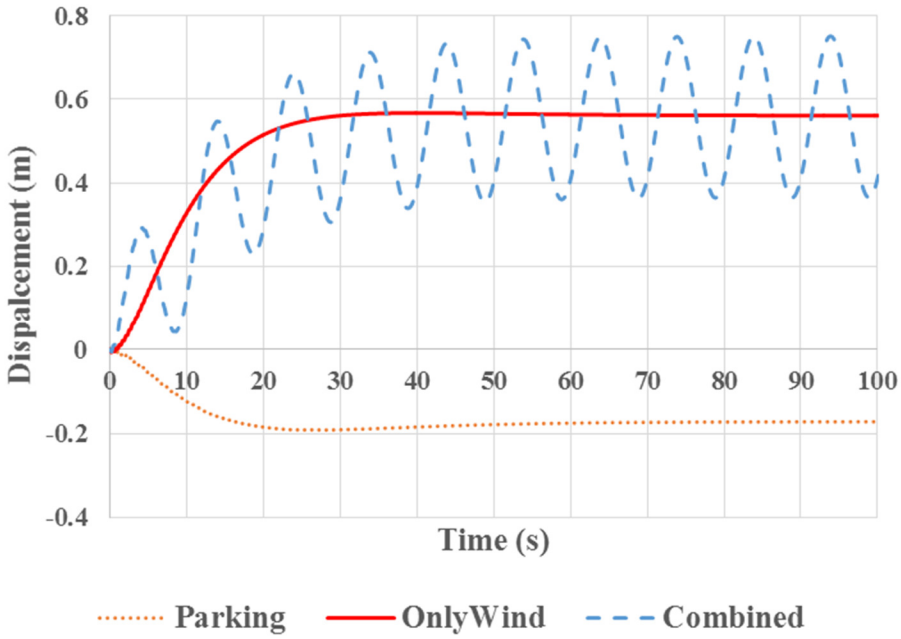

Figure 2.24 Platform Surge Motion – Comparison to confirm coupling process.

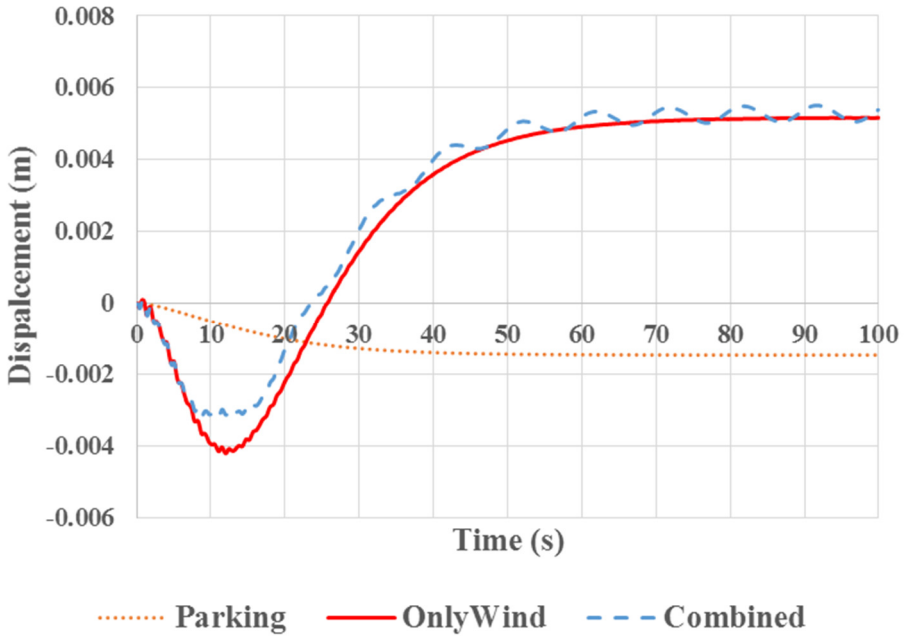

Figure 2.25 Platform Sway Motion – Comparison to confirm coupling process.

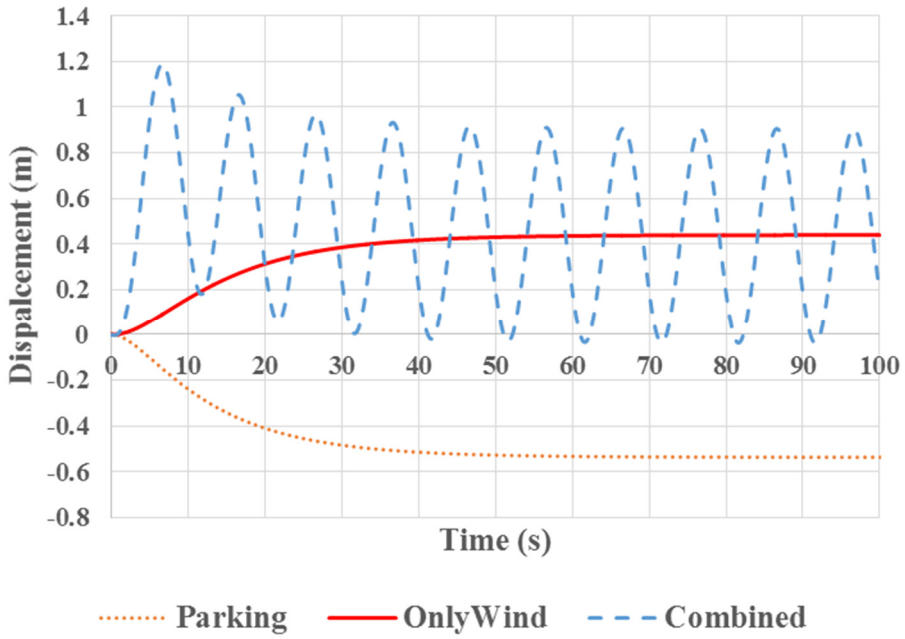

Figure 2.26 Platform Heave Motion – Comparison to confirm coupling process.

The maximum platform displacement in heave direction (Figure 2.26) when combined loading is acting on the platform is found to be 1.2m for the present model and environmental conditions considered. The combined dynamic response can also be observed for the platform displacement in sway direction. However, it can be observed that sway is not a predominant motion.

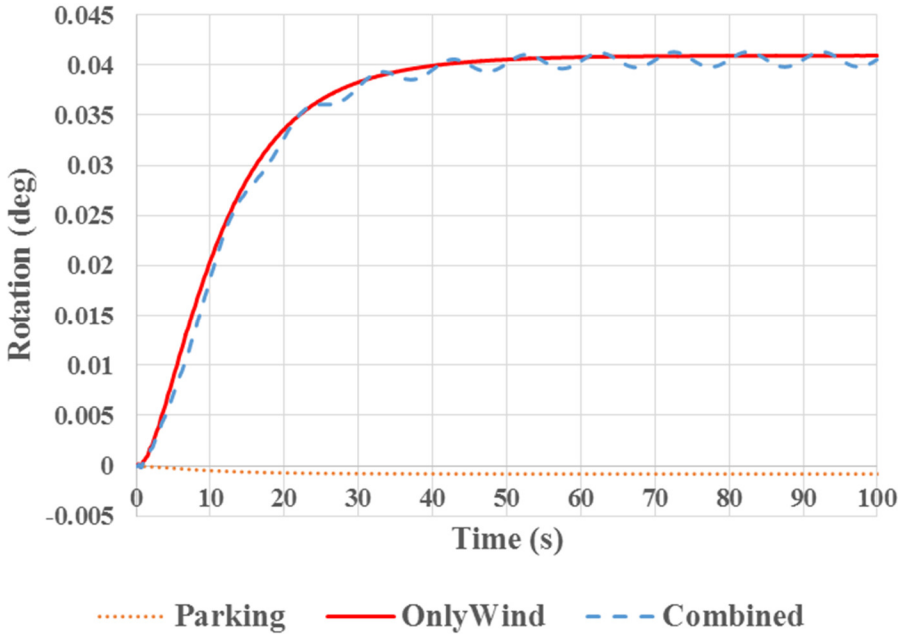

Figure 2.27 Platform Roll Motion – Comparison to confirm coupling process.

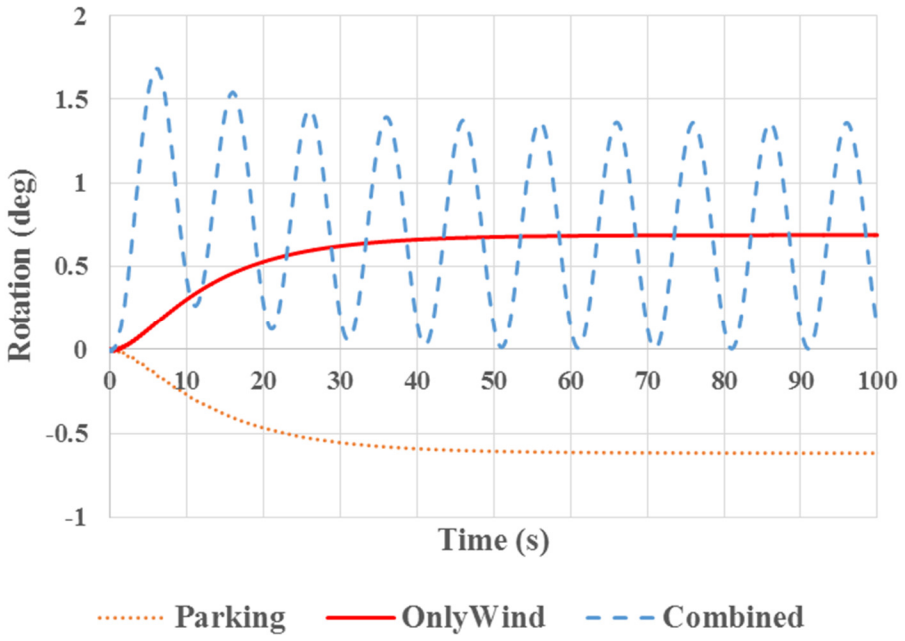

Figure 2.28 Platform Pitch Motion – Comparison to confirm coupling process.

Figure 2.28 shows the platform pitch when subjected to steady wind and regular wave and this induces a maximum inclination of about 1.7deg for the platform. The rotation in roll direction (Figure 2.27) and rotation in yaw direction (Figure 2.29) is found to be small.

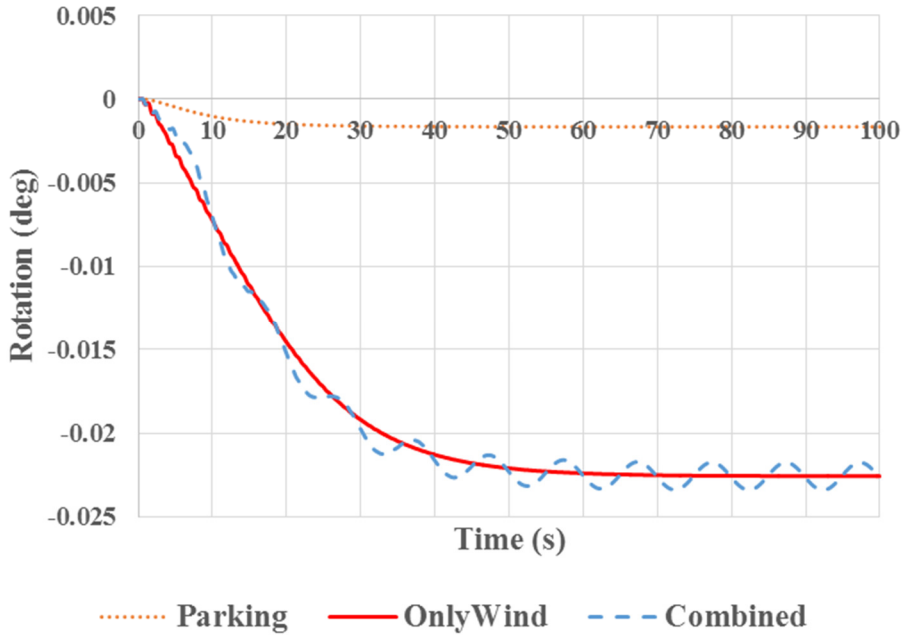

Figure 2.29 Platform Yaw Motion – Comparison to confirm coupling process.

The combined dynamic response is confirmed for platform heave motion and its working feature is confirmed. The displacement in heave direction at junction is shown in Figure 2.30. The reaction force (Figure 2.31) confirms the dynamic behavior which is explained by taking into account of wave period response. Thus, the working feature of coupled simulation process is confirmed.

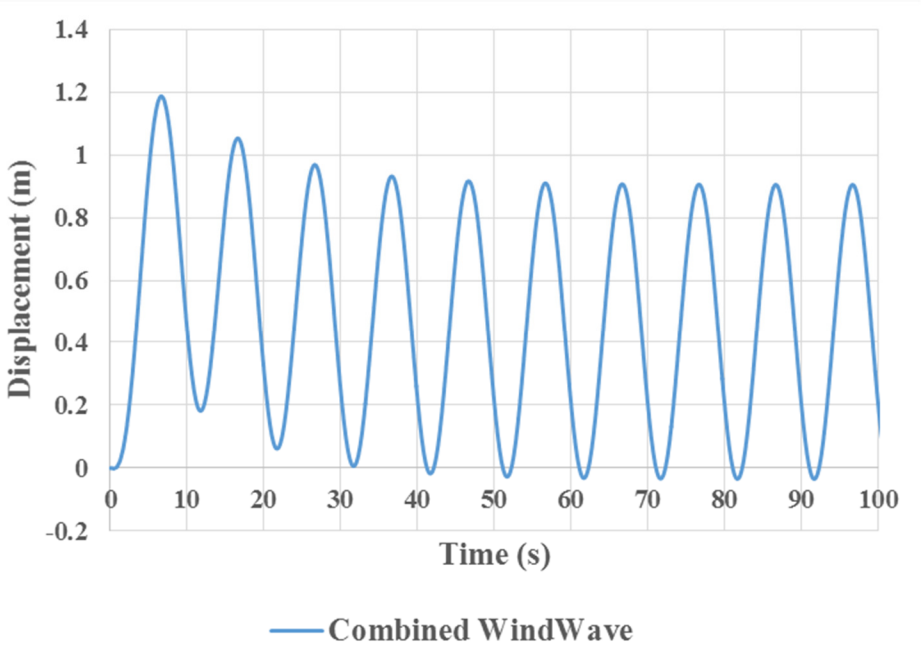

Figure 2.30 Displacement in Heave direction at junction – Combined.

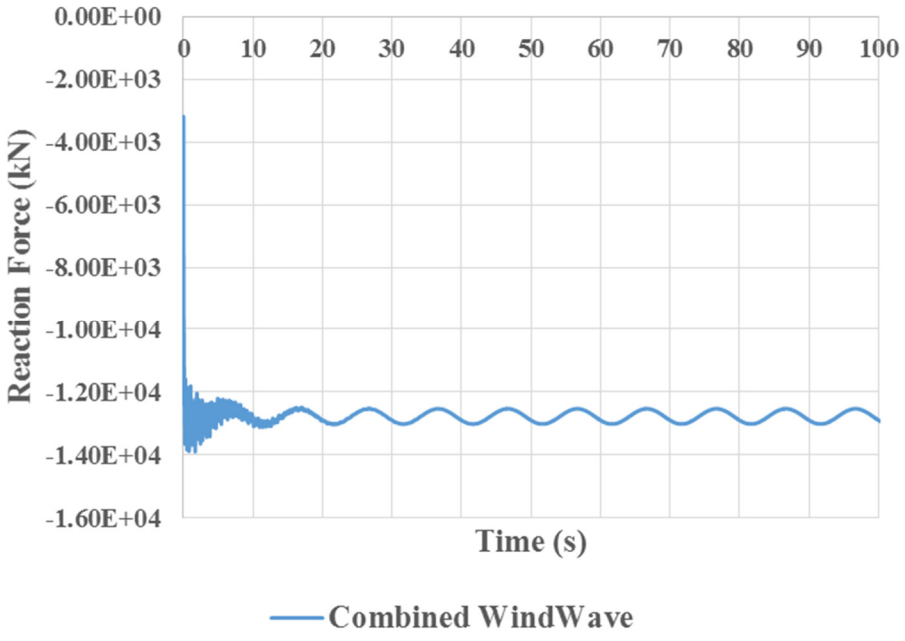

Figure 2.31 Reaction Force in Heave direction at junction – Combined.

The differences between onshore wind turbine and floating offshore wind turbine systems are compared. Firstly, tower base loads is considered. Figure 2.32 shows tower base force in heave direction. It is evidently observed that dynamic effect is observed for floating case. Similar dynamic behavior is observed for tower base moment in pitch direction (Figure 2.33).

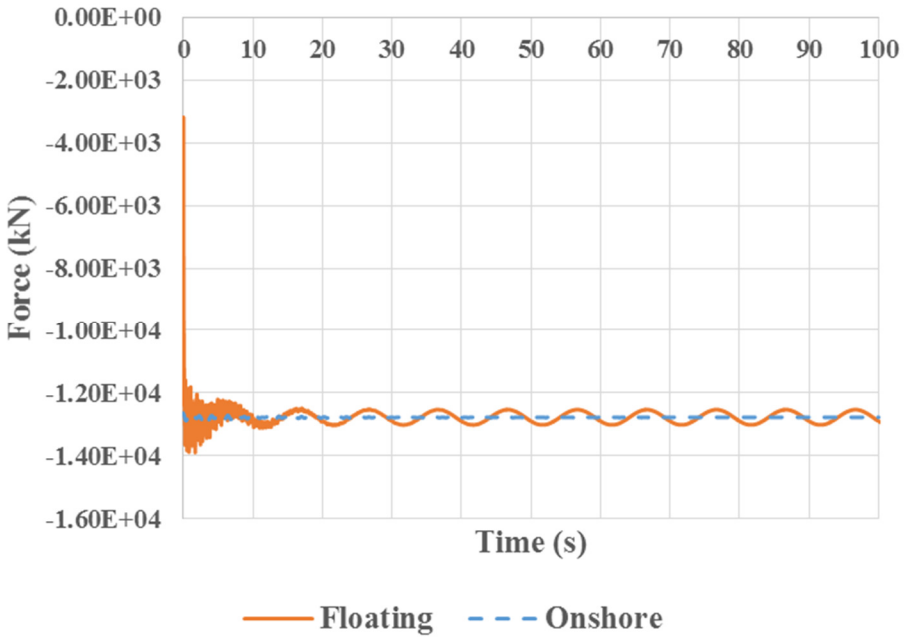

Figure 2.32 Tower Base Load F_z – Onshore vs Floating.

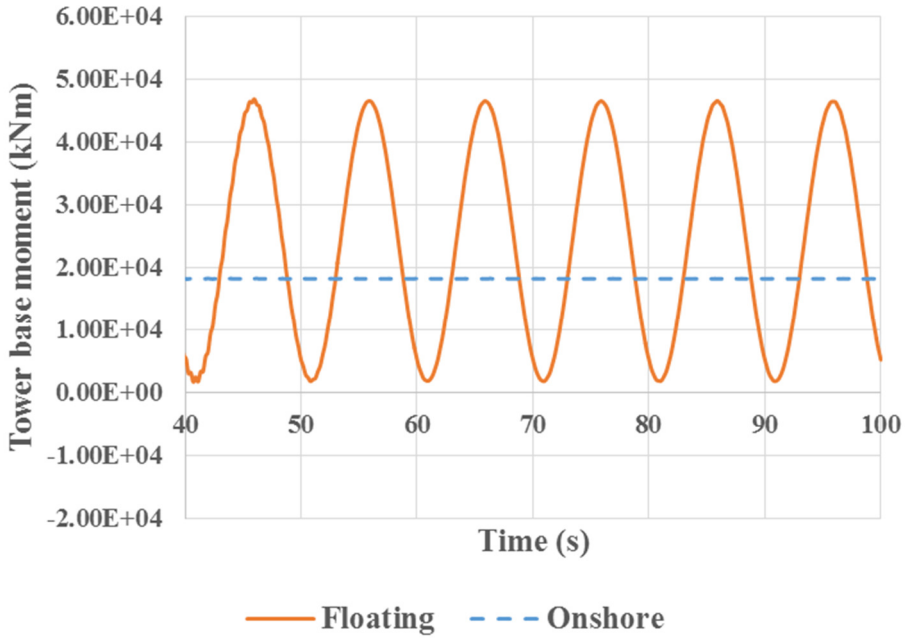

Figure 2.33 Tower Base Moment M_y – Onshore vs Floating.

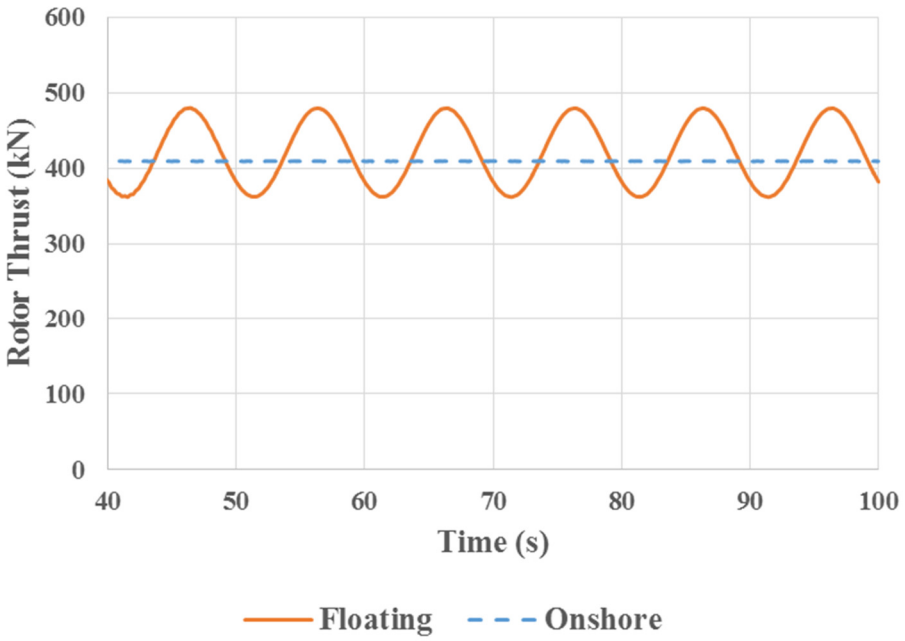

Figure 2.34 Rotor Thrust – Onshore vs Floating.

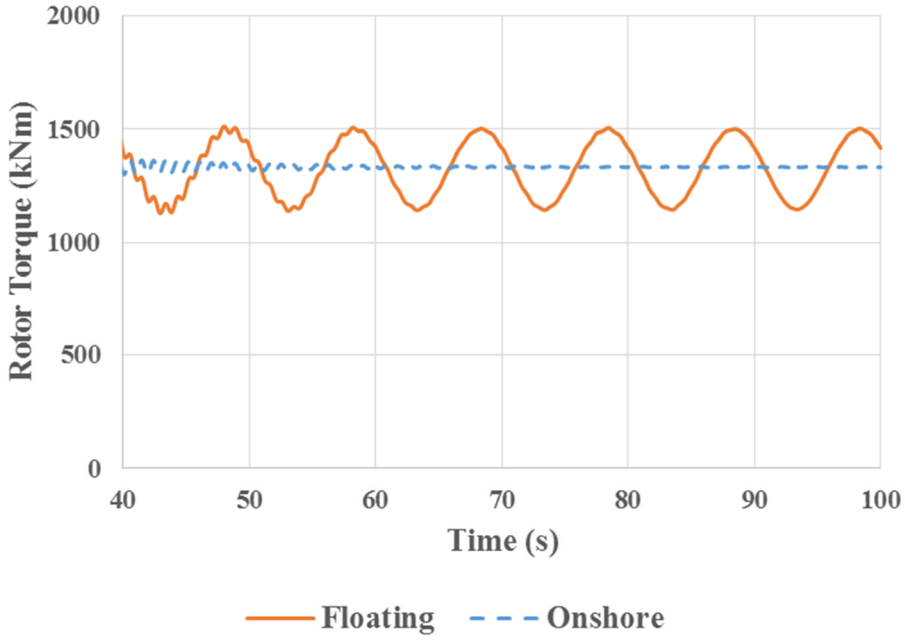

Figure 2.35 Rotor Torque – Onshore vs Floating.

Secondly, rotor loads mainly rotor thrust and rotor torque is considered. Figures 2.34 and 2.35 shows the mutual effect of the floating platform on rotor loads. The dynamic behavior of both rotor thrust and rotor torque follows the wave pattern with same period of 10s and thus mutual influence

of floater on rotor loads is confirmed for steady wind and regular waves. This confirms that a holistic aero-hydro dynamic coupling tool is developed for the analysis of FOWT systems. However, the developed coupling tool needs to be validated for it to be used for response analysis of FOWT systems. Chapter 3 discusses the validation of the developed coupled tool.

3 Validation of Coupled Tool

It is important to validate the developed coupled simulation tool to be able to practically use it for response analysis of FOWT systems. It is also important to understand the flexibility feature of the present analysis tool. Firstly, the model for analysis for validation is discussed followed by validation strategy. Further, results of validation are discussed.

3.1 Model for Analysis

FOWT is modelled to accommodate the NREL 5MW Baseline wind turbine [43]. For the analysis purpose, OC3-Hywind SPAR model is selected. OC3 stands for Offshore Code Comparison Collaboration project [44] by NREL. A flexible spar model is created in DYNABEAM and compared. The idea is to have qualitative similarities between the models. This will be further explained in the validation strategy.

3.1.1 Model in FAST – Rigid OC3-Hywind SPAR

The tower is cantilevered at an elevation of 10 m above the SWL to the top of the floating platform, which for the purposes of analysis is considered to be a rigid body as shown in Figure 3.1. This is the limitation of the model in FAST. This model will be taken as reference for all simulations between flexible and rigid models.

The draft of the platform is 120m. Between the top and bottom of the platform, the OC3-Hywind spar-buoy consists of two cylindrical regions connected by a linearly tapered conical region. The cylinder diameter of 6.5m above the taper is more slender than the cylinder diameter of 9.4m below the taper to reduce hydrodynamic loads near the free surface. The linearly tapered conical region extends from a depth of 4m to a depth of 12m below the SWL. The hydrodynamic modelling is carried out using WAMIT [45]. The properties of the OC3-Hywind spar are summarized in Table 3.1.

Table 3.1 OC3-Hywind spar structural properties.

Total Draft	120 m
Elevation to Platform Top Above SWL	10 m
Depth to Top of Taper Below SWL	4 m

Depth to Bottom of Taper Below SWL	12 m
Platform Diameter Above Taper	6.5 m
Platform Diameter Below Taper	9.4 m
Platform Mass, Including Ballast	7,466,330 kg
CM Location Below SWL	89.9155 m
Platform Roll Inertia about CM	4,229,230,000 kg.m^2
Platform Roll Inertia about CM	4,229,230,000 kg.m^2
Platform Roll Inertia about Platform Centerline	164,230,000 kg.m^2

CM: Centre of Mass, SWL: Still Water Level

(Reproduced from Reference [44])

Figure 3.1 Illustration of the NREL 5-MW wind turbine on the OC3-Hywind spar. (Reproduced from Reference [44])

The mass, including ballast, of the floating platform is 7,466,330kg. This mass was calculated such that the combined weight of the rotor-nacelle assembly, tower, and platform, plus the weight of the mooring system in water, balances with the buoyancy (i.e. weight of the displaced fluid) of the undisplaced platform in still water. This mass is centered (i.e. the CM of the floating platform, including ballast, is located) 89.9155m along the platform centerline below the SWL. The roll and pitch inertias of the floating platform about its CM are 4,229,230,000kg.m^2 and the yaw inertia of the floating platform about its centerline is 164,230,000kg.m^2. To prevent it from drifting, Statoil's Hywind platform is moored by a system of three catenary lines. Additional springs are provided to increase the yaw stiffness. For the flexible model, it is important that similar guidelines be followed while creating the model. The rigid model of FAST will be modeled as flexible model in the DYNABEAM.

3.1.2 Model in DYNABEAM – Designed Flexible SPAR

A flexible floater model is developed using the DYNABEAM module. The floating spar model described in the previous section is replicated consisting of hull and beam elements. A schematic representation is shown in Figure 3.2. It can be observed that spar model is regarded as flexible with 10 hull elements (nodes) and 9 beam elements connecting the nodes.

The designed spar model is qualitatively similar to the OC3-Hywind spar model having similar mass distribution, draft and thereby the CM of the floating platform. To arrive at this, firstly the hydrostatic balance is achieved in DYNABEAM module. The masses other than the platform mass i.e., tower mass, hub mass, nacelle mass and blade mass is modelled as lumped mass in DYNABEAM. This lumped mass is distributed between Node 9 and Node 10 in the present model while evaluating the model usage in DYNABEAM. During coupling, lumped is not considered and tower, hub and nacelle masses are modelled in FAST directly. Mooring lines are provided to avoid the drifting of the platform using linear mooring system. Yaw stiffness in flexible model is increased to match with the parking condition natural frequency of the FAST model.

After the hydrostatic balancing is achieved, flexible floater model is used for coupled analysis. For coupling purposes, a junction is selected. In the present analysis, this junction is selected at Node 10. At this junction, the motions are coupled by weak coupling algorithm explained in the previous chapter. It is at this junction the platform motions and reaction forces and moments are exchanged at each time step. The blade pitch and torque control is suppressed for simplicity in all the simulations in this chapter.

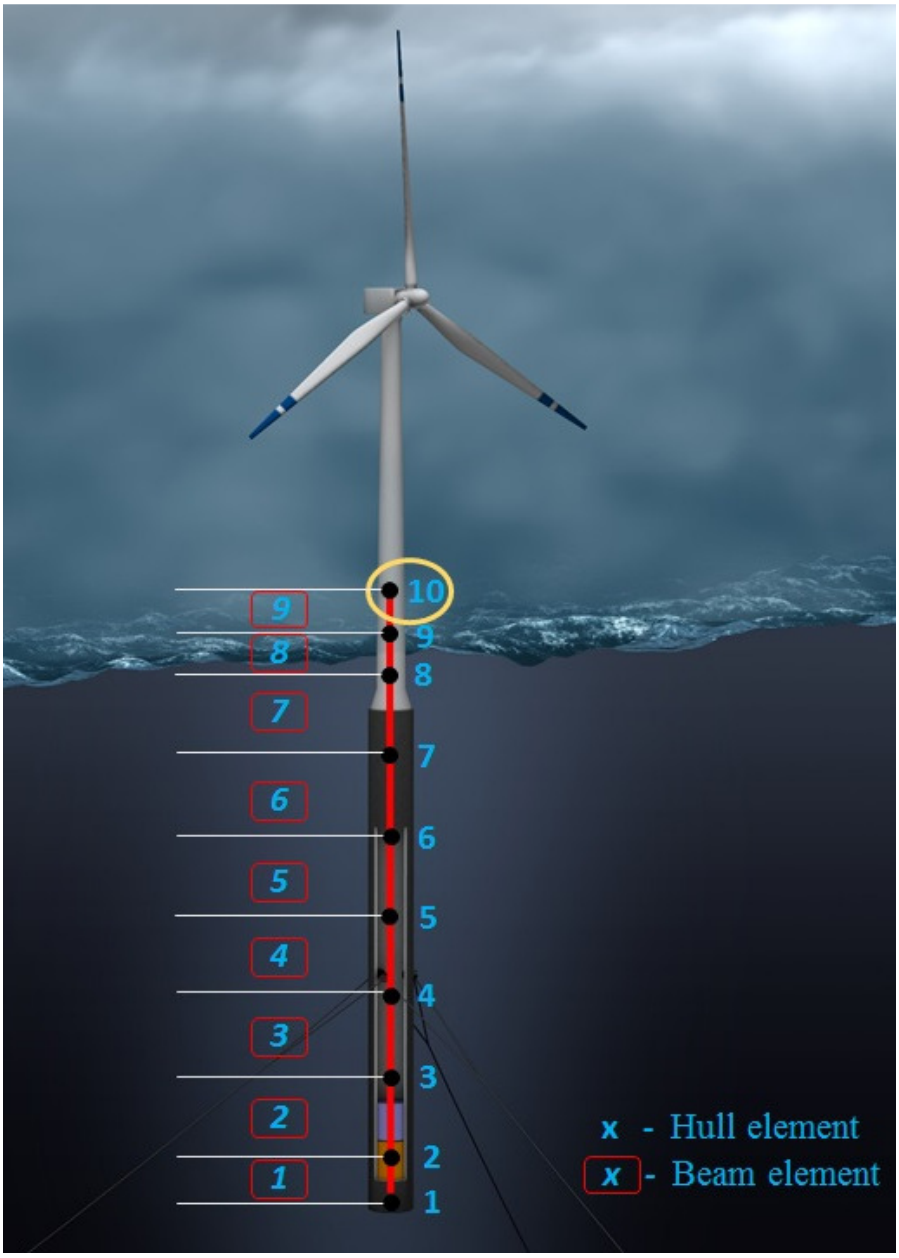

Figure 3.2 Illustration of flexible spar modeling in DYNABEAM showing junction. (Reproduced and modified from Reference [44])

3.2 Validation strategy

To validate the developed coupled analysis tool, it is important to select the appropriate model and technique. To this regard, the public data available from FAST is utilized. OC3-Hywind spar is a well-established offshore development model for FOWT systems.

It becomes important to have similar motion characteristics to say that rigid floater model is qualitatively similar to flexible model designed and developed for coupling. Pitch tilt angle is targeted for this purpose after achieving hydrostatic balance [46]. Pitch angle is one of the most important feature to be considered for a FOWT system since the rotor thrust at the nacelle level causes the floater to tilt as observed in the preliminary results in Chapter 2. The designed model must be able to provide enough restoring moment against the pitch tilt. Therefore, the pitch tilt angle shall be matched between the rigid and flexible models. The models are acclaimed to be qualitatively similar if they have similar response of pitch tilt angle for the same wind thrust provided the model is balanced in heave.

Validation strategy thus includes firstly to balance the flexible model in heave motion and secondly to match the pitch tilt angle for the same rotor thrust. With this validation strategy, the model is validated as well as the coupled simulation tool and in turn incorporating the flexibility of floater into the system. The validated results are presented in the following section.

3.3 Results and discussion

Firstly, rigid body floater is considered and simulation results are obtained from FAST with various environmental conditions i.e., parking, only-wind and combined wind and wave conditions. Parking is a condition when the FOWT is parked in still water with no wind or wave loads. It indicates the balance between the gravity and buoyancy forces and act as a guideline for further comparisons. Mainly, three cases are considered for coupled analysis response similar to the one discussed in Chapter 2.

1. Case (i) Parking – No wind, no wave
2. Case (ii) Only-wind – Steady wind
3. Case (iii) Combined – Steady wind, Regular wave

The same co-ordinate system is used for both wave and wind loads. The conventional directions are explained in the Figure 3.3 at tower base. Rigid body results as well as flexible floater results for the coupled simulation is presented here.

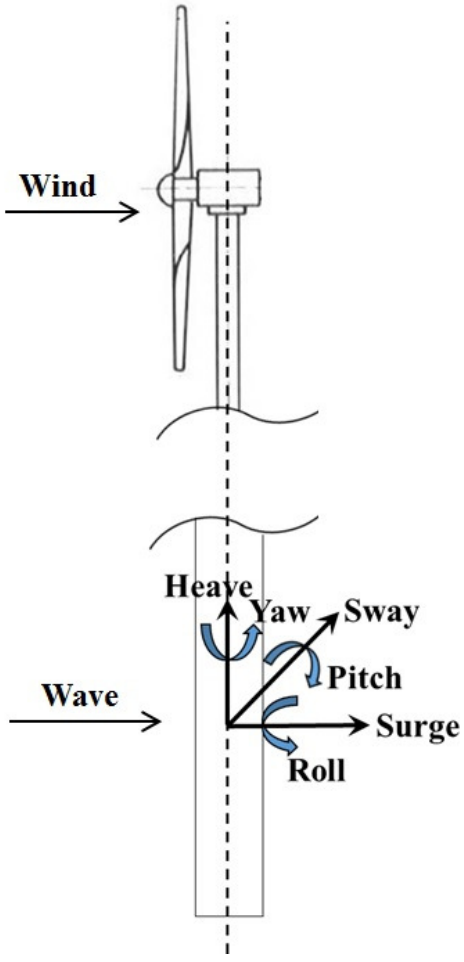

Figure 3.3 Wind and wave directions.

3.3.1 Rigid model vs Flexible model

1. Case (i) Parking

Parking test results are summarized firstly for rigid floater from FAST. Figures 3.4 and 3.5 show the heave and pitch motion of the OC3-Hywind spar buoy floater respectively. We can observe that these values are close to zero as the model is perfectly balanced in heave and pitch tilt angle is close to zero because wind thrust is turned off. It should also be noted that these motions are evaluated at the platform CM.

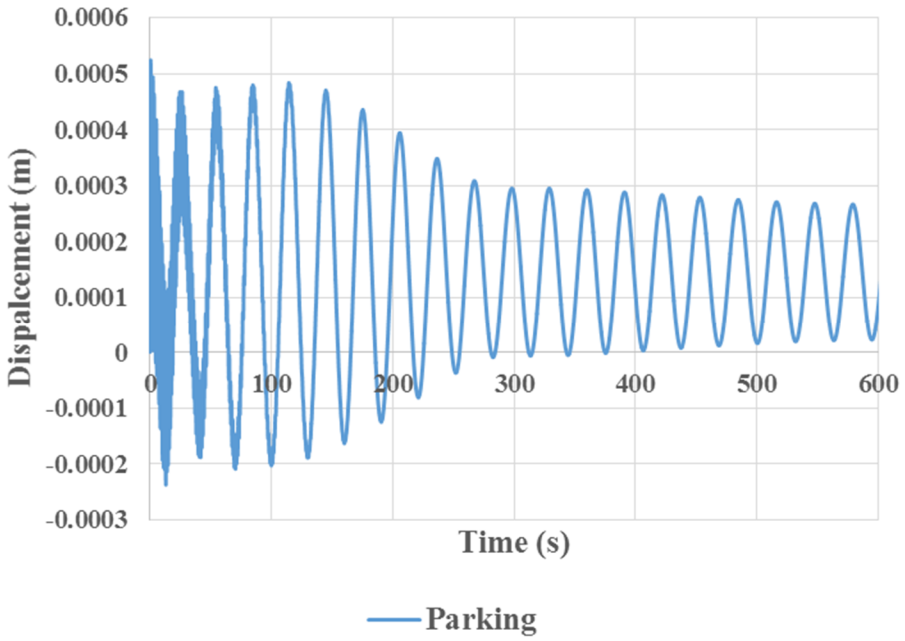

Figure 3.4 Rigid floater – Heave displacement – Parking.

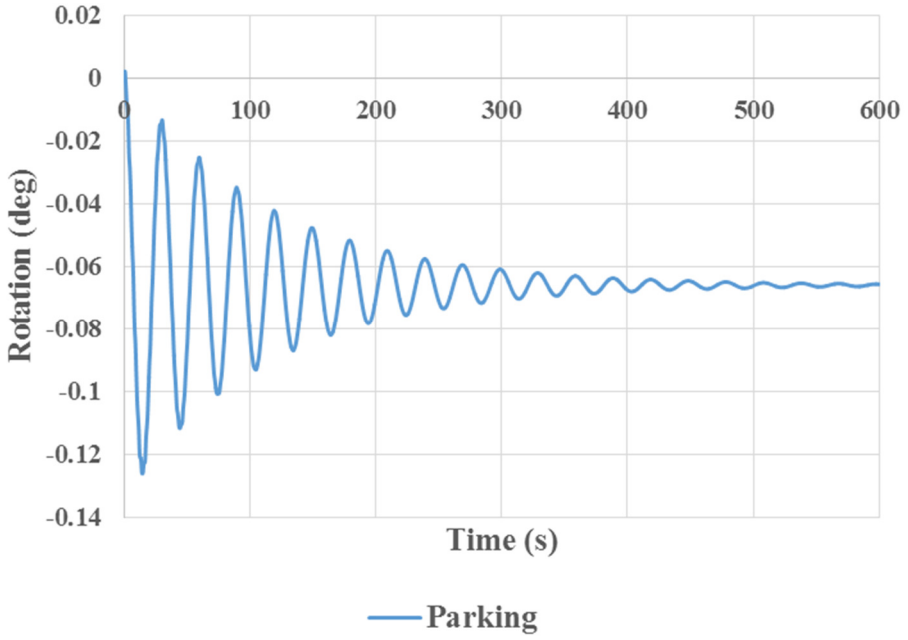

Figure 3.5 Rigid floater – Pitch tilt angle – Parking.

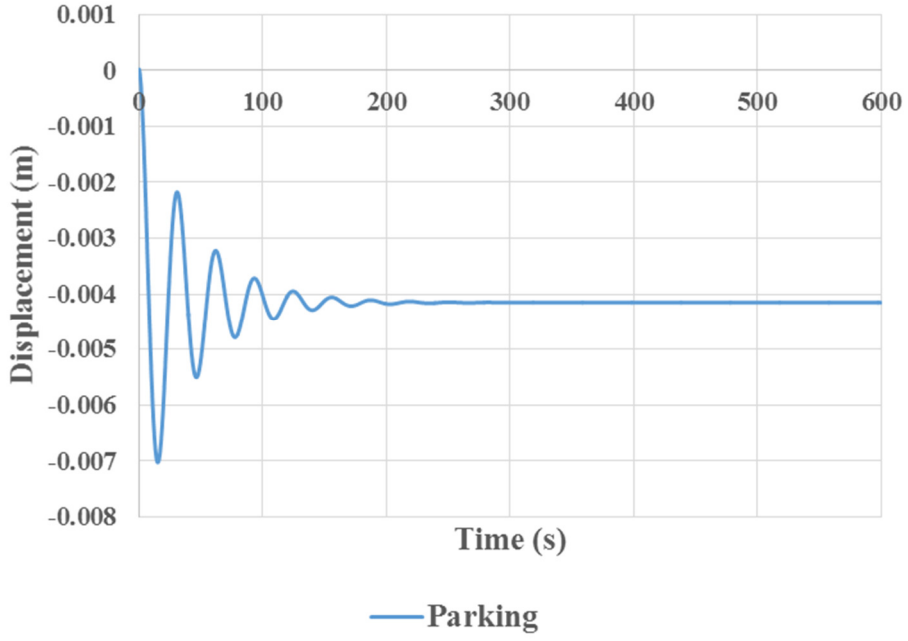

Figure 3.6 Flexible floater – Heave displacement at junction – Parking.

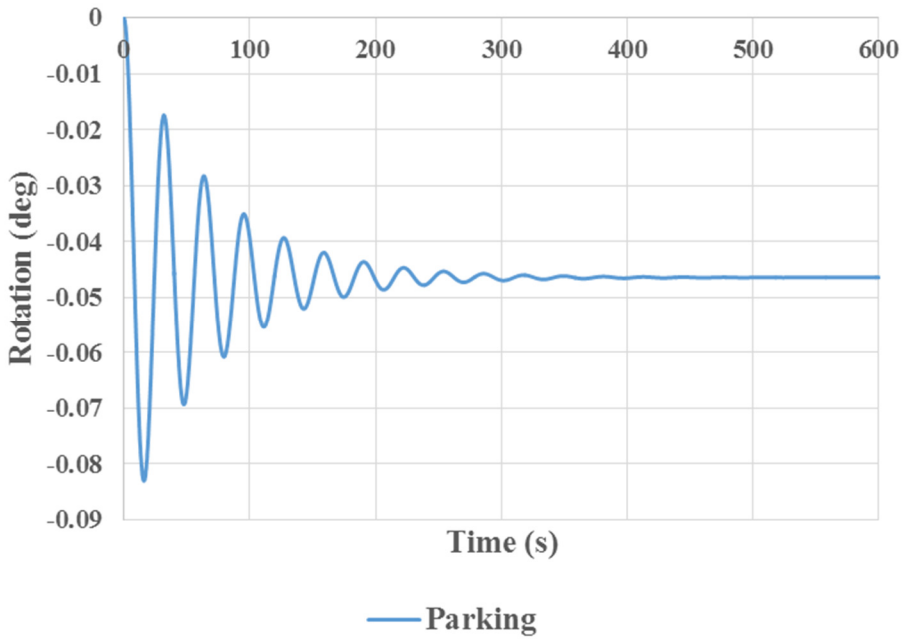

Figure 3.7 Flexible floater – Pitch tilt angle at junction – Parking.

Figures 3.6 and 3.7 show the parking test results for the flexible model developed in FAST-DYNABEAM coupling. Here, the pitch tilt angle and heave displacement refers to motions exchanged at junction in coupling. It can be concluded that the flexible model designed is balanced in heave and pitch.

2. Case (ii) Only-wind

Now, let us go into the validation of the flexible model. As explained in the validation strategy, the pitch tilt angle is targeted for this. For simplicity, only-wind case is considered in the beginning. Steady wind speed of 7mps is considered. It can be observed from Figure 3.8 that there is a static tilt angle of 2.1 degrees in pitch motion when the motion of rigid spar model is considered when subjected to steady wind of 7mps.

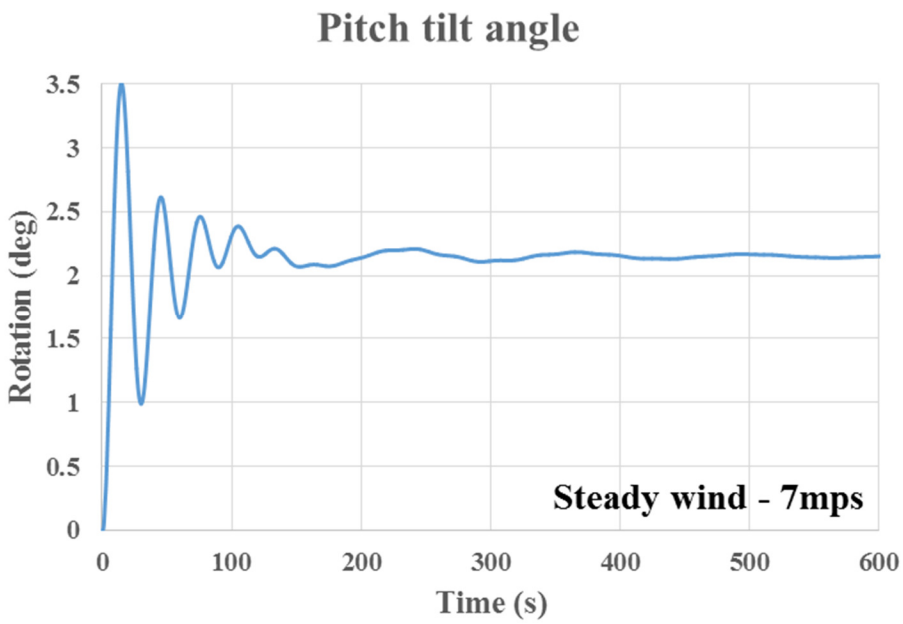

Figure 3.8 Rigid floater – Pitch tilt angle – Only-wind.

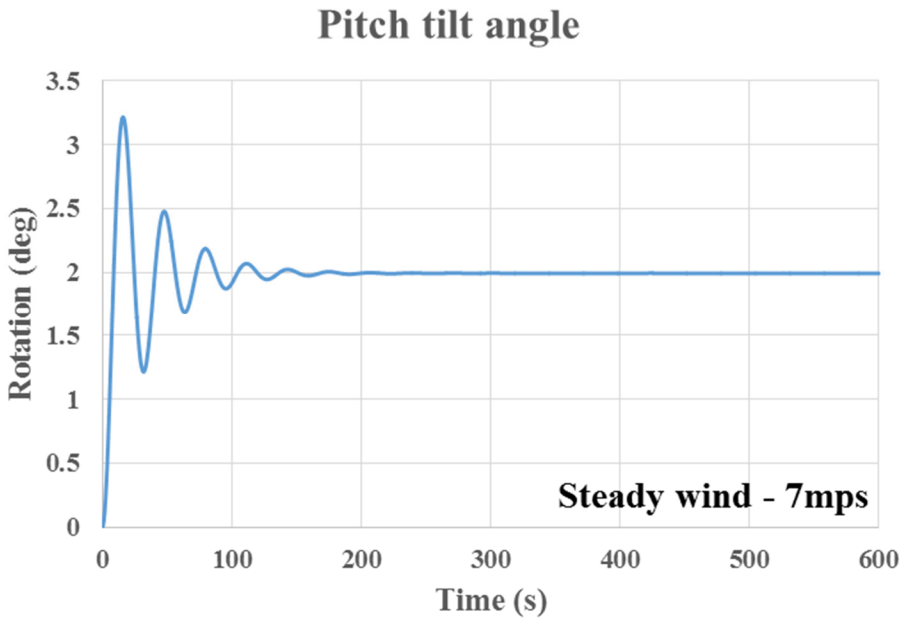

Figure 3.9 Flexible floater – Pitch tilt angle at junction – Only-wind.

The pitch tilt angle in Figure 3.8 is targeted and coupled simulation result for flexible floater is obtained as shown in Figure 3.9. It can be observed that the pitch angle is 2 degrees. It is almost comparable with the pitch motion of the rigid body. The restoring moment in DYNABEAM model is giving slightly larger value as compared to the rigid body spar model. There is also a slight

difference in the center of buoyancy between the models and the volume of water displaced is a little different between the models. However this difference is not very significant for the qualitative analysis and comparison. From these plots, it can be concluded that the pitch tilt angle between the models is almost same.

3. Case (iii) Combined

Validation is continued for combined cases from now on. Combined case of wind and wave is now considered obtained from the coupled simulation method and compared with the flexible model. The following regular wave conditions are considered in combined case. Table 3.2 summarizes the various conditions. Time series of the heave displacement and pitch angle at the junction for various conditions of the regular waves is presented. It is compared with the flexible model for each case.

Table 3.2 Regular wave conditions for Validation

Wave amplitude (m)	1	1	1	1
Time period (s)	20	12	8	5

The heave displacement for Flexible Model in DYNABEAM is evaluated at the junction selected. It can be observed from Figures 3.10 and 3.11 that the response of the FOWT is combined dynamic response. The static component of the pitch tilt angle is arising from the wind thrust and the sinusoidal part with time period of 20 seconds arises from the wave load. It can be observed that there are 5 peaks within time of 200s and 300s owing to the fact of response to the wave loading.

There is slight change in the mean value owing to the fact of different imbalance between the models initially. And the change in amplitude is due to varied hydrodynamic modelling between the models. The hydrodynamic added mass and damping used for OC3-Hywind spar is different from the one used for the flexible model in DYNABEAM. Similar results are shown for other regular wave conditions. Figure 3.12 to Figure 3.17 summarizes this for different wave time periods. A good agreement could be observed between the flexible and rigid models.

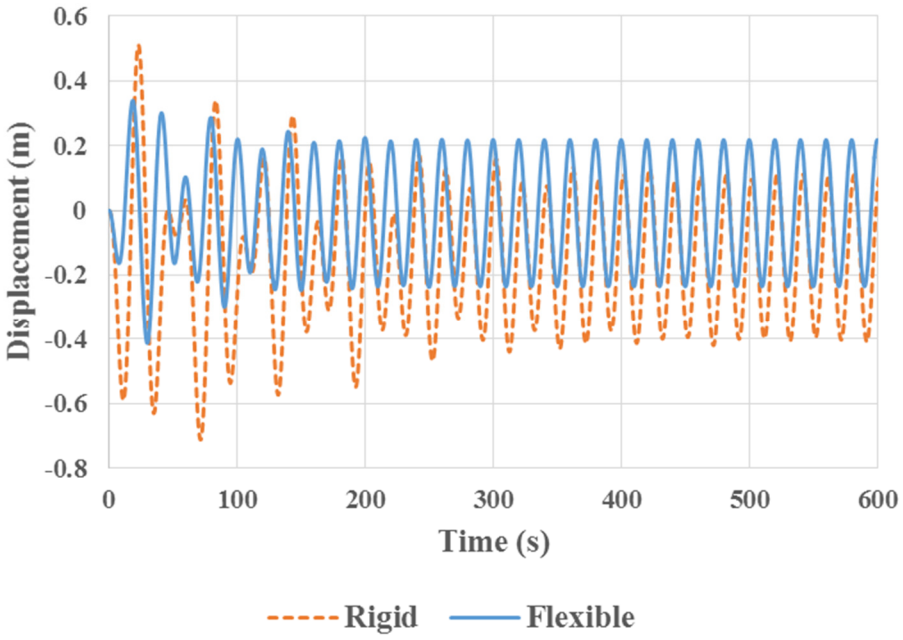

Figure 3.10 Heave displacement – Combined – 7mps, 1m and 20s.

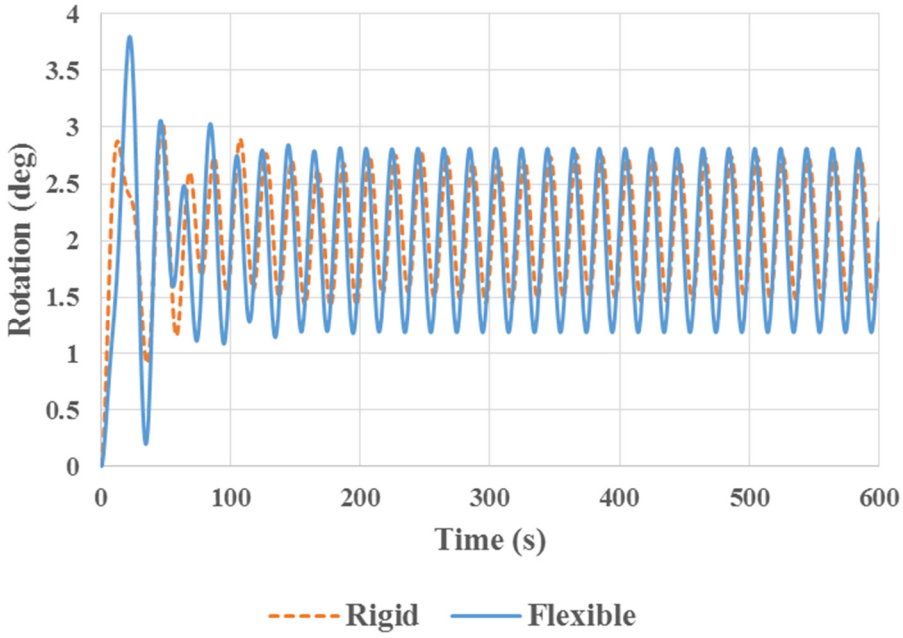

Figure 3.11 Pitch tilt angle – Combined – 7mps, 1m and 20s.

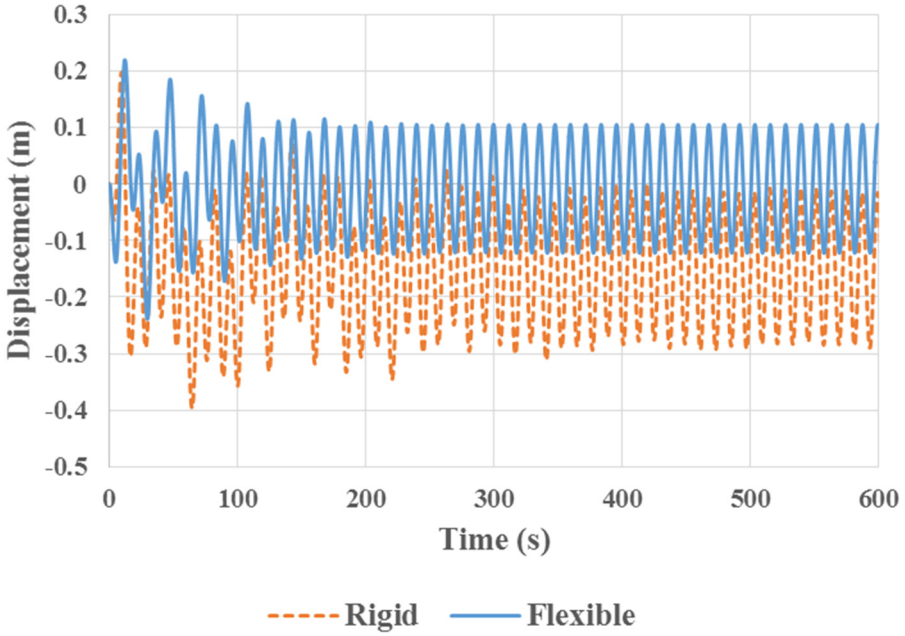

Figure 3.12 Heave displacement – Combined – 7mps, 1m and 12s.

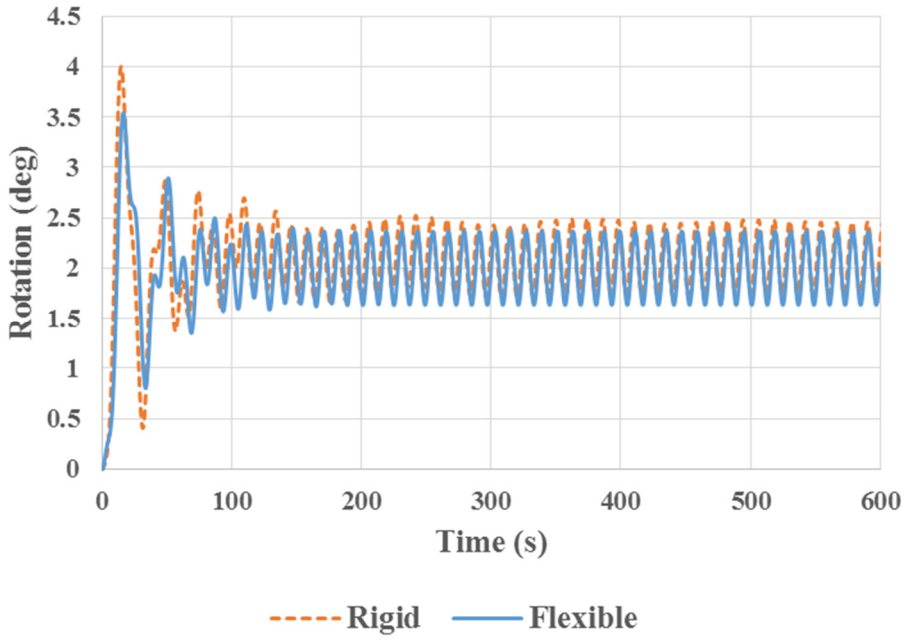

Figure 3.13 Pitch tilt angle – Combined – 7mps, 1m and 12s.

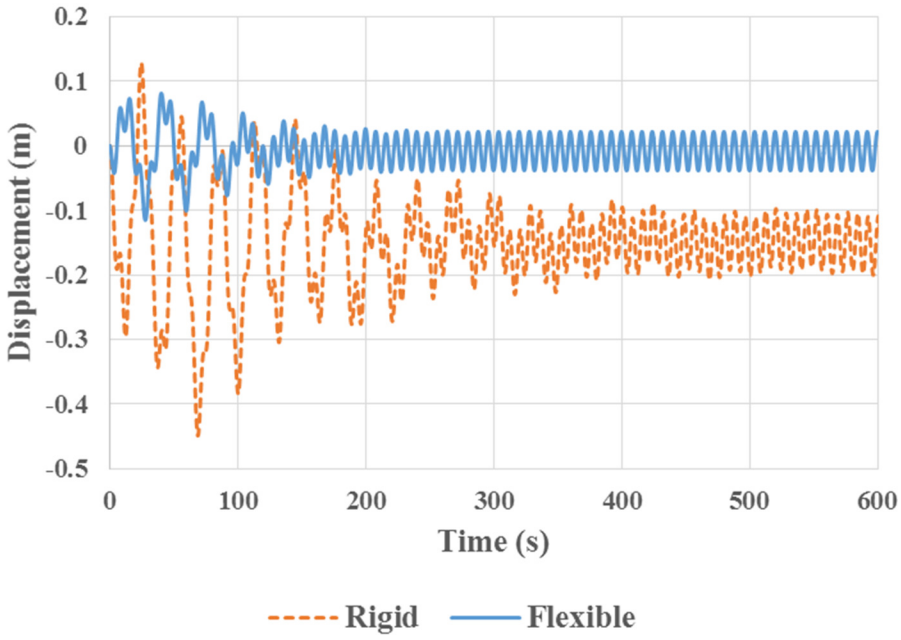

Figure 3.14 Heave displacement – Combined – 7mps, 1m and 8s.

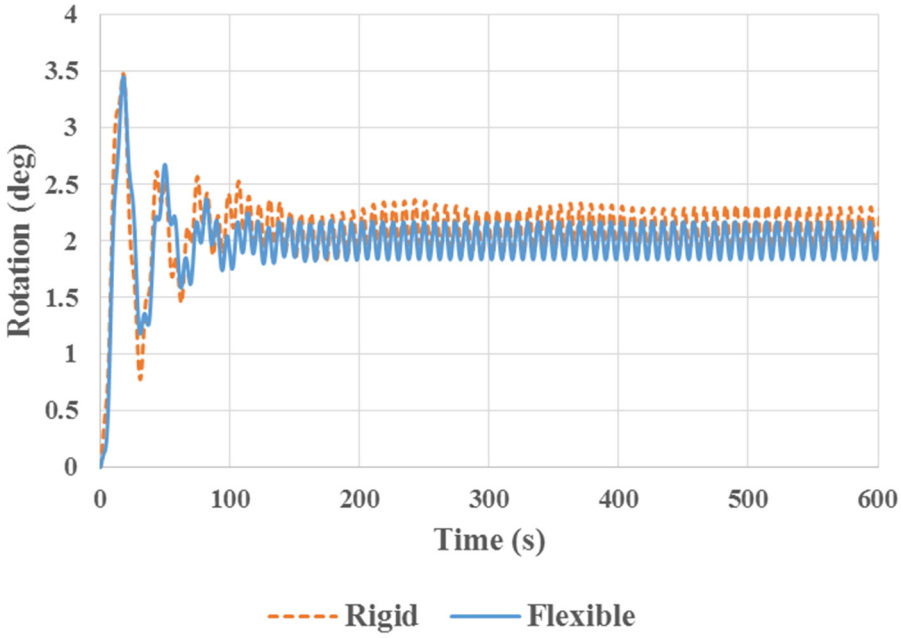

Figure 3.15 Pitch tilt angle – Combined – 7mps, 1m and 8s.

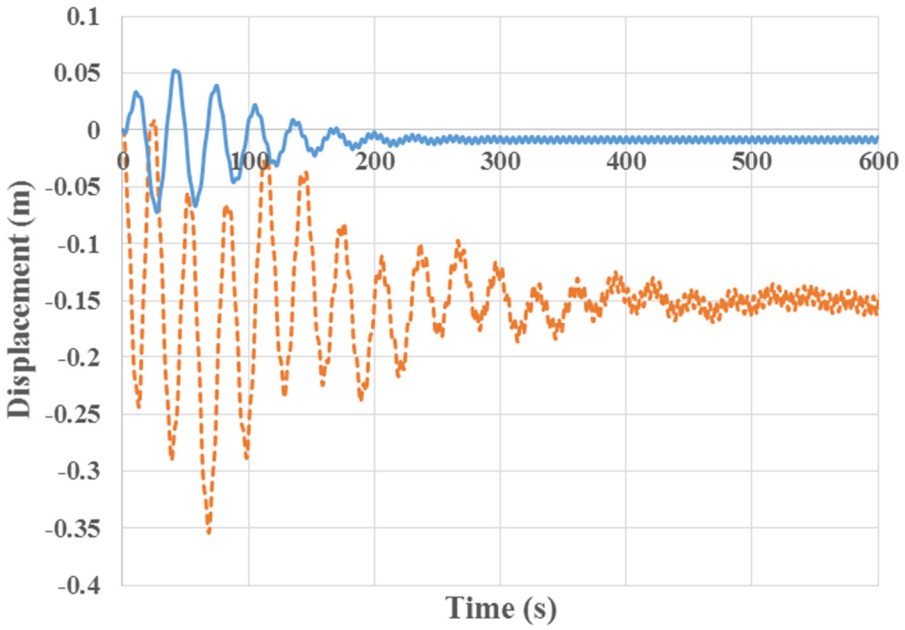

Figure 3.16 Heave displacement – Combined – 7mps, 1m and 5s.

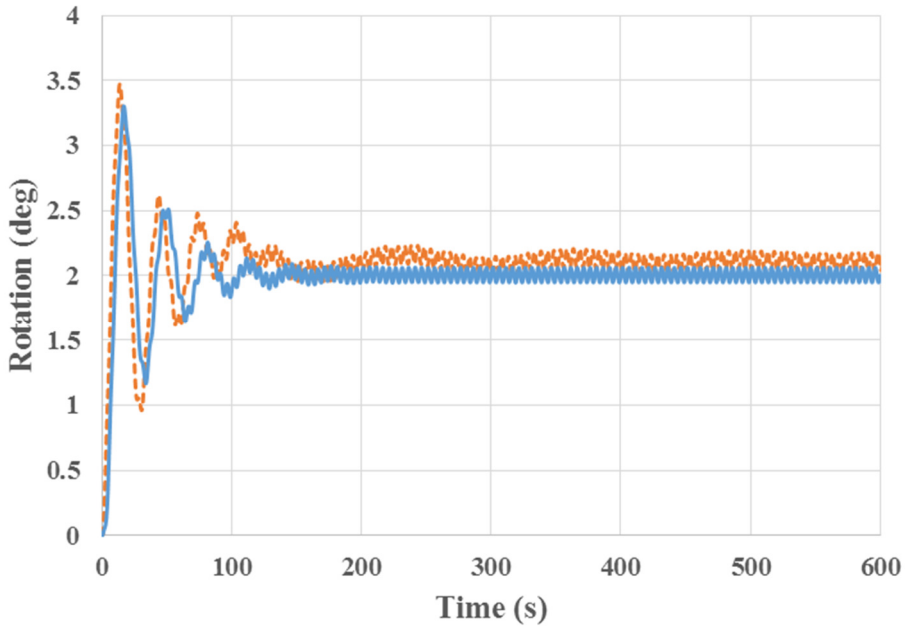

Figure 3.17 Pitch tilt angle – Combined – 7mps, 1m and 5s.

All the above conditions are used to validate the model designed and the simulation code. It is important to note that the heave displacement and pitch angle for the flexible model are measured at the junction. To validate the model further, RAOs is plotted for heave and pitch motions comparing the response of the rigid and flexible models. Figures 3.18 and 3.19 show the heave RAO and the pitch RAO respectively. The heave motion is normalized with the wave amplitude

and pitch motion is normalized with wave slope for obtaining such RAOs. It can be observed that there is good agreement between the rigid and flexible models. It can also be observed that the response tends to maximum towards angular frequency of 0.2 rad/s or time period of 30s owing close to the natural frequency of the floater.

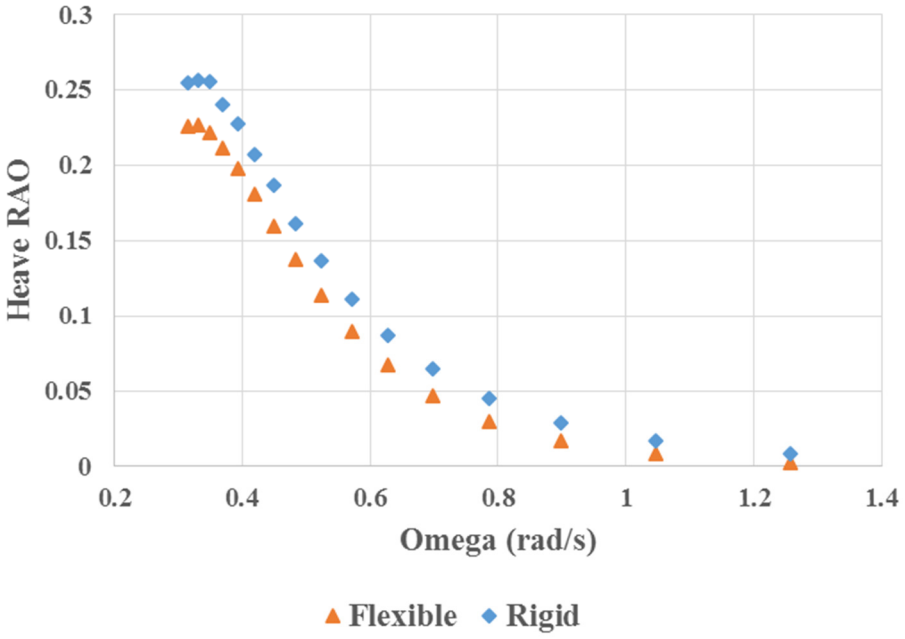

Figure 3.18 Heave RAO.

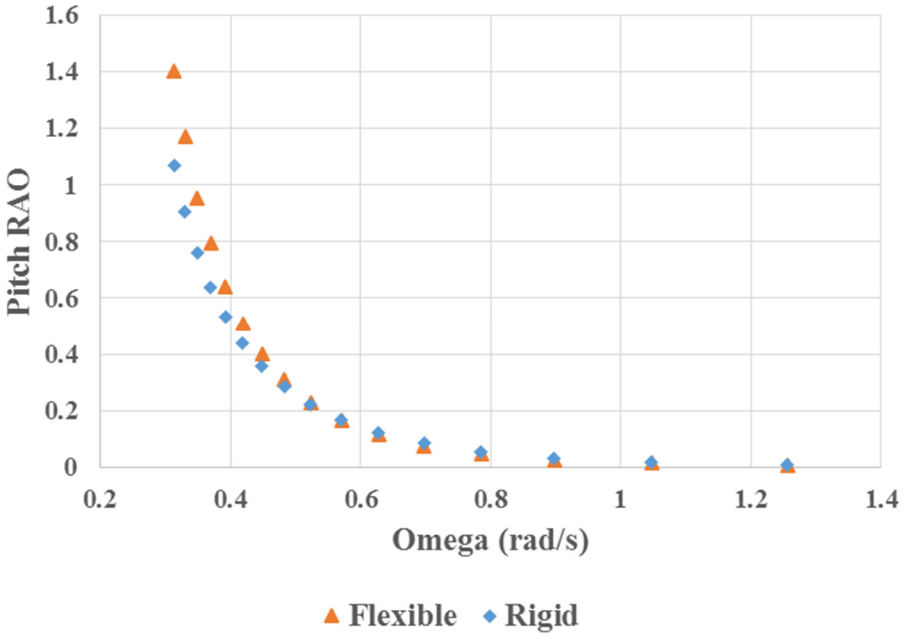

Figure 3.19 Pitch RAO.

3.3.2 Roll and Yaw Motions

Further, validation is carried for non-symmetric motions. Figure 3.20 to Figure 3.27 show the roll and yaw motions respectively for a combined case of steady wind 7mps and regular waves of amplitude 1m and wave periods of 20s, 12s, 8s and 5s to show the tendency of non-symmetric motions in the coupled simulation.

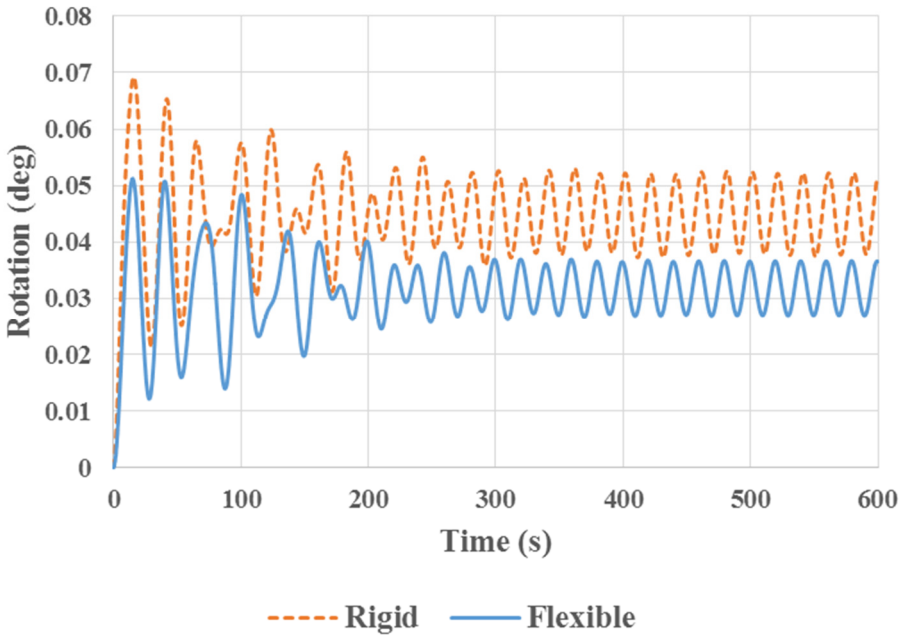

Figure 3.20 Roll angle – Combined – 7mps, 1m and 20s.

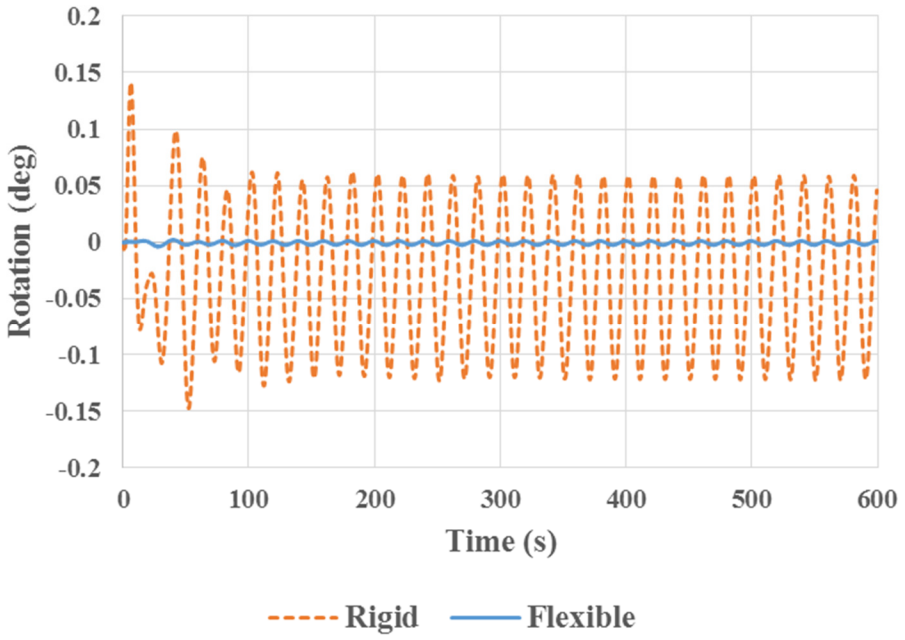

Figure 3.21 Yaw angle – Combined – 7mps, 1m and 20s.

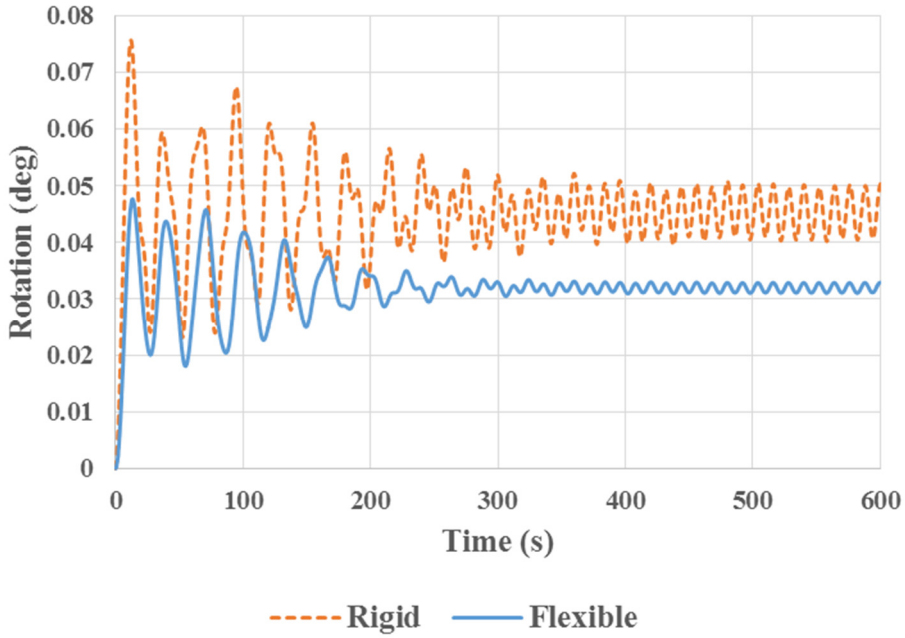

Figure 3.22 Roll angle – Combined – 7mps, 1m and 12s.

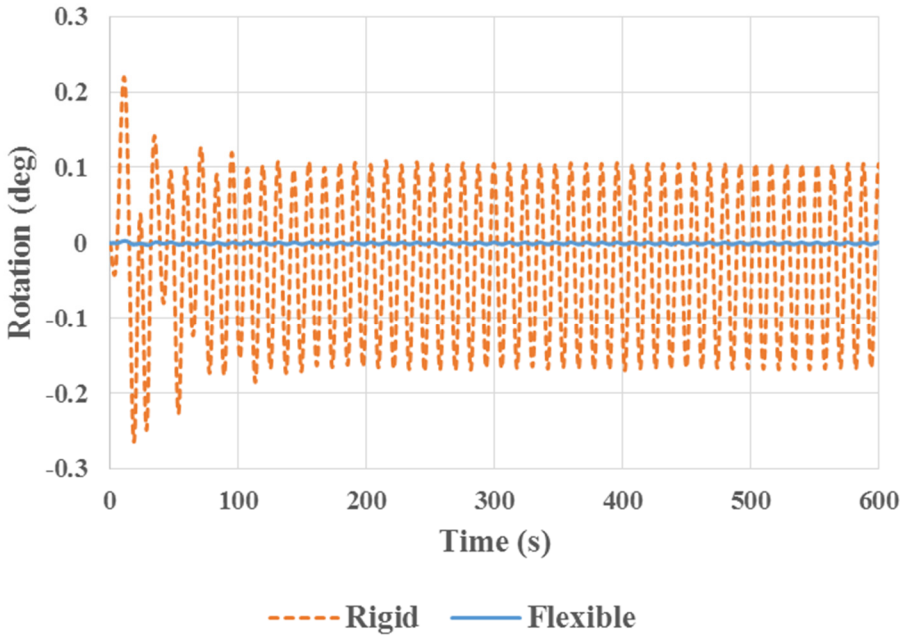

Figure 3.23 Yaw angle – Combined – 7mps, 1m and 12s.

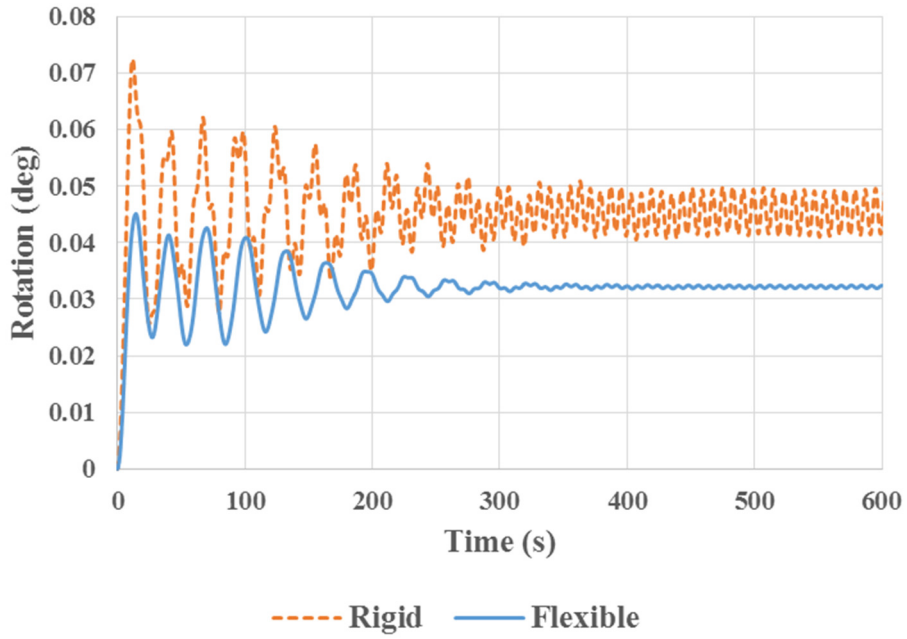

Figure 3.24 Roll angle – Combined – 7mps, 1m and 8s.

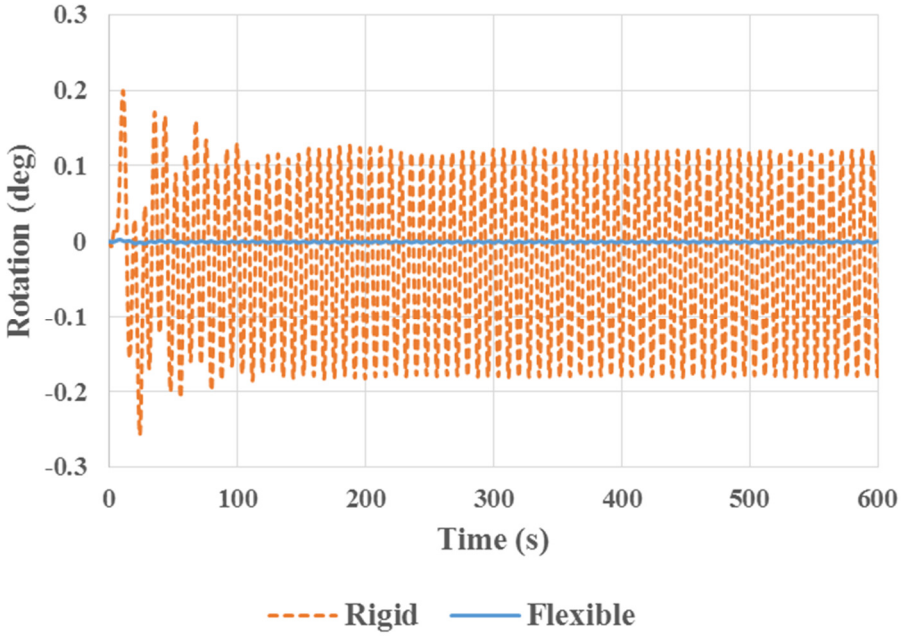

Figure 3.25 Yaw angle – Combined – 7mps, 1m and 8s.

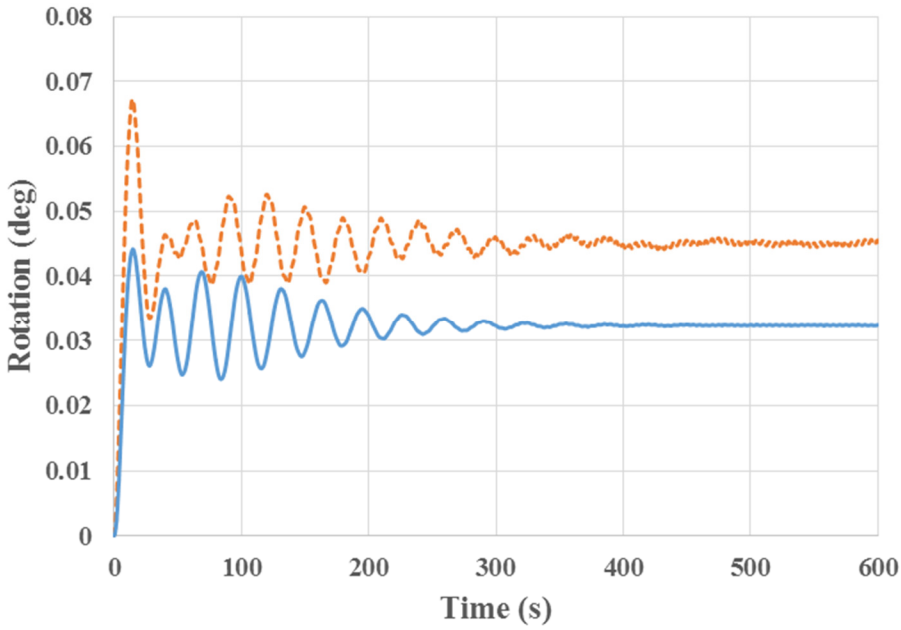

Figure 3.26 Roll angle – Combined – 7mps, 1m and 5s.

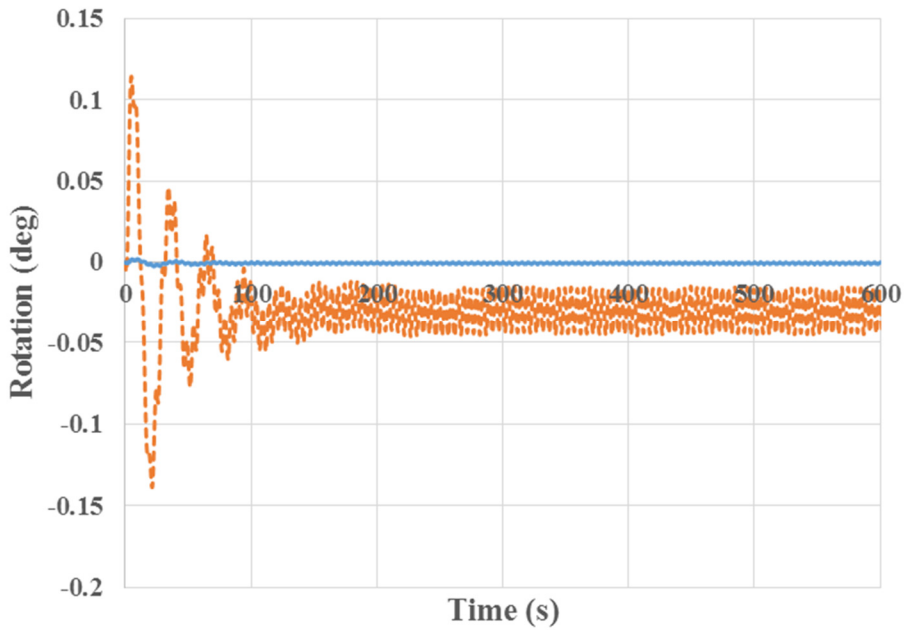

Figure 3.27 Yaw angle – Combined – 7mps, 1m and 5s.

It is important here to note that the roll and yaw motions are appreciably small in magnitude and they are not the dominant motions. The tendency of motions in the flexible model obtained is in good agreement with the rigid body results with slight discrepancies which could be attributed to varied yaw stiffness modelling between the models. Therefore, the flexible model designed is validated using the OC3-Hywind spar model and in turn the coupled simulation tool is validated.

3.3.3 Flexibility Demonstration

One of the primary objectives of developing this coupled tool is to incorporate flexibility of the floater. This section demonstrates the effect of flexibility in modelling. It is possible to evaluate forces and moments at any location of the platform in a single step adopting the newly coupled tool. Platform is subjected to only-wind condition (steady wind of 7mps) and vertical bending moments are measured at various nodes of the flexible model. Figure 3.28 describes the vertical bending moment measured at different nodes. This is compared with combined condition (wave amplitude 1m and wave period 16s) described as CombinedUpper and CombinedLower. CombinedUpper and CombinedLower refers to the range of vertical bending moment evaluated at different times in the time series. Due to the dynamic response of the FOWT system, the vertical bending moment takes maximum and minimum values at different time instances which are extracted and plotted to understand the flexibility feature. It can be observed from the Figure 3.28 that the maximum vertical bending moment occurs slightly below the still water level as per the

convention used. It is about 22.5m from the level of partially submerged hull element near Node 7 in the flexible model designed. This demonstrates the advantage of the developed coupled tool which can be used to directly obtain structural forces and moments in one-step process.

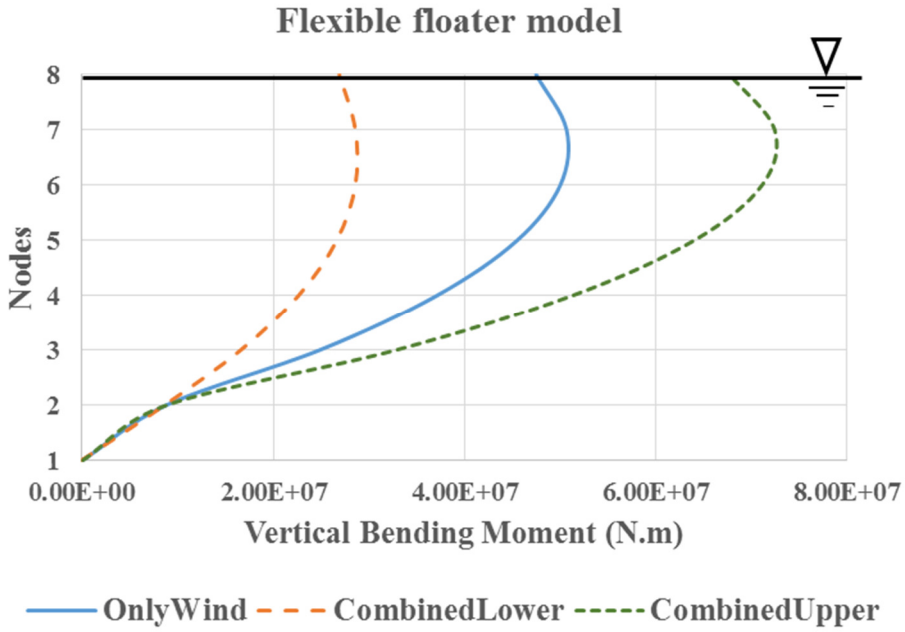

Figure 3.28 Demonstration of flexibility of floater.

3.4 Conclusions

In this chapter, the coupled simulation tool which considers flexibility of the floater is validated and found to be versatile to obtain the combined response of wind and wave for any FOWT system. The new tool successfully considers the flexible floater while predicting the response. The following specific conclusions are deduced:

- Hydrostatic balance is obtained for the new model proposed and parking tests concluded the phenomenon.

- Pitch tilt angle of about 2 degrees is observed for the model considered and this is the result of rotor thrust developed for a steady wind of 7mps. This value is in good agreement with the established offshore design model OC3-Hywind spar provided by FAST.

- Validation methodology employed proved to be effective and valid. Thus, this methodology can be extended for various types of FOWT systems.

- It was also shown that there is good agreement in roll and yaw motions. Even though such motions are non-symmetric motions, a good agreement is obtained using the developed coupled simulation tool.

4 Blade Pitch Control

4.1 Introduction

Blade pitch control is a feature of nearly all large modern horizontal-axis wind turbines. While operating, a wind turbine's control system adjusts the blade pitch to keep the rotor speed within operating limits as the wind speed changes. Feathering the blades stops the rotor during emergency shutdowns, or whenever the wind speed exceeds the maximum rated speed. During construction and maintenance of wind turbines, the blades are usually feathered to reduce unwanted rotational torque in the event of wind gusts.

NREL 5MW wind turbine [43] is selected as a reference turbine in this study and it adopts a conventional variable-speed, variable blade-pitch-to-feather configuration. In such wind turbines, the conventional approach for controlling power-production operation relies on the design of two basic control systems: a generator-torque controller and a full-span rotor-collective blade-pitch controller. The two control systems are designed to work independently, for the most part, in the below-rated and above-rated wind-speed range, respectively. The goal of the generator-torque controller is to maximize power capture below the rated operation point. The goal of the blade-pitch controller is to regulate generator speed above the rated operation point.

Baseline generator-torque controller and baseline blade-pitch controller as explained by Jonkman et al in the technical report "*Definition of a 5-MW Reference Wind Turbine for Offshore System Development*" [43] is adopted and reproduced in the following sections. After the explanation of control system used, malfunction simulation in the study is described. Further, the numerical tool which incorporates blade pitch control malfunction is developed. The results and discussions are shown for the models analyzed when it is subjected to blade pitch control malfunction.

4.1.1 Baseline Generator Torque Controller

The generator torque is computed as a function of the filtered generator speed. In this variable speed controller, the generator torque-generator speed relationship is divided into five control regions namely: 1, 1½, 2, 2½, and 3. Region 1 is a control region before cut-in wind speed. In this region, the generator torque is zero and wind is not used to capture the power but to start up and accelerate the rotor. Region 2 is a control region for optimizing power capture. Optimal tip-speed ratio is maintained is this region and generator torque is proportional to the square of the generator speed. Region 3 is a control region in which constant generator power is maintained by setting the generator torque as inversely proportional to the generator speed. Region 1½ is a linear transition

between Regions 1 and 2 also called as start-up region. This region is used to set the lower limit of generator speed to optimize the operational speed range of the wind turbine Region 2½ is a linear transition between Regions 2 and 3 having a torque slope equivalent to the slope of an induction machine. This region is required for 5-MW turbine case to set upper limit tip speed and thus noise emissions at rated power.

It is important to determine the peak power coefficient. Power coefficient as a function of the tip-speed ratio and blade-pitch surface is determined by running FAST with AeroDyn simulations at a different rotor speeds and various rotor-collective blade-pitch angles. The wind speed is fixed at 8m/s. The peak power coefficient is evaluated to be 0.482 from simulations and found to occur at a tip-speed ratio of 7.55 and a collective blade pitch of 0.0˚. With the assumed gearbox ratio of 97:1, optimal constant of proportionality is obtained for the Region 2 and is equal to 0.0255764 Nm/rpm^2. With the rated generator speed of 1173.7 rpm, rated electric power of 5 MW, and a generator efficiency of 94.4%, the rated mechanical power is 5.296610 MW and the rated generator torque is 43,093.55 Nm. Region 1½ is defined to include the range of generator speeds between 670 rpm and 30% above this value (i.e. 871 rpm). It is confirmed from the actual REpower 5M machine [47] that the minimum generator speed of 670 rpm corresponds to the minimum rotor speed of 6.9 rpm. The transitional generator speed is assumed between Regions 2½ and 3 and taken to be 99% of the rated generator speed i.e, 1,161.963 rpm. In Region 2½, the generator-slip percentage is taken to be 10%, in as per the value used in the DOWEC study [48]. Figure 4.1 shows the resulting generator torque versus generator speed response curve.

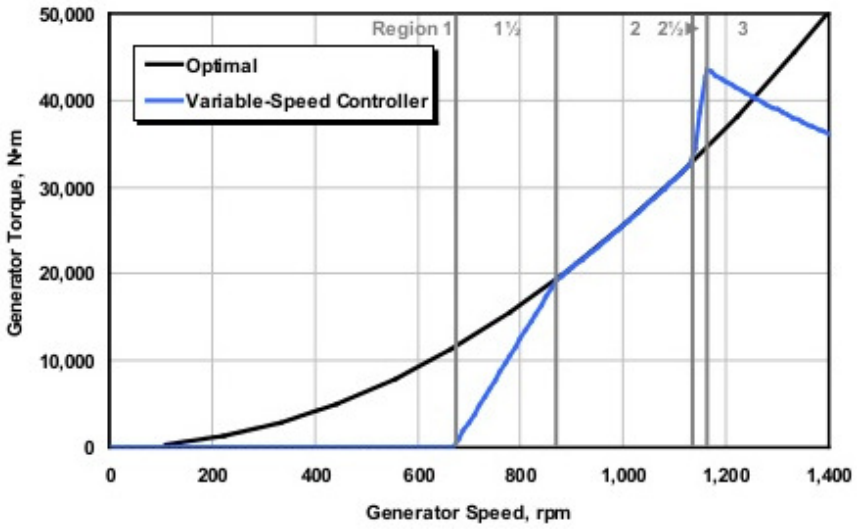

Figure 4.1 Torque-versus-speed response of variable-speed controller. (Reproduced from Reference [43])

There is no need to include a control loop for damping drivetrain torsional vibration in the controller because of the high inherent structural damping of the drivetrain. However, to improve the output power quality, a conditional statement on the generator torque controller is placed. The condition states as if it were in Region 3, so that the torque would be computed, regardless of the

generator speed, whenever the previous blade-pitch-angle command is 1º or greater. This results in efficient power output but at the expense of short term overloading of the generator and the gearbox. Therefore, the value of torque is saturated to a maximum of 10% above rated, or 47,402.91 Nm to avoid any excessive overloading. A torque rate limit of 15,000 Nm/s is also enforced. In Region 3, the blade-pitch control system as described in Section 4.1.2 takes over.

4.1.2 Baseline Blade Pitch Controller

Rotor collective blade pitch controller is incorporated in this study in the Region 3. Proportional-Integral (PI) control with gain scheduling is adopted on the speed error between the filtered generator speed and the rated generated speed (1173.7 rpm) to obtain the full-span rotor-collective blade-pitch-angles.

A simple single degree of freedom (single DOF) model of the wind turbine is used for designing the blade-pitch control system. The angular rotation of the shaft is this DOF since the objective of the blade-pitch control system is to regulate the generator speed. It is beneficial to examine the equation of motion of this single DOF system to calculate the required control gains. The equation of motion by using a simple free-body diagram of the drivetrain can be written as follows.

$$T_{Aero} - N_{Gear}T_{Gen} = (I_{Rotor} + N_{Gear}^2 I_{Gen})\frac{d}{dt}(\Omega_0 + \Delta\Omega) = I_{Drivetrain}\Delta\dot{\Omega} \qquad (\mathbf{4.1})$$

where T_{Aero} aerodynamic torque at the low speed shaft, T_{Gen} is the generator torque at high speed shaft, N_{Gear} is the gearbox ratio (high speed to low speed), $I_{Drivetrain}$ is the drivetrain inertia cast to the low speed shaft, I_{Rotor} is the rotor inertia, I_{Gen} is the generator inertia relative to the high speed shaft, Ω_0 is the rated low speed shaft rotational speed, $\Delta\Omega$ is the small perturbation of low speed shaft rotational speed about the rated speed, $\Delta\dot{\Omega}$ is the low speed shaft rotational acceleration, and t is the simulation time.

As explained earlier (in Figure 4.1), the generator torque is inversely proportional to the generator speed in Region 3 to maintain constant generator power. This is expressed as per Equation (4.2).

$$T_{Gen}(N_{Gear}\Omega) = \frac{P_o}{N_{Gear}\Omega} \qquad (\mathbf{4.2})$$

where P_o is the rated mechanical power and Ω is the low speed shaft rotational speed.

The aerodynamic torque in Region 3 by assuming negligible variation can be expressed similarly as described in Equation (4.3).

$$T_{Aero}(\theta) = \frac{P(\theta, \Omega_o)}{\Omega_o} \qquad (\mathbf{4.3})$$

where P is the mechanical power and θ is the full-span rotor-collective blade-pitch angle.

Now, using first-order Taylor series expansion of Equations (4.2) and (4.3), we can see that

$$T_{Gen} \approx \frac{P_o}{N_{Gear}\Omega_o} - \frac{P_o}{N_{Gear}\Omega_o^2}\Delta\Omega \tag{4.4}$$

and

$$T_{Aero} \approx \frac{P_o}{\Omega_o} + \frac{1}{\Omega_o}\left(\frac{\partial P}{\partial \theta}\right)\Delta\theta \tag{4.5}$$

where $\Delta\theta$ is a small perturbation of the blade-pitch angles about their operating point. This is related to the rotor-speed perturbations using the proportional-integral-derivative (PID) control as follows,

$$\Delta\theta = K_P N_{Gear}\Delta\Omega + K_I \int_0^t N_{Gear}\Delta\Omega\, dt + K_D N_{Gear}\Delta\dot{\Omega} \tag{4.6}$$

where K_P, K_I, and K_D are the blade-pitch controller proportional, integral, and derivative gains, respectively.

Assuming $\dot{\varphi} = \Delta\Omega$, combining and simplifying the above expressions, the equation of motion for the rotor-speed error can be expressed as per Equation (4.7).

$$\left[I_{Drivetrain} + \frac{1}{\Omega_o}\left(-\frac{\partial P}{\partial \theta}\right)N_{Gear}K_D\right]\ddot{\varphi} + \left[\frac{1}{\Omega_o}\left(-\frac{\partial P}{\partial \theta}\right)N_{Gear}K_P - \frac{P_o}{\Omega_o^2}\right]\dot{\varphi} + \left[\frac{1}{\Omega_o}\left(-\frac{\partial P}{\partial \theta}\right)N_{Gear}K_I\right]\varphi = 0 \tag{4.7}$$

Let us assume,

$$M_\varphi = \left[I_{Drivetrain} + \frac{1}{\Omega_o}\left(-\frac{\partial P}{\partial \theta}\right)N_{Gear}K_D\right]$$

$$C_\varphi = \left[\frac{1}{\Omega_o}\left(-\frac{\partial P}{\partial \theta}\right)N_{Gear}K_P - \frac{P_o}{\Omega_o^2}\right]$$

$$K_\varphi = \left[\frac{1}{\Omega_o}\left(-\frac{\partial P}{\partial \theta}\right)N_{Gear}K_I\right]$$

From Equation (4.7), we can infer that the rotor-speed error which is PID-controlled will respond as a second-order system. The natural frequency, $\omega_{\varphi n}$, and damping ratio, ζ_φ, of the system will be as per Equations (4.8) and (4.9).

$$\omega_{\varphi n} = \sqrt{\frac{K_{\varphi}}{M_{\varphi}}} \tag{4.8}$$

and

$$\zeta_{\varphi} = \frac{C_{\varphi}}{2\sqrt{K_{\varphi} M_{\varphi}}} = \frac{C_{\varphi}}{2 M_{\varphi} \omega_{\varphi n}} \tag{4.9}$$

The sensitivity of aerodynamic power to the rotor-collective blade-pitch angle, $/\partial\theta$, is negative in Region 3 for an active pitch-to-feather wind turbine. The derivative term then acts to increase the effective inertia of the drivetrain since control gains are positive. The proportional term estimates damping, and the integral term estimates the restoring. Also, in Region 3 to maintain constant power output, since the generator torque decreases with increasing speed error, we can observe that the generator-torque controller presents a negative damping in the speed error response [as indicated by the $-P_o/\Omega_o^2$ term in Equation (4.7)]. The proportional term in the blade-pitch controller compensates this negative damping.

While designing the blade-pitch controller, Hansen [49] suggests to neglect the derivative gain, ignoring the negative damping from the generator torque controller, and targeting the response characteristics by using $\omega_{\varphi n}$ = 0.6 rad/s and ζ_{φ} = 0.6 to 0.7. This description leads to proportional and integral gains expressions once we know the sensitivity of aerodynamic power to collective blade pitch, $\partial P/\partial\theta$.

$$K_P = \frac{2 I_{Drivetrain} \Omega_o \zeta_{\varphi} \omega_{\varphi n}}{N_{Gear}\left(-\frac{\partial P}{\partial \theta}\right)} \tag{4.10}$$

and

$$K_I = \frac{I_{Drivetrain} \Omega_o \omega_{\varphi n}^2}{N_{Gear}\left(-\frac{\partial P}{\partial \theta}\right)} \tag{4.11}$$

The blade-pitch sensitivity, $\partial P/\partial\theta$, is an aerodynamic characteristic of the rotor which depends on the wind speed, rotor speed and blade-pitch angle. By performing a linearization analysis in FAST with AeroDyn, the parameters are calculated for the NREL offshore 5MW baseline wind turbine. This is done by selecting a number of steady and uniform wind speeds at the rated rotor speed of 12.1 rpm and at the corresponding blade-pitch angles that produce the rated mechanical power of 5.296610 MW in the linearization analysis. At each operating point, the collective blade pitch angle is varied and resulting change in aerodynamic power is measured. The partial derivative is then evaluated using the central difference technique in FAST. A slightly modified copy of FAST with AeroDyn is created and utilized such that the linearization process would go

well with the frozen-wake assumption. The frozen-wake assumes wake velocities to be constant while the blade-pitch angle is varied. Linearization thus gives accurate results for heavily loaded rotors in Region 3 for operating points closest to rated. Table 4.1 presents the results and this is used to simulate blade pitch control malfunction in the present study.

Table 4.1 Sensitivity of Aerodynamic Power to Blade Pitch in Region 3.

Wind Speed (m/s)	Rotor Speed (rpm)	Pitch Angle (deg)	$\partial P/\partial\theta$ (watt/rad)
11.4 – Rated	12.1	0.00	-28.24E+6
12.0	12.1	3.83	-43.73E+6
13.0	12.1	6.60	-51.66E+6
14.0	12.1	8.70	-58.44E+6
15.0	12.1	10.45	-64.44E+6
16.0	12.1	12.06	-70.46E+6
17.0	12.1	13.54	-76.53E+6
18.0	12.1	14.92	-83.94E+6
19.0	12.1	16.23	-90.67E+6
20.0	12.1	17.47	-94.71E+6
21.0	12.1	18.70	-99.04E+6
22.0	12.1	19.94	-105.90E+6
23.0	12.1	21.18	-114.30E+6
24.0	12.1	22.35	-120.20E+6
25.0	12.1	23.47	-125.30E+6

(Reproduced and modified from Reference [43])

From Table 4.1, it can be understood that the aerodynamic power sensitivity to collective blade pitch varies substantially over Region 3. Therefore, constant PI gains are not sufficient for effective speed control. It can also is noticed that the pitch sensitivity varies almost linearly with blade pitch angle.

$$\frac{\partial P}{\partial \theta} = \left[\frac{\frac{\partial P}{\partial \theta}\,(\theta = 0)}{\theta_K}\right]\theta + \left[\frac{\partial P}{\partial \theta}(\theta = 0)\right] \qquad (\mathbf{4.12}\boldsymbol{a})$$

or

$$\frac{1}{\frac{\partial P}{\partial \theta}} = \frac{1}{\frac{\partial P}{\partial \theta}\,(\theta = 0)\left(1 + \frac{\theta}{\theta_K}\right)} \qquad (\mathbf{4.12}\boldsymbol{b})$$

where $\frac{\partial P}{\partial \theta}\,(\theta = 0)$ is the pitch sensitivity at rated and θ_K is the blade-pitch angle at which the pitch sensitivity has increased 2 times its value at the rated operating point [see Equation (4.13)].

$$\frac{\partial P}{\partial \theta}\,(\theta = \theta_K) = 2\frac{\partial P}{\partial \theta}(\theta = 0) \qquad (\mathbf{4.13})$$

The first and second terms in square brackets on the right hand side of Equation (4.12a) respectively signifies the slope and intercept of the best-fit line. This result for NREL 5MW baseline wind turbine is calculated and presented in Figure 4.2.

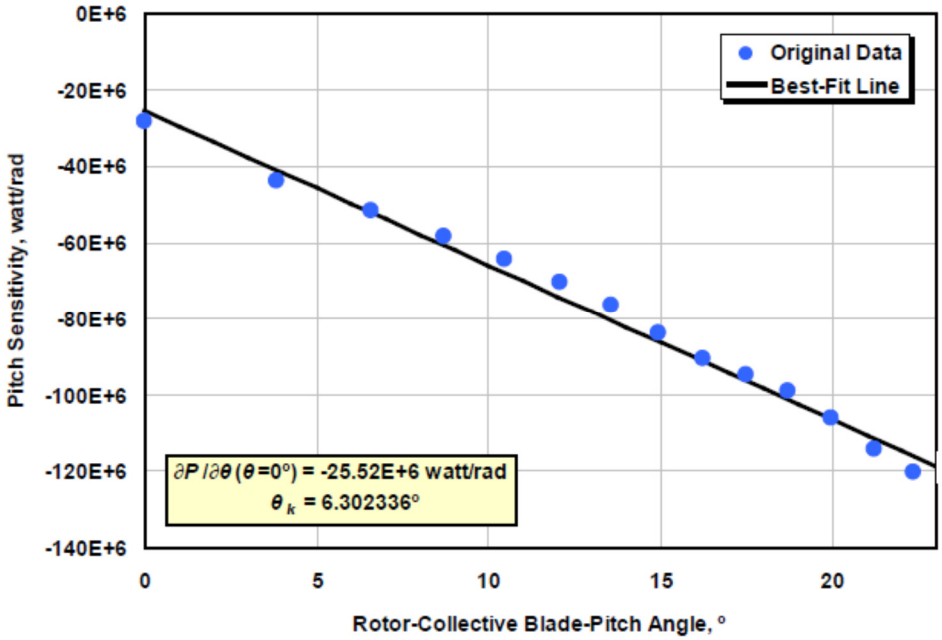

Figure 4.2 Best-fit line of pitch sensitivity in Region 3.
(Reproduced from Reference [43])

The pitch sensitivity and blade-pitch angle linear relationship gives a simple methodology for implementing gain scheduling which is based on blade-pitch angle summarizes as follows.

$$K_P(\theta) = \frac{2I_{Drivetrain}\,\Omega_o\zeta_\varphi\omega_{\varphi n}}{N_{Gear}\left(-\frac{\partial P}{\partial \theta}(\theta = 0)\right)}GK(\theta) \qquad (\mathbf{4.14})$$

and

$$K_I(\theta) = \frac{I_{Drivetrain}\,\Omega_o\omega_{\varphi n}^2}{N_{Gear}\left(-\frac{\partial P}{\partial \theta}(\theta = 0)\right)}GK(\theta) \qquad (\mathbf{4.15})$$

where $GK(\theta)$ is dimensionless gain correction factor [49], depending on the blade-pitch angle.

$$GK(\theta) = \frac{1}{1 + \frac{\theta}{\theta_K}} \qquad (\mathbf{4.16})$$

While implementing gain-scheduled PI blade pitch controller, the previous controller time step blade-pitch angle is used to compute the gain-correction factor for the next time step.

The proportional, integral and derivative gains are then evaluated using the properties of the baseline wind turbine response characteristics [49]. The resulting gains are as follows, $K_P(\theta = 0^0)$ = 0.01882681s, $K_I(\theta = 0^0)$= 0.008068634, and K_D = 0.0 s^2. Figure 4.3 summarizes the gains at different blade-pitch angles. The gain-correction factor is also summarized in the same figure. While determining K_P, the upper value of the damping ratio range, ζ_φ= 0.7, is used to compensate for neglecting negative damping from the generator-torque controller.

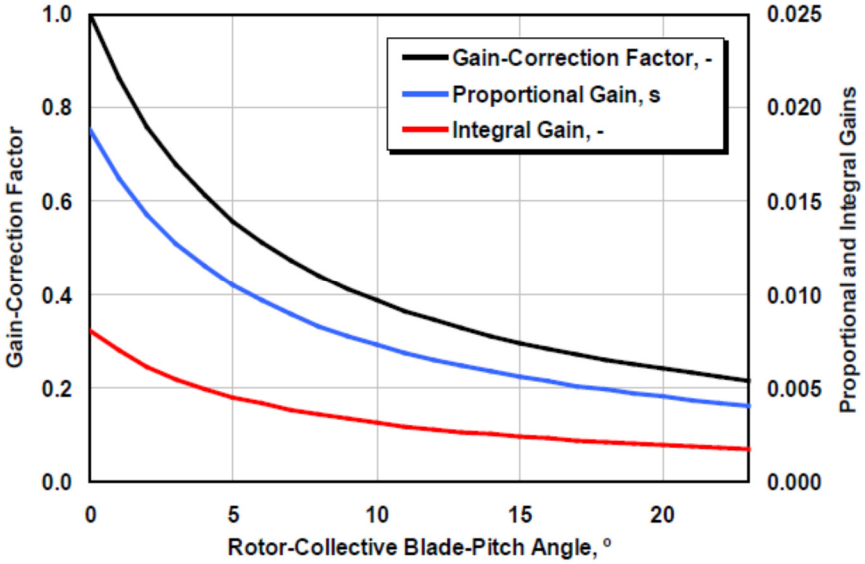

Figure 4.3 Blade-pitch control system gain-scheduling law. (Reproduced from Reference [43])

The absolute value of blade-pitch rate limit is set to 8°/s. This is equivalent to the blade-pitch rate limit of conventional 5MW systems based on General Electric (GE) Wind's long-blade test program. The minimum and maximum blade-pitch are respectively set to 0° and 90°. The lower limit is the set blade pitch for maximizing power in Region 2, as explained previously. The upper limit is almost similar fully feathered blade pitch condition for constant torque. To obtain a fast response in the transitions between the two regions (i.e. Region 2 and Region 3), the integral term in the PI controller is saturated between these limit boundaries. Thus, an extreme event of malfunction can be simulated by setting the blade pitch angle manually which will be used to simulate the malfunction.

4.2 Simulation of Blade Pitch Malfunction

The malfunction of the blade pitch control for FOWT system needs to be addressed and this section describes the simulation method malfunction for an extreme event. The malfunction of blade pitch control is simulated by abruptly stopping the collective pitch control in time-series simulation. This is done by manually setting the time for start and stop of the blade pitch control.

Figure 4.4 explains the concept adopted for simulating control malfunction. It can be observed that constant blade pitch controller is employed until a specified time, TPitManS. At this time instant, the malfunction of blade pitch control is simulated until TPitManE using a ramped function. Thus the coupled simulation response after TPitManE is without the controller and structural and motion characteristics of the floating structure as well as the rotor dynamics can be predicted in a single time-series simulation for a specified environmental condition. It is to be noted that the start and end of the malfunction can be set as required. In the present research, malfunction time is set as 1 second for convenience which could be treated as time for a control system to fail mechanically.

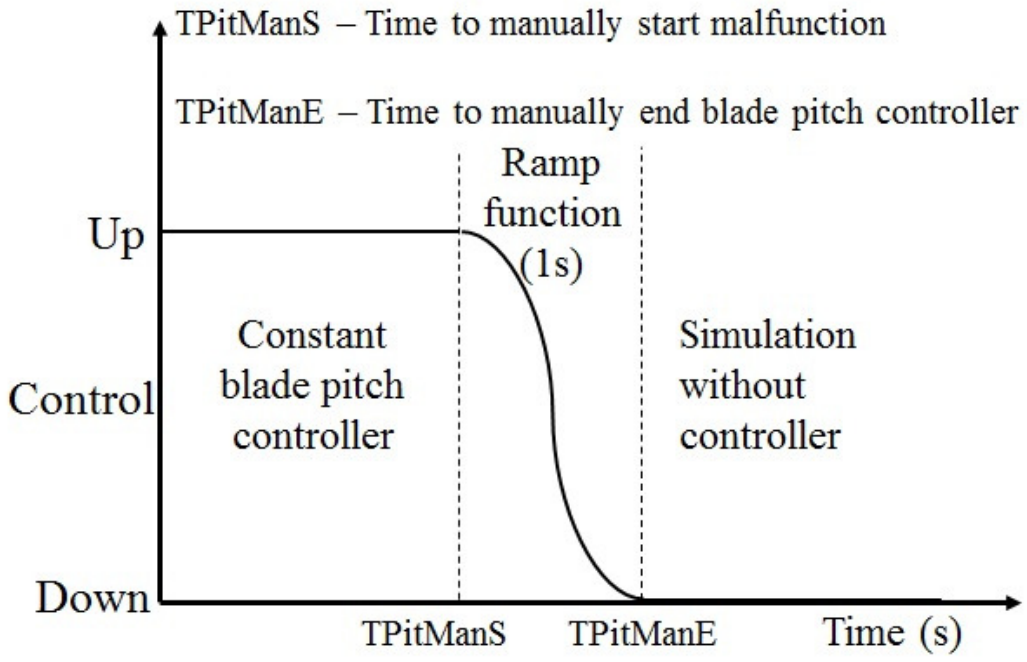

Figure 4.4 Simulation of Blade Pitch Malfunction.

Before discussing the simulation results, the model for analysis is described.

4.3 Model for Analysis

Two types of platform models are adopted for the analysis, a flexible SPAR model and a flexible semi-submersible model. FOWT system for both the cases is modelled to accommodate the NREL 5MW Baseline wind turbine. The versatility of the coupled code is shown by adopting different floater models.

4.3.1 Flexible SPAR Model

A flexible floater model is developed using the DYNABEAM module. The floating spar is a full scale model consisting of hull and beam elements with a knob column in the middle. The principal particulars of the flexible SPAR platform is tabulated in Table 4.2 [50].

Table 4.2 Principal particulars of SPAR platform.

Total Draft	109.3 m
Elevation to Platform Top Above SWL	10 m
Diameter of water plane	7 m
Diameter of knob column	25 m
Length of middle column	11.5 m
Position of the middle column Below SWL	10 m
Platform Mass, Including Ballast	7,940,000 kg
CM Location Below SWL	54.7 m
KG (with wind turbine)	54.6 m
KB	76.1 m
GM (with wind turbine)	28.5 m

(Reproduced and modified from Reference [50])

A schematic representation is shown in Figure 4.5. It can be observed that spar model is regarded as flexible platform with 10 hull elements (nodes) and 9 beam elements connecting the nodes. The full scale spar model is designed using a scaled model used for experimentation. To arrive at this, firstly the hydrostatic balance is achieved in DYNABEAM module. The masses other than the platform mass i.e., tower mass, hub mass, nacelle mass and blade mass is modelled as lumped mass in DYNABEAM. This lumped mass is distributed between Node 9 and Node 10 in the present model while evaluating the model usage in DYNABEAM. During coupling, lumped is not considered and tower, hub and nacelle masses are modelled in FAST directly. Mooring lines are provided to avoid the drifting of the platform using linear mooring system. Mooring stiffness of

the flexible model is adjusted according to match the targeted natural frequencies in the scaled modeled experiment.

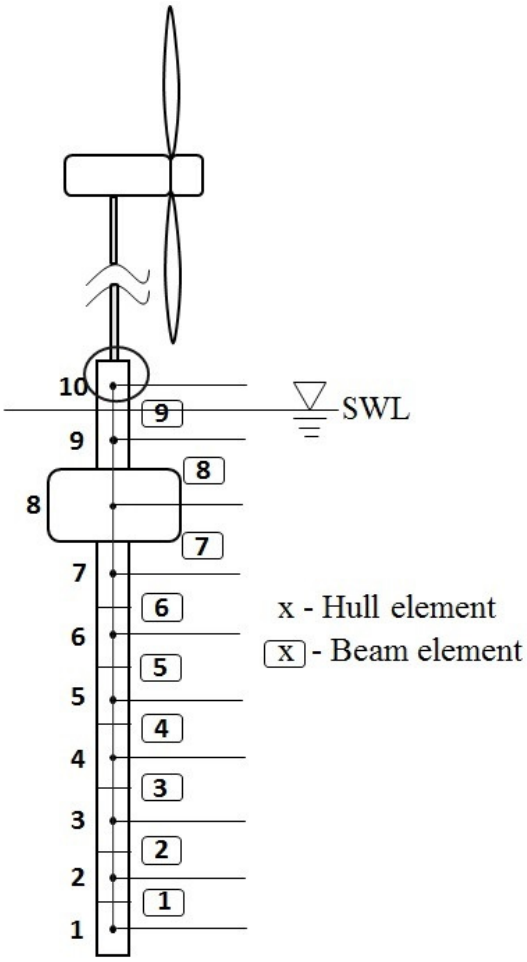

Figure 4.5 Illustration of flexible SPAR modeling in DYNABEAM showing junction.

After the hydrostatic balance is achieved, flexible floater model is used for coupled analysis. For coupling purposes, a junction is selected. In the present analysis, this junction is selected at Node 10. At this junction, the motions are coupled by weak coupling algorithm. It is at this junction the platform motions and reaction forces and moments are exchanged at each time step.

4.3.2 Flexible Semi-submersible Model

A flexible semi-submersible model is also developed using the DYNABEAM module. The principal particulars of the flexible semi-submersible model is tabulated in Table 4.3 [51]. It is to be noted that overall mass consisting of the floating platform, tower and rotor-nacelle assembly is used to arrive at hydrostatic balance of the FOWT system during coupling.

A schematic representation is shown in Figure 4.6. It can be observed that the floater consists of 27 nodes and correspondingly 27 beam elements connecting the nodes. It can also be observed that the junction selected in case of semi-submersible is Node 15 where the platform motions and forces and moments are exchanged between the aerodynamic and hydrodynamic modules. It is at this location the NREL 5MW Baseline turbine is accommodated in the coupled analysis.

Table 4.3 Principal particulars of Semi-submersible platform.

Total Draft	25 m
Platform Mass	12,600,000 kg
Distance between columns	75 m
Column Diameter	11 m
Column Height	33 m
Column Height (accommodating tower)	53 m
Lower hull breadth	6 m
Lower hull depth	6 m
GM (with wind turbine)	8.3 m

(Reproduced and modified from Reference [51])

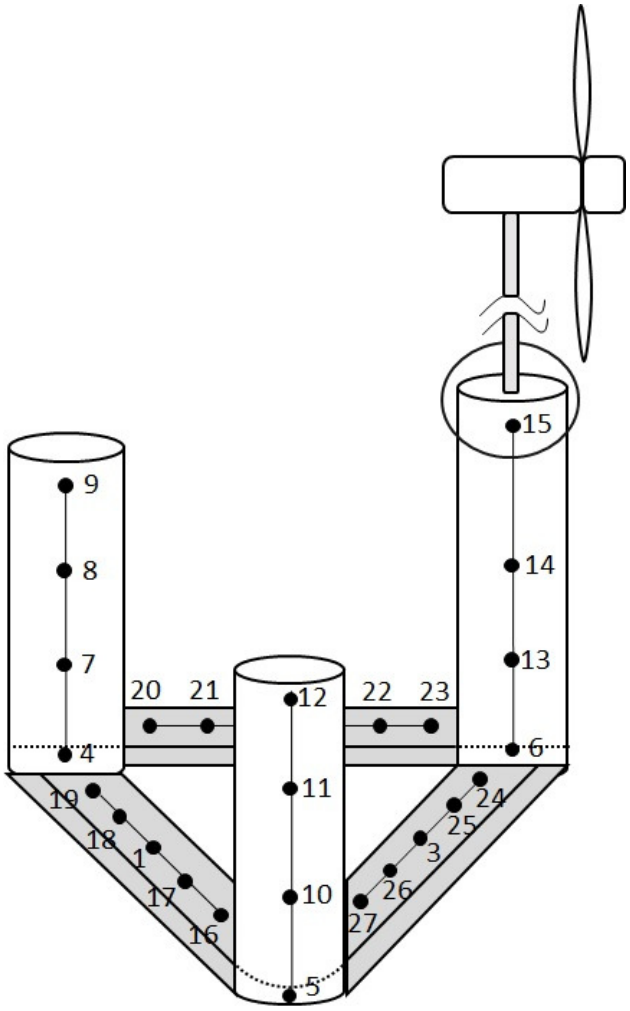

Figure 4.6 Illustration of flexible semi-submersible modeling in DYNABEAM showing junction.

Linear mooring lines are provided at Nodes 4, 5 and 6 to avoid drifting of the semi-submersible platform. The purpose of designing semi-submersible model is to demonstrate the flexibility feature of the coupled tool developed. In this study, all results of blade pitch malfunction will be shown for both the flexible models and compared.

4.4 Validation of Numerical Simulation

It is important to validate the developed numerical simulation code. In this study, the numerical simulation is validated qualitatively using scaled model tank test results. A series of experiments were conducted by Mizukami et al [50] on scaled model of the SPAR discussed in the previous section. The experimental study showed the motion characteristics of wind turbine on a floating platform in blade pitch control malfunction for a model scale ratio of 100. The motion characteristics obtained experimentally for the scale model is compared qualitatively with the numerically simulated results for the full scale model of the same SPAR type FOWT [52].

Firstly, the rotor thrust measured at the rotor-nacelle level is targeted. Figure 4.7 shows the experimental plot of the horizontal force variation with and without the blade pitch control for various wind speeds. Validation strategy involves reproducing such plot qualitatively and further comparing the behavior of platform motions between experiments and simulations.

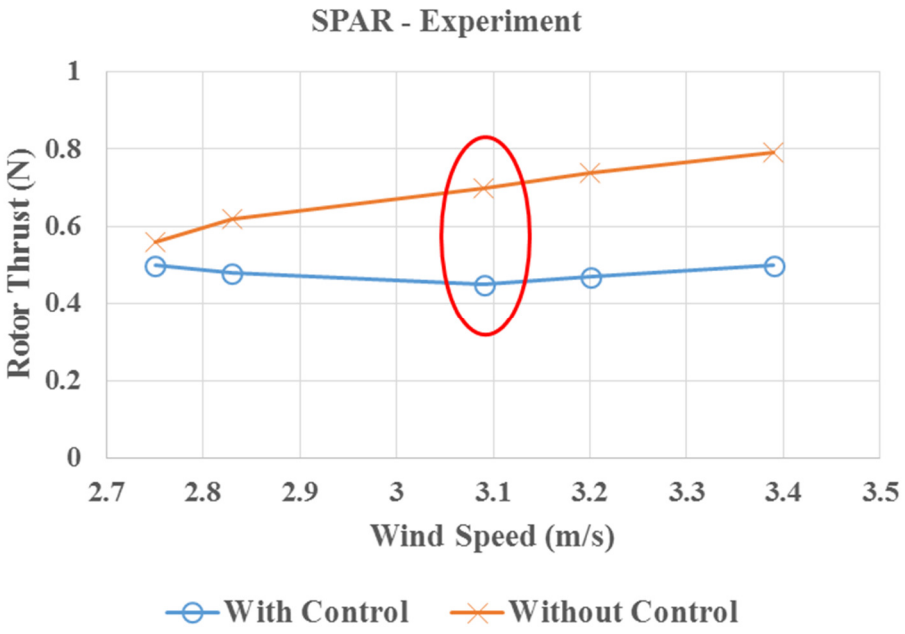

Figure 4.7 Rotor Thrust – Experiment.

It can be observed from Figure 4.7 that the rotor thrust measured are 0.45N and 0.7N with and without control respectively for the wind speed case of 3.1 m/s. In real scale, these values corresponds to 450kN and 700kN according to Froude scaling law. With prime objective of validation, Figure 4.8 is numerically obtained from the coupled tool. Constant blade pitch control is employed as discussed in the previous section until first 100 seconds of the simulation and malfunction occurs thereafter and simulation is continued without control.

In the simulation within control region, hydrostatic and steady wind coupled result can be observed. The dynamic amplification within first 50 seconds of the simulation is mainly from the controlled pitch angle trying to stabilize the coupled system. Two peaks within 50 seconds indicates the natural frequency of decay of the FOWT system. The rigid body motion of the floater is reflected in Figure 4.8 and thus relative velocity of floater motion affects the rotor characteristics. At 100 seconds, malfunction of control occurs and we can observe abrupt increase of rotor thrust from 450kN to 700kN. It is observed that the targeted values of rotor thrust can be reflected by the coupled numerical simulation in real scale. It is to be noted that these predictions are obtained for wind speed of 9.25mps and constant blade pitch angle of 4.5 degrees in simulations.

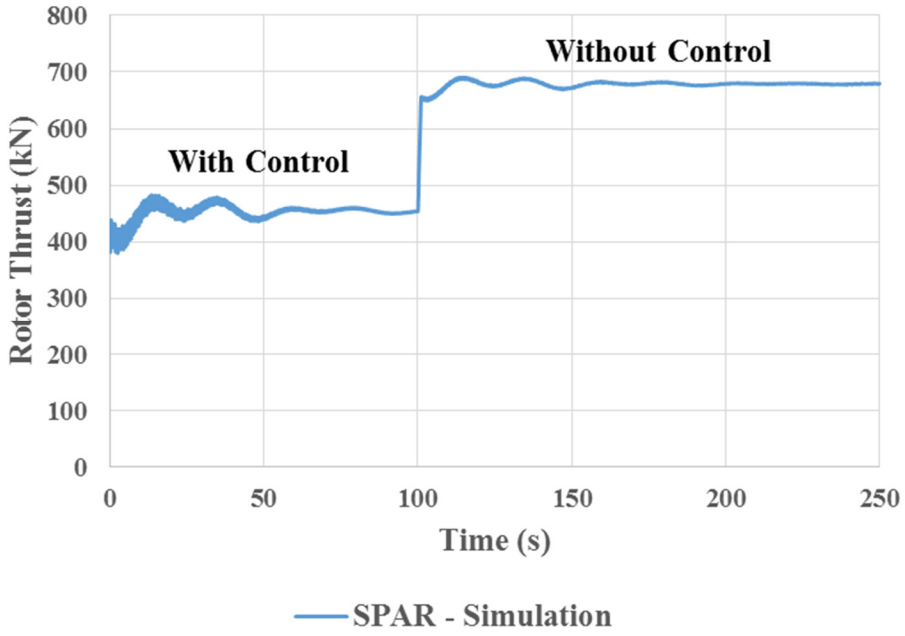

Figure 4.8 Rotor Thrust – Simulation.

Validation is further continued for platform motions. Figures 4.9 and 4.10 shows the experimental and simulated pitch tilt angle during malfunction of blade pitch angle for the same case of wind. In experiments, malfunction occurs at 70 seconds and there is increase of pitch tilt angle due to control failure. This behavior tendency is simulated in the numerical code as shown in Figure 4.10. The malfunction behavior is simulated at 100 seconds and pitch angle increases from about 1 degrees to 2 degrees. The results cannot be compared quantitatively because of difference in the test conditions and modeling. The mass distribution and location of GM is different between the scaled experimental model and that of the real scale model designed. However, similar tendency in behavior is observed and thus the results can be qualitatively correlated based on the malfunction of blade pitch control.

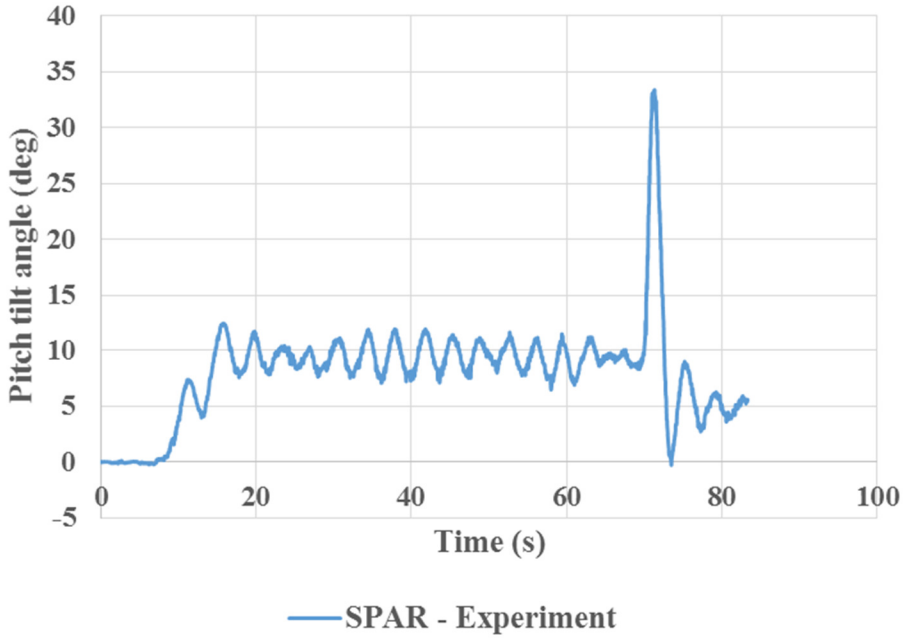

Figure 4.9 Pitch tilt angle – Experiment.

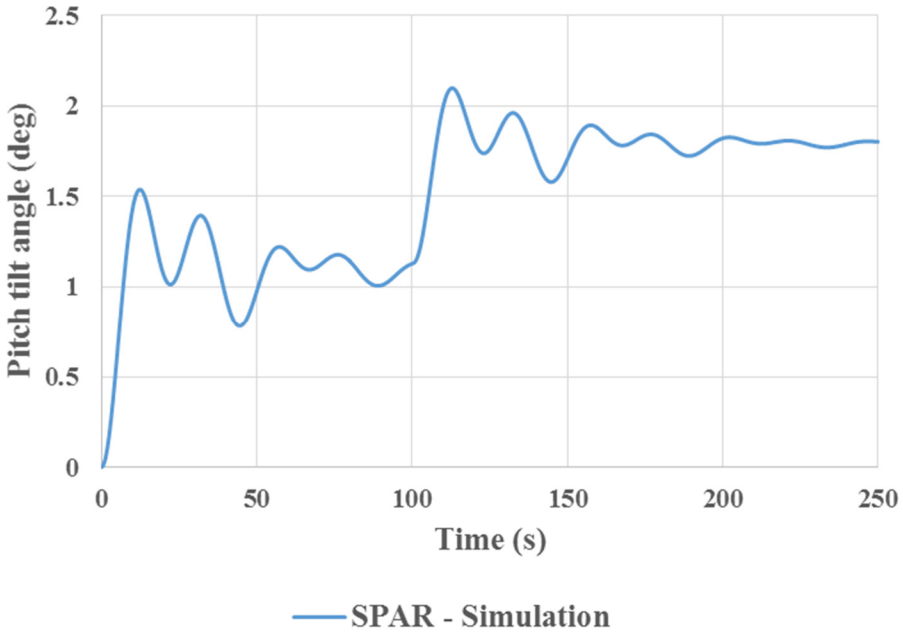

Figure 4.10 Pitch tilt angle – Simulation.

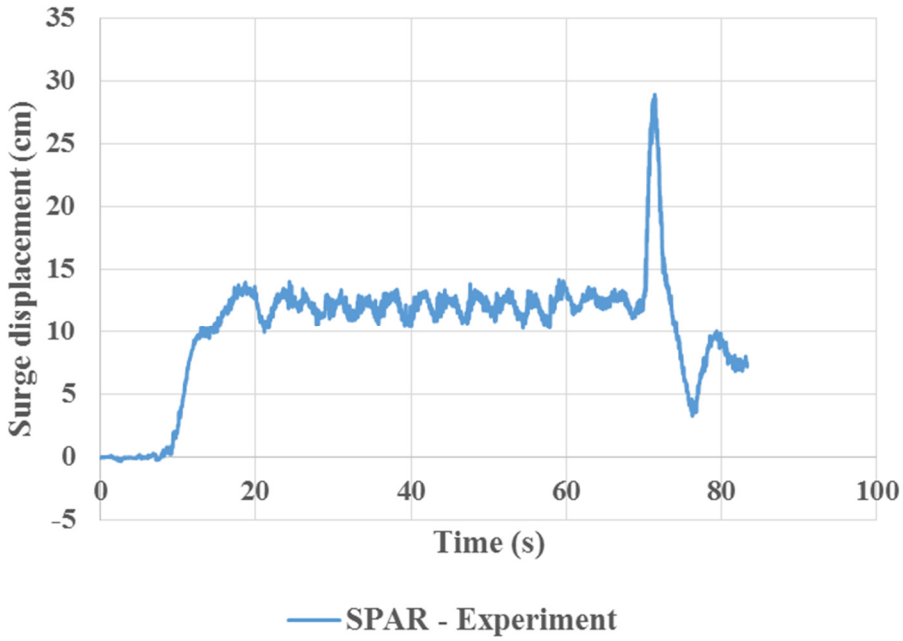

Figure 4.11 Surge displacement – Experiment.

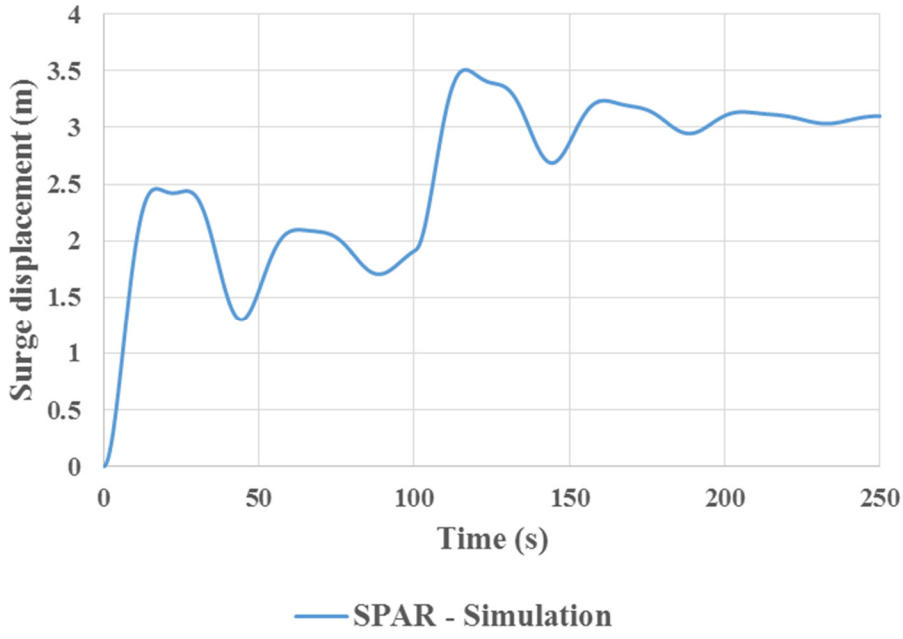

Figure 4.12 Surge displacement – Simulation.

Figures 4.11 and 4.12 shows the experimental and simulated surge displacement during malfunction of blade pitch angle. It can be observed that the surge motion can also be qualitatively compared between experiments and simulations for malfunction behavior. The surge displacement increased from about 13cm to 30cm due to malfunction in case of experiments. Similar behavior

is simulated utilizing the code and result for malfunction at 100 seconds is obtained as shown in Figure 4.12.

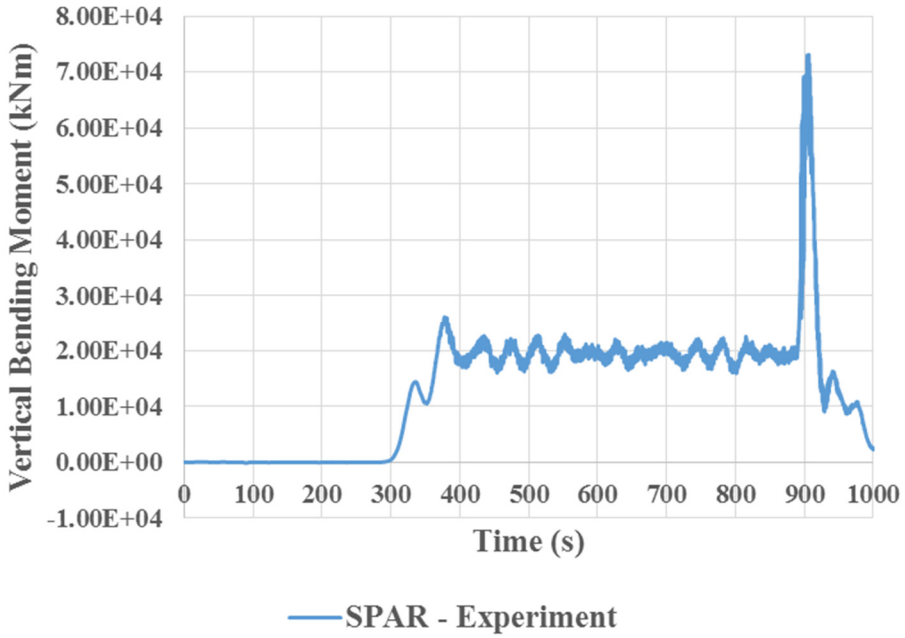

Figure 4.13 Vertical Bending Moment – Experiment (Scaled up).

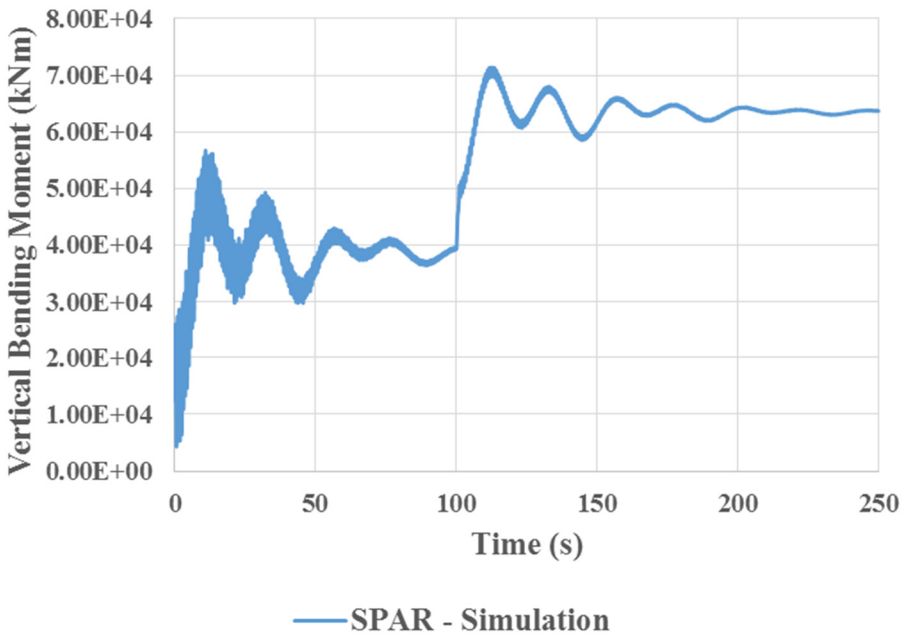

Figure 4.14 Vertical Bending Moment – Simulation.

Figure 4.13 shows experimental vertical bending moment measured at the tower base during malfunction. The structural vibrations before the malfunction arises from imbalance of rotor blades

in the experiments. It is observed that vertical bending moment increases to 7.1 $x10^4$kNm due to malfunction in case of experiment after scaling up. Figure 4.14 simulates this result and predicts the vertical bending as $7.1x10^4$kNm which is same considering scaling law. This prediction confirms the validity of the simulation and coupled tool is thus validated qualitatively.

4.5 Results and discussion

After validation, the blade pitch control malfunction of FOWT system is demonstrated for the two flexible platforms designed. Steady wind speed of 18mps is selected for all demonstrations. For simplicity, tower is modelled as a uniform rigid tower. The working feature of the malfunction is confirmed in Figure 4.15 for steady wind speed of 18mps.

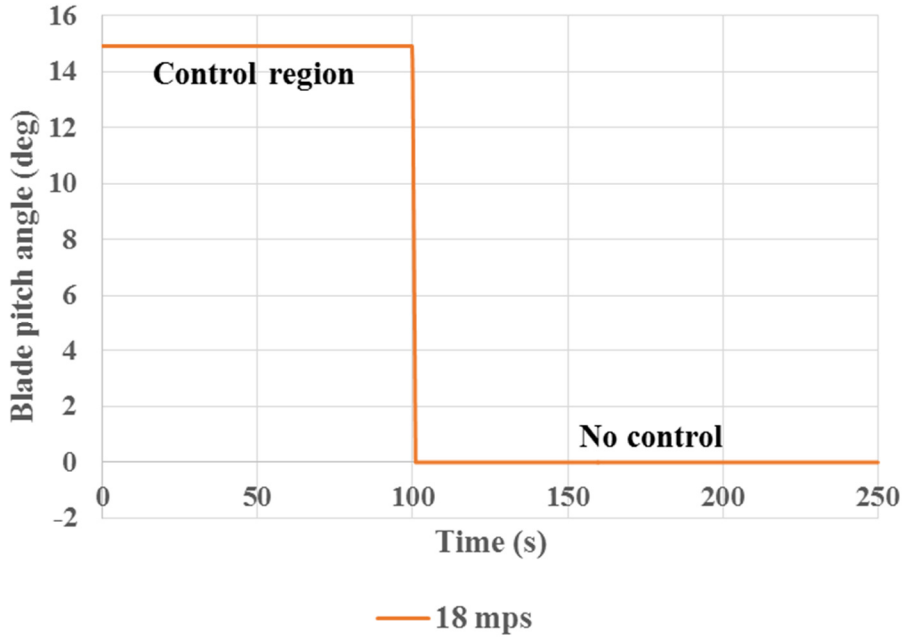

Figure 4.15 Blade Pitch Control Malfunction – 18mps.

As discussed in Table 4.1, the constant collective blade pitch angle for wind speed of 18mps is 14.92 degrees to obtain the rated power output. Thus, the simulation time series shows the control region up to 100 seconds where constant pitch angle of 14.92 degrees can be observed. The time-series beyond 100 seconds is used to simulate the response after blade pitch control malfunction.

Mainly, two cases are considered for coupled analysis response.

(1) **Case (i)** Only-wind – Steady wind

(2) **Case (ii)** Combined – Steady wind, Regular wave

4.5.1 Case (i) Only-wind

Only-wind is a case when the FOWT is subjected to only steady wind during coupled simulation. Wave loading is suppressed to understand the structural response to steady wind. Figure 4.16 shows the pitch tilt angle evaluated at the junction of respective demonstration models.

Figure 4.16 Pitch tilt angle – Only-wind.

In the control region, the static tilt angle of 1 degree and 2 degrees is predicted for SPAR and semi-submersible models respectively in pitch motion. This is caused due to wind thrust as wave loads are suppressed in the present simulation. The difference in pitch tilt angle between the models is due to the varied restoring moment arising from the varied model configurations. In the no control region, it can be observed that the pitch tilt angle predicted for SPAR model is about 3.5 degrees and for semi-submersible model is close to 5.3 degrees. There is an abrupt increase in the pitch motion characteristics for both the models due to the collective blade pitch control failure. This result confirms the malfunction behavior.

Rotor thrust before and after malfunction for only-wind case is shown in Figure 4.17. It can be observed that before the malfunction of pitch control system, the rotor thrust of 450kN is predicted. There is abrupt increase in the rotor thrust to about 1200kN beyond the control region after malfunction. The rotor thrust predictions for both the models is almost same and slight change in the magnitude owes to the different hydrostatic balance of the FOWT models. The hydrostatic restoring for the SPAR model is more than that for semi-submersible model based on different model configurations and depending on the partially submerged volume of the floating platform.

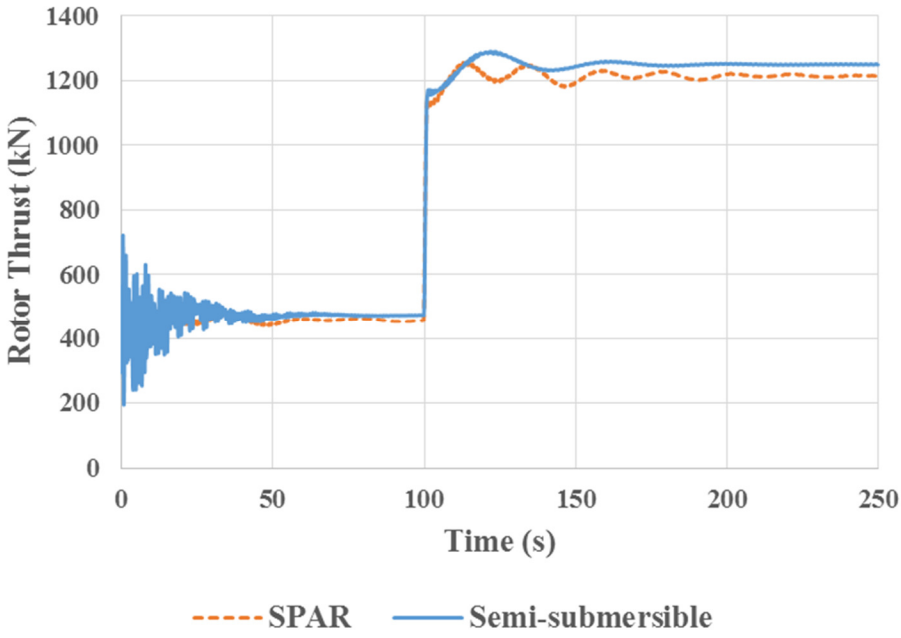

Figure 4.17 Rotor Thrust – Only-wind.

To understand the effects of malfunction on structural loading, the vertical bending moment at the tower base is simulated. It can be observed from Figure 4.18 that there is increase in the vertical bending moment after malfunction.

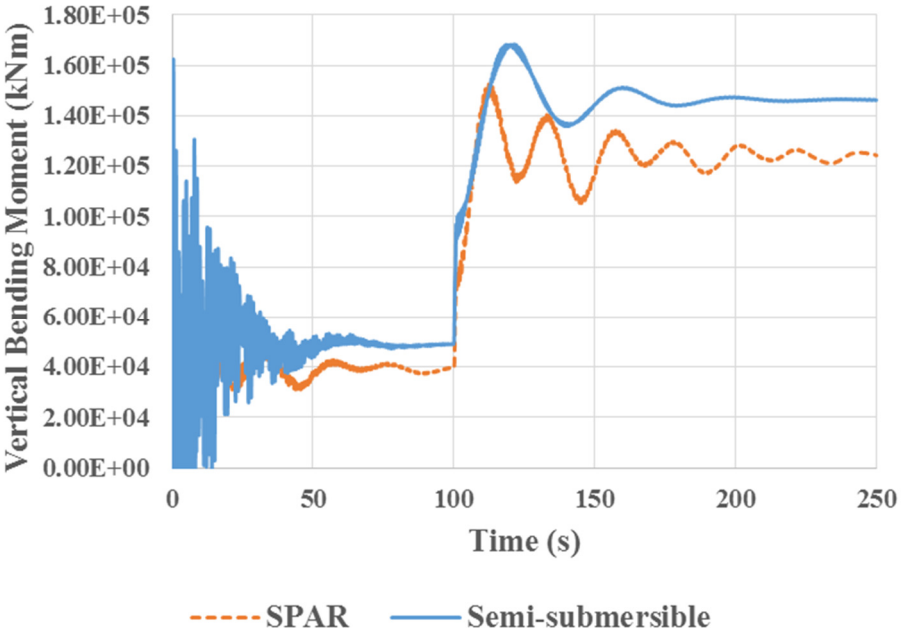

Figure 4.18 Vertical Bending Moment – Only-wind.

The difference in magnitude of the vertical bending moment arises from slightly different initial hydrostatic balance. However, for qualitative comparisons it can be neglected as the malfunction

phenomenon is predicted by both the models. It can be concluded from only-wind case simulations that there is increase in the rotor thrust and vertical bending moment at the tower base because of blade pitch control malfunction. To understand the behavior under the combined effect of wind and wave, further simulations are carried out for the combined case.

4.5.2 Case (ii) Combined

Combined is a case when the FOWT is subjected to steady wind and regular wave during coupling. Combined response of FOWT is demonstrated for a regular wave case of wave amplitude 1m and time period 10s. Figure 4.19 shows the coupled simulation of pitch tilt angle evaluated for a combined case for the two models. Time series of the pitch tilt angle shows the dynamic response of the FOWT. It can be observed that there are 5 peaks within time of 50s and 100s owing to the fact of response to the wave loading. The dynamic response of the two models is qualitatively compared.

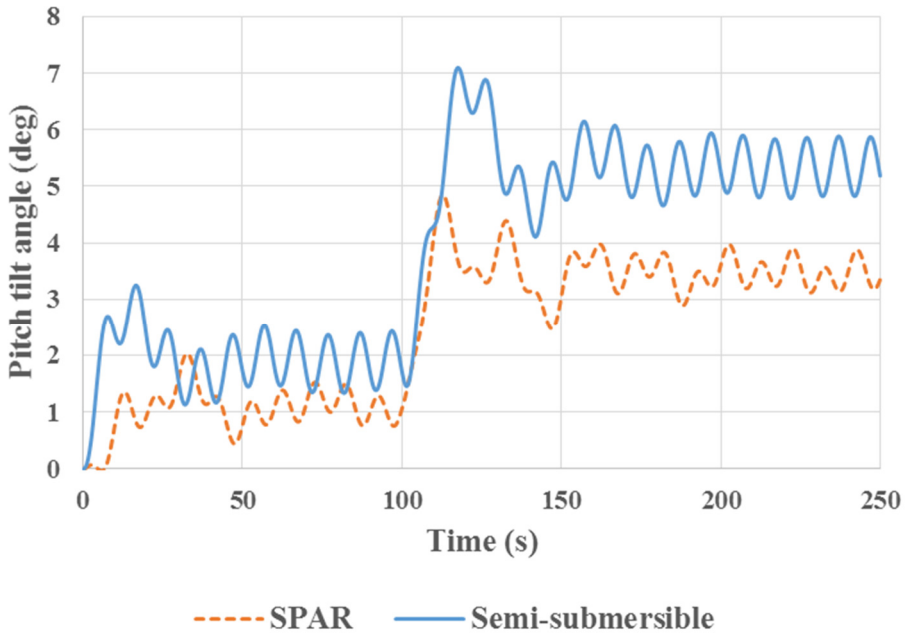

Figure 4.19 Pitch tilt angle – Combined.

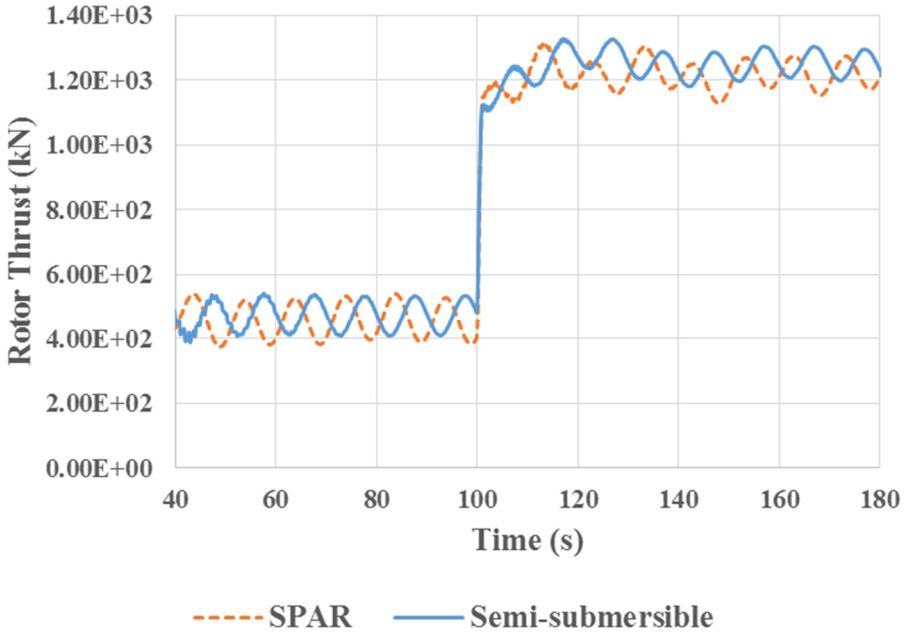

Figure 4.20 Rotor Thrust – Combined.

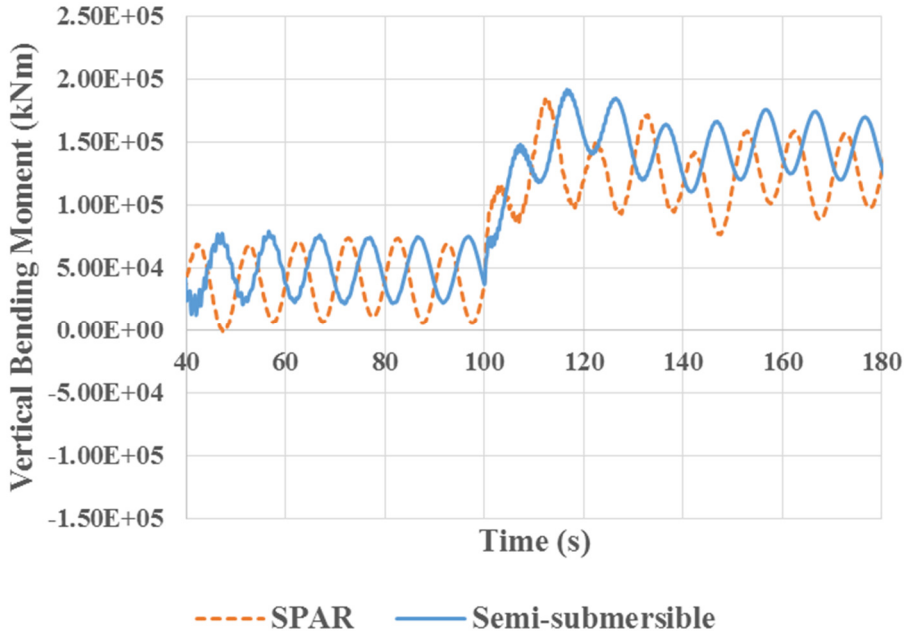

Figure 4.21 Vertical Bending Moment – Combined.

Figures 4.20 and 4.21 show the rotor thrust and vertical bending moment for the combined case. As previously, malfunction of the blade pitch is predicted for the combined case which would be critical from design point of view of FOWT systems. It can be clearly observed that the wave loading is reflected in the combined response of vertical bending moment evaluated at the tower base as well. There are 5 peaks observed between 100s and 150s owing to wave loading and a

maximum bending moment is close to 1.80×10^5kNm. It can also be observed from Figure 4.20 that the bending moment evaluated for the semi-submersible model is slightly larger than for the SPAR model. This can be explained mainly based on the model characteristics of the semi-submersible. However, the behavior of the malfunction for both the models can be observed which is similar to each other and models can be compared qualitatively. The numerical simulation code predicts the malfunction behavior for both the demonstration models.

4.5.3 Comparisons with Onshore Case

In this section, the vertical bending moment evaluated at tower base for onshore and floating platform is compared. In this simulation, the tower is no more treated rigid and the whole FOWT system is modelled as flexible. To simulate tower flexible modes, the whole structural model of SPAR is modelled using DYNABEAM. The platform motions, and forces and moments are exchanged at the top of the tower and coupled results are obtained. FAST is utilized for only aerodynamic calculations. This is achieved by considering the reference tower height as 1m. Tower draft and location of platform reference are changed accordingly to suit the flexible SPAR simulation in the platform input data of FAST. The malfunction behavior is simulated at 50 seconds of the time series.

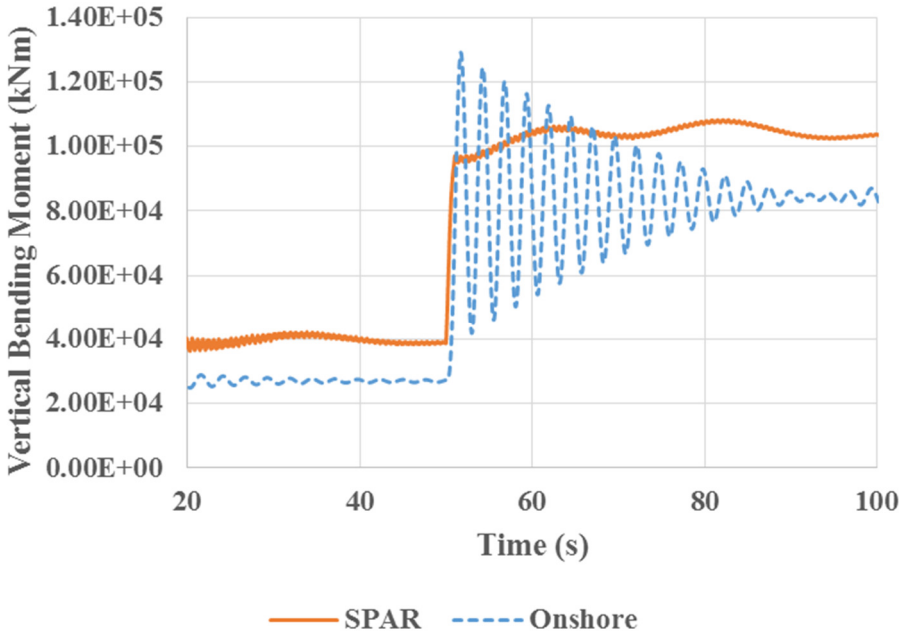

Figure 4.22 SPAR versus Onshore.

Figure 4.22 shows the comparison of the malfunction behavior for the SPAR type floater against the onshore fixed case. It can be observed that the vertical bending moment increases in the case

of floating platform. The static increase is due to the static pitch angle of the floater when subjected to wind loading. The dynamic behavior is mainly due to the coupling of floater dynamics. The abrupt change of the rotor thrust induces the tower flexible modes and structural vibrations for the onshore case while almost only rigid body motions are the dominant for the floating case with almost no excitation of the flexible vibration mode.

The maximum bending moment due to malfunction of pitch control for the onshore case is found to be 1.2×10^4kNm for the steady wind of 18mps and the value of maximum bending moment for transient phase of the onshore case is larger than the floating case. Also, the time duration during which the vertical bending moment takes the maximum value is different which may result in quite different collapse behavior of FOWT systems due to malfunction of blade pitch control.

4.6 Conclusions

In this chapter, the coupled simulation code is developed which considers the flexibility of the floater and blade pitch control malfunction. The simulation tool is validated and found to be useful to obtain the combined response of wind and wave for FOWT systems considered. The new tool successfully considers the blade pitch malfunction while predicting the response. The following specific conclusions can be deduced.

1) It is found that there is increase of rotor thrust due to the assumed collective blade pitch control malfunction by about 2.5 times than that of the controlled case for steady wind speed of 18mps.

2) The performance of both the floater models, SPAR and semi-submersible is found to be similar while predicting malfunction behavior and maximum vertical bending moment evaluated is almost comparable.

3) It is found that there is increase of vertical bending moment due to malfunction of blade pitch control. The level of increase between the floating SPAR and onshore as well as the time duration during which vertical bending moment takes maximum value is different. After malfunction, onshore is dominated by high frequency structural vibrations whereas the floating case has relatively low frequency structural vibrations.

4) It can be concluded that abrupt change of thrust induces tower flexible modes in onshore wind turbines while rigid body motions are dominant for FOWT systems.

The present chapter was focused on blade pitch control malfunction behavior of FOWT systems. Since it is found that the time duration at which the vertical bending moment takes maximum value is different during malfunction, it may lead to quite different collapse of FOWT systems [53]. Thus, it is desired to understand the collapse behavior of FOWT systems due to malfunction of blade pitch control. Therefore elastic-plastic analysis is performed for FOWT system in Chapter 5 and parametric dependencies for collapse behavior is discussed in Chapter 6.

5 Elastic and Elastic-Plastic Response Analysis

This chapter discusses about the elastic and elastic-plastic response analysis approach for FOWT systems. The elastic-plastic analysis is carried out from accidental limit design point of view after the malfunction of blade pitch control. The collapse behavior is simulated and efforts are made to understand the behavior for a flexible FOWT in the plastic region. With this approach, it is possible to predict the failure modes of the FOWT due to the blade pitch control malfunction and in turn the important parameters for risk assessment can be obtained. This chapter gives importance to the engineering application of the developed coupled concept for the FOWT systems to assess loads due to extreme event of control failure and its influence with environmental conditions.

5.1 Elastic response – Analytical comparisons

Before going into elastic-plastic analysis, elastic response is discussed by comparisons with the analytical solutions. The analytical solution for the pitch tilt angle can be obtained from the following relation.

$$\rho g V * GM * \theta_P = F * l \tag{5.1}$$

where ρ is the density of water, g is acceleration due to gravity, V is the volume of the submerged platform, GM is metacentric height, θ_P is the predicted pitch tilt angle, F is the rotor thrust force and l is the lever arm distance between the acting point of rotor thrust and the center of gravity of the whole FOWT systems.

In this section, numerical simulation predicted is compared with the analytical solution. Before that, the working feature of blade pitch control malfunction is understood with the help of model scale experiment results. A series of experiments conducted by Mizukami et al [50] as explained in the previous chapter is used for analytical explanations. The experimental study showed the motion characteristics of wind turbine on a floating platform in blade pitch control malfunction for a model scale ratio of 100. The rotor thrust measured in the case of 3.1m/s wind speed were 0.45N and 0.7N for with and without control respectively as shown in the Figure 4.7 in Chapter 4. In real scale, these values corresponds to 450kN and 700kN according to Froude scaling law. Such abrupt increase of rotor thrust values was obtained from simulation code and working feature of blade pitch control malfunction was verified.

With prime objective of comparison, Figure 5.1 is numerically obtained from the coupled tool targeting the above mentioned rotor thrust values. Constant blade pitch control is employed as discussed in the previous chapter until first 100 seconds of the simulation and malfunction occurs thereafter and simulation is continued without control. It is to be noted that these predictions are obtained for wind speed of 9.25mps and constant blade pitch angle of 4.5 degrees in simulations.

In the simulation within control region, hydrostatic and steady wind coupled result can be observed. The dynamic amplification within first 50 seconds of the simulation is mainly from the controlled pitch angle trying to stabilize the coupled system. Two peaks within 50 seconds indicates the natural frequency of decay of the SPAR FOWT system. At 100 seconds, malfunction of control occurs and we can observe abrupt increase of pitch tilt angle from about 1.1degrees to 1.8 degrees. It was verified that the targeted values of rotor thrust can also be reflected by the coupled numerical simulation in real scale.

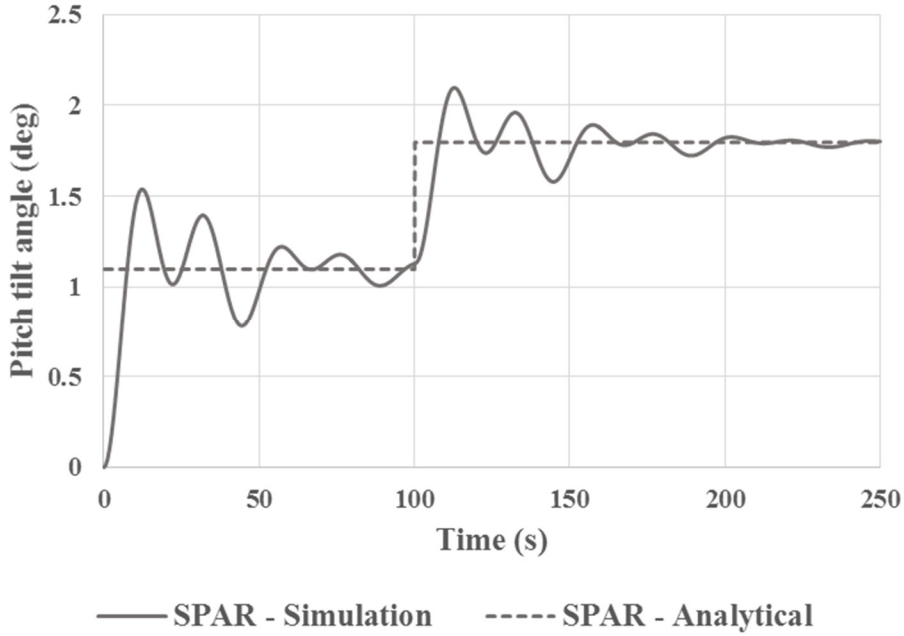

Figure 5.1 Pitch tilt angle – Comparison with analytical solution.

Figure 5.2 shows the simulated vertical bending moment measured at the tower base during malfunction and predicts the maximum vertical bending moment to be 7.1×10^4kNm. This value is comparable with the maximum vertical bending moment obtained during Mizukami's scaled model experimental result [50] of 7.1Nm. This prediction confirms the validity of the simulation code as shown in Chapter 4 and coupled tool is thus compared with analytical solution.

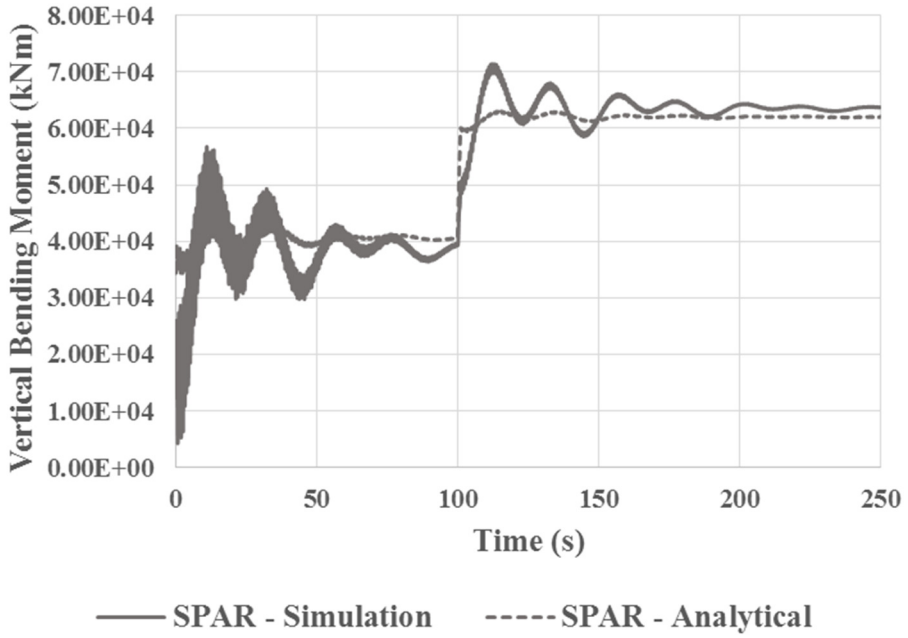

Figure 5.2 Vertical Bending Moment – Comparison with analytical solution.

Now, further comparisons with the analytical solution is carried out for SPAR and semi-submersible models explained in the previous chapter. Figure 5.3 shows the comparisons between the SPAR and semi-submersible models. For better understanding, the elastic results are compared with the analytical predictions.

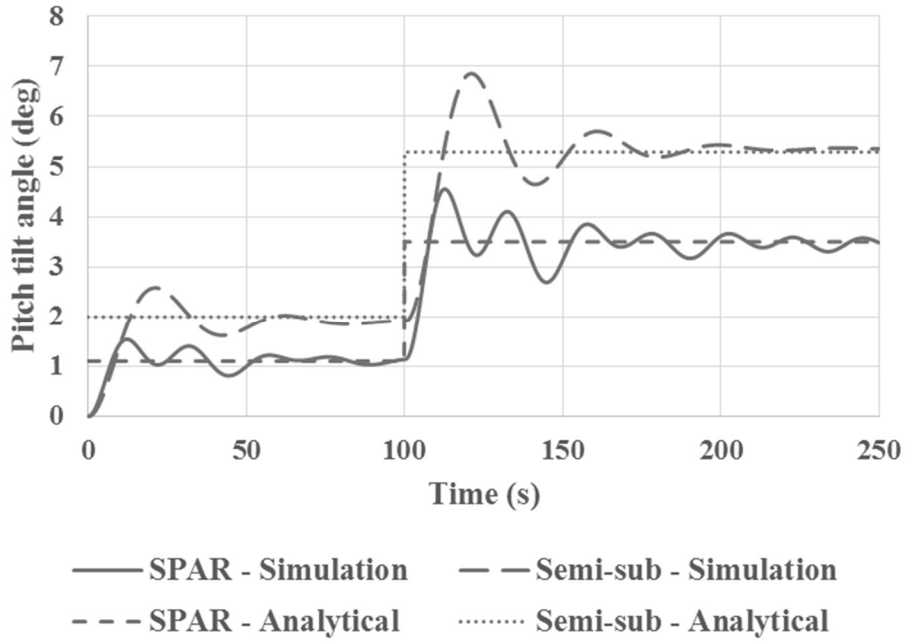

Figure 5.3 Pitch tilt angle – Comparison with analytical solution for different models.

In the control region, the static tilt angle of 1.1 degrees and 2 degrees is predicted for SPAR and semi-submersible models respectively in pitch motion. This is caused due to wind thrust as wave loads are suppressed in the present simulation. The difference in pitch tilt angle between the models is due to the varied restoring moment arising from the varied model configurations. In the no control region, it can be observed that the pitch tilt angle predicted for SPAR model is about 3.5 degrees and for semi-submersible model is close to 5.3 degrees. There is an abrupt increase in the pitch motion characteristics for both the models due to the collective blade pitch control failure.

Before going into the elastic-plastic analysis, the influence of structural modeling on the elastic response of the FOWT system is discussed in the next section.

5.2 Elastic response – Structural modeling

This section is dedicated to explain the influence of flexibility of the floating structure and tower structure on the structural response of FOWT systems. The effect of structural modelling is discussed on the elastic response considering blade pitch control malfunction for a fully flexible FOWT system. A SPAR type FOWT system accommodating the NREL 5MW Baseline wind turbine is considered as previously. Tower is no more modelled as a rigid body. A schematic representation of the model is as shown in Figure 5.4. It can be observed that spar type FOWT model is regarded as flexible with 15 hull elements (nodes) and 14 beam elements connecting the nodes.

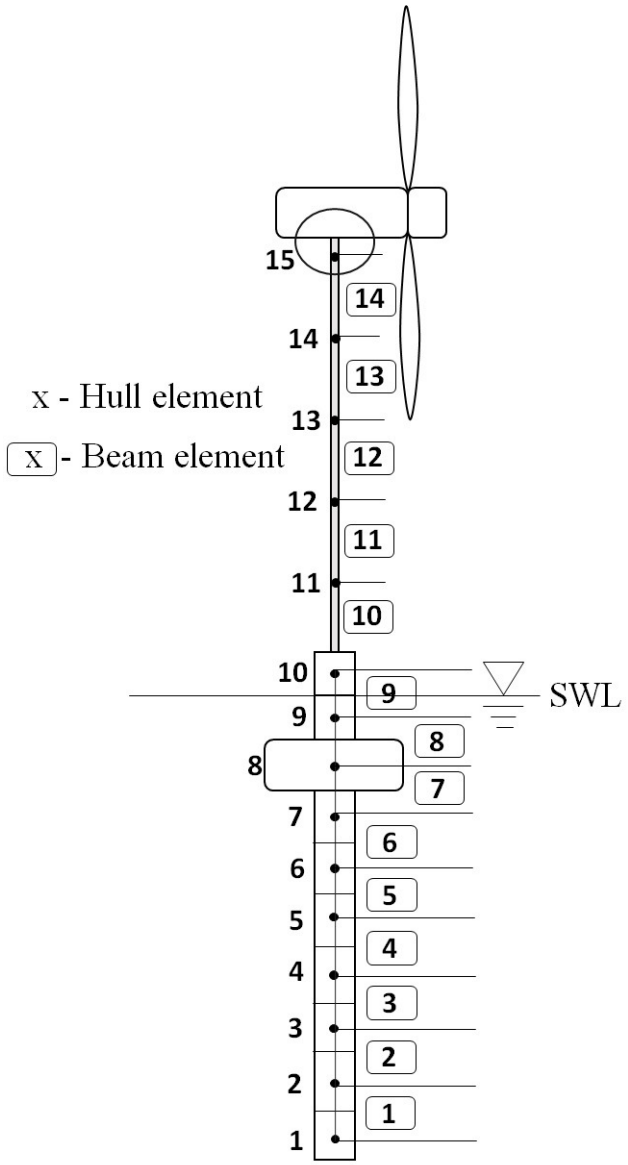

Figure 5.4 Schematic representation of a fully flexible FOWT system (Illustration only).

Two structural models are prepared for the floating foundation to show the structural modeling influence on the structural response. In one model, the foundation is modeled as flexible beam (Flexible Case) while the foundation is modeled as rigid body in the other model (Rigid Case). The tower is modeled as a flexible beam in both the models. For the flexible stiffness of the tower and steel made spar, a realistic values are taken from the reference [43]. In addition, a completely rigid model (FTRigid Case) in which both tower and floater are modelled as rigid is prepared for comparisons. A description of various structural modeling is summarized in Figure 5.5.

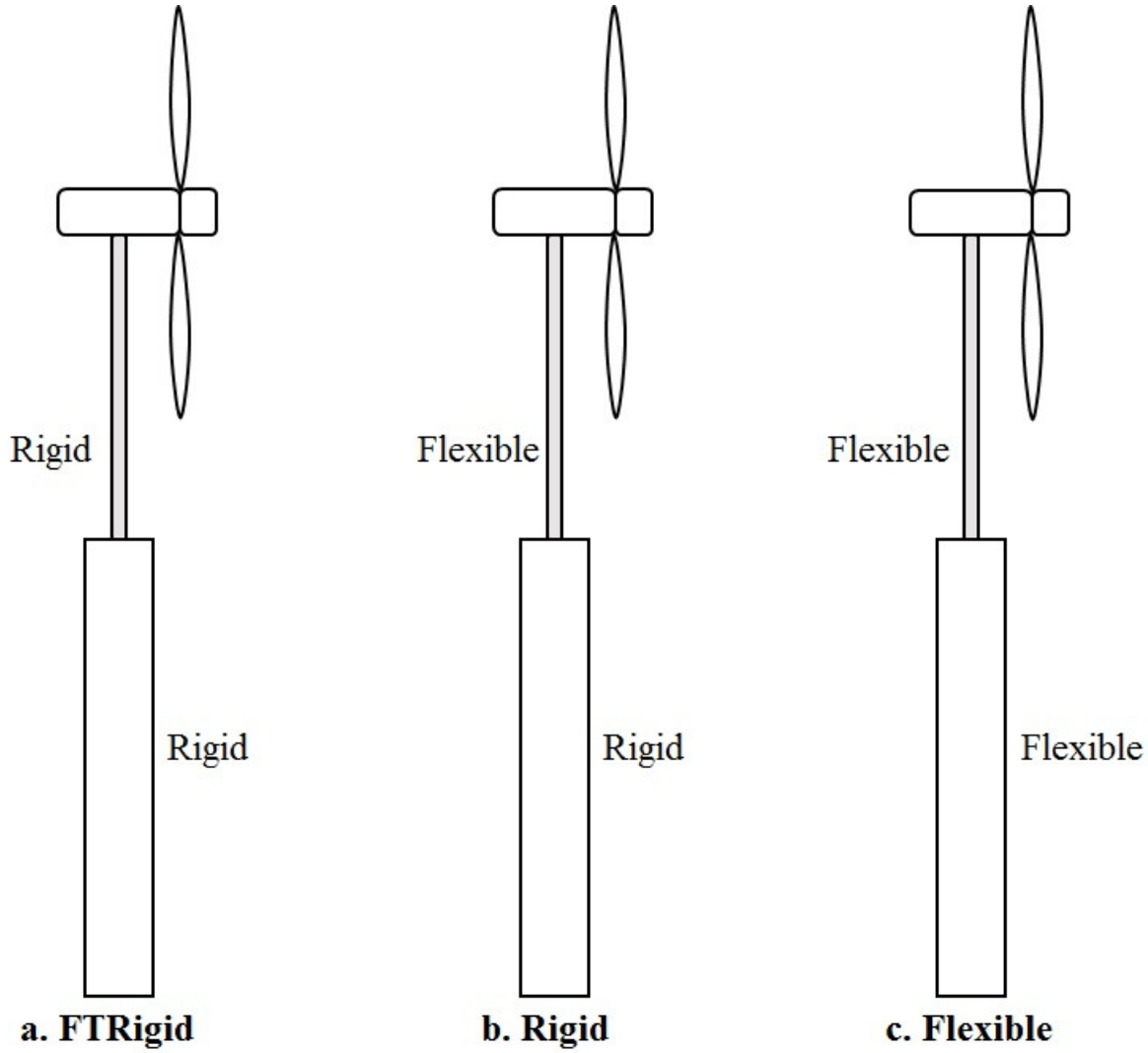

Figure 5.5 Structural Modeling to demonstrate flexibility.

Steady wind speed of 18m/s is considered. Wave load is suppressed in this simulation to clearly understand the response to different structural modelling. Blade pitch control is activated during the simulation. The goal of the constant blade-pitch controller is to regulate generator speed above the rated operation point (11.4m/s) so that the desired power of 5-MW is captured at all times as explained in previous chapter. Blade pitch controller is incorporated within the rotor dynamics and

thus rotor-control-floater coupled response of the FOWT system can be obtained which consists of rotor dynamics with blade pitch control and floating structure dynamics.

Figure 5.6 shows a comparison of time histories of rotational displacement at the tower bottom (node 10 in Figure 5.4) between Rigid and Flexible cases. The FOWT tilts by about 2 degrees under the assumed condition. It has a transient motion at the beginning, however, the transient part decays and comes to a stationery response to the natural period (about 20s) of the FOWT system around the mean tilt angle. The malfunction of controller occurs at 50s of the simulation after which the displacement increases rapidly. There are almost no distinct difference between the two simulation results except the high frequency structural vibration. FTRigid case (both floater and tower regarded as rigid) is also plotted to show the influence of flexibility of the tower on response. It is noted that there is a slight difference in the pitch tilt angle predicted when both tower and floater are modelled as rigid. The predicted value is slightly less than when flexibility in the structural modeling is considered. Thus, flexibility of structure influences the elastic structural response of FOWT systems.

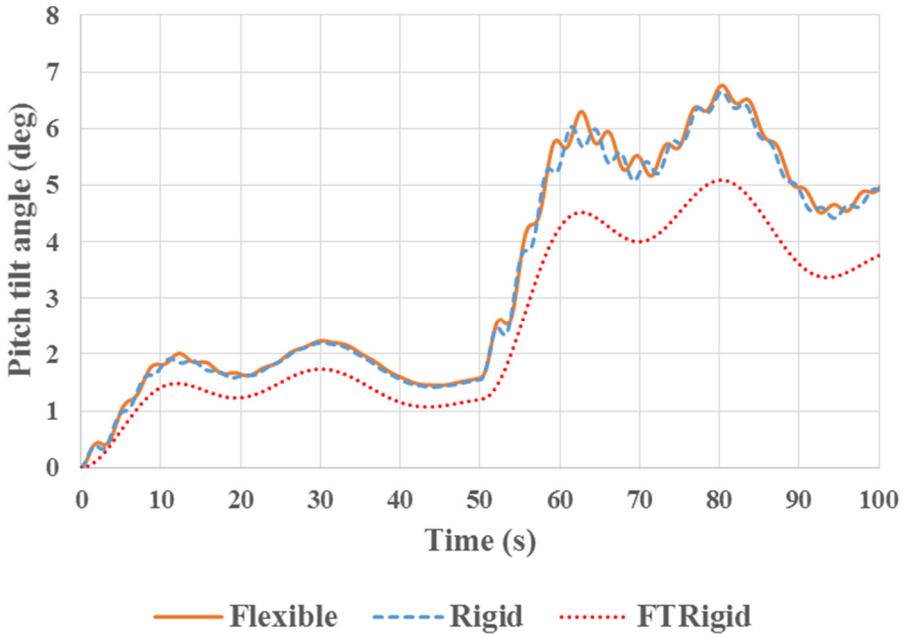

Figure 5.6 Pitch tilt comparison – Effect of Structural Modeling.

Figure 5.7 is plotted to observe the comparison between the FTRigid Case and Flexible Case for structural vertical bending moment evaluated at tower bottom (element 10 in Figure 5.4). We can observe the FTRigid is predominated by the rigid body motion of the floater (natural period of 20s) which is reflected in the simulation result. In case of Flexible Case, the structural vibrations (of about 3.2s) is observed. This proves that the flexibility of structure influences the structural response of FOWT systems and it is important to consider flexibility of both floater and tower structure while evaluating the structural loads coming onto the FOWT system.

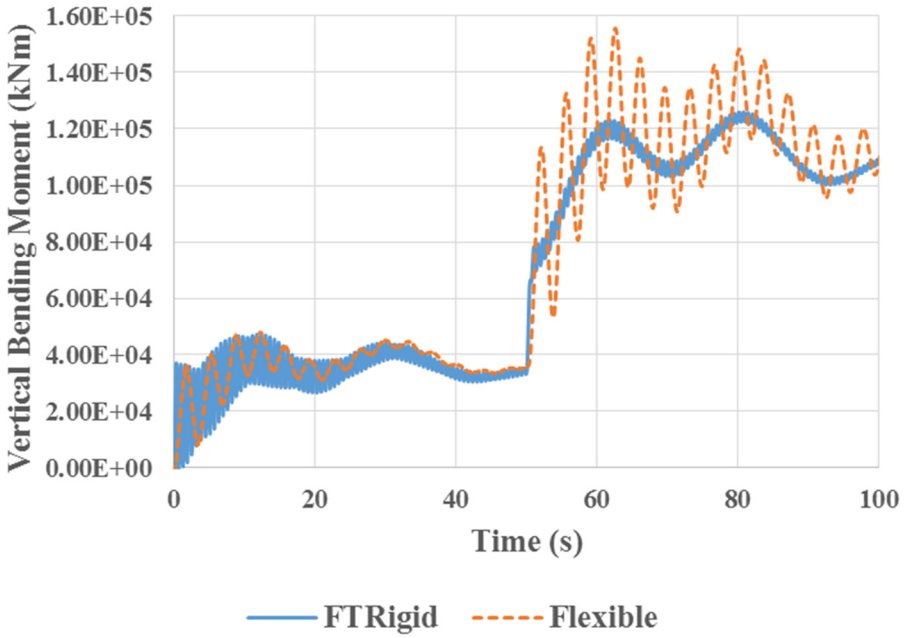

Figure 5.7 Vertical Bending Moment – FTRigid vs Flexible.

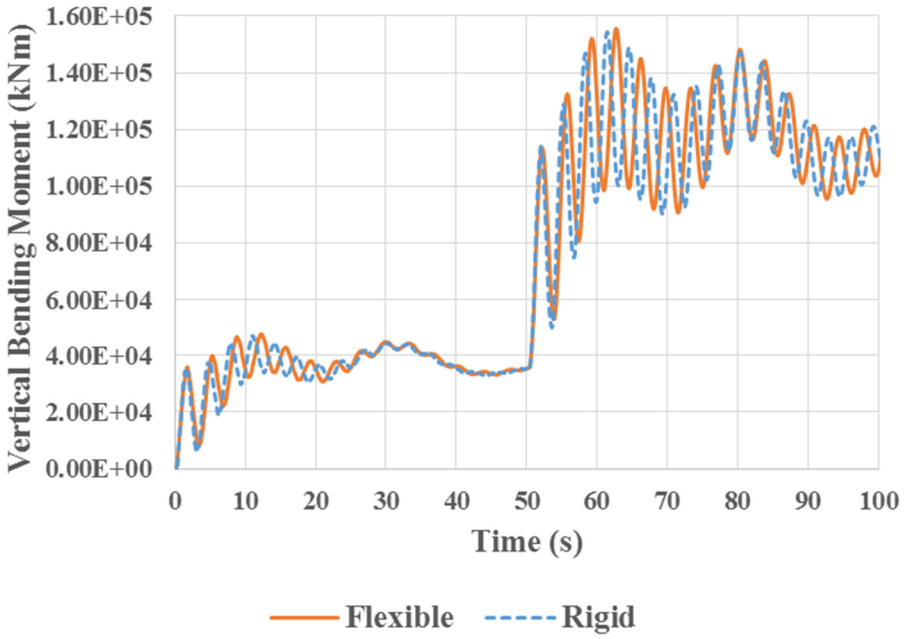

Figure 5.8 Vertical Bending Moment – Rigid vs Flexible.

Figure 5.8 shows a comparison of tower bottom (element 10 in Figure 5.4) bending moment time histories between the two cases (Flexible and Rigid). It is inferred that the structural modelling by considering flexibility of floater has an influence on the structural load of the FOWT system considered. Apparently, the natural period of the tower structural vibration is 3.2s for Flexible

Case while it is 3.0s for Rigid Case. This shows that floater flexibility influences the overall elastic structural response of the FOWT system.

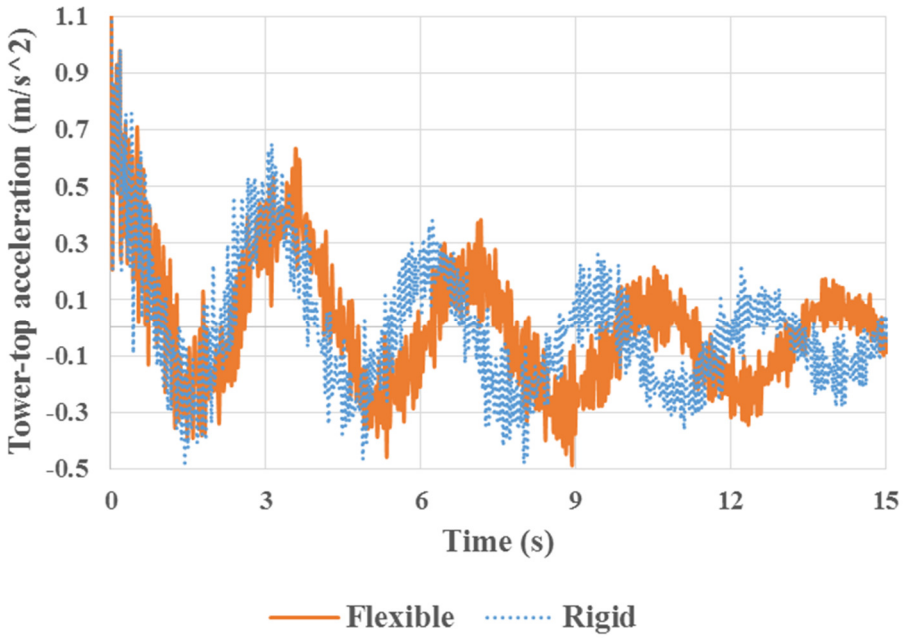

Figure 5.9 Tower-top acceleration – Rigid vs Flexible (Zoomed 15s).

Further, Figure 5.9 shows a comparison of tower top acceleration time histories between the two cases zoomed for first 15s of the simulation. Similar structural vibration components are observed even at the tower-top. It is thus proved that the structural modeling and flexibility has influence on the FOWT system. It is also pointed out that the two time histories are similar in terms of the vibration magnitudes for the assumed steady wind case. With the developed coupled simulation methodology, it is possible to model the flexibility of the floater and tower. The foundation flexibility is found to affect the elastic response of the FOWT system.

Now, the elastic-plastic behavior analysis is considered from the viewpoint of collapse due to malfunction of the blade pitch control. Section 5.3 describes the theoretical modeling for the elastic-plastic behavior analysis.

5.3 Theoretical Modeling

The coupling strategy explained in the previous chapter is utilized for the elastic-plastic analysis for understanding the collapse behavior of the FOWT system. In this chapter, the collapse behavior is simulated at the tower base as it could be one of the most critical failure location. In reality, it is also well known that the collapse usually occurs at the weakest cross-section while other sections remain unaffected. Thus, only one weakest section i.e., tower base location is selected. A piece-wise linear spring model is adopted at junction of the two modules for elastic-plastic analysis as shown in Figure 5.10.

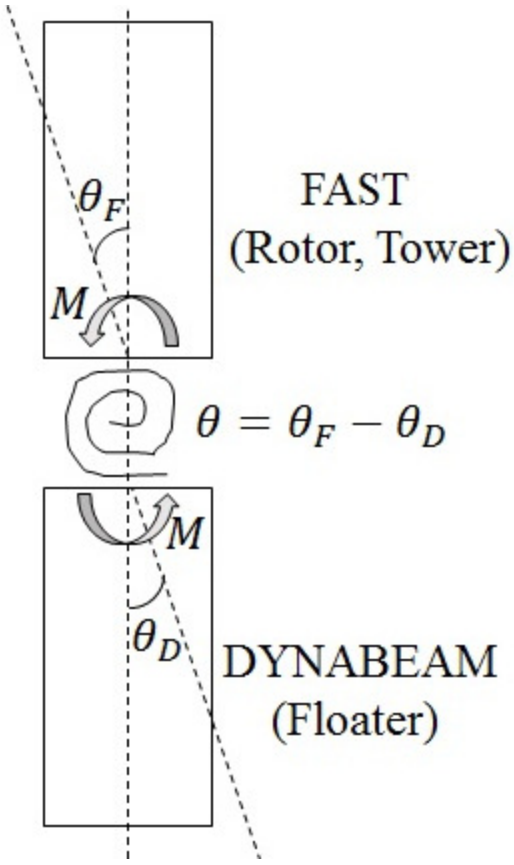

Figure 5.10 Theoretical model for elastic-plastic analysis.

The relative rotational angle between the FAST and DYNABEAM modules is used to obtain the vertical bending moment. It follows the relation as follows.

$$M = M(\theta) \tag{5.2}$$

$$M(\theta) = k_R\theta \tag{5.2'}$$

where k_R is the secant stiffness of the non-linear spring, $\theta = (\theta_F - \theta_D)$ is the relative rotational angle at the assumed collapsing section, θ_F is the rotational angle of FAST side at the tower base,

θ_D is the rotational angle of DYNABEAM side at the tower base and $M(\theta)$ is the vertical bending moment evaluated. It is possible to obtain element moment output from DYNABEAM directly which is balanced with $M(\theta)$ at the collapsing section. With this methodology, the FOWT can be evaluated in the plastic region after the vertical bending moment exceeds the ultimate capacity of the non-linear rotational spring and in turn it is possible to understand the collapse behavior of the FOWT.

In this study, the piece-wise linear spring model represents the relation between the rotation and the vertical bending moment including the recovery of bending rigidity when unloaded. Such a capacity curve relation is exemplified in Figure 5.11. From the capacity curve, it can be noted that the path AB represents the elastic region of the analysis. The point B represents the vertical bending moment reaching the ultimate capacity of the section. The path BC lies in the plastic region and collapse extent of the section can be discussed here. CD represents the unloading path showing the recovery of bending rigidity after collapse in the plastic region. The idealized capacity curve represents both yielding and buckling collapse behavior.

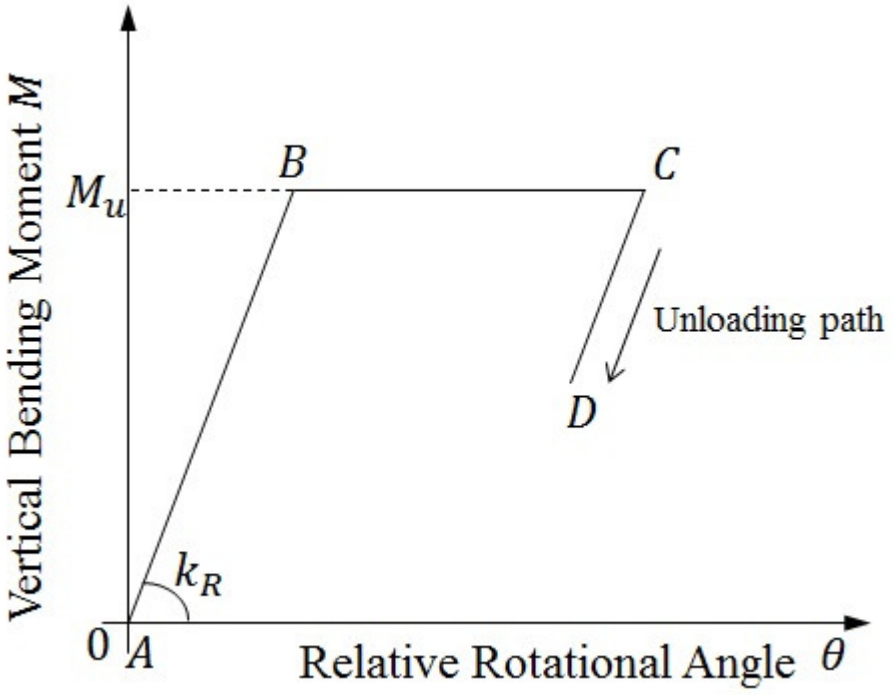

Figure 5.11 Capacity curve.

5.4 Elastic-plastic behavior demonstration

This section elaborates the elastic-plastic analysis and collapse behavior results as per the methodology explained in earlier sections. Elastic-plastic analysis is demonstrated for the flexible SPAR model under only-wind conditions. The coupling technique is modified to feedback the reaction moment only for the pitch degree of freedom. The moment-rotational angle relationship is obtained during coupling and maximum bending moment after malfunction of blade pitch control is targeted for understanding collapse behavior.

Capacity curve for elastic-plastic analysis is selected as per the plastic moment calculated. The diameter of cylindrical cross-section is assumed to be 6.3m with thickness of 0.03m for collapse behavior analysis for demonstrating elastic-plastic behavior. Young's modulus of the material is 200GPa. Using these assumptions, the collapsing moment of the section is calculated and the value is set to be 1.53×10^5kN.m. The slope and relative rotation angle for the capacity curve can be thus obtained correspondingly for the elastic region.

For simplicity, the tower is modelled as a uniform rigid tower to reduce computational time and cost since capturing the malfunction and understanding the collapse behavior are the prime objectives in this chapter. The rigid body motion during collapse is the target of the present research and thus elastic deformation of tower is neglected.

Figure 5.12 shows the vertical bending moment for malfunction at 50s. The short period (about 1-2seconds) owes to the fact of tower-rotational spring system vibrations reflected in the simulation (See Figure 5.10). The period of about 15s is also observed in the simulation which is from the rigid body motion of the platform. The plastic deformation region can be easily observed between 70s and 80s of the simulation where the bending moment takes the largest value.

The capacity curve (Figure 5.13) is used to explain the elastic-plastic behavior. The moment-rotational angle relationship curve shows the elastic region behavior until the yield point i.e., vertical bending moment is less than the plastic moment defined for the section. Collapse occurs once bending moment exceeds the maximum capacity of the section at the tower base of the FOWT. This can be observed in the linear region between 0.06 degrees and about 0.1 degrees which can be termed as the collapse extent of the section considered. Further, the tower regains the bending rigidity and simulation is continued. The unloading path clearly shows the value of about 1.2×10^5kNm in the plastic region. This value can be correspondingly verified at about 85s of the simulation in Figure 5.12.

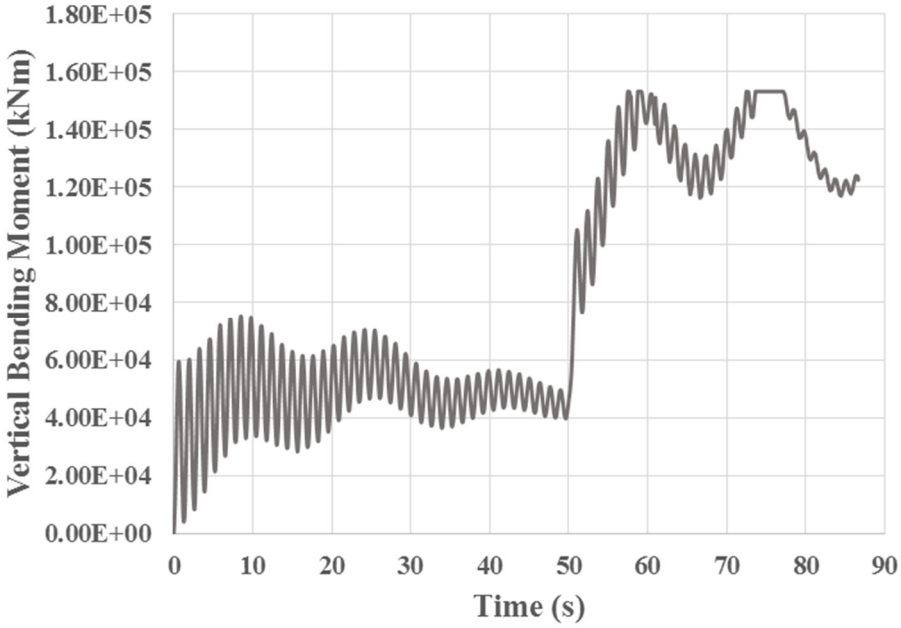

Figure 5.12 Vertical bending moment – Collapse behavior.

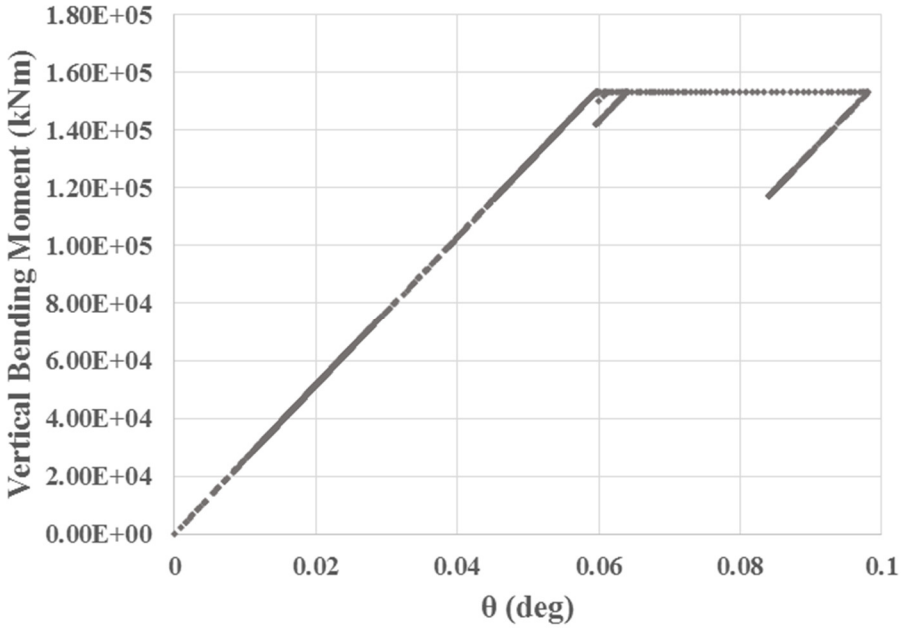

Figure 5.13 Capacity curve – Demonstration.

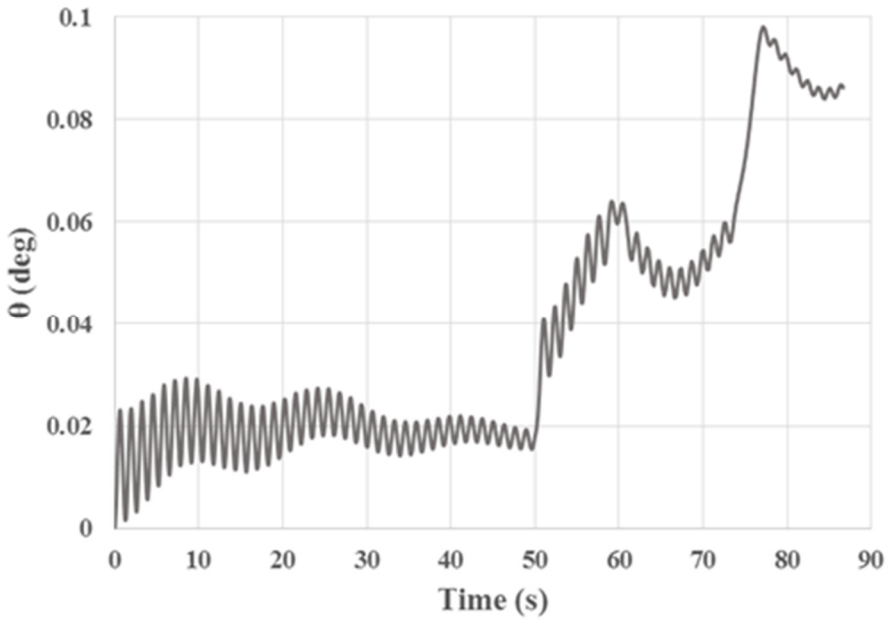

Figure 5.14 Relative rotational angle time-series.

To further understand the collapse behavior, the time history of the rotational angle is plotted in Figure 5.14. A minor collapse around 60s and another collapse around 75s can be observed at the same location which in turn can be corresponded to the vertical bending moment time-series. Collapse extent of about 0.1 degrees is observed for the SPAR platform considered at the tower base for the assumed capacity. These collapses are small and tower regains the structural bending rigidity. However, this phenomenon will be critical for a different capacity curve and might lead to complete collapse of the tower.

A large collapse occurrence phenomenon is simulated to demonstrate the severity of blade pitch control malfunction on structural load. The capacity of the ultimate moment is reduced by about 5% i.e., the ultimate moment of 1.4×10^5kNm is used for the tower section by assuming a diameter of 6m. In comparison with the previous simulations, only the capacity curve is changed to demonstrate large collapse. Figure 5.15 shows the comparison of pitch tilt angle for floater (θ_D) and tower (θ_F) for an only-wind case of 18mps when collapse occurs at the floater-tower junction. We can infer that the tower tilt angle (θ_F) increases drastically due to malfunction of blade pitch and the section is not able to withstand the increased vertical bending moment due to dynamic effect. The relative angle between θ_D and θ_F grows while θ_D does not grow to the same extent as θ_F. Thus, it can be understood that the tilt angle increases abruptly due to collapse of tower.

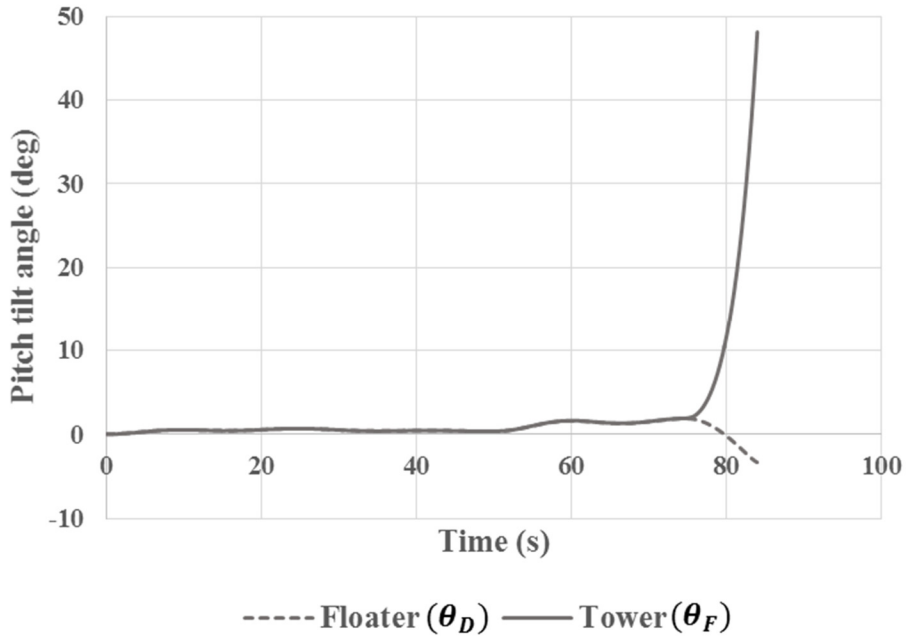

Figure 5.15 Pitch tilt angle – Collapsed tower.

The present section is focused on elastic-plastic behavior of FOWT systems under blade pitch control malfunction and demonstrated two collapse scenarios. A small (or partial) collapse where the tower regains the bending rigidity and a large (or complete) collapse where the tower falls down completely for a steady wind case of 18mps. However, the behavior of collapse of FOWT systems may vary different FOWT systems depending on the various environmental conditions. This collapse is different from collapse behavior of ship structures [54] and thus it is desired to understand the collapse behavior of FOWT systems from parametric dependencies point of view in the coming sections. Small (or partial) collapses where the tower regains bending rigidity are targeted to discuss the parametric dependencies of different strength models and various environmental conditions.

5.5 Conclusions

This chapter demonstrated the elastic and elastic-plastic response behavior analysis methodology by adopting a coupled simulation code which considers the blade pitch control malfunction. The simulation tool is found to be useful to obtain the combined response of wind and wave for FOWT systems considered. The collapse performance of a SPAR platform under blade pitch control malfunction is evaluated and it is found to be an effective methodology from structural point of view for clarifying the behavior under accidental limit state. The following specific results can be summarized.

1) The structural modeling of floater and tower plays an important role while evaluating the structural loads and overall elastic response of the FOWT system. It is found that the natural period of the structural vibrations increases for flexible floater by about 10% than when the floater is modelled as a rigid body.

2) The floater dynamics is found to affect the maximum tower-base vertical bending moment and a larger thrust load is predicted than the one obtained by the thrust curve under the assumed blade pitch control malfunction. When predicting the maximum load after the malfunction, the dynamic analysis may be necessary.

3) Elastic-plastic behavior analysis conclusively evaluates the response of the FOWT systems considered in both elastic and plastic regions.

4) The tower structure collapses and falls down completely when it is subjected to extreme vertical bending moment exceeding the ultimate strength capacity by about 5%. From design point of view, it is important to give a sufficient safety margin to the tower structure against the extreme moment due to blade pitch control malfunction.

It is desirable to understand the parametric dependencies for collapse behavior of FOWT systems due to various environmental conditions. Such discussion is carried out in Chapter 6 for effective understanding of collapse behavior of FOWT systems.

6 Parametric Studies for Collapse Behavior

The parametric dependencies including strength models, combined effect of wind and wave and onshore vs floating platform are conducted in this chapter. The SPAR model described previously is utilized for the analysis except for a different mass distribution. The flexible SPAR model described in Chapter 3 was created with a top heavy turbine system to match the scaled model used for experiment. However, after validation and realizing the tendency of behavior, the tower-top mass is distributed realistically and this SPAR model after redistributing is utilized for all further analysis and collapse behavior.

6.1 Different strength models

Firstly, the collapse behavior due to different strength models is discussed. Steady wind case of 18mps is selected and wave load is suppressed for all simulations in this section. Three different strength models are discussed to understand the collapse behavior when the collapsing moment is varied for the same case of environmental conditions (steady wind of 18mps) when subjected to blade pitch control malfunction.

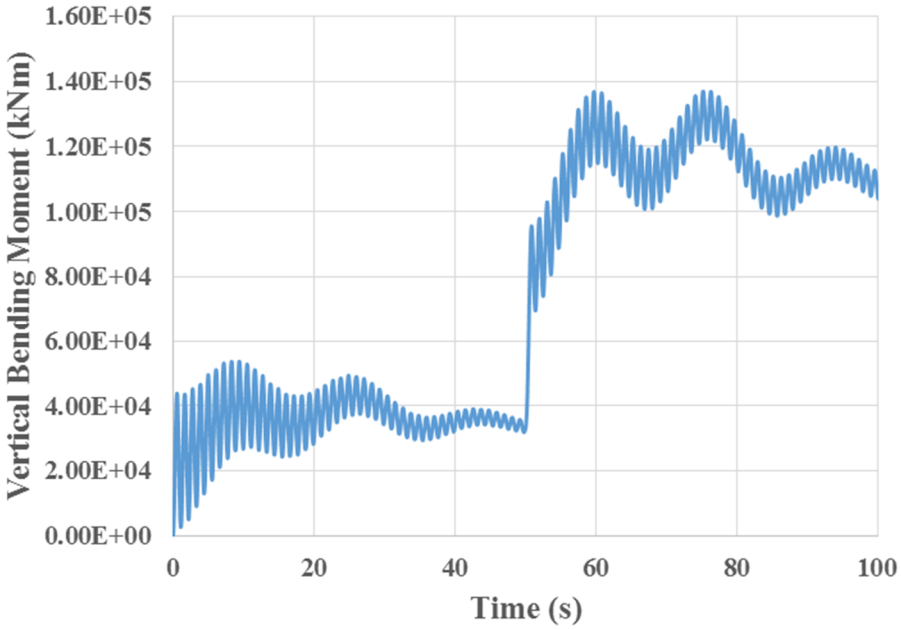

Figure 6.1 Vertical Bending Moment – Strength Model 1.

The diameter of cylindrical cross-section is assumed to be 6.3m with thickness of 0.03m for collapse behavior analysis in this section. Young's modulus of the material is 200GPa. Using these assumptions, the collapsing moment of the section is calculated and in this section the value is set to $1.53x10^5$kN.m. The slope and relative rotation angle for the capacity curve can be thus obtained correspondingly for the elastic region. The blade pitch malfunction is simulated at 50seconds of the simulation. The maximum value of vertical bending moment can be observed in Figure 6.1 after blade pitch malfunction at about 60s. This simulation is carried out for effective comparisons to show no collapse condition. The corresponding moment-curvature relationship is plotted in Figure 6.2. It can be observed that the vertical bending moment always lies in the elastic region and there is no collapse at the junction. It is also possible to observe the maximum vertical bending moment developed is $1.37x10^5$kN.m which is less than the model capacity of $1.53x10^5$kN.m.

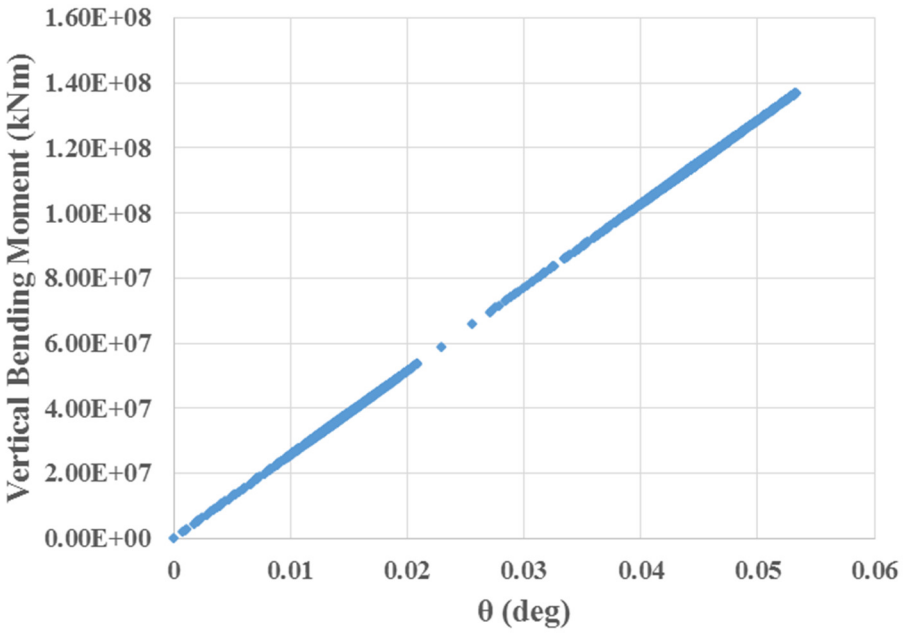

Figure 6.2 Moment-curvature relationship – Strength Model 1

Now, to understand the effect of different strength model, the capacity of the section is reduced. The diameter of cylindrical cross-section is reduced to 5.8m and 5.75m with same thickness as previously to understand the effect of strength models. Correspondingly we obtain the capacity (ultimate moment capacity) for the respective cases as $1.30x10^5$kN.m and $1.28x10^5$kN.m. Blade pitch malfunction is simulated at 50seconds as previously. Figure 6.3 shows the partial collapse at tower base around 75seconds of the simulation for the strength model 2 (diameter of cross-section 5.8m). However the tower regains bending rigidity and the collapse extent of about 0.07degrees is observed in the plastic region (Figure 6.4). The idea behind such simulation is to understand the how sensitive the collapse is for different capacity curves.

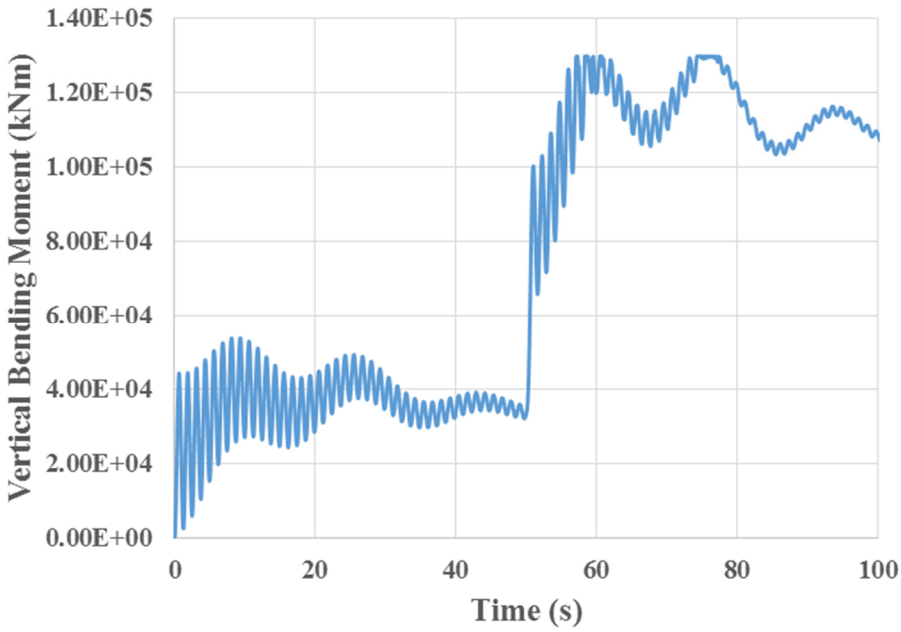

Figure 6.3 Vertical Bending Moment – Strength Model 2.

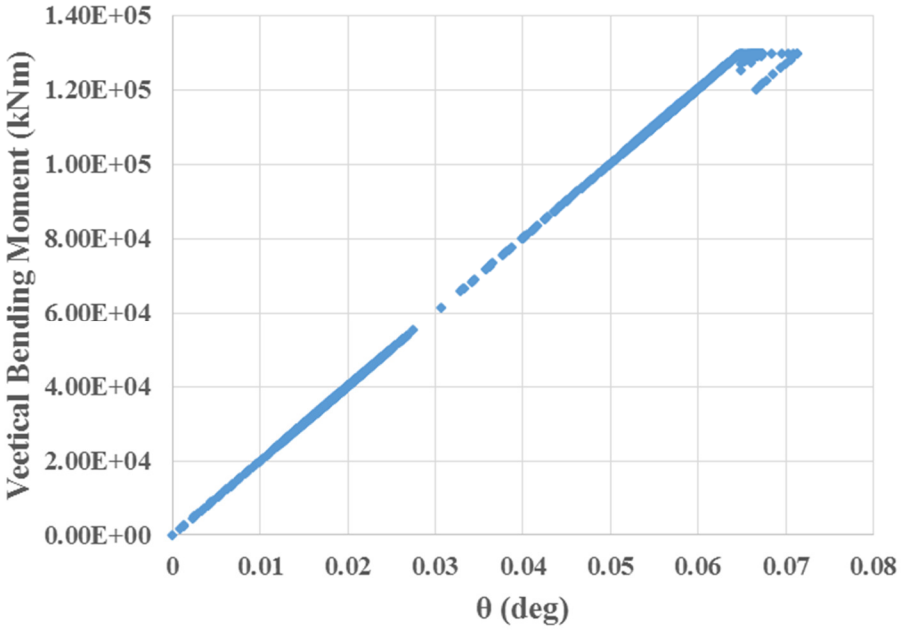

Figure 6.4 Moment-curvature relationship – Strength Model 2.

The simulations are further carried out for strength model 3 (diameter of cross-section 5.75m). Figure 6.5 shows the vertical bending moment time series for this case. It can be observed that even with about 1.5% decrease in the capacity leads to much higher collapse extent of 0.55degrees (Figure 6.6). The collapse behavior is thus sensitive to the different capacity curves utilized while

designing the tower structure. Designers need to be careful while evaluating the risks involved in the collapse due to sectional capacity and provide adequate scantlings to the tower structure to avoid damage to the main structure.

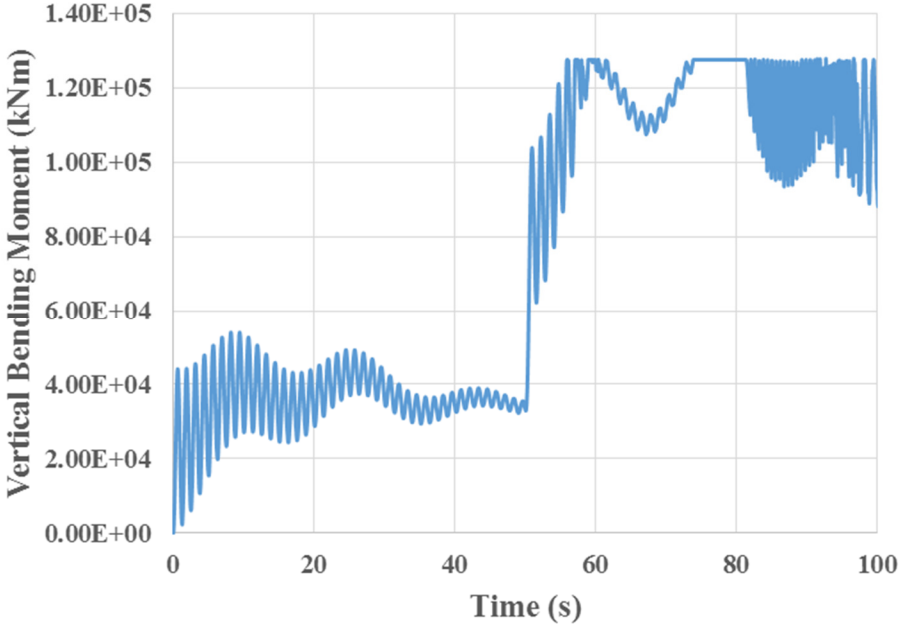

Figure 6.5 Vertical Bending Moment – Strength Model 3.

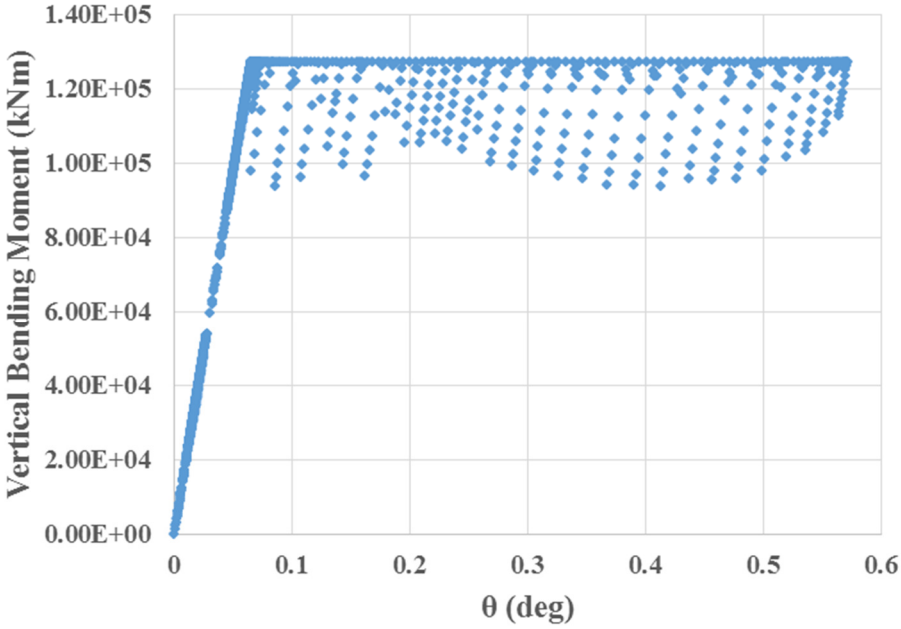

Figure 6.6 Moment-curvature relationship – Strength Model 3.

Table 6.1 summarizes how different strength models affects the collapse behavior for the cases considered.

Table 6.1 Influence of different strength models – Only Wind (18mps).

Capacity	Diameter of cross-section (m)	Collapsing moment (kNm)	Collapse extent (deg)
Strength Model 1	6.3	1.53×10^5	No collapse
Strength Model 2	5.8	1.30×10^5	0.07
Strength Model 3	5.75	1.28×10^5	0.55

6.2 Combined effect of wind and wave

This section describes collapse behavior after malfunction of blade pitch control when combined loading of wind and wave acts on the FOWT system. Figures 6.7 and 6.8 are plotted to show the difference between only wind and combined wind and wave loading. Figure 6.7 shows the pitch tilt angle at the junction between FAST and DYNABEAM modules. It clearly shows the time period of oscillation equal to 15s corresponding to the rigid body motion in pitch direction when subjected to only steady wind condition of 18mps. The control malfunction occurs at 50s and maximum pitch tilt angle of approximately 1.9degrees is observed around 78s of the simulation. The capacity of the strength model 1 is adopted as explained in the previous section. Thus, there is no collapse in this case due to steady wind of 18mps.

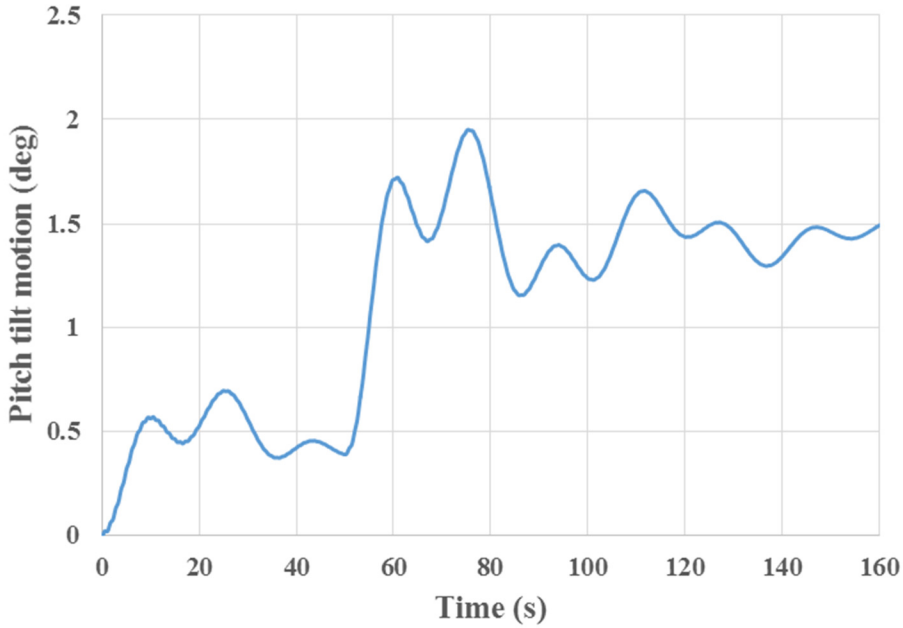

Figure 6.7 Pitch tilt angle – OnlyWind (18mps).

To understand the complete behavior, combined loading is applied for the same case of steady wind. Regular wave of wave period 8s and wave amplitude 0.5m is selected to demonstrate the combined loading condition. Figure 6.8 shows the pitch tilt angle for the combined case. 5 peaks between 120s and 160s can be observed which corresponds to dynamic behavior due to wave period of 8s. Also, the maximum pitch angle of about 2.1 degrees is observed for the combined case which is larger response than for the only-wind case.

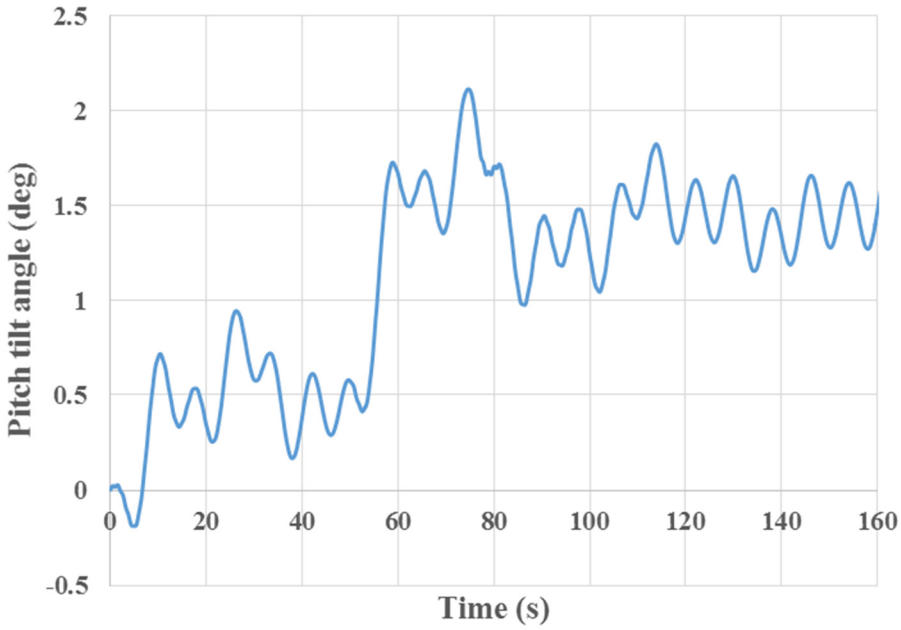

Figure 6.8 Pitch tilt angle – Combined (18mps, 8s, 0.5m).

Due the larger response when subjected to combined loading, there is partial collapse of the structure at the tower base even in the case of strength model 1 for combined loading. Figure 6.9 shows the vertical bending moment time series evaluated at the junction between the modules. Dynamic behavior due to wave loading can be observed throughout the time series. 5 peaks between 120s and 160s confirms the response due to regular wave of period 8s. The malfunction at 50s increases the vertical bending moment and due to combined loading collapse occurs. We can observe the collapse between 70s and 80s of the simulation in Figure 6.9. The moment-curvature relationship is also plotted in Figure 6.10 and a collapse extent of about 0.1degrees can be observed for the combined environmental case considered for the evaluated FOWT system.

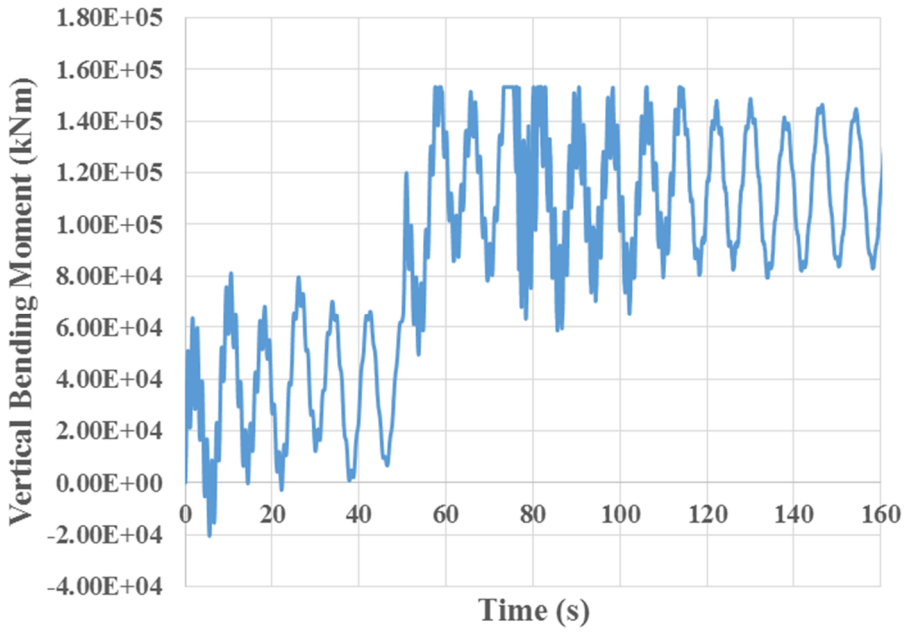

Figure 6.9 Vertical Bending Moment – Combined (18mps, 8s, 0.5m).

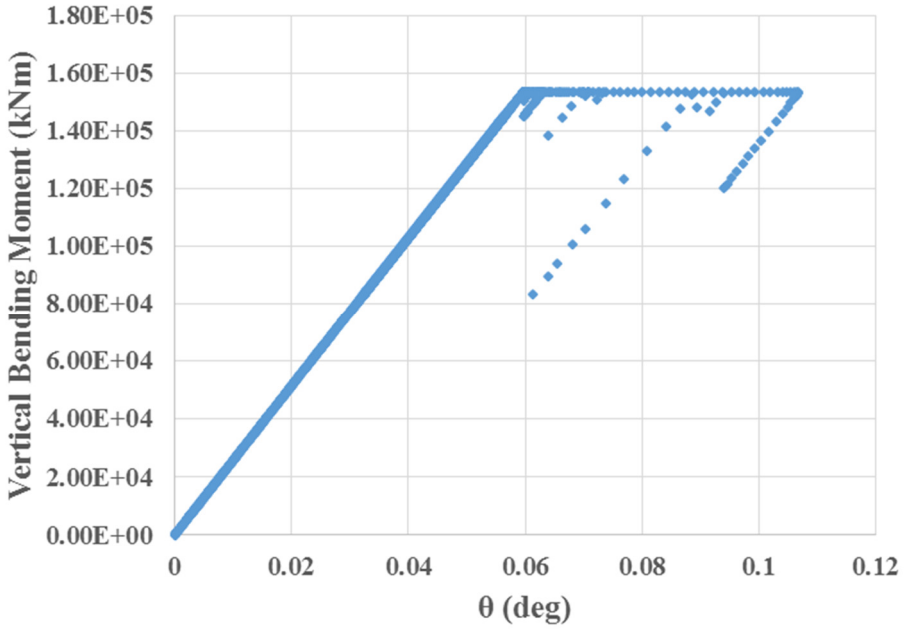

Figure 6.10 Moment-curvature relationship – Combined (18mps, 8s, 0.5m).

Thus, the effect of combined loading is demonstrated and discussed for a case of regular wave and steady wind. It is understood that the response is larger for combined loading and collapse occurs even for the diameter cross-section of 6.3m (strength model 1). Previously, the structure did not collapse while using strength model 1 when only wind environmental condition was used. It is therefore necessary to consider the effect of combined loading while evaluating the collapse

behavior characteristics and sufficient safety factor needs to be considered. Now, it is desirable to understand about the collapse scenarios for various wave amplitudes and wave periods.

6.2.1 Influence of wave amplitude

To understand the influence of wave amplitudes on the collapse behavior, wave period of 8s and steady wind of 18mps are kept constant and only wave amplitudes are modified. Three cases of wave amplitudes are discussed. Wave amplitude of 0.5m was already showed from Figure 6.8 to 6.10. Figures 6.11, 6.12 and 6.13 summarizes the pitch tilt angle, vertical bending moment time-series and moment-curvature relationships respectively for the wave amplitude of 0.6m.

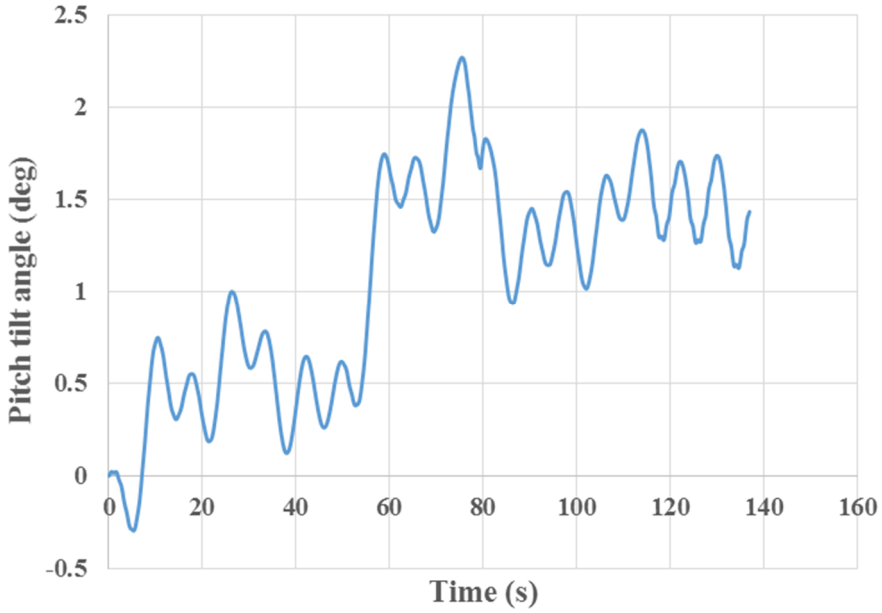

Figure 6.11 Pitch tilt angle – Combined (18mps, 8s, 0.6m).

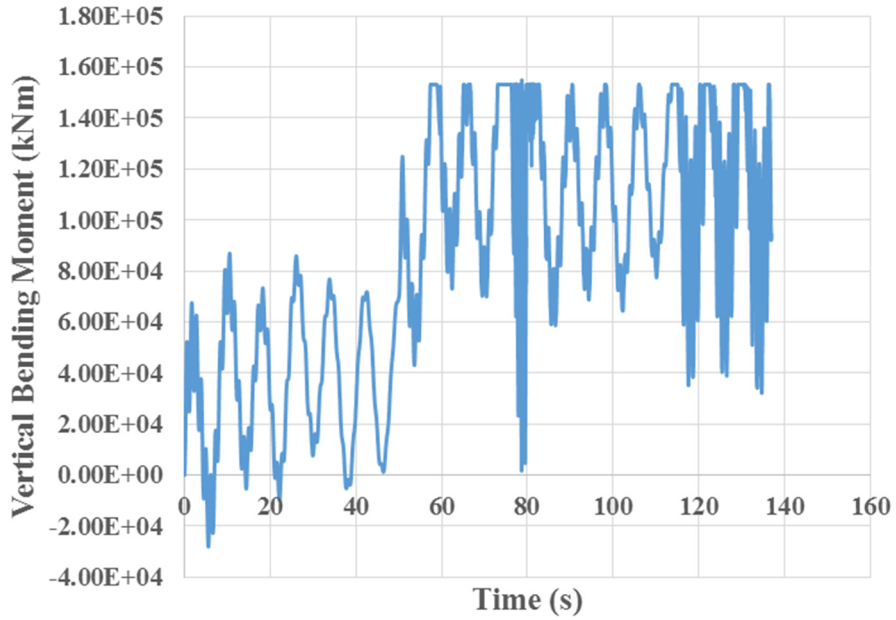

Figure 6.12 Vertical Bending Moment – Combined (18mps, 8s, 0.6m).

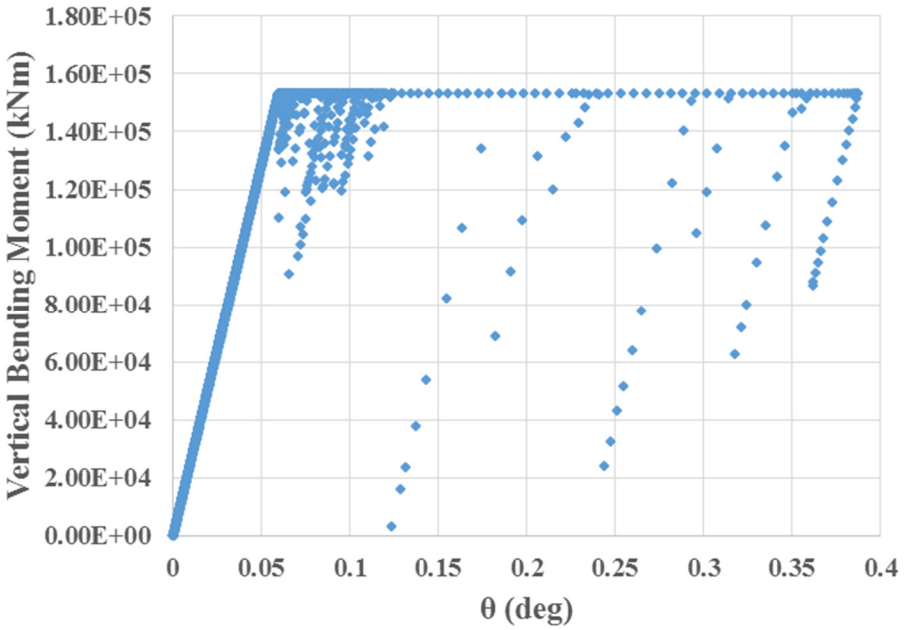

Figure 6.13 Moment-curvature relationship – Combined (18mps, 8s, 0.6m).

We can observe that response for 0.6m wave amplitude is larger than that for the 0.5m wave amplitude. The maximum pitch tilt angle of approximately 2.25degrees is observed from Figure 6.11 and correspondingly slightly larger vertical bending moment. Thus, due to larger response, the collapse extent observed for this case is about 0.4degrees from Figure 6.13 after malfunction of blade pitch control. Similar simulations are carried out for wave amplitude of 0.7m.

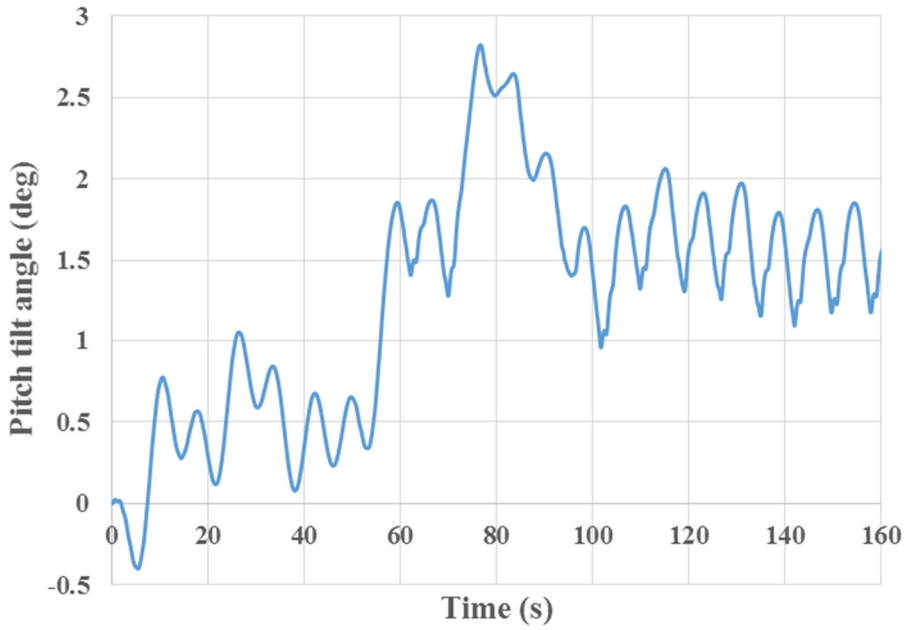

Figure 6.14 Pitch tilt angle – Combined (18mps, 8s, 0.7m).

Figures 6.14, 6.15 and 6.16 shows the pitch tilt angle, vertical bending moment time-series and moment-curvature relationship respectively for the wave amplitude of 0.7m. The maximum pitch tilt angle of approximately 2.75degrees is observed after malfunction. This value is about 0.5degrees larger than for the case of wave amplitude 0.6m. This shows the high sensitivity to wave amplitudes. Correspondingly, the collapse extent of 1.4degrees is observed in this case.

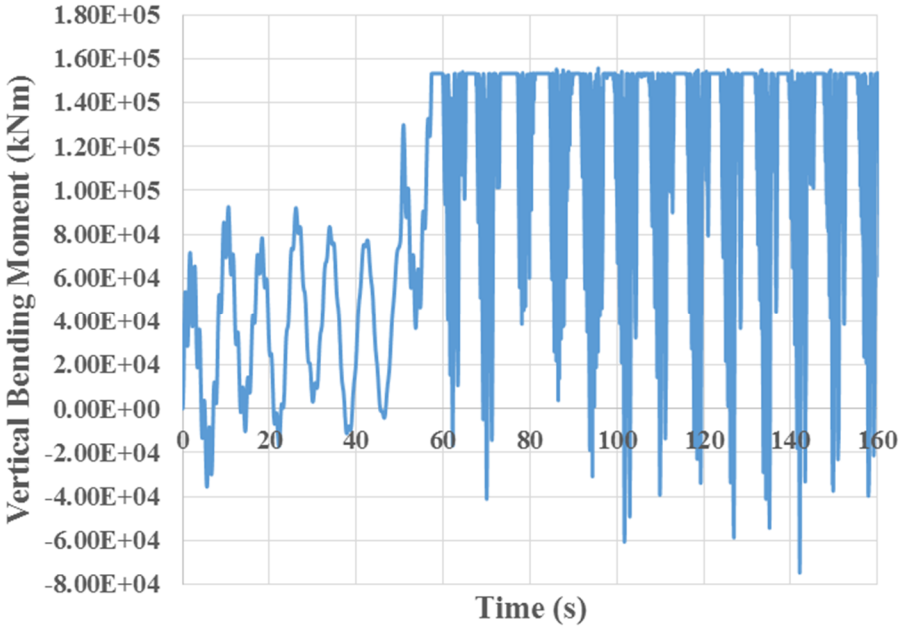

Figure 6.15 Vertical Bending Moment – Combined (18mps, 8s, 0.7m).

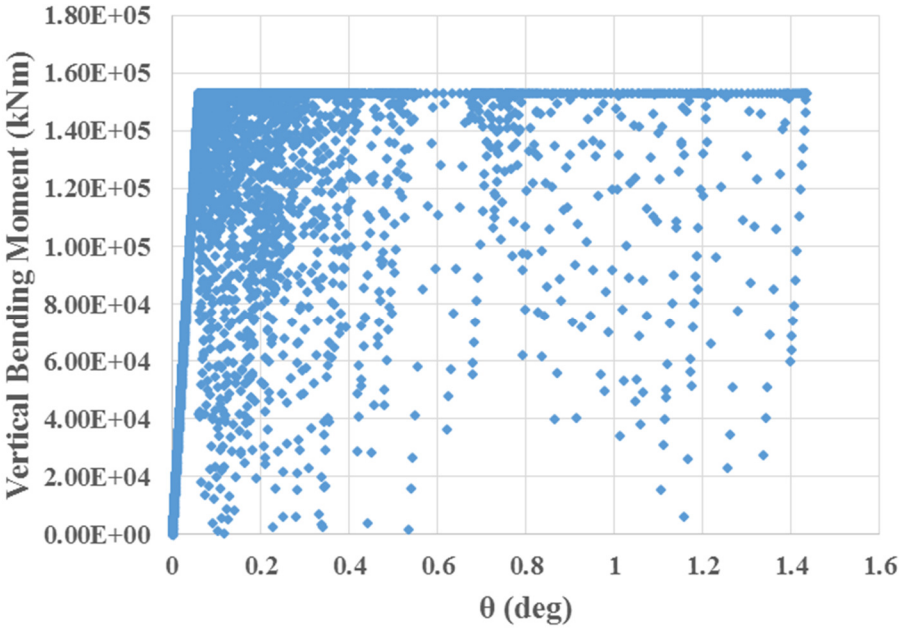

Figure 6.16 Moment-curvature relationship – Combined (18mps, 8s, 0.7m).

Table 6.2 summarizes the influence of wave amplitude for the combined loading condition on the collapse behavior of the FOWT system considered for the steady wind of 18mps and wave period of 8s. It can be observed that the collapse extent increases as wave amplitude increases. Thus, it is important to consider the wave amplitude variation while designing the accidental limit state of FOWT system when subjected to blade pitch control malfunction.

Table 6.2 Influence of wave amplitude – Combined case (Steady wind 18mps).

Wave Period (s)	Wave Amplitude (m)	Maximum pitch angle (deg)	Collapse extent (deg)
8	0.5	2.1	0.1
	0.6	2.25	0.4
	0.7	2.75	1.4

6.2.2 Influence of wave period

This section discusses the influence of varied wave periods on the collapse behavior of FOWT system considered. Steady wind of 18mps and wave amplitude of 0.5m are selected for all the simulations in this section. Figures 6.8 to 6.10 shows the simulation results for wave amplitude of 0.5m and wave period of 8s. Now, let us consider wave periods of 10s and 12s for comparisons.

Figures 6.17, 6.18 and 6.19 shows the pitch tilt angle, vertical bending moment time-series and moment-curvature relationships respectively for the wave period of 10s.

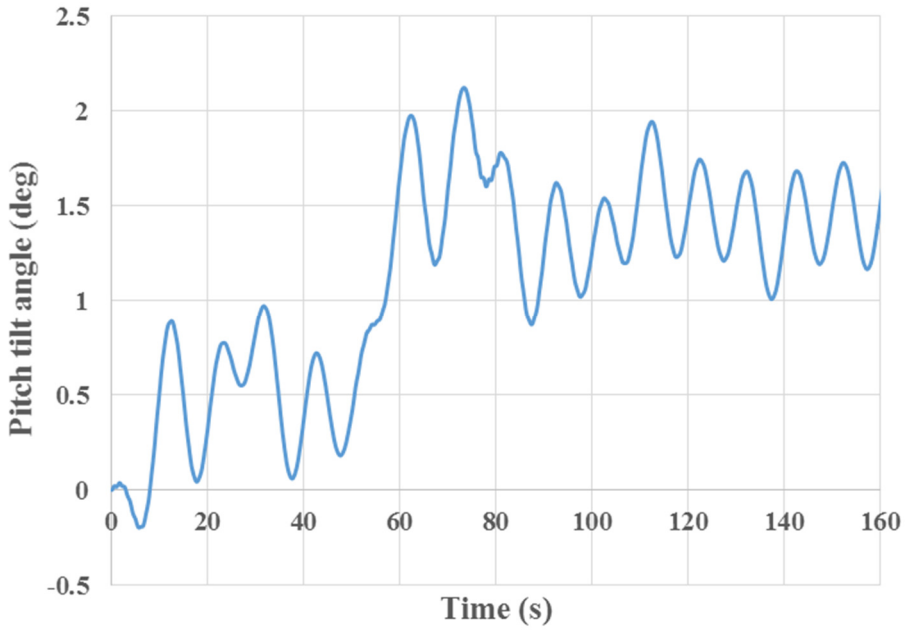

Figure 6.17 Pitch tilt angle – Combined (18mps, 10s, 0.5m).

As expected, the pitch tilt angle increases abruptly after the malfunction at 50s from Figure 6.17. We can observe 6 peaks between 100s and 160s of the simulation which corresponds to the dynamic response due to regular wave of period 10s. Similar dynamic response can also be observed from Figure 6.18.

It can also be confirmed that the maximum pitch tilt angle of 2.1degrees is observed for this combined loading case and collapse extent close to 0.11degrees is obtained as per Figure 6.19.

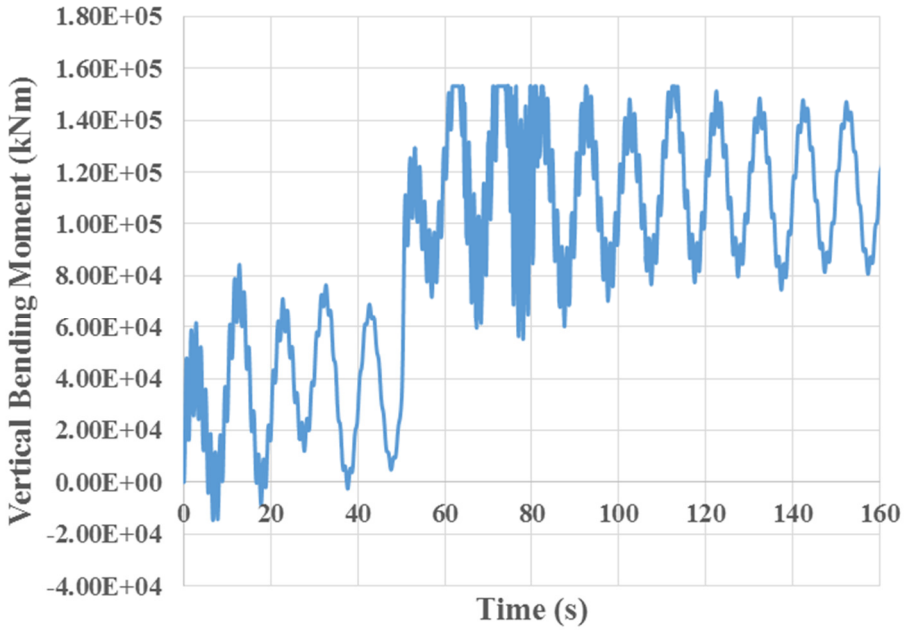

Figure 6.18 Vertical Bending Moment – Combined (18mps, 10s, 0.5m).

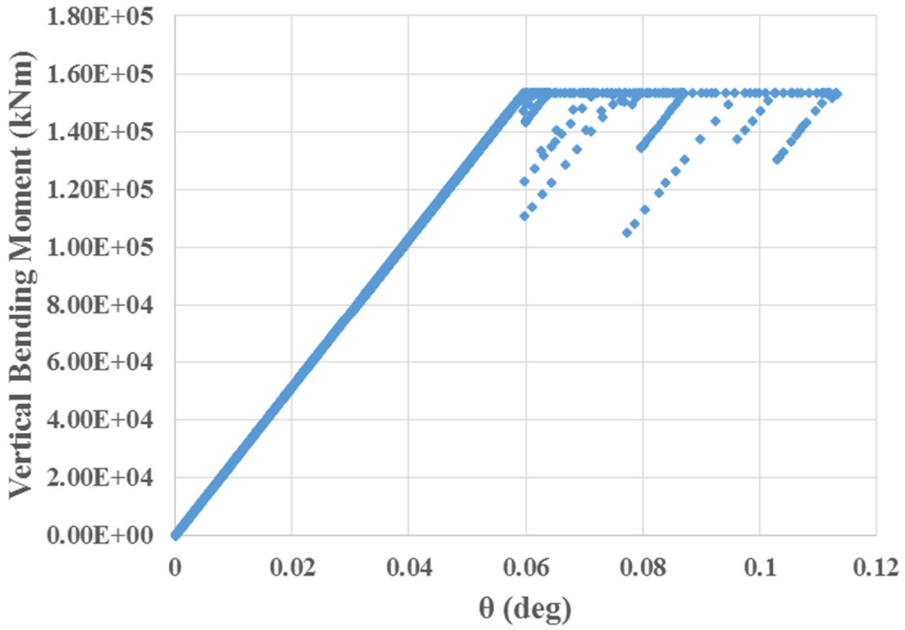

Figure 6.19 Moment-curvature relationship – Combined (18mps, 10s, 0.5m).

Figures 6.20, 6.21 and 6.22 the pitch tilt angle, vertical bending moment time-series and moment-curvature relationships respectively for the wave period of 12s.

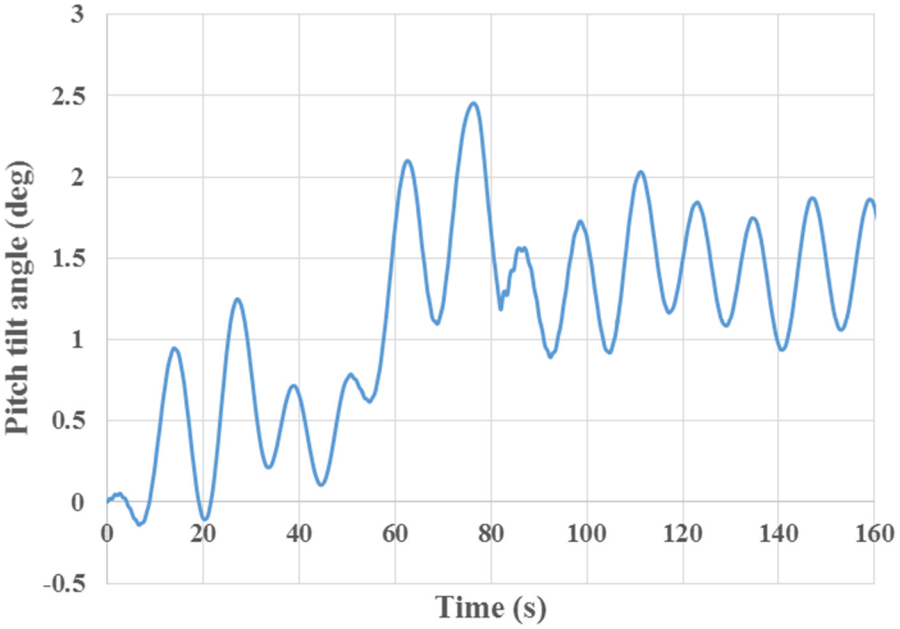

Figure 6.20 Pitch tilt angle – Combined (18mps, 12s, 0.5m).

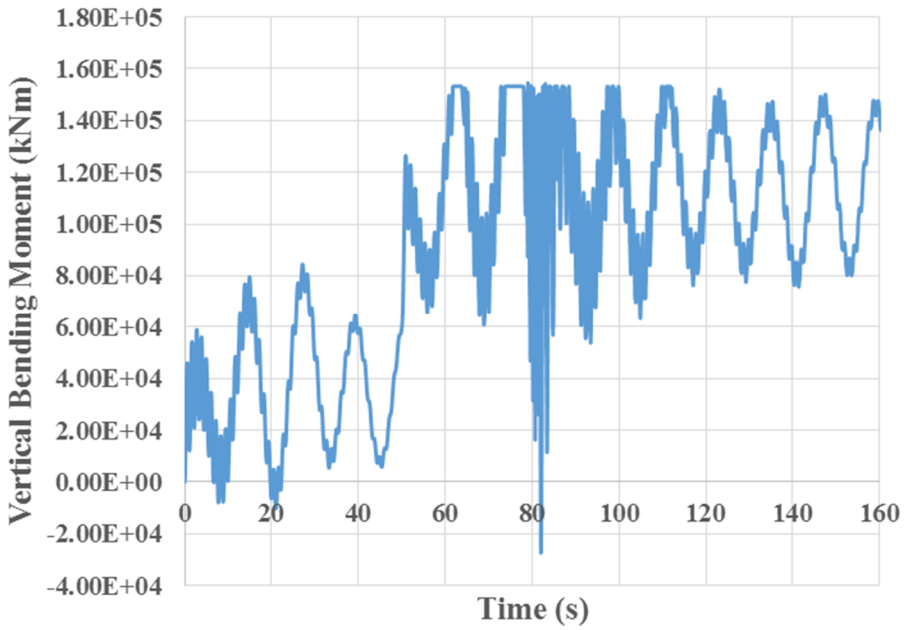

Figure 6.21 Vertical Bending Moment – Combined (18mps, 12s, 0.5m).

As expected, the pitch tilt angle increases abruptly after the malfunction at 50s from Figure 6.20. We can observe 5 peaks between 100s and 160s of the simulation which corresponds to the dynamic response due to regular wave of period 12s. Similar dynamic response can also be observed from Figure 6.21.

It can also be confirmed that the maximum pitch tilt angle of approximately 2.5degrees is observed for this combined loading case and collapse extent close to 0.5degrees is obtained as per Figure 6.22.

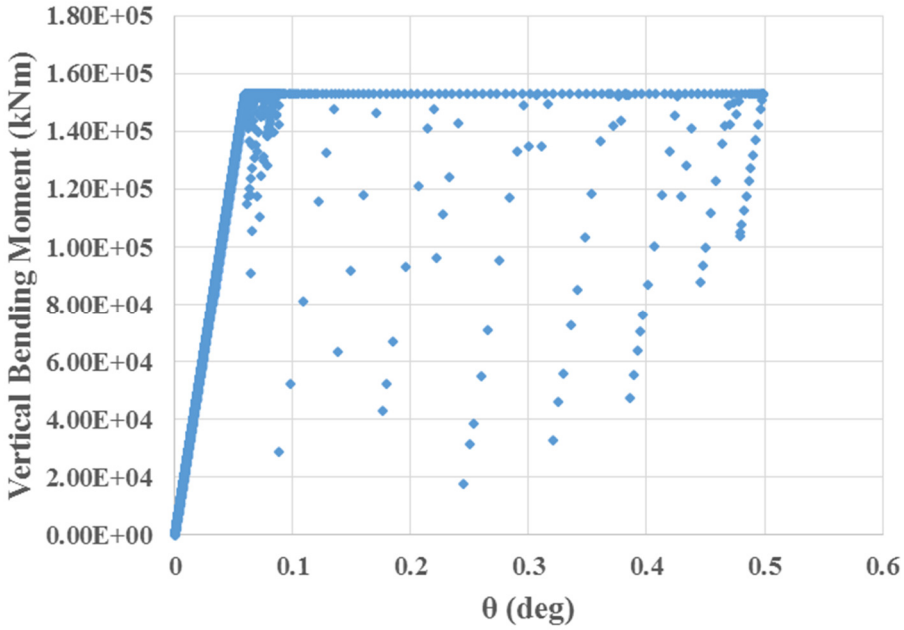

Figure 6.22 Moment-curvature relationship – Combined (18mps, 12s, 0.5m).

Table 6.3 summarizes the influence of wave period for the combined loading condition on the collapse behavior of the FOWT system considered for the steady wind of 18mps and wave amplitude of 0.5m. It can be observed that the collapse extent increases as wave period increases. Thus, it is important to consider the wave period variation while designing the accidental limit state of FOWT system when subjected to blade pitch control malfunction.

Table 6.3 Influence of wave period – Combined case (Steady wind 18mps).

Wave Amplitude (m)	Wave Period (s)	Maximum pitch angle (deg)	Collapse extent (deg)
0.5	8	2.1	0.1
	10	2.15	0.11
	12	2.5	0.5

6.3 Onshore vs Floating platform

Even though the comparison between the onshore and floating platform was performed in Chapter 4, the comparison did not discuss about the collapse behavior. Thus, in this section onshore and floating SPAR models are compared from collapse behavior analysis point of view. Firstly, onshore case is simulated for elastic response behavior by simulating the non-linear rotational spring system (explained in Section 5.2) attached to ground instead of the platform. The response of such a system is obtained and shown in Figure 6.23. The pitch tilt angle as expected must be close to zero. We can also observe tower-rotational spring system vibrations with period of about 1-2 seconds. It is possible to observe the increase in the pitching motion at the tower base even though it is not significant.

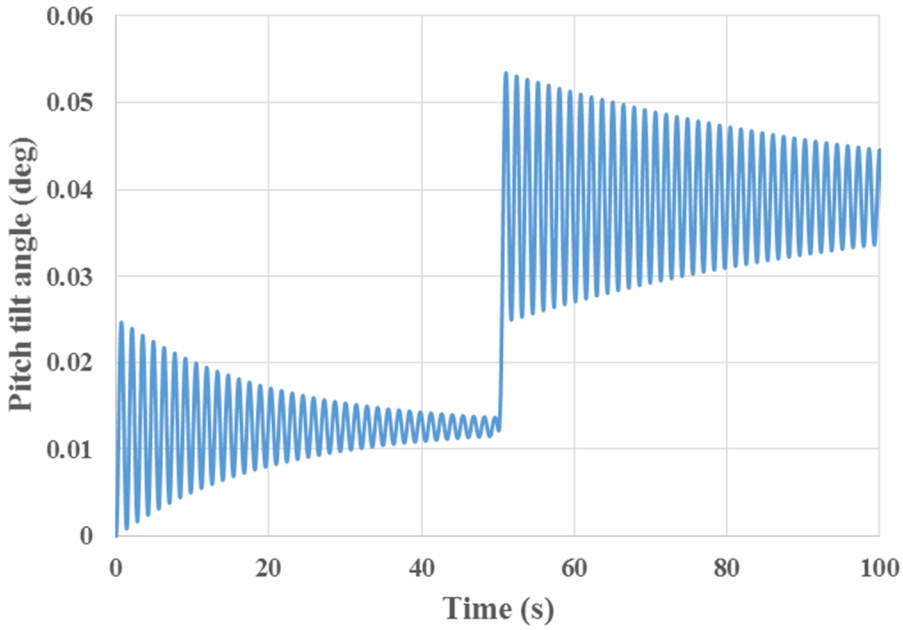

Figure 6.23 Pitch angle at tower base – Onshore – Strength Model 1.

Figure 6.24 shows the vertical bending moment obtained during elastic response for onshore simulation. It is noted that maximum vertical bending moment after malfunction is about 1.37×10^5kN.m. This result is simulated for effective comparison between the onshore and floating SPAR when collapse occurs and therefore the maximum vertical bending moment is adjusted. The same strength models adopted in Section 6.2 will be used for all the comparisons. Figures 6.23 and 6.24 corresponds to strength model 1 and thus response is elastic.

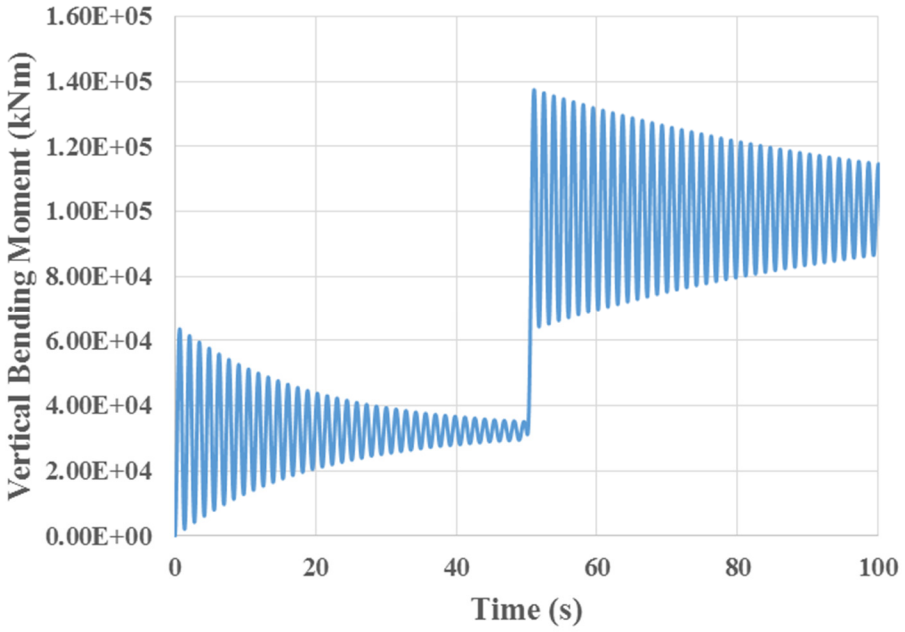

Figure 6.24 Vertical Bending Moment – Onshore – Strength Model 1.

Now, let's adopt strength model 2 and obtain the simulations for the steady wind case of 18mps and then compare onshore and floating SPAR.

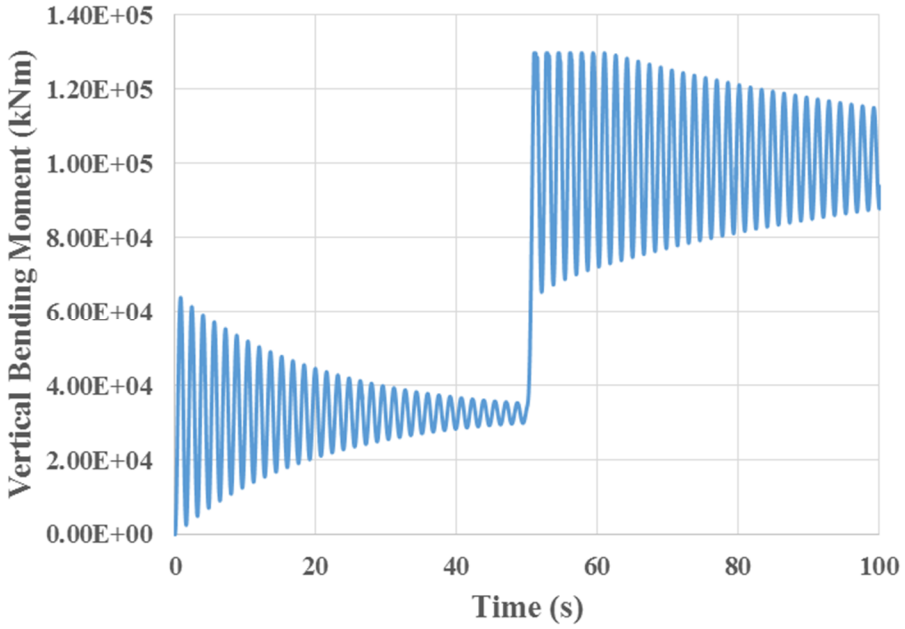

Figure 6.25 Vertical Bending Moment – Onshore – Strength Model 2.

Figure 6.25 shows the partial collapse at the tower base for the onshore case and the corresponding collapse extent is also plotted in Figure 6.26. Since the collapsing moment for strength model 2 is less than the maximum vertical bending moment developed due to malfunction, we can observe

the collapse around 50s to 55s of the simulation. The collapse extent of 0.07degrees is observed from Figure 6.26.

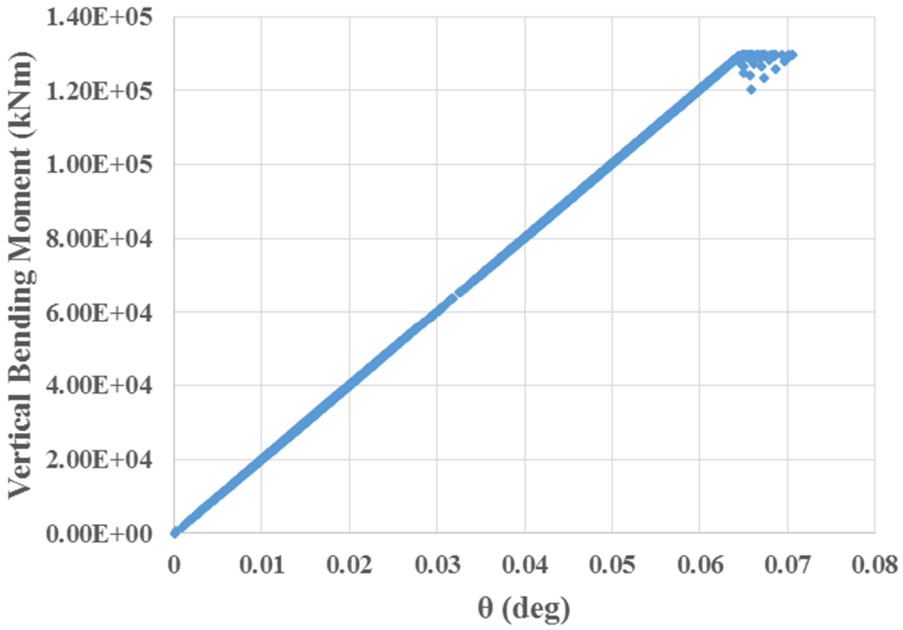

Figure 6.26 Moment-curvature relationship – Onshore – Strength Model 2.

Now, for the same strength model 2, the vertical bending moment time-series is simulated which is shown in Figure 6.27. The rigid body motion of the floater is reflected in this simulation and collapse occurrence between 75s and 80s is also clear. Figure 6.28 is obtained to find out the elastic-plastic response and collapse extent of 0.07 degrees can be observed. This value is almost close to the one obtained for onshore.

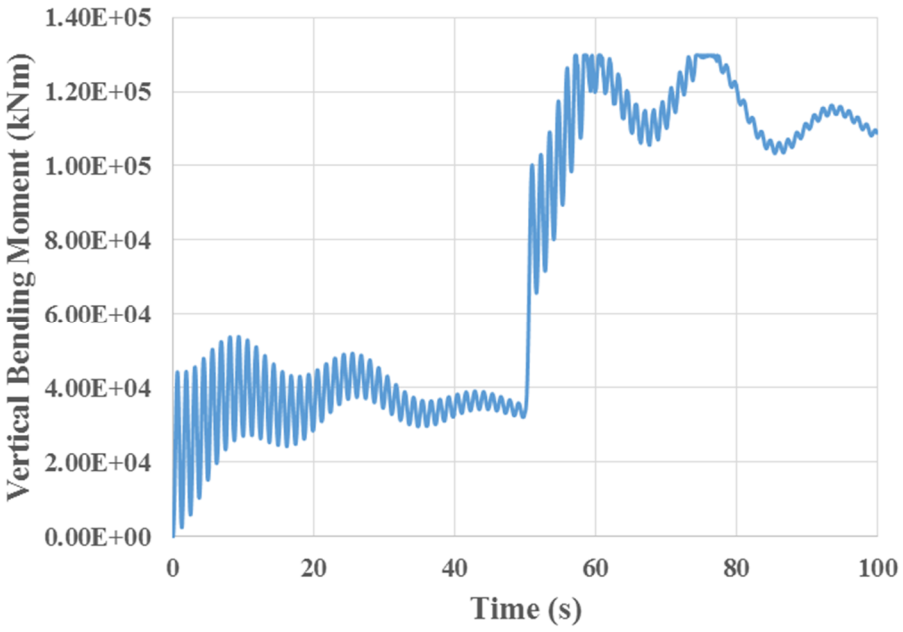

Figure 6.27 Vertical Bending Moment – Floating SPAR – Strength Model 2.

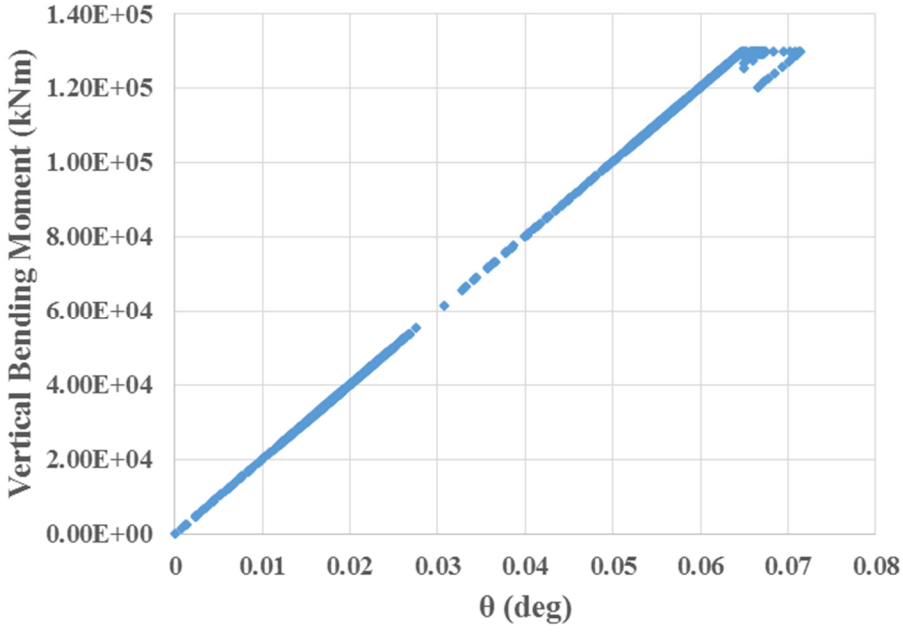

Figure 6.28 Moment-curvature relationship – Floating SPAR – Strength Model 2.

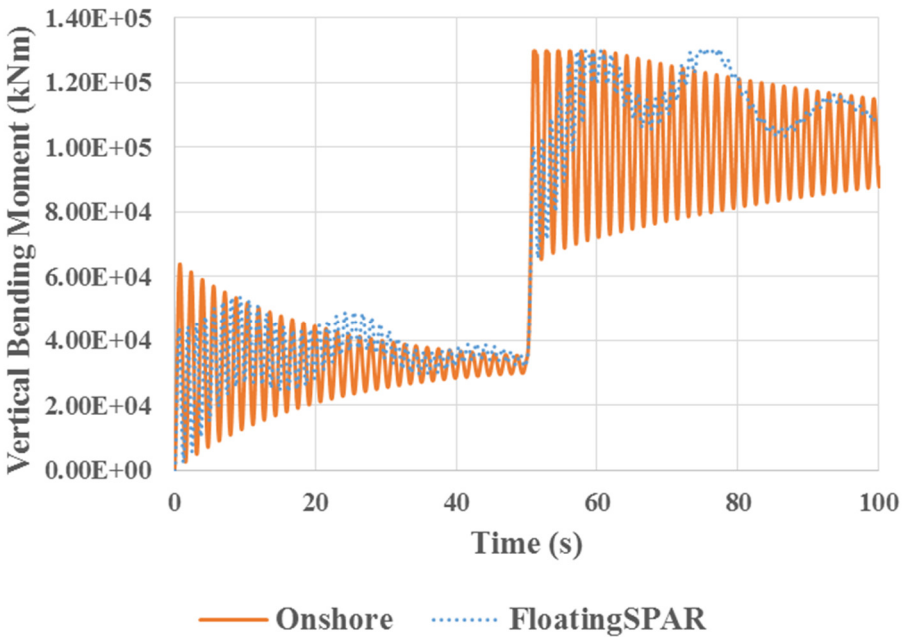

Figure 6.29 Vertical Bending Moment – Onshore vs Floating SPAR – Strength Model 2.

Both onshore and floating are compared in Figure 6.29. The time duration at which the bending moment takes maximum value is different between the onshore and floating SPAR. However the maximum value of vertical bending moment and collapse extent is same for the onshore and floating SPAR cases. The onshore case is dominated by tower-rotational spring system vibrations and in floating SPAR case is dominated by rigid body motion of the floater.

Further comparisons by adopting strength model 3 is carried out and onshore and floating SPAR are compared. The onshore vertical bending moment and moment-curvature relationship is shown in Figures 6.30 and 6.31 respectively when strength model 3 is adopted in the simulation.

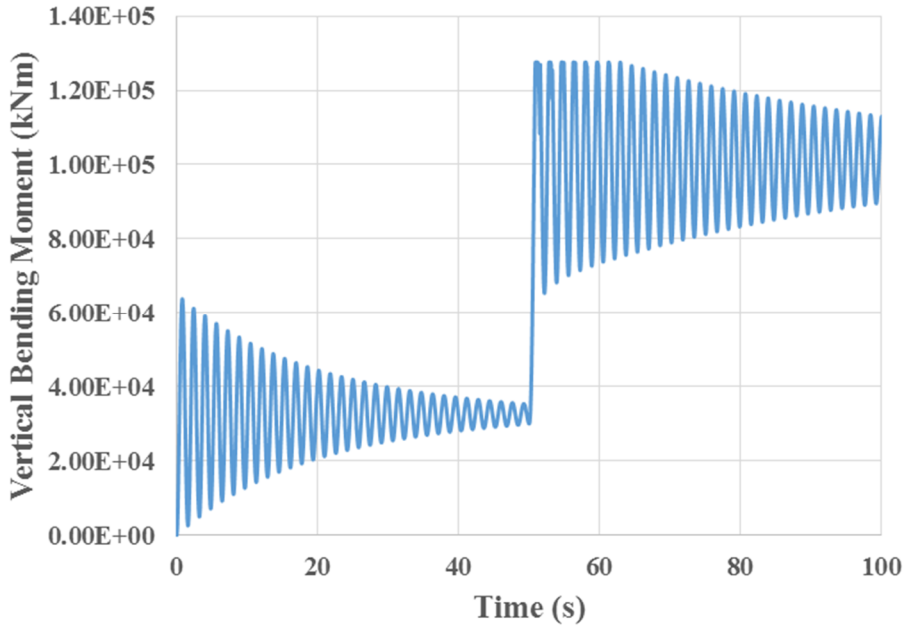

Figure 6.30 Vertical Bending Moment – Onshore – Strength Model 3.

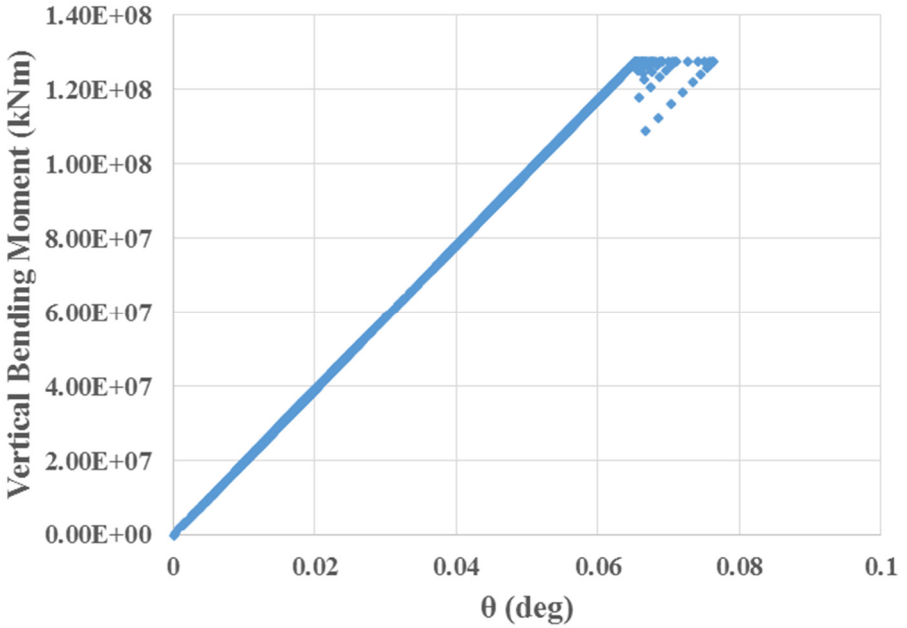

Figure 6.31 Moment-curvature relationship – Onshore – Strength Model 3.

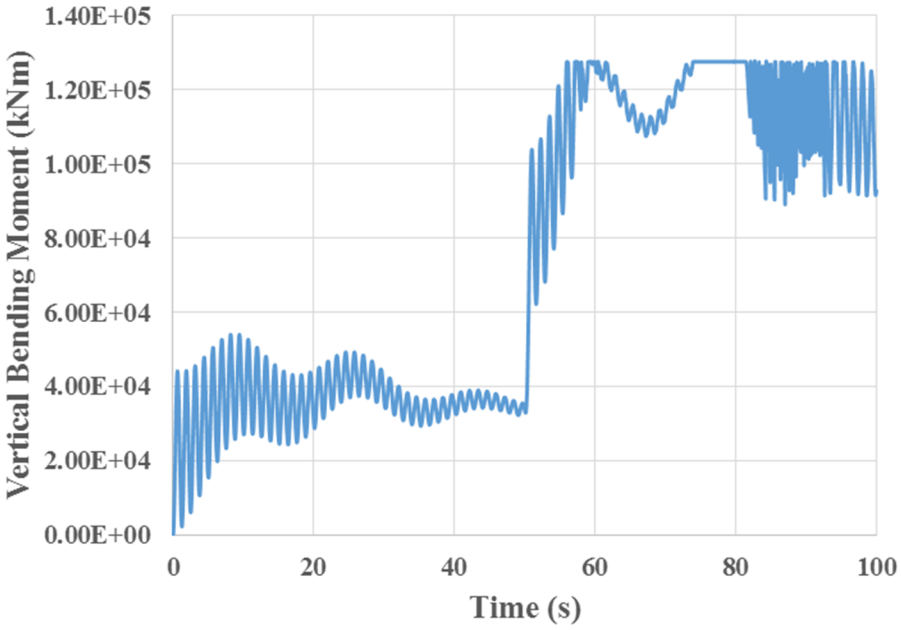

Figure 6.32 Vertical Bending Moment – Floating SPAR – Strength Model 3.

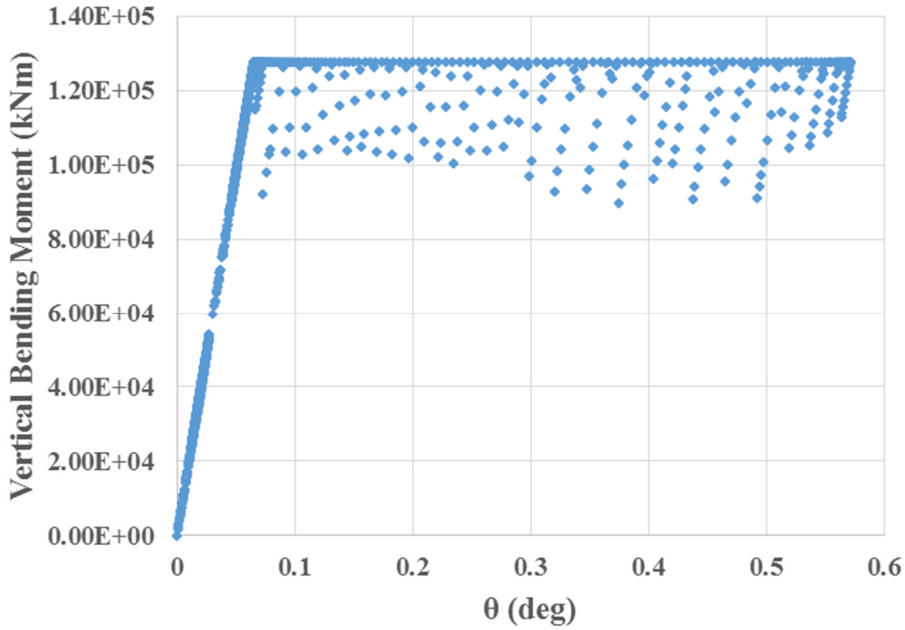

Figure 6.33 Moment-curvature relationship – Floating SPAR – Strength Model 3.

The strength model 3 simulations for the floating SPAR are shown in Figures 6.32 and 6.33. The collapse extent as previously observed is 0.55degrees. However this value for onshore is not changed much for the onshore (0.07degrees both the cases). This owes to the fact that the duration of the vertical bending moment taking maximum value in case of floating SPAR is longer than that for the onshore case. This difference is due to the rigid body motion of the floating platform. Hence it is important to evaluate the risk associated with blade pitch control malfunction for the

case of FOWT systems carefully. The present results of strength model 3 shows that the blade pitch control malfunction may have more severe consequences for floating platform than for the onshore case.

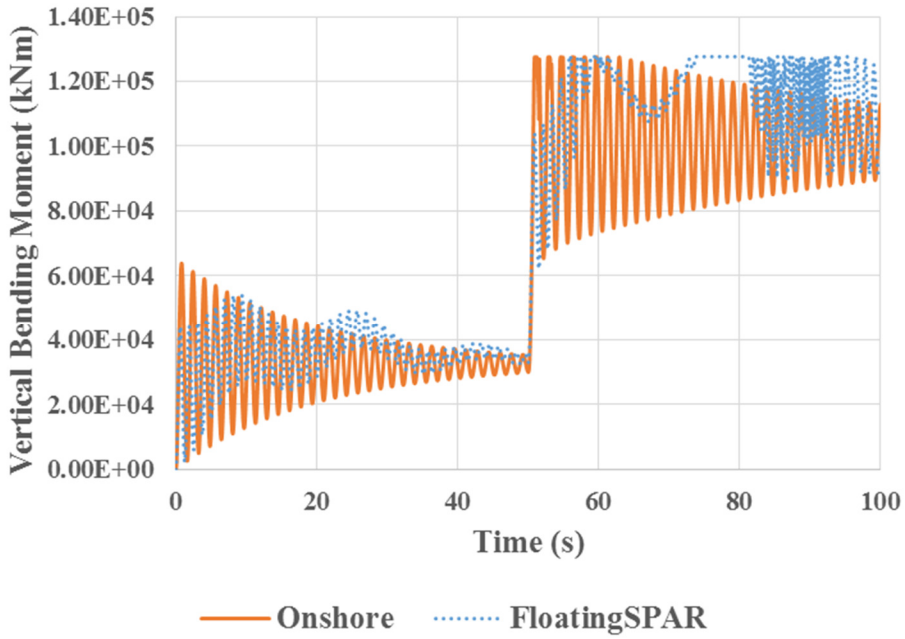

Figure 6.34 Vertical Bending Moment – Onshore vs Floating SPAR – Strength Model 3.

Figure 6.34 shows the comparison for onshore and floating SPAR for the strength model 3. It can observed that the collapse pattern is quite different for floating SPAR than the onshore. The collapse is induced by rigid body motions and pitch tilt angle in case of the floating SPAR and for onshore it is dominated mainly by tower vibrations. Thus, this needs to be kept in mind while designing the scantlings for the tower structure of FOWT systems. Adequate strength with safety margin has to be given for strengthening the main structure for the extreme condition and accidental load due to malfunction of blade pitch control. This would be an important and necessary guideline for accidental limit state for FOWT systems [55]. Table 6.4 summarizes the onshore vs floating platform comparisons for the collapse behavior of FOWT systems.

Table 6.4 Comparison of onshore vs floating platform – Only Wind (18mps).

Capacity	Diameter of cross-section (m)	Collapse extent (deg)	
		Onshore	Floating SPAR
Strength Model 1	6.3	No collapse	No collapse
Strength Model 2	5.8	0.07	0.07
Strength Model 3	5.75	0.07	0.55

6.4 Conclusions

This chapter discussed the collapse behavior of the SPAR type FOWT system considered from the parametric dependencies point of view for effective understanding of the designers while considering malfunction related challenges. The following specific conclusions can be deduced for the analyzed model.

5) The collapse extent which is used as a measure of collapse behavior at the tower base showed that it is highly sensitive to the environmental conditions and might lead to an altogether different type of collapse if the environmental conditions change.

6) The collapse extent is found to increase with the increasing wave amplitudes and wave periods. The influence of increased wave period and increased wave amplitude for the similar characteristics of strength models showed the parametric sensitivity of wave amplitude and wave period for the collapse of FOWT systems.

7) The collapse extent of 0.55 degrees is found for the floating SPAR case as compared to 0.07 degrees for onshore case for the same strength model. This concludes that the floating platform collapses larger than the onshore case for the similar environmental and strength conditions.

The present chapter was focused on elastic-plastic behavior analysis of FOWT systems subjected to blade pitch control malfunction and highlighted the various parameter dependencies and their behavior to the collapse of FOWT systems. The coupled simulation code is adopted for elastic-plastic behavior analysis which predicts the response in both elastic and plastic regions. Chapter 7 concludes the findings of this study.

7 Conclusions

In this study, a numerical simulation code for the response of FOWT (Floating Offshore Wind Turbine) is addressed. A holistic analysis methodology for a coupled system consisting the main floater, tower, rotor, blades and blade pitch control, is developed. The developed methodology considers hydrodynamics, aerodynamics and control for understanding the response of the FOWT systems under the combined loading of wind and wave. The coupled simulation tool is found to be effective to predict the combined response.

A hydrodynamic time-domain code, named as DYNABEAM is coupled with FAST, an aerodynamic code simulator using a weakly coupled algorithm. The coupling strategy to incorporate the floater dynamics, rotor dynamics and control is found to be effective for understanding the overall response of FOWT systems as one package. The floater is modelled as an elastic frame structure consisting of hull and beam elements and hydrodynamic evaluation for the main floater is made by using linear potential theory. Blade element momentum theory is adopted to evaluate the aerodynamic loads. Weakly coupling methodology is employed to obtain the interaction behavior between the floater, tower and rotor-nacelle assembly. The coupling process works fine for the models designed and considered for analysis.

To confirm the validity of the proposed time-domain coupled numerical model, the simulation results are compared against well-established OC3 project model provided by NREL. OC3-Hywind spar model is selected for this purpose and the spar is remodeled in DYNABEAM. Not only the heave motion and pitch motion (symmetric motions) of floater but also the roll and yaw motions (non-symmetric motions) are compared between the simulation results and OC3 model results. The flexibility feature of floater is also demonstrated.

The coupled simulation tool proved to be useful when the overall structural response has to be evaluated considering flexibility of the floater and tower. This is demonstrated by preparing two structural models having flexible tower and foundation, one with flexible floater foundation and other with rigid floater foundation. The structural response due to the flexibility of floater is found to affect the structural load in terms of increased natural period by about 10% when evaluated against the rigid modeling of floater.

After the validation and proving the flexibility feature of the numerical model, blade pitch control malfunction is investigated. Blade pitch control malfunction is incorporated into the coupled simulation tool and simulated abruptly in time-series and response to an accidental event of malfunction is evaluated. It is found out that, due to malfunction of blade pitch control the rotor thrust increases abruptly. This results in increased structural bending moment measured at the tower base. This increased structural load causes the structure of collapse if adequate safety factor is not provided against the malfunction of blade pitch control. The numerical simulation using experimental data and similar tendency is observed and the tool is qualitatively validated.

Finally, elastic-plastic behavior analysis methodology is developed adopting coupled simulation code which considers the flexibility of the floater and blade pitch control malfunction. The simulation tool is found to be useful to obtain the combined response of wind and wave for FOWT systems considered. The collapse performance of a SPAR platform under blade pitch control malfunction is evaluated and it is found to be an effective methodology from structural point of view for clarifying the behavior under accidental limit state. The elastic-plastic behavior analysis is carried out and demonstrated for the various environmental conditions and parametric dependencies for collapse behavior of SPAR FOWT system is understood.

Finally, the following specific conclusions of the thesis can be derived:

- Pitch tilt angle of about 2 degrees is observed for the redesigned flexible model of OC3 Hywind spar in DYNABEAM, utilized for validation. This prediction is the result of rotor thrust developed for a steady wind of 7mps and the value is found to be in good agreement with the established offshore design model OC3-Hywind spar provided by FAST.

- Validated methodology employed proved to be effective and valid to accommodate combined loading. Thus, this holistic coupling methodology can be extended for various types of FOWT systems.

- It was also shown that there is a good agreement in roll and yaw motions. Even though such motions are non-symmetric motions, a good agreement is obtained using the developed coupled simulation tool.

- Collective pitch malfunction which may be too severe and an extreme event, was adopted as part of accidental limit state study. It is found that there is an increase of rotor thrust due to the assumed blade pitch control malfunction by about 2.5 times than that of the controlled case for steady wind speed of 18mps for the NREL 5MW wind turbine considered.

- The performance of both the designed floater models, SPAR and semi-submersible is found to be similar while predicting malfunction behavior and maximum tower-base vertical bending moment evaluated is almost comparable. Thus it can be concluded that the malfunction behavior definitely affects the structural loads for various types of FOWT systems. It is thus desirable to evaluate the performance of various FOWT systems due to blade pitch control malfunction.

- It is found that there is an increase of vertical bending moment due to malfunction of blade pitch control, the resulting increased thrust and dynamic amplification. The level of the increase between the floating SPAR and onshore as well as the time duration during which vertical bending moment takes maximum value is different. The onshore case takes maximum value of bending moment soon after malfunction whereas the floating SPAR

model takes maximum bending moment later based on rigid body motions of the floater. After malfunction, onshore is dominated by high frequency tower structural vibrations whereas the floating case has relatively low frequency floater structural vibrations.

- It can be concluded that abrupt change of thrust induces tower flexible modes in onshore wind turbines while rigid body motions are dominant for FOWT systems. The SPAR platform performance showed that the rigid body motions of the floater dominate for the case of FOWT systems.

- The floater dynamics is found to affect the maximum tower-base vertical bending moment and a larger thrust load is predicted than the one obtained by the thrust curve under the assumed collective blade pitch control malfunction. When predicting the maximum load after the malfunction, the dynamic analysis will be necessary.

- Elastic-plastic behavior analysis conclusively evaluates the response of the FOWT systems considered in both elastic and plastic regions. The methodology adopted in this study is found to be effective while predicting both elastic and plastic responses.

- The tower structure collapses and falls down completely when it is subjected to extreme vertical bending moment exceeding the ultimate strength capacity by about 5%. This indicates that the tower collapse may occur immediately when the maximum vertical bending moment exceeds the capacity of the structure. For design, it is then necessary to give a sufficient safety margin to the tower structural strength against the extreme structural load due to floater dynamics.

- The collapse extent which is used as a measure of collapse behavior at the tower base showed that it is highly sensitive to the environmental conditions (such as wind, wave) and might lead to an altogether different type of collapse if the environmental conditions change.

- The collapse extent is found to increase with the increasing wave amplitudes and wave periods. The influence of increased wave period and increased wave amplitude for the similar characteristics of strength models showed the parametric sensitivity of wave amplitude and wave period for the collapse of FOWT systems.

- For a given magnitude of maximum vertical bending moment, collapse extent of 0.55 degrees is found for the floating SPAR case as compared to 0.07 degrees for onshore case under the same strength model. This is due to the difference in time duration of structural vertical bending moment exceeding the collapsing moment for SPAR and onshore cases. This concludes that the floating platform collapses larger than the onshore case for the similar environmental and strength conditions. This means that the collapse behavior for FOWT systems is more critical than for onshore cases.

Future works may be indicated as follows. Even though the proposed methodology has been proved for predicting the response FOWT system in both elastic and plastic regions, coupling the present model with non-linear effects of mooring may be necessary especially when the non-linear surge motion becomes dominant. Besides, the validation work for blade pitch control malfunction should be performed by conducting some more model tests. In this study, an extreme event of collective pitch control, with one second of ramp for the abrupt termination is considered. The response behavior could be varied if we adopt different control strategies and it is important to investigate such response behavior. It is also important to consider the consequence of failure events such as blade hitting the tower, blade brake failure and tower collapse. Therefore for the design of FOWT systems, strategy design of control is requisite which could be redesigned based on ultimate and fatigue strengths in the future. It is also important to consider various other FOWT systems consisting of different floaters such as semi-submersible, TLP, barge to arrive at general and specific conclusions for collapse behavior of FOWT systems. From the viewpoint of risk evaluation for accidental limit state, more realistic capacity curves for analyzing the structural post-ultimate strength behavior under extreme condition is also an interesting research topic.

Acknowledgements

First and foremost, I would like to convey my deepest gratitude and thanks to my supervisor and mentor, Associate Professor Kazuhiro Iijima for his patience, constant encouragement, enthusiasm, and the vast knowledge base he provided me with during my entire 5 years graduate student life in Osaka University.

I also want to express my heartfelt thanks to Professor Masahiko Fujikubo, for inspiring me with the research sprite and kindness and giving me an opportunity to study in Osaka University. Under his supervision, I could understand the responsibility of a world-class researcher and leader, which will help me guide through my life no matter what I will do in the future.

A very special thanks goes out to Professor Naoki Osawa and Professor Hiromichi Akimoto, both of whom reviewed, commented and gave insights to my doctoral thesis with one hundred percent sincerity.

I am very grateful to Professor Yasunori Nihei and Professor Naoyuki Hara, for providing much needed expert guidance and high-level experimental data without which the validation work would not have been possible.

I want to express my thanks to assistant professor, my good friend, Mr. Tatsumi, for his warm help during my study and daily life with whom I shared the research space for one full year.

I highly appreciate the consistent assistant from the laboratory secretary, Miss Ohkita. I also wish to acknowledge all the students in Ship structural integrity laboratory for their help. It has been a great journey learning with you.

I would also like to acknowledge all the professors in my department who gave expert lectures and also my professors back in India who laid foundation for my study. Without the knowledge I learned, it would have been impossible to complete this thesis.

The financially support from the Japanese Government (MONBUKAGAKUSHO: MEXT) scholarship is gratefully acknowledged.

I am grateful to the Mother Nature to bless me with good friends for life I made in Osaka. Their unmatched support and guidance is acknowledged.

Last but not the least, I would like to thank my family, my parents and my ever inspiring brother for their unconditional love and support through my entire life. I must acknowledge my dear companion, Darshani, who has been with me every step of the way.

References

[1] E. W. E. Association, “Deep water: The next step for offshore wind energy”, 2013.

[2] N. Armaroli and V. Balzani, Powering Planet Earth: Energy Solutions for the Future, 2012.

[3] “Offshore Wind Energy,” Environmental and Energy Study Institute, 2010.

[4] Wikipedia “http://en.wikipedia.org/wiki/Offshore_wind_power,” [Online].

[5] A. Smith, T. Stehly and W. Musial, “2014-2015 Offshore Wind Technologies Market Report,” Technical Report NREL/TP-5000-64283, September 2015.

[6] Deepwater Wind “http://dwwind.com/,” [Online].

[7] W. Musial, S. Butterfield and A. Boone, "Feasibility of Floating Platform Systems for Wind Turbines," the 23rd ASME Wind Energy Symposium, Reno, Nevada, January 5–8, 2004.

[8] C. Watanabe, “http://www.bloomberg.com/news/articles/2012-03-29/floating-windmills-in-japan-help-wind-down-nuclear-power-energy”, 2012 [Online].

[9] Carbon Trust, “Appraisal of the Offshore Wind Industry in Japan”, 2014

[10] T. Ishihara, “Fukushima Floating Offshore Wind Farm Fukushima Floating Offshore Wind Farm Demonstration Project”.

[11] Ishihara T, “Fukushima Floating Offshore Wind Farm Demonstration Project (Fukushima FORWARD),” Fukushima Offshore Wind Consortium, 2015.

[12] Utsunomiya T, Shiraishi T, Sato I, Inui E and Ishida S, “Floating offshore wind turbine demonstration project at Goto Islands, Japan,” OCEANS 2014 – Taipei, ISBN 978-1-4799-3645-8, IEEE, April 2014.

[13] B. Bulder and et al, “Study to Feasibility of and Boundary Conditions for Floating Offshore”, ECN, MARIN, TNO, TUD, MSC, Lagerway the Windmaster, 2002.

[14] K. H. Lee, "Responses of Floating Wind Turbines to Wind and Wave Excitation," MSc Thesis. University of Michigan, 2005.

[15] E. N. Wayman, P. D. Sclavounos, S. Butterfield, J. Jonkman and W. and Musial, "Coupled Dynamic Modeling of Floating Wind Turbine Systems," 2006 Offshore Technology Conference, 1–4 May 2006, Houston, May 2006.

[16] E. Wayman, "Coupled Dynamics and Economic Analysis of Floating Wind Turbine Systems," M.S. Dissertation, Department of Mechanical Engineering, Massachusetts Institute of Technology, Cambridge, MA, USA, June 2006.

[17] Z Gao, “Offshore Renewable Energy,” 19th International Ship and Offshore Structures Congress (ISSC), 7-10 September 2015.

[18] A. Robertson, "Offshore code comparison collaboration continuation within iea wind task 30: phase ii results regarding a floating semisubmersible wind system," Proceedings of 33th International Conference on Offshore Mechanics and Arctic Engineering OMAE2014, pp. OMAE2014-24040, 8–13 June 2014.

[19] Y. Bae and M. Kim, "Coupled dynamic analysis of multiple wind turbines on a large single floater," Ocean Engineering, 2014.

[20] E. E. Bachynski and T. Moan, "Design considerations for tension leg platform wind turbines," Marine Structures, 2012.

[21] T. Ishihara, K. Kagaya and Y. Kikuchi, "Water tank experiment and dynamic analysis of floating offshore wind turbine system considering combined hydrodynamic loadings," Proceedings of the 35th wind energy symposium, 2013.

[22] Caithness Windfarm Information Forum 2015: Summary of Wind Turbine Accident data to 31 December 2015 (www.caithnesswindfarms.co.uk), December 2015.

[23] Riso DTU: Final report on investigation of a catastrophic turbine failures, February 22 and 23, 2008, December 2008.

[24] SEATEC: Accident analysis report on the 19th wind turbine at Wind Park Kasatori (in Japanese), June 2013.

[25] The Irish News: Blade control fault blamed for wind turbine collapse at County Tyrone in Northern Ireland, February 2013.

[26] Jonkman J and Marshall B, “FAST User’s Guide”, Technical Report, NREL/EL-500-38230, August 2005.

[27] IEC/TS 61400-13 ed. 1 “Wind Turbine Generator Systems – Part 13: Measurement of Mechanical Loads.” International Electrotechnical Commission (IEC), 2001.

[28] Buhl Jr., M.L. “A Simple Mode-Shape Generator for Both Towers and Rotating Blades.” *NWTC Design Codes (Modes)*, http://wind.nrel.gov/designcodes/preprocessors/modes/. Last modified April 29, 2002; accessed July 9, 2002.

[29] Laino, D.J.; Hansen, A.C. “User’s Guide to the Wind Turbine Dynamics Computer Software AeroDyn.” Salt Lake City, Utah: Windward Engineering, LC, August 2001.

[30] Moriarty, P.J. and Hansen, A.C. “AeroDyn Theory Manual”, Technical Report, NREL/TP-500-36881, January 2005.

[31] Leishman, J.G and Beddoes, T.S. "A Generalized Model for Airfoil Unsteady Behavior and Dynamic Stall Using the Indicial Method." Proceedings from the 42nd Annual Forum of the American Helicopter Society, Washington, DC, pp. 243-266, 1986.

[32] Leishman, J.G and Beddoes, T.S, "A Semi-Empirical Model for Dynamic Stall." Journal of the American Helicopter Society, 34 (3), pp. 3-17, 1989.

[33] Glauert, H. "Airplane Propellers." Aerodynamic Theory (W. F. Durand, ed.), Div. L, Chapter XI. Berlin: Springer Verlag, 1935.

[34] Leishman, J.G. "Principles of Helicopter Aerodynamics." Cambridge University Press, pp. 78-127, 2000.

[35] Manwell, J.F.; McGowan, J.G.; Rogers, A.L. "Wind Energy Explained: Theory, Design and Application." New York: John Wiley & Sons, 2002.

[36] Burton, T.; Sharpe, D.; Jenkins, N.; Bossanyi, E. "Wind Energy Handbook," New York: Wiley & Sons, 2001.

[37] Kane, T.R. and Levinson, D.A.; "Dynamics: Theory and applications", McGraw-Hill Book Company, 1985.

[38] Ma C, Iijima K and Nihei Y, "Strongly Coupled Method for Predicting the Response of Flexible FOWT With Mooring and its Experimental Validation", Proceedings of ASME 2014, 33rd International Conference OMAE2014-24625.

[39] Kochiro Yoshida, Massahiko Osaki, "A Dynamic Response Analysis Method of Tension Leg Platforms Subjected to Waves", Journal of the Faculty of Engineering, the University of Tokyo, Vol.XXXVII, No.4, 1984.

[40] Iijima K, Kawai M, Nihei Y, Murai M and Ikoma T, Conceptual Design of a Single-Point-Moored FOWT and Tank Test for Its Motion Characteristics, Proceedings of ASME 2013, 32nd International Conference OMAE2013-11259.

[41] Sharath S, Iijima K and Fujikubo M, "Development of Coupled Simulation between FAST and Hydro-Structural Code for FOWT", Proceedings of JASNAOE Spring Meeting, 2015S-OS1-10, May 2015.

[42] Chong Ma, Misako Kawai, Kazuhiro Iijima, Tomoki Ikoma, Yasunori Nihei, Motohiko Murai, "Experimental Study on New Design for FOWT with SPM System", Annual Spring Meeting, The Society of Naval Architects of Japan, 2013.

[43] Jonkman J, Butterfield S, Musial W and Scott G, "Definition of a 5-MW Reference Wind Turbine for Offshore System Development", Technical Report, NREL/TP-500-38060, February 2009.

[44] Jonkman J. and Musial W., "Offshore Code Comparison Collaboration (OC3) for IEA Task 23 Offshore Wind Technology and Deployment", Technical Report, NREL/TP-5000-48191, December 2010.

[45] Lee C.H, "WAMIT Theory Manual", Massachusetts Institute of Technology, Report No. 95-2, October 1995.

[46] Sharath S., Iijima K. and Fujikubo M., "Coupled Simulation between FAST and Hydro-Structural Code for a Floating Offshore Wind Turbine and its validation", Proceedings of the 23rd Ocean Engineering Symposium, JFOES and JASNAOE, August 2015.

[47] REpower Systems, "Repower 5M" (Online Publication), January 4, 2005, http://www.repower.de/typo3/fileadmin/download/produkte/5m_uk.pdf

[48] Kooijman, H. J. T., Lindenburg, C., Winkelaar, D., and van der Hooft, E. L., "DOWEC 6 MW Pre-Design: Aero-elastic modeling of the DOWEC 6 MW pre-design in PHATAS," DOWEC Dutch Offshore Wind Energy Converter 1997–2003 Public Reports [CD-ROM], DOWEC 10046_009, ECN-CX--01-135, Petten, the Netherlands: Energy Research Center of the Netherlands, September 2003.

[49] Hansen, M. H., Hansen, A., Larsen, T. J., Φye, S., Sørensen, and Fuglsang, P., "Control Design for a Pitch-Regulated, Variable-Speed Wind Turbine", Risø-R-1500(EN), Roskilde, Denmark: Risø National Laboratory, January 2005.

[50] Mizukami Y, Nihei Y, Hara N and Iijima K, "A study on motion characteristics of wind turbine on a floating platform in blade pitch control malfunction", Proceedings of JASNAOE Spring Meeting, May 2015.

[51] Iijima K, Kawai M, Nihei Y, Murai M and Ikoma T, "Conceptual Design of a Single-Point-Moored FOWT and Tank Test for Its Motion Characteristics", Proceedings of ASME 2013, 32nd International Conference OMAE2013-11259.

[52] Sharath S, Iijima K, Nihei Y and Hara N, "Coupled Simulation between FAST and Hydro-Structural Code for a flexible FOWT considering blade pitch control malfunction", Proceedings of ASME 2016, 35th International Conference OMAE2016-54352.

[53] Iijima K, Suzaki Y and Fujikubo M, "Scaled model tests for the post-ultimate strength collapse behaviour of a ship's hull girder under whipping loads", Journal of Ships and Offshore Structures, January 2014.

[54] Iijima K, Kimura K, Xu W and Fujikubo M, "Hydroelasto-plasticity approach to predicting the post-ultimate strength behavior of a ship's hull girder in waves", Journal of Marine Science and Technology, Vol. 16, pp. 379-389, 2011.

[55] IEC 61400-1:2005 Report "Wind turbines - Part 1: Design requirements"